A STUDY OF J/ψ PRODUCTION IN 260 GEV π^--NUCLEUS COLLISIONS

BY
CHRIS ADOLPHSEN
DECEMBER, 1985

Enrico Fermi Institute

The University of Chicago

Dissertation

A STUDY OF J/ψ PRODUCTION IN 260 GEV π^--NUCLEUS COLLISIONS

BY
CHRIS ADOLPHSEN
DECEMBER, 1985

THE UNIVERSITY OF CHICAGO

A STUDY OF J/ψ PRODUCTION IN 260 GEV π^--NUCLEUS COLLISIONS

A DISSERTATION SUBMITTED TO
THE FACULTY OF THE DIVISION OF THE PHYSICAL SCIENCES
IN CANDIDACY FOR THE DEGREE OF
DOCTOR OF PHILOSOPHY

DEPARTMENT OF PHYSICS

BY
CHRIS E. ADOLPHSEN

CHICAGO, ILLINOIS
DECEMBER, 1985

ACKNOWLEDGEMENTS

The efforts of a number of people went toward making this experiment a success. For their excellent work in the design and construction of the MWPC electronics, I thank Harold Sanders and the Electronic Development Group. The technical support staff were a big help in the construction of our detectors and deserve acknowledgement. They include Dick Armstrong, Rudi Gabriel, Rich Northup, Archie Ryan and Larry Fiscelli.

It is a pleasure to thank my collaborators: from Chicago, Jim Pilcher, Kelby Anderson, Wyatt Merritt, Jim Alexander, John Conway, and Joel Heinrich; from Princeton, Stew Smith, Frank Shoemaker, Kirk McDonald, Bill Louis, John Greenhalgh, Sandro Palestini, and Cristina Biino; and from Iowa State University, Eli Rosenberg and Dave Simpson. For sharing his technical knowledge with me both on and off Lake Michigan, I extend special thanks to Kelby Anderson. Finally, I thank Jim Pilcher, my thesis sponsor, for his many helpful comments on this thesis.

TABLE OF CONTENTS

Chapter

LIST OF TABLES

LIST OF ILLUSTRATIONS

ABSTRACT

Results are presented on the measurement of J/ψ production in the interactions of 260 GeV/c negative pions with a tungsten target. The data sample consists of nearly 80 thousand di-muons from J/ψ decays. From the good acceptance properties of the detector, a fairly complete determination of the forward production cross section was achieved. The J/ψ and ψ' cross sections are reported as are the differential J/ψ cross sections in X_F, P_T^2 and the angular variables describing the di-muon decays.

The differential cross section in X_F is examined within the framework of the fusion model to extract the gluon structure function of the pion and nucleon. The results agree well with expectations and other measurements. The large P_T^2 cross section is compared with a model which assumes that the fundamental production mechanism is $gg \to gJ/\psi$. However, the predicted cross sections are an order of magnitude smaller than the data and fail to match the observed angular distributions.

CHAPTER I

HADRONIC J/ψ PRODUCTION

1.1 Introduction

Of the hundreds of subatomic particles that have been observed in nature, those which interact strongly (hadrons) are by far the most numerous and diverse. These states are believed to be composed of more fundamental spin one-half particles called quarks (q) and anti-quarks ($\overline{q}$). Hadrons of integral spin (mesons) are viewed as $q\overline{q}$ pairs and those of half-integral spin (baryons) are qqq or $\overline{q}\,\overline{q}\,\overline{q}$ combinations. Although free quarks have not been observed, their characteristics, and indeed existence, has been inferred from the static properties of hadrons and short distance probes of matter. Their principle distinction from leptons (e.g., the electron) appears to be only that they are subject to strong interactions.

In the classification scheme of hadrons proposed over two decades ago by Gell-Mann and Zweig,[1] three quarks (u, d, s) were able to account for the observed states. However, a fourth quark 'flavor' referred to as charm (c) was postulated at this time to construct a symmetric model of the weak interactions with the four known leptons (e, ν_e, μ, ν_μ).[2] The first experimental evidence of the existence of a new quark flavor came with the observations in November of 1974 of a e^+e^- resonance (3.1 GeV/c^2) by independent research groups at BNL[3] and SLAC.[4] It was called the J/ψ as a combination of names suggested by each of its discoverers. The unique feature of the J/ψ was its narrow decay width ($\Gamma = .06\ MeV$) relative to other mesons ($\Gamma > 1\ MeV$). From its observed properties, it is thought to be a vector state of a charmed and anti-charmed quark pair ($c\overline{c}$). It was not until 1976 that a meson (D: 1.9 GeV/c) consistent with having net charm (e.g., $c\overline{d}$) was discovered.[5]

Other particles which have the characteristics of a $c\overline{c}$ state (charmonium) were observed in e^+e^- interactions soon after the J/ψ discovery. Their spectroscopy has been well described in non-relativistic models[6] where the charmed quark mass is assumed to be approximately $M_{J/\psi}/2$. In this picture, the J/ψ is identified as the lowest energy radial state of the L = 0, S = 1 series. Figure 1 illustrates the states in the charmonium system with masses below the $D\overline{D}$ threshold.

Over the last ten years, the J/ψ has been observed in fixed target experiments using nearly every type of available secondary beam. These include hadrons[7-13] (π, K, p, $\overline{p}$), leptons[14-16] (μ, ν, $\overline{\nu}$) and photons.[16-18] The usual mode of identifying the J/ψ or the ψ' is through reconstructing their decays to lepton pairs. In this channel, the ψ' signal is roughly 50 times smaller than the J/ψ.

The experiment reported here measured di-muon production in the collisions of a 260 GeV/c negative pion beam with a tungsten target. Although the emphasis of the experiment was on the study of massive, non-resonant pair production, the large sample of J/ψ decays (80,000) also provided an opportunity to study its production characteristics. The unique feature of the detector was its good acceptance properties in the kinematic region where the pair is produced with a large fraction of the beam momentum. This allowed us to extend the study of J/ψ production into a kinematic area that had not been well measured in the past.

At present, the mechanisms leading to J/ψ production in hadronic reactions are not well understood. In this chapter, the current models of J/ψ production are examined. The predictions from these models are compared to our data in the last chapter. To begin, the basic ideas on hadron structure are reviewed and the information needed for the model calculations is given.

1.2 Hadron Structure

The evidence for quark currents in hadrons has come from probes of matter at scales much smaller than the hadron size. The most direct experimental approach has been the measurement of the inelastic scattering of leptons by nucleons (see Figure 2a). The general form of the cross section for this process in the single photon exchange approximation can be written as[19]

$$\frac{d\sigma^2}{dQ^2 d\upsilon} = \frac{4\pi^2\alpha^2}{Q^4}\,\frac{E'}{E\upsilon}\left(F_2(\upsilon,Q^2)\cdot\cos^2\frac{\theta}{2} + \frac{\upsilon}{M_n{}^2}\cdot F_1(\upsilon,Q^2)\cdot\sin^2\frac{\theta}{2}\right) \qquad [1.1]$$

where

E, E' = lepton lab energy before and after scattering
θ = scattering angle of the lepton in the lab frame
$Q^2 = -(l - l')^2$; l, l' = initial and final state lepton four momentum
$\upsilon = 2P\cdot(l - l')$; P = nucleon four momentum ($P^2 = M_n^2$).

The Lorentz invariant and dimensionless functions F_1 and F_2 represent the unknown couplings of the nucleon to the lepton current.

The simpliest derivation of these couplings from the viewpoint of a hadron as a composite system has been done via the parton model.[20] By 'parton', one generally means any particle at the sub-nucleon level. In this application however, which had led to the development of this model, it refers specifically to those particles which couple to the photon in the same manner as a lepton (i.e., a Dirac particle). The tenets of this model are that for inelastic interactions at short time/distance scales (Q^2, $\upsilon >> M_n^2$), the hadron can be treated as a collection of on-shell (i.e., not virtual) partons of negligible mass. These particles are characterized by the fraction, x, of the hadron's momentum they carry as viewed in a reference frame where the hadron has a large momentum ($|\vec{P}| >> M_n$). Their transverse momentum components, k_t, relative to the hadron's direction are assumed to be small ($k_t < M_n$). The internal structure of the hadron is represented by the probability for parton i to have a momentum fraction x and will be denoted here by $g_i(x)$. A more commonly referred to measure of this distribution is the *structure function*, $f_i(x)$, which is defined as $x\cdot g_i(x)$.

In the parton description of the deep inelastic scattering process, the lepton exchanges a photon with one of the constituents in the hadron (see Figure 2b). The calculation of the cross section in this case is straightforward assuming that the final state parton is on-shell and that the hadronization of the final state system can be ignored. Comparing the results to the general expression given above yields the relations[19]

$$F_2(\upsilon, Q^2) = \frac{2Q^2}{\upsilon}\cdot F_1(\upsilon, Q^2) = \sum_i \int_0^1 e_i^2\cdot f_i(x)\cdot\delta(x - \frac{Q^2}{\upsilon})\, dx \qquad [1.2]$$

where e_i is the charge of parton i in units of the electron's charge. Thus, in this model, F_1 and F_2 are only functions of the quantity Q^2/υ which is the momentum fraction of the struck parton. This simplification is referred to as Bjorken scaling and is a direct consequence of the fact that the parton-lepton scattering is assumed to be elastic. The equality $F_2(x) = 2xF_1(x)$ follows from the conservation of helicity in parton scattering in the relativistic limit. Thus the parton model gives two predictions for the characteristics of F_1 and F_2 independent of the specific forms of the parton structure functions. Experimentally[21] scaling is observed to be approximate in that the measured values of F_2 at fixed x vary within a factor of two over Q^2 ranges as large as $1 < Q^2 < 100\ GeV^2/c^2$. Also, the measured ratio $2xF_1/F_2$ is consistent with unity at the 10% level. The deviations from scaling have been reasonably well explained by strong interaction effects. This will be discussed in the next section.

The most complete measurements of the nucleon structure functions have been done using neutrinos instead of charged leptons as the probe in the deep inelastic scattering process. The advantage of this approach is that generalized cross section includes a third coupling, F_3, which when averaged for ν and $\bar{\nu}$ scattering, can be written as the difference of the parton and anti-parton structure functions. Since F_2 in this case is a sum of structure functions, a comparison of the F_2 and F_3 distributions extracted from the cross section measurements provides a means of isolating the parton components. In the picture that emerges from this study, the dominant contribution to F_2 for $x > .2$ is from the quarks associated with the classification scheme of the nucleons; 'uud' for protons and 'ddu' for neutrons. They are referred to as the *valence* quarks and their contribution at lower x can also be determined. This interpretation is supported by the fact that the number of valance quarks estimated from integrating the total measured momentum density is consistent with three.[24]

As x approaches zero, the contribution to F_2 from anti-partons becomes dominant. Such partons are assumed to arise from quark pair production processes so an equivalent distribution of quarks should be present. This symmetry thus allows one to isolate the various pieces of the total quark distribution. The members of these pairs are called *sea* quarks and their momentum distribution near $x = 0$ is roughly $1/x$ as expected naively from the analogous process in electromagnetic interactions. The nucleon structure function measurements show that roughly 15% of the momentum is carried by the sea and 35% by the valence quarks. The remaining 50% is assumed to be carried by the quanta exchanged in quark interactions.

1.3 Quantum Chromodynamics and Nucleon Structure Functions

To further elaborate on the topic of hadron structure, a brief review of the fundamentals of the current theoretical view of strong interactions is needed. This theory, called quantum chromodynamics (QCD),[22] has been under test for the last ten years without any major inconsistencies and has been fairly successful in describing a wide range of 'hard' scattering phenomena such as the production of large transverse momentum jets in hadron collisions. In form, it is similar to the quantum electrodynamic (QED) treatment of electromagnetic processes in that the forces are assumed to be mediated by massless vector bosons. In this case, they are called gluons and the source charges of these fields are referred to as color. Each quark flavor comes in three varieties of color that are represented as a triplet of the group SU(3). In the formulation of QCD to be gauge invariant under local rotations of the color 'coordinates', one type of gluon is associated with each of the eight generators of the SU(3) group. The fact that some of these generators do not commute allows for gluon-gluon couplings which are not possible for photons in the QED description. Despite these complications, the amplitudes calculated for simple perturbative processes not involving gluon-gluon interactions reduce to the equivalent QED result with a change in the normalization.

The feature of QCD that makes perturbative calculations imaginable in a world of strongly bound quarks is that the quark-gluon coupling strength, α_s, decreases as the distance scale of the interaction becomes smaller. The expression for the evolution of α_s is $12\pi/(25\cdot\ln(W^2/\Lambda^2))$ where Λ is a fundamental constant of the theory and W^2 is a measure of the interaction scale (e.g., Q^2 in deep inelastic scattering).* The least ambiguous estimates of Λ have been obtained from the ratios of the radiative to hadronic decays widths of the Υ states.** Comparing the measurements of these ratios, which are expected to be roughly proportional to α_s/α, to the predictions calculated to second order in perturbation theory yields $\Lambda = 120 \pm 80\ MeV/c$.[23] The value of α_s derived from this result that is appropriate to the J/ψ production mechanisms discussed later is .28 ± .8 .

---

* This result was obtained assuming four excited quark flavors in a single loop correction to the gluon propagator.

** The Υ states are viewed as bound pairs of *bottom* (b) quarks ($m_b \approx 4.8\ GeV/c^2$) analogous to the charmonium system.

In an analysis of deep inelastic scattering which incorporates QCD, the notion of a 'bare' parton distribution is not valid since the lowest order strong interaction corrections (see Figures 1c to 1e) are large. It has been shown, however, that such interactions can be factorized into a non-perturbative piece, which one treats as part of the definition of the structure functions, and a perturbative part which includes the large momentum transfer regime of the radiation and pair productions processes shown in Figure 1. As a result, the change in the structure functions between two values of Q^2 (both large) can be predicted since only the strong interaction corrections in the perturbative region differ in these cases. One expects the structure function distributions to shift toward smaller values of x as Q^2 increases. In naive terms, this results because the phase space for gluon radiation increases with larger Q^2 so a quark is likely to lose more momentum while being 'measured' by the photon probe.

The CDHS group[24,25] has analyzed the Q^2 dependence of their structure functions data within this framework and find a reasonable agreement with expectations. The value of Λ was actually derived in this comparison and is consistent with the results noted above. The gluon structure function can also be extracted in this approach since gluons contribute to the 'observed' quark distributions through pair production as illustrated in Figure 2e. This measurement will be described later.

For the analysis in this work that required estimates of the nucleon structure functions, the CDHS results evaluated at $Q^2 = M^2_{J/\psi}$ were used. They are

$$\begin{aligned} f_{u/p}(x) &= 2.4 \cdot x^{53} \cdot (1-x)^{2.9} \qquad [1.3] \\ f_{d/p}(x) &= 1.4 \cdot x^{53} \cdot (1-x)^{3.9} \\ f_{sea}(x) &= .25 \cdot (1-x)^{8.2} \end{aligned}$$

where $f_{u/p}$ and $f_{d/p}$ denote the valence structure functions of a proton. The quark contributions to the sea term, f_{sea}, are expressed by $.2 \cdot f_{sea} = f_{u,sea} = f_{\overline{u},sea} = f_{d,sea} = f_{\overline{d},sea} = 2 \cdot f_{s,sea} = 2 \cdot f_{\overline{s},sea}$. The specific measurements by the CDHS group showing that $f_{d/p}(x)/f_{u/p}(x) \sim (1-x)$ and $f_{s,sea} \approx .25 \cdot (f_{u,sea} + f_{d,sea})$ were used to obtain these results while the equality between the $f_{u,sea}$ and $f_{d,sea}$ distributions was assumed. The structure functions of the neutron follow from the above results by isospin symmetry (i.e., with u and d interchanged). For the applications of these distributions considered here, statistical errors in their measurement can be ignored.

1.4 The Drell-Yan Model

The most successful extension of the ideas developed in deep inelastic scattering to hadron-hadron interactions has been in the description of non-resonant lepton pair production at large mass. As proposed by Drell and Yan, these pairs are produced from the annihilation of a quark in one hadron with an anti-quark in the other (see Figure 3a). Although the basic sub-process in both the Drell-Yan mechanism and deep inelastic scattering is electromagnetic, the situation is more complicated in the former reaction from a QCD perspective since the incident quarks can interact with spectator partons in the other hadron before it annihilates. Recent theoretical work has shown that this effect does not destroy the ability to treat the parton distributions in each hadron independently when calculating the annihilation cross section or any other hard scattering process.[26] An important result of this factorization study is that the structure functions that enter into the calculations for pair production can be identified with the deep inelastic scattering results with Q^2 replaced by the square of the invariant mass of the pair, M^2.

To illustrate these ideas, consider muon pair production from the interactions of two hadrons, h_1 and h_2, whose center of mass energy is $S_o^{1/2}$. The cross section is given by

$$\frac{d\sigma}{dM} = \sigma_o(M)\cdot\int dx_1\cdot dx_2 \;\; \kappa(x_1,x_2,S_o)\cdot\delta(M^2 - x_1\cdot x_2\cdot S_o) \qquad [1.4]$$

$$\cdot \sum_{i=u,d,s} e_i^2\cdot\big(g_{q_i/h_1}(x_1,M^2)\cdot g_{\overline{q}_i/h_2}(x_2,M^2) + g_{\overline{q}_i/h_1}(x_1,M^2)\cdot g_{q_i/h_2}(x_2,M^2)\big)$$

where $e_i^2\cdot\sigma_o$ is the $q_i\overline{q}_i$ annihilation cross section, $4\cdot\pi\cdot\alpha^2\cdot e_i^2/(9\cdot M^2)$. The delta function in this expression constrains the quark pairs to have an invariant mass equal to that of the observed di-muon. In the parton model, κ is equal to unity which reduces the cross section to the form for two colliding quark 'beams'. In the QCD improved picture of this process, this factor is included to account for strong interaction corrections beyond those implicit in the use of quark distributions measured in deep inelastic scattering. However, the calculations of κ that have been done to order α_s show it to be nearly independent of M^2 or the quark momentum fractions.[27] Comparing the di-muon cross sections measured from pN or $\bar{p}$N interactions with the above predictions using the CDHS structure functions yields $\kappa \approx 2$ when it is treated as a constant factor.[28] Although the theoretical expectations for κ are similar, it has not been conclusively shown that higher order corrections do not drasticly alter this large lowest order result.

Historically, equation 1.4 has been used to derive the structure functions from lepton pair data with κ included as an overall normalization parameter. This is particularly revealing in the case of pion induced pair production since the pion structure functions have not been measured by the deep inelastic scattering approach. To discuss the methods involved, a further description of the kinematics of lepton pair production is necessary. Since it is also relevant to the J/ψ analysis presented here, the full set of variables will be defined for the πN interactions of this work.

The two muon momentum vectors measured in pair production yield six independent variables: four describe the characteristics of the sum of the muon four momenta and two specify the angular degrees of freedom in the pair's rest frame. In our study, the former are defined as

$M =$ invariant mass of the pair

$P_T =$ transverse momentum of the di-muon relative to the incident pion direction

$X_F =$ the ratio of pair's longitudinal momentum, P_L in the pion-nucleon center of mass frame to its maximum value, where

$$P_{L,max} = \frac{S_o^{1/2}}{2} \cdot \left[(1 - \frac{M^2}{S_o})^2 - \frac{4 \cdot P_T^2}{S_o} \right]^{\frac{1}{2}} . \qquad [1.5]$$

The term in the bracket is nearly unity in our application since $S_o \approx 500\ GeV$. Without this factor, X_F reduces to the standard definition of Feynman X variable, $2 \cdot P_L / S_o^{1/2}$, that is applicable in the asymptotic limit, $S_o \rightarrow \infty$. In the expression for $P_{L,max}$, the mass of the recoil system is ignored since it can be as low as the nucleon mass, M_n, and would contribute only as a $1 - M_n^2/S_o$ factor.

$\Phi_{lab} =$ azimuth of the P_T vector about the beam axis (its exact definition is given later when the apparatus coordinate system is defined). Since our target and beam were unpolarized, the measured cross sections should be independent of this variable.

The coordinate system in the di-muon rest frame used to specify the angular variables is shown in Figure 4. This particular reference system is called the Collins-Soper frame[29] and is defined such that the polar axis $\hat{Z}$ bisects the pion and the nucleon momentum directions. The reason for this choice is described below. With these coordinate axes, the momentum vector, $P^*_{\mu^+}$, of the positive muon in this frame defines the variables

$$\cos(\theta) = \frac{P^*_{\mu^+}\cdot\hat{Z}}{|P^*_{\mu^+}|} \qquad \phi = \tan^{-1}\left(\frac{P^*_{\mu^+}\cdot\hat{X}}{P^*_{\mu^+}\cdot\hat{Y}}\right) . \qquad [1.6]$$

The angle between pion and nucleon momentum vectors is approximately $\tan^{-1}(P_T/M)$ and thus ϕ is undefined in the $P_T \rightarrow 0$ limit.

In the naive calculation of the $q\bar{q} \rightarrow \mu^+\mu^-$ angular cross section, the strong interactions are ignored. Since these produce the P_T of the pairs, there is an ambiguity as to the 'actual' annihilation axis when trying to compare the predicted cross sections with the data. The use of the Collins-Soper frame averages this uncertainty between the beam and target directions. If the P_T cross sections are calculable, however, the choice of reference frame is arbitrary.

The question of the dynamical origin of the transverse momentum of the di-muons also has to be addressed when attempting to calculate the momentum fractions of the annihilating quarks from the kinematic variables measured for a di-muon. Since there is not a well defined theoretical approach, the simplest method is generally used where the P_T of the muon pair and the initial quarks are treated as zero when deriving these quantities. The equations that result will be referred to as the ***fusion constraints*** and are given below.

$$x_\pi \cdot x_n = M^2/S_o \equiv \tau \qquad [1.8]$$

$$x_\pi - x_n = X_F\cdot(1 - \tau) \qquad [1.9]$$

Here x_π and x_n are the momentum fractions of the quarks in the pion and nucleon respectively. Solving for the momentum fractions yields

$$x_\pi = .5\cdot\left(X_F\cdot(1-\tau) + (X_F{}^2\cdot(1-\tau)^2 + 4\cdot\tau)^{1/2}\right) \qquad [1.10]$$

$$x_n = .5\cdot\left(-X_F\cdot(1-\tau) + (X_F{}^2\cdot(1-\tau)^2 + 4\cdot\tau)^{1/2}\right) . \qquad [1.11]$$

If one were to assume that the P_T of a muon pair is the sum of an initial transverse momenta of each of annihilating quarks, then the momentum fractions derived would only change on the order of P_T^2/S_o from those obtained using the above expressions.

Treating κ as a constant and using the definitions that have been given, equation 1.4 can be reexpressed as*

$$\frac{d\sigma}{dX_F dM^2} = \frac{\kappa \cdot \sigma_o}{x_\pi + x_n} \qquad [1.12]$$

$$\cdot \sum_{i=u,d,s} e_i^2 \cdot \left(f_{q_i/\pi}(x_\pi, M^2) \cdot f_{\overline{q}_i/n}(x_n, M^2) + f_{\overline{q}_i/\pi}(x_\pi, M^2) \cdot f_{q_i/n}(x_n, M^2) \right) .$$

This relation is used to extract the structure functions from the di-muon cross section measurements. This is done in the $M > 4\ GeV/c^2$ mass region where Drell-Yan production is thought to be the dominant source of di-muons. Due to the limited mass range of the data (usually up to 8 GeV/c^2), the structure functions are usually assumed to be independent of M^2 in these calculations.

For applications requiring the pion structure functions in this study, the measurements from the NA3 experiment[30] were used. These distributions were derived from data taken with both π^+ and π^- beams so that the sea and valence terms could be extracted separately. They are

$$f_{v/\pi}(x) = .69 \cdot x^{.45} \cdot (1 - x)^{1.2} \qquad [1.13]$$

$$f_{sea/\pi}(x) = .29 \cdot (1 - x)^{8.4}$$

where the valence term was obtained assuming G-parity invariance: $f_{v/\pi} \equiv f_{\overline{u}/\pi^-} = f_{d/\pi^-} = f_{u/\pi^+} = f_{\overline{d}/\pi^+}$. The constraint that allows the κ factor to be determined is that the valence distributions are normalized to equal the number of quarks (e.g., $\int g_{\overline{u}/\pi^-}(x)\,dx = 1$). The sea distribution, which is assumed to be composed of equal numbers of u, d and s quarks and anti-quarks, is not well determined although it has little effect on the results here. From calculations[31] of the Q^2 type of scaling violations discussed earlier, these functions should not change significantly for M^2 evaluated at $M^2_{J/\psi}$. A bigger effect is from the errors

---

* In all cross section expressions differential in X_F in this work, factors that differ from unity by M^2/S_o or P_T^2/S_o are omitted for simplicity.

on these measurements which will be considered later.

One piece of evidence that suggests one is measuring the quark distributions in these studies is that the $\cos(\theta)$ distribution over most of the X_F range is consistent with the $1+\cos^2(\theta)$ prediction for the annihilation process. Also, the ratio of the π^+ to π^- induced di-muon production is roughly equal to the naive expectations of e_d^2/e_u^2 in the kinematic regions where the sea contributions are expected to be small.[12] Finally, the nucleon structure functions, which are most accurately obtained from pN and $\bar{p}N$ data with this method, are consistent with the deep inelastic scattering results.[30]

1.5 J/ψ Production Through Direct Quark Fusion

With the successes of the parton model in describing most of the features of high mass di-muon production, it is natural to try to extend these ideas to the case of the J/ψ. The translation involves replacing the $q\bar{q}$ annihilation cross section with the Breit-Wigner resonant production formula. This formula relates the decay widths of the J/ψ to various parton pairs, to the cross section for the inverse production reaction. Of the possibilities, the gluon fusion process, $gg \rightarrow J/\psi$, is not allowed since a spin 1 state cannot be formed from two massless vector bosons that is symmetric under interchange. Even for off-shell gluons, the reaction cannot proceed due to the violation of G-parity as applied to color SU(3).[19] Thus, one is left with either the electromagnetic production from $q\bar{q}$ annihilation (Figure 3b) or the strong fusion of quarks which proceeds through a minimum of three gluons (Figure 3c). Using the narrow width approximation for the J/ψ ($\Gamma = 63\ KeV$), the Breit-Wigner relation yields

$$\sigma_{q_i\bar{q}_i} = \frac{4\cdot\pi^2}{3\cdot M^3_{J/\psi}}\cdot\Gamma_{J/\psi \rightarrow q_i\bar{q}_i}\cdot\delta(1 - M^2/M^2_{J/\psi})$$

as the sub-process cross section for quark flavor i. Since the strong decays account for most of the J/ψ width, one can use $\Gamma_{J/\psi \rightarrow q_i\bar{q}_i} = 1/3\cdot\Gamma_{J/\psi \rightarrow all}$ as an estimate when evaluating this expression. Replacing $e_i^2\cdot\sigma_o\cdot\kappa$ in equation 1.4 by the above result and integrating over mass and positive X_F gives,

$$\sigma_{J/\psi}(X_F{>}0) \approx \frac{4\cdot\pi^2}{9\cdot M^3_{J/\psi}}\cdot\Gamma_{J/\psi \rightarrow all}\cdot F_{q\bar{q}}(\tau_{J/\psi}) \ ; \ \tau_{J/\psi} \equiv \frac{M^2_{J/\psi}}{S_o} \qquad [1.15]$$

where

$$F_{q\bar{q}}(\tau_{J/\psi}) = \int_{o}^{1} \sum_{i=u,d,s} \left(f_{q_i/\pi}(x_\pi)\cdot f_{\bar{q}_i/n}(x_n) + f_{\bar{q}_i/\pi}(x_\pi)\cdot f_{q_i/n}(x_n)\right) \frac{dX_F}{x_\pi + x_n} \; . \quad [1.16]$$

The structure functions are evaluated at $M = M_{J/\psi}$ in the convolution integral, $F_{q\bar{q}}(\tau_{J/\psi})$, which is generally referred to as the *excitation function.* Using the quark distributions defined earlier produces $F_{q\bar{q}}(\tau_{J/\psi}) \approx .3$ for S_o appropriate to our beam energy. This yields $\sigma_{J/\psi}(X_F > 0) \approx 1$ *nb.*/nucleon which is about a factor of one hundred smaller than the measurements in this region of τ. If one takes the extreme view that all J/ψ production occurs electromagnetically, and thus weights the structure function products in equation 1.16 according to e_i^2, a similarly small prediction is found.

1.6 Charmed Quark Fusion

In the early studies attempting to explain hadronic J/ψ production, it was also realized that the predictions for strong fusion of light quarks fell far short of the observed cross sections. This prompted speculation that the J/ψ was produced through the fusion of charmed sea quarks coming from each of the colliding hadrons (these quarks were treated as massless although little justification was given).[32] One characteristic prediction of these models is that the J/ψ should be produced in association with other charmed mesons. These mesons result from the remaining imbalance of charmed quarks in the beam and target hadrons. This prediction is true also for the generation of charmonium in either the multi-peripheral type of processes[33] or the more current 'string' models[34] which attempt to explain multi-hadron production as initiated from the scattering of light quarks. Experimentally, this possibility has been examined by looking for extra muons in coincidence with the production of this resonance with the idea that they may be the result of D meson decays. One study[35] finds that at a 90% confidence level, $\sigma_{J/\psi,D,\bar{D}}/\sigma_{J/\psi} < .016$. Thus, this type of production cannot account for a large fraction of the J/ψ cross section.

1.7 Charmonium Decays

Another early model of J/ψ hadronic production attributed its large cross section to the decays of higher mass charmonium states.[36] In particular, the predicted cross sections for P-wave states, χ_J with spin $J = 0,1,2$, and their known branching ratio to the J/ψ were able to account for the measured J/ψ cross section. These predictions are similar to the fusion calculation discussed earlier except that gluon - gluon fusion also contributes to the production of even-spin χ states. The weak point of these calculations, however, is that the hadronic decay widths of these states are not known and so the values of $\Gamma_{\chi \rightarrow q\bar{q}}$ and $\Gamma_{\chi \rightarrow gg}$ have to be estimated from theoretical considerations.

In recent years, there have been a number of experiments to measure this mode of J/ψ production. The method is to observe the radiative transitions of the χ states by reconstructing the χ mass from the J/ψ and the photon. For pion induced production, the most statistically significant results have been obtained by the WA11 group[37] at CERN. They observed a few hundred decays in the interactions of 185 GeV/c negative pions with a beryllium target. From these data they conclude that 18 ± 4 % of the J/ψ's produced were from χ_1 radiative decays and 13 ± 2 % from the χ_2 transitions. The χ_0 signal was not observed which is likely the result of its factor of 10 smaller branching ratio to the J/ψ. The decay contributions were derived assuming that the photon is emitted isotropically and that the differential production cross section of the χ states is the same as that of the J/ψ's. Measurements by other groups with pion beam energies of 38[38] and 225[39] GeV/c find fractions that are consistent with the above results. The production of χ's has also been measured in proton - proton interactions at a center of mass energy of 62 GeV/c and is found to account for about 50% of the total J/ψ cross section.[40]

The production of the J/ψ through ψ' decays is much more easily determined since the ψ' cross section is measured in the same manner as the J/ψ and its branching ratio to this state is known. As will be discussed in the last chapter, our data indicate that about 7% of the J/ψ's result from this process. Since the hadronic decays of other charmonium states to a J/ψ have not been measured, it is not known if the direct J/ψ production cross section, $\sigma_{J/\psi,\mathrm{direct}}$, is smaller than one would deduce from the known indirect sources. One notes, however, that the value of $\sigma_{\psi',\mathrm{direct}}/\sigma_{J/\psi,\mathrm{direct}}$ measured in a photoproduction experiment is in agreement with that predicted for pion and proton induced production by correcting the measured values of $\sigma_{\psi'}/\sigma_{J/\psi}$ for the decay contributions that are known. If the J/ψ to ψ' direct cross section ratio is independent of the production reaction, then a factor of two smaller value of $\sigma_{J/\psi,\text{direct}}$ for pion production would yield a significant disagreement with the photoproduction measurements. Specific values of these cross sections are given in section 7.3 where our results are discussed.

In our examination of possible J/ψ production mechanisms, it will be assumed that the decay modes measured thus far are the only ones contributing significantly. In this case, the WA11 measurements indicate that $\sigma_{J/\psi,\text{direct}}$ is about 60% of $\sigma_{J/\psi}$ and it is in proportion to the other charmonium cross sections as follows.

$$\sigma_{J/\psi,\text{direct}} : \sigma_{\chi_1} : \sigma_{\chi_2} : \sigma_{\psi'} \;=\; 1 : 1.0 \pm .3 : 1.3 \pm .4 : .25 \pm .06 \qquad [1.17]$$

1.8 Generalized Fusion Predictions

After accounting for the decay contributions, the direct J/ψ cross section is still about 60 times larger than the predictions based on $\Gamma_{J/\psi \to \text{hadrons}}$. The current approaches that attempt to explain this difference consider modes of J/ψ production that require interactions with the spectator system. Figures 5a and 5b illustrate the lowest allowed diagrams in this case for both gg and $q\bar{q}$ initiated production. Here, color and spin-parity conservation constraints are realized through interactions involving other initial state particles and thus there are no correspondences between these reactions and the decay modes of the J/ψ. The single photon exchange process is not considered since spectator interactions are not necessary for it to occur and are thus unlikely to be the cause of the large difference between the direct fusion predictions and the measured cross sections. (note that the cross section predictions for other electromagnetic processes such as Drell-Yan production and $e^+ + e^- \to$ hadrons are in much better agreement with observations).

Although these ideas may be intuitively appealing, they are not easily translated into calculable cross sections. The simplest treatment of this problem assumes that the spectator interactions are 'soft' so that the fusion constraints can still be used to derive the momentum fractions of the incident partons.[13,46]

The gg and $q\bar{q}$ partons cross sections in this case are treated as unknowns. One does not predict the absolute J/ψ cross sections but uses their measured values to obtain information on the magnitude of the quark and gluon contributions to its production. Also, the gluon structure functions can be derived from the differential cross sections in X_F using methods similar to that applied to obtain the quark structure functions. As will be apparent later, there are consistency checks of these assumptions that can be made using the data. In section 1.10, a less empirical treatment of these production modes is discussed and a prediction for the relative magnitude of the parton cross sections is given.

To examine the more general approach, let the unknown parton cross sections be represented by

$$\sigma_{i,j} = K^j{}_i \cdot \delta(1 - M_i^2/M_j^2) \qquad [1.18]$$

where M_i is the invariant mass of the incident $i=q\bar{q}$ or gg pair, and M_j is the mass of the charmonium state j ($= J/\psi$, χ_1, χ_2, ψ'). The $X_F > 0$ J/ψ cross section is written

$$\sigma(X_F>0) = \sum_j \left(K^j{}_{gg} \cdot F_{gg}(\tau_j) \cdot B(j \rightarrow J/\psi) + K^j{}_{q\bar{q}} \cdot F_{q\bar{q}}(\tau_j) \cdot B(j \rightarrow J/\psi) \right) \qquad [1.19]$$

where $F_{q\bar{q}}(\tau_j)$ is defined in equation 1.16 and

$$F_{gg}(\tau_j) \equiv \int_0^1 \frac{f_{g/\pi}(x_\pi) \cdot f_{g/n}(x_n)}{x_\pi + x_n} \, dX_F \quad ; \tau_j = M_j^2/S_o \, . \qquad [1.20]$$

Here, $f_g(x)$ is the gluon structure function and $B(j \rightarrow J/\psi)$ is the branching ratio of charmonium state j to decay to a J/ψ (note $B \equiv 1$ for $j = J/\psi$).

As an application of this formalism, estimates were made of the relative size of the gluon contribution to J/ψ production in $\pi^- N$ and $\bar{p}N$ interactions. The method uses the production cross sections that have been measured in both particle and anti-particle beams. Since the the gluon fusion cross sections and excitation functions are the same in each case, the predictions can be made independent of the gluon structure functions. To do the calculation, the excitation functions for producing the χ_1, χ_2 and ψ' states were set equal to that of the J/ψ. Specific estimates of these functions show that this is a good approximation for the application considered here. With this assumption and the definitions

$$F_{gg} \equiv F_{gg}(\tau_{J/\psi}) \qquad K_{gg} \equiv \sum_j K^j{}_{gg} \cdot B(j \rightarrow J/\psi) \qquad [1.21]$$

$$F_{q\bar{q}} \equiv F_{q\bar{q}}(\tau_{J/\psi}) \qquad K_{q\bar{q}} \equiv \sum_j K^j{}_{q\bar{q}} \cdot B(j \rightarrow J/\psi)$$

the production cross section is written

$$\sigma(X_F > 0) = K_{gg} \cdot F_{gg} + K_{q\bar{q}} \cdot F_{q\bar{q}} \, . \qquad [1.22]$$

To compare π^+ and π^- induced J/ψ production, only hydrogen target measurements were used. Those obtained from isoscalar targets should be equal by isospin invariance if strong interactions are the dominant source of production. Values measured on platinum (Z/A = .4) targets[13], for example, agree within 2% and thus are consistent with this assumption.

The fraction of J/ψ's produced from gluon fusion in $\pi^- p$ interactions, $R^{\pi^-}_{gg}$, is expressed in this model as,

$$R^{\pi^-}_{gg} \equiv \frac{K_{gg} \cdot F_{gg}}{K_{gg} \cdot F_{gg} + K_{q\bar{q}} \cdot F^{\pi^-}_{q\bar{q}}} = 1 - \frac{1 - \sigma(\pi^+ p)/\sigma(\pi^- p)}{1 - F^{\pi^+}_{q\bar{q}}/F^{\pi^-}_{q\bar{q}}} \, . \qquad [1.23]$$

Using the quark structure functions defined earlier to evaluate the ratio of the $\pi^+ p$ to $\pi^- p$ excitation functions at the values of τ appropriate to the measurements[41] yields the values below.

Beam Energy	$\sigma(\pi^+ p)/\sigma(\pi^- p)$	$F^{\pi^+}_{q\bar{q}}/F^{\pi^-}_{q\bar{q}}$	$R^{\pi^-}_{gg}$
39.5	.78 ± .09	.50	.56 ± .18
150.	.95 ± .03	.69	.84 ± .10
200.	.92 ± .03	.72	.71 ± .11

The errors on $R^{\pi^-}_{gg}$ do not account for the uncertainties in the measurements of the quark structure functions although their contribution in each case is estimated to be less than a third of that from the cross section ratios. Repeating these calculations for measurements[41] of J/ψ production in proton and antiproton interactions with heavy targets gives the following values.

Beam Energy	$\sigma(pN)/\sigma(\bar{p}N)$	$F^{p}_{q\bar{q}}/F^{\bar{p}}_{q\bar{q}}$	$R^{\bar{p}}_{gg}$
39.5	.19 ± .04	.06	.13 ± .04
150.	.48 ± .07	.24	.31 ± .06
200.	.71 ± .10	.28	.60 ± .14

Thus for both incident π^-'s and $\bar{p}$'s, which each contain valence anti-quarks, the predicted gluon fusion contribution is much different than the $R_{gg} = 0$ result expected if only direct fusion is allowed.

The measurements of $d\sigma/dX_F$ provide additional information on the gluon induced component of J/ψ production within the fusion model. Using the version of equation 1.19 differential in X_F, one fits the X_F cross section to the sum of the quark and gluon fusion spectra. The shape of the former distribution is fixed while the latter is allowed to vary using parametrizations for the gluon structure functions. Besides yielding the gluon distribution, this procedure gives the values for parton cross sections. In the next two sections, the expectations for these results are discussed and in section 7.4 this formalism is applied to our data.

1.9 Gluon Structure Functions

Before considering some of the experimental measurements of the gluon structure functions, it is useful to note some of the theoretical prejudices on this subject. The most commonly quoted form of $f_g(x)$ is based on the counting rule arguments that were originally purposed to predict the large x behavior of the quark structure functions. In one derivation of these rules, a naive perturbative calculation is done for the amplitude of one parton to acquire nearly all of the hadron's momentum through a series of gluon exchanges involving each of the other constituents.[42] The large x form of the structure function that results is $(1 - x)^n$ where n is equal to twice the total number of partons minus three. The quark structure function parameters obtained in this manner are $n = 1$ for a pion and $n = 3$ for a nucleon, and are in fair agreement with the data. Treating the gluon as a constituent in addition to the quarks yields $n = 3$ (5) for its structure function in a meson (baryon).

It has been argued, however, that these rules are not applicable to gluons.[43] The principal authors of the counting rules have in fact presented results for these distributions based on a naive treatment of the gluon bremsstrahlung of the quarks.[44] The calculations differ from those used to determine the Q^2 evolution of the quark structure functions in that bound state effects are modeled and the results are not limited to the regime of large momentum transfers to the gluons. One of their conclusions is that if the quark structure functions at high x have the form, $(1 - x)^{n-1}$, then the resulting shape of the gluon structure function in this x region is $(1 - x)^n$. From the quark structure function measurements given earlier, one then expects n = 2.2 for the gluon spectrum in pions and n = 3.9 for that in protons. The low x behavior of the gluon distribution is predicted to have the form $1/x$ as expected from the analogous bremsstrahlung process in QED.

Given these results, the gluon structure functions are most simply represented by $(1 - x)^n$ to match the expectations in both the high and low x regions (note $f_g(x) = x \cdot g_g(x)$). This function can be normalized by using the momentum conservation constraint that the sum of the integrated gluon and quark structure functions equal unity. From the quark measurements given, one finds that the total momentum fraction carried by the gluons is within a few percent of .5 for both pions and nucleons. With this information, the *standard* form of the gluon structure function is defined for our analysis as follows.

$$f_g(x) = .5 \cdot (n+1) \cdot (1 - x)^n \qquad [1.24]$$

The only claims of a direct measurement of the gluon structure function of the pion have been from the analysis of J/ψ and Υ data by the methods discussed here. Without detailing the various assumptions used in these determinations, one notes that values of n extracted using the above expression are in the range of 2 to 3.[13,45,46] Although the cross sections from πN interactions in these cases also yield a measure of the gluon structure function of the nucleon, a more sensitive determination of this distribution is obtained by extending these methods to the pN, $\bar{p}N$, or γN results. Here, the measurements of n vary from 4 to 7. [13,15,16,45,47]

As discussed earlier, the gluon distribution in a nucleon can be inferred from the Q^2 variation of the quark structure functions. The CDHS group has parametrized their results[25] in a form that can be easily evaluated at any scale. For $Q^2 = M^2_{J/\psi}$, the behavior of the gluon structure function near x =0 is $(1-x)^{7\pm1}$ while at $x = .10$, which is the largest value relevant in the fits to our $d\sigma/dX_F$ data, it is of the form, $(1-x)^{6\pm1}$.

1.10 Duality Predictions

A theoretical framework that has been used to calculate the charmonium cross sections from gg and $q\overline{q}$ interactions is referred to as semi-local duality. The duality in this case is the relation between parton and hadron production. This connection is made clearer in a more justifiable form of these arguments applied to charmonium and charmed meson production in e^+e^- interactions.[48] In this case, the following expression can be shown to be approximately valid for 'small' values of k ($k \geq 1$).

$$\int_0^\infty \frac{\sigma(s\colon e^+e^- \rightarrow \text{charm})}{s^k}\, ds = \int_{4 \cdot m_c^2}^\infty \frac{\sigma(s\colon e^+e^- \rightarrow c\overline{c})}{s^k}\, ds \qquad [1.25]$$

The left hand side of this equation is the integral of the bound and open charm cross sections weighted by an inverse power of the square of the e^+e^- center of mass energy, s. This is equated to the corresponding moment of the free charmed quark production cross section whose threshold is the square of twice the charmed quark mass, m_c. Thus, the charmed quark production cross section is related to that for the 'dressed' meson products in a non-local manner. Since the charmed quark mass is not independently known, it can be derived from these equations. Using just the single photon exchange diagram to calculate $\sigma(s\colon e^+e^- \rightarrow c\overline{c})$ yields values for m_c of about 1.25 GeV/c^2 for any k from 1 through 4.

The 'semi-local' attribute refers to the applications of the above relation in which the integrals are evaluated over finite ranges of s. For example, this idea was used with moderate success before the J/ψ was discovered to predict the $e^+e^- \rightarrow$ hadrons cross section above $s = 1.2\ GeV^2$ based on parton cross sections normalized within the duality framework to match the integral of the ω and ϕ cross sections below this region.[49] The partition of the s integration, however, is not well justified theoretically.

The main assumption made in applying these ideas to hadronic interactions is that the gg and $q\overline{q}$ production of charmonium states are 'dual' to their production of charmed quark pairs with an invariant mass in the range of $2 \cdot m_c$ to twice the D meson mass, $2 \cdot m_D$.[50] Thus, the duality relation is used even though some of the direct charmonium production channels are not allowed (e.g $gg \rightarrow J/\psi$ cannot occur). From the model of charmonium production that has been developed from this assumption,[45,47] one predicts the ratio of $q\bar{q}$ to gg bound state production cross sections to be

$$\frac{K^j_{q\bar{q}}}{K^j_{gg}} = \frac{\int_{4\cdot m_c^2}^{4\cdot m_D^2} \sigma(s:\ q\bar{q} \rightarrow c\bar{c})\ ds/s}{\int_{4\cdot m_c^2}^{4\cdot m_D^2} \sigma(s:\ gg \rightarrow c\bar{c})\ ds/s} \qquad [1.26]$$

where s is the square of the parton-parton center of mass energy. Since this ratio is independent of the state produced, any linear combinations of cross sections such as those used to define $K_{q\bar{q}}$ and K_{gg} in equation 1.21 are expected to have the same ratio. Evaluating equation 1.26 using $m_c = 1.25\ GeV/c^2$ and the cross sections[47] calculated from the lowest order $c\bar{c}$ production diagrams yields a value of 1.4 .

To test this result, it was used together with specific estimates of the gluon structure functions to predict the J/ψ production ratios, $\sigma(pN)/\sigma(\bar{p}N)$, $\sigma(pN)/\sigma(\pi^- N)$ and $\sigma(\pi^+ p)/\sigma(\pi^- p)$. The gluon excitation function was computed using the CDHS measurement of the gluon structure function for the nucleon and the parametrization in equation 1.24 with $n = 2.2$ for that of the pion. The predictions and measurements[41] are listed below.

Beam	$\sigma(\pi^+ p)/\sigma(\pi^- p)$		$\sigma(pN)/\sigma(\bar{p}N)$		$\sigma(pN)/\sigma(\pi^- N)$	
Energy	pred.	meas.	pred.	meas.	pred.	meas.
39.5	.76	.78 ± .09	.29	.19 ± .04	.20	.18 ± .04
150.	.93	.95 ± .03	.72	.48 ± .07	.60	.42 ± .04
200.	.95	.92 ± .03	.77	.71 ± .10	.68	.53 ± .05

Assuming other values of n within the range of 2 to 3 or letting the CDHS gluon structure function vary within its errors changes these predictions by less than the uncertainty in the measured values. Thus, the predicted π^+ to π^- ratios are in good agreement with the data while the conclusions from the other comparisons are less clear.

If one instead derives $K_{q\bar{q}}/K_{gg}$ from the $\sigma(\pi^+ p)/\sigma(\pi^- p)$ measurements using the excitation functions as evaluated above, a value of 1.35 ± .4 is obtained.

This result provides a useful point for comparison when other experimental constraints on this quantity are considered in the last chapter.

1.11 Gluon Radiation Model

The large P_T behavior of the J/ψ production cross section has been studied by considering the 'hard' scattering limit of such processes as shown in Figure 5a and 5b.[51–53] In this case, the final state gluons are treated as free and perturbative QCD is used to evaluate the scattering amplitudes. To examine this model further, specific predictions for our data are considered. In this application, the following points are relevant.

- Only the lowest order gluon scattering diagram (Figure 5c) was considered: quark induced production is expected to be small in comparison. Since higher order diagrams of these types have not been computed, it is not clear in what P_T regime such a treatment is valid.
- The contributions to the differential cross section from the decays of other charmonium states were assumed to be in proportion to that from directly produced J/ψ's. For χ production in proton-proton collisions at least, one finds the measured cross sections in P_T are similar to that of the J/ψ.[40]
- The strong coupling strength, α_s, was treated as a constant in the calculations. The gluon structure functions were likewise assumed scale independent.

In the remainder of this section, some of details of the calculations are discussed and in section 7.5, comparisons are made with our data.

The problem faced when computing the amplitude for the $gg \to gJ/\psi$ process is how to treat the coupling of a $c\bar{c}$ pair to the J/ψ bound state (this coupling is symbolized by the circle in Figure 5c). Since the charmonium system is well described in non-relativistic models, the approximation is made that the charmed quarks have zero relative motion in the J/ψ. The J/ψ four momentum, $p_{J/\psi}$, thus equals twice that of the charmed quarks. Letting v and $\bar{u}$ denote the charmed quark spinors and λ their helicity eigenvalues, this approximation is equivalent to representing a J/ψ in state $\lambda_{J/\psi}$ in the amplitude calculation as

$$C \cdot \sum_{\lambda_c, \lambda_{\bar{c}}} < \lambda_c, \lambda_{\bar{c}} | \lambda_{J/\psi} > \cdot v(\lambda_{\bar{c}}, p_{J/\psi}/2) \cdot \bar{u}(\lambda_c, p_{J/\psi}/2) \ . \qquad [1.27]$$

The constant, C, can be expressed in terms of the decay width of the J/ψ to lepton pairs by using the above expression in calculating this particular process.

In terms of the Lorentz invariants,

$$s \equiv (p_{g/\pi} + p_{g/n})^2 \quad t \equiv (p_{J/\psi} - p_{g/\pi})^2 \quad u \equiv (p_{J/\psi} - p_{g/n})^2 \qquad [1.28]$$

which are defined from the J/ψ and incident gluon four momenta, the $gg \rightarrow gJ/\psi$ cross section computed with the above approximation is

$$\frac{d\sigma}{dt} = \frac{5 \cdot \pi \cdot \alpha_s^3 \cdot M_{J/\psi}^3}{16 \cdot \alpha^2 \cdot s^2} \cdot \Gamma_{J/\psi \rightarrow l^+ l^-} \cdot A(s,t) \qquad [1.29]$$

where

$$A(s,t) = \frac{s^2 \cdot (s - M_{J/\psi}^2)^2 + t^2 \cdot (t - M_{J/\psi}^2)^2 + u^2 \cdot (u - M_{J/\psi}^2)^2}{(s - M_{J/\psi}^2)^2 \cdot (t - M_{J/\psi}^2)^2 \cdot (u - M_{J/\psi}^2)^2} \; . \qquad [1.30]$$

With this parton level result, the next consideration is how to obtain the J/ψ production cross section in πN scattering.

Since the radiated gluon in the $gg \rightarrow gJ/\psi$ reaction is unobserved, the measured kinematic variables of the J/ψ do not uniquely specify the momentum fractions of the incident gluons. To see what additional variables are required, consider the following expressions for the momentum fractions which are written as functions of the J/ψ energy, $E_{J/\psi}$, and longitudinal momentum, $P_{L,J/\psi}$, in the pion-nucleon center of mass frame and the corresponding quantities for the radiated gluon, E_g and $P_{L,g}$.

$$x_\pi = \left(E_{J/\psi} + E_g + (P_{L,J/\psi} + P_{L,g})\right) / S_o^{1/2} \qquad [1.31]$$

$$x_n = \left(E_{J/\psi} + E_g - (P_{L,J/\psi} + P_{L,g})\right) / S_o^{1/2} \qquad [1.32]$$

Since it is assumed in the cross section calculations that the incident gluons have zero transverse momentum relative to the hadron directions, the P_T of the J/ψ equals that of the radiated gluon. With this choice of variables, the only quantity that is required beyond X_F and P_T to determine all the momenta in the parton process is $P_{L,g}$. Thus, in computing the cross section for producing a J/ψ at a given X_F and P_T, the parton cross section is integrated over the range of $P_{L,g}$.

To obtain this result, one first notes that the total J/ψ cross section in the parton model formalism is given by

$$\sigma_{J/\psi} = \int g_{g/\pi}(x_\pi)\cdot g_{g/n}(x_n)\cdot d\sigma/dt \quad dx_\pi dx_n dt \, . \qquad [1.33]$$

With the appropriate change of variables,

$$dx_\pi dx_n dt = \frac{x_n\cdot x_\pi}{E_g\cdot E_{J/\psi}}\cdot\left(\frac{S_o - M^2_{J/\psi}}{4} - P_T^2\right)^{1/2}\cdot dP_{L,g}dX_F dP_T^2 \qquad [1.34]$$

it is simple to show

$$\frac{d\sigma}{dX_F dP_T^2} = \left(\frac{S_o - M^2_{J/\psi}}{4} - P_T^2\right)^{1/2}\cdot\int_{P_{L,g}^{\min}}^{P_{L,g}^{\max}} \frac{dP_{L,g}}{E_g\cdot E_{J/\psi}}\cdot f_{g/\pi}(x_\pi)\cdot f_{g/n}(x_n)\cdot\frac{d\sigma}{dt} \, . \qquad [1.35]$$

The integration limits are defined by

$$P_{L,g}{}^{\frac{\max}{\min}} = \pm\frac{1}{2}\left(S_o{}^{1/2} - (E_{J/\psi} \pm P_{L,J/\psi}) - \frac{P_T^2}{S_o^{1/2} - (E_{J/\psi} \pm P_{L,J/\psi})}\right) \qquad [1.36]$$

and the parton cross section variables are related to those in the pion - nucleon center of mass frame as follows.

$$s = x_\pi\cdot x_n\cdot S_o \qquad t = -x_n\cdot(E_g + P_{L,g}) \qquad [1.37]$$

Even though $d\sigma/dt$ is finite for $P_T^2 \rightarrow 0$, the hadron cross section diverges logarithmically in this limit as a result of the $1/E_g$ term. Although one can model the transverse momentum of the incident gluons to make the result finite, this was not done for the comparisons made here since the main interest is in the large P_T predictions.

A dimensional analysis of the total cross obtained from equation 1.35 shows that it can be written as

$$\frac{M^3_{J/\psi}\cdot\sigma_{J/\psi}}{\Gamma(J/\psi \rightarrow l^+l^-)} = h(M^2_{J/\psi}/S_o) \qquad [1.38]$$

where h is some function. Since the cross section for ψ' production should have a similar form, one can predict the ψ' to J/ψ cross section ratio from this scaling relation. This is discussed further in section 7.3 where a comparison to our data is made.

1.12 Angular Distribution Predictions

The angular distributions of the muon pairs reconstructed in the J/ψ rest frame provide a measure of its polarization and hence give information on the production mechanism. If the beam and target are unpolarized, the general form of decay distribution of a J/ψ produced at a given X_F and P_T is,[54]

$$\frac{d\sigma}{d\phi d\cos(\theta)} \sim 1 + \alpha\cdot\cos^2(\theta) + \beta\cdot\sin(2\theta)\cos(\phi) + \gamma\cdot\sin^2(\theta)\cos(2\phi)\,. \qquad [1.39]$$

Here the coefficients are unique to the coordinate system chosen to specify the angular variables. As discussed in section 1.4, the Collins-Soper reference system is assumed in this work.

Since there is no simple fusion mechanism to explain J/ψ production, the angular distributions for the P_T integrated cross sections cannot be calculated. For production at large P_T production, however, one can estimate α, β, and γ based on the $gg \rightarrow gJ/\psi$ production process. These predictions are given below and are compared with the data in section 7.6.

For these calculations, one defines the average of a function, $X(s,t)$, at given X_F and P_T as its convolution with $gg \rightarrow gJ/\psi$ cross section. Ignoring normalization factors, this is written as

$$<X> \equiv \int_{P_{L,g}^{\min}}^{P_{L,g}^{\max}} \frac{dP_{L,g}}{E_g\cdot E_{J/\psi}}\cdot f_{g/\pi}(x_\pi)\cdot f_{g/n}(x_n)\cdot\frac{d\sigma}{dt}\cdot X(s,t)\,. \qquad [1.40]$$

The specific functions in this application are

$$X_0 \equiv \frac{1}{2}\cdot\left(1 + \frac{4\cdot s^3\cdot M_{J/\psi}^2}{B(s,t)}\right)\cdot\frac{ut}{(s+t)\cdot(s+u)} \qquad [1.41]$$

and

$$X_1 \equiv \frac{2\cdot s\cdot M_{J/\psi}}{B(s,t)}\cdot(stu)^{1/2}\cdot\left(t\cdot\frac{s+u}{s+t} - u\cdot\frac{s+t}{s+u}\right) \qquad [1.42]$$

where

$$B(s,t) = s^2\cdot(s - M_{J/\psi}^2)^2 + t^2\cdot(t - M_{J/\psi}^2)^2 + u^2\cdot(u - M_{J/\psi}^2)^2\,. \qquad [1.43]$$

The angular distribution coefficients are related to the 'averages' of these functions by

$$\alpha = \frac{<1> - 3\cdot<X_0>}{<1> + <X_0>} \quad \beta = \frac{<X_1>}{<1> + <X_0>} \quad \gamma = \frac{<X_0>}{<1> + <X_0>} \cdot [1.44]$$

With these equations then, one can compute α, β and γ for any X_F and P_T of the J/ψ.

CHAPTER II

THE EXPERIMENT

2.1 History of the Experiment

The data presented here were obtained from the third of a series of di-muon experiments performed at the Fermi National Accelerator Laboratory by people mainly from the University of Chicago and Princeton University. The first of these experiments, E331, was proposed to determine whether di-muon production could account for the anomalously large signal of prompt single muons that had been observed in some experiments. The J/ψ was discovered at the time of the construction of this experiment and thus became one of the points of study. The general features of its production were derived from the $\approx$ 2000 events recorded from the decays of this state.[11] Experiment E444 obtained a much larger di-muon sample and used the data in the non-resonant mass region, $4 < M < 8$ GeV/c^2, to confirm a number of predictions of the Drell-Yan model and for the first time determine the pion structure function. From the nearly 60 thousand J/ψ's measured using various beams and targets, a fairly complete survey of its production characteristics was obtained.[12]

Our experiment, E615, was designed to do a high statistics study of continuum production to be able to discern any M^2 dependence of the pion structure functions. The method purposed for this study involves running at two pion beam energies, $P_{\pi^-} = 260$ and 80 GeV/c, and comparing the structure functions derived from the M $\approx$ 4 GeV/c^2, $P_{\pi^-} = 80$ GeV/c data with those from the M $\approx$ 8 GeV/c^2, $P_{\pi^-} = 260$ GeV/c results. This choice of settings allows the same x_n region of the nucleon distributions to be used when extracting the pion structure functions in each case. Even without determining the structure functions, scale breaking will be apparent if the shape of $d\sigma/dX_F$ is not the same for the two beam energies since the values of M^2/S_o are approximately equal. Another emphasis in the design of the experiment was on the measurement of the angular variables describing di-muon production. The high X_F $\cos(\theta)$ distribution for

$M > 4\ GeV/c^2$ is of particular interest since E444 found that it differed from the Drell-Yan model prediction.

In this thesis, the data presented are limited to that taken in the spring of 1982 as a test run of the detector in its configuration to measure production from 260 GeV/c pions. Roughly 1300 events were measured with $M > 4\ GeV/c^2$ which is comparable with the number obtained by E444. The results from the analysis of these events are in good agreement with that from the previous experiment.[55] Although the proposal for this experiment emphasized the non-resonant mass region, the acceptance at the J/ψ mass was not compromised in the test run and about 80 thousand J/ψ's were recorded. Since this first run, the main sequence of data taking has been completed and the analysis of nearly 55 thousand events with $M > 4\ GeV/c^2$ and two million J/ψ's is under way by other members of the group.

2.2 Design of the Experiment

The layout of the experiment is shown in Figure 6. Before discussing the details of the various elements, a brief summary of its general features will be given together with some of the considerations that went into choosing this particular arrangement.

One of three main components that made up the apparatus was the 7.4 meter dipole *selection magnet.* It was located just downstream of the target and served to reduce the rate of background events by bending low momentum muons away from the detectors. Hadrons remaining from the beam or produced in the target were absorbed in the material that filled the volume between the pole pieces of the magnet. This magnet was followed by the spectrometer which consisted of sets of drift and multi-wire proportional chambers placed on either side of a dipole *analyzing magnet.* The position information on the particles obtained from these chambers was used to reconstruct their trajectories and thus determine, in particular, their momenta. The last component of the apparatus was the six scintillation counter hodoscope banks (denoted $A \rightarrow F$) that were interspersed among the other elements. The information on the number and position of the 'struck' counters determined whether all the data relating to the event should be read and recorded to tape. The basic requirement of this trigger system was that at least two ***hits*** occur in each bank which preferably selected di-muons over the more dominant single particle events.

The basic philosophy that guided the design of the experiment was to maintain sensitivity to the full range of most of the variables describing di-muon production and yet be able to collect enough data so the structure function comparisons would be statistically meaningful. With the currently available high intensity pion beams, the limitation in obtaining data arises not so much from the small magnitude of the cross sections at high mass ($M \geq M_{J/\psi}$), but from the relative trigger rate from background events. In the remainder of this section, a discussion is given of the sources of these backgrounds and how the methods used to suppress them determined the general acceptance properties of our apparatus. In latter chapters, it will be seen how the resolution in the measurement of the di-muon kinematic variables was affected by the choices made in this regard.

The most obvious background one faces in doing a di-muon experiment is from hadrons produced in the target since they outnumber the high mass signal by more than a million to one. For experiments attempting to run with a high intensity beam, it is necessary to prevent the direct exposure of the detectors to these particles. In our case, enough material ($\approx$ 17 absorption lengths) was placed downstream of the target so the hadronic showers were highly depleted before reaching the spectrometer. To decrease the likelihood that the remaining flux of low momentum hadrons would cause a trigger, two one-meter thick steel walls were placed downstream of the spectrometer to shield the furthermost hodoscope banks. With this configuration, the only high energy charged particles that should have appeared in the detectors were muons since they lost on average only 6 GeV of energy when traversing the length of the apparatus.

Some experiments place holes in the absorber and the detectors so the high intensity forward hadronic component does not interact. This allows the spectrometer to be moved closer to the target since the wide angle showers are more easily contained. However, the size of the holes required usually causes the loss of nearly all events in the high X_F and high $\cos(\theta)$ regions. Because of the importance of these kinematic areas to our study, this method was not used.

The effect on the di-muon acceptance from the use of an absorber is most easily seen in the case where there are no magnetic fields present. The limitation in solid angle coverage is then apparent since the transverse size of the spectrometer cannot be arbitrarily increased in practical terms to compensate for its increased distance from the target. To get an idea of what is lost, consider the expression, $M \approx \Theta_{-+}(P_{\mu^+}P_{\mu^-})^{1/2}$, which relates the mass of the pair to the opening angle of the muons in the lab frame, Θ_{-+}, and the lab momentum of each muon, P_{μ^+} and P_{μ^-}. Since the average of the quantity, $P_{\mu^+}P_{\mu^-}$, is largest for pairs of a given mass at $X_F = 1$, the opening angles of the muons are 'small' in this regime so their acceptance into the spectrometer is maximum. As X_F decreases, $<P_{\mu^+}P_{\mu^-}>$ becomes smaller so the acceptance is reduced due to the greater angular dispersion of the muons. Also for X_F small or negative, the momentum of the muons is small enough that their energy loss becomes significant. The combination of these effects, even with the inclusion of magnetic fields, restricts experiments like ours to measuring the positive X_F region.

Given that the trigger rate problem from hadrons can be solved by using an absorber, one is left to contend with the full spectrum of di-muons from both prompt sources and accidental pairs. For the former contribution, one finds from the measurements[11,12] of $d\sigma/dM$ that the low mass ($M < M_{J/\psi}$) pairs would readily dominate the events of interest if all di-muons were recorded (see Figure 7). Fortunately, the low mass production cross section is heavily weighted toward small X_F where a pair's total momentum ($P_S \equiv P_{\mu^+} + P_{\mu^-}$) is in proportion to its mass ($P_S \approx P_{\pi^-}M/S_o^{1/2}$) while its opening angle is approximately independent of M. These conditions then make it efficient to use a magnetic field in the absorber area to separate the low X_F pairs by their mass. To see roughly how this works, consider a class of symmetric events ($P_{\mu^+} \approx P_{\mu^-}$, $P_T \approx 0$) where the muons travel nearly parallel to the bend plane of the magnet and are *in-benders* in the sense that each particle bends toward the beam axis. Since their initial angles to the beam axis are roughly equal, the horizontal displacements of these muons in the spectrometer are a function only of their total momenta and hence their mass.

This effect was exploited in the design of our experiment by making the fields strengths of the selection magnet such that the low mass pairs of this type were bent outside the spectrometer while the high mass events were focused into the aperture of the analyzing magnet (note also that the muon energy loss in the absorber greatly reduced the acceptance of pairs with M < 1 GeV/c^2). In examining the data, one finds that the event topology described above is in fact a fair representation of the surviving low X_F events. This restrictive phase space admitted about 1% of the high mass events and less than .1% of the low mass pairs in the $X_F \approx 0$ region. When accounting for the difference in the acceptance at larger X_F, which actually favored the lower mass events, the net effect was to reduce the number of low mass pairs which entered our spectrometer by about a factor of five relative to the J/ψ signal. However, this still left a seventy to one ratio of low to high mass pairs within the active region of the apparatus.

The length of the magnet required to achieve the amount of bending for this selection process and to aid in the suppression of other backgrounds made the separation between the target and spectrometer longer than was necessary from the absorber considerations alone. Although part of the acceptance loss at low X_F that occurred from this increase in distance was compensated by the focusing properties of the magnet, the loss of a large fraction of the low X_F events was affordable since the production cross section is maximum in this region. However, special considerations had to be made to retain events with $|\cos(\theta)|$ near unity for all X_F values since one of the muons in such pairs is produced with a small momentum. This results since the muon is generated nearly anti-parallel to the beam direction as viewed in the di-muon rest frame. The other muon thus appears with a large momentum by comparison. Preserving a 'reasonable' acceptance for high mass events with this topology was a major guideline when the magnet sizes and field strengths were determined for our experiment.

The last type of background one has to consider in a di-muon experiment is from the accidental combinations of non-prompt muons. Their contribution has the potential of dominating even the low mass signal since it increases in proportion to the square of the beam intensity. One of the major sources of single muons that can form such pairs is the decay of pions or kaons produced in the target. Since the average momentum of these muons is much smaller than that from high mass pairs, one is again motivated to place a magnetic field in the absorber region. Our selection magnet was able to sweep roughly 90% of the decay muons outside the spectrometer which left a flux on the order of .1% of the beam intensity.

The decay of pions in the beam is another source of muons that can give rise to a large background of accidental pairs. One has to desensitize the trigger against these particles since their momentum is too large ($P_\mu > .6 \cdot P_{\pi^-}$) for a sweeping magnet to have much effect. In our experiment, counters were positioned upstream of the target to produce a trigger veto signal if muons were detected outside of the beam pipe. Also, the downstream hodoscope banks were deadened in regions near the beam axis so the component of muons in the beam would pass through the apparatus undetected. The combination of these steps decreased the number of muons 'seen' by the trigger logic to the level of that from the secondary hadron decays. The deadened regions in the hodoscope banks had little effect on the di-muon acceptance except for those events produced at high X_F and $\cos(\theta)$ near -1. In this kinematic region, the negative muon has the same characteristics as the beam decays. For $X_F > .6$ and $\cos(\theta) < -.8$, about 50% of the J/ψ decays were lost as a result of the beam holes.

During the run, where the typical beam intensity was 10^8 pions per one second spill, about 25% of the triggers were from accidental pairs. As with the prompt di-muon signal, the invariant mass distribution of these pairs peaked in the low mass region. However, the spectrum fell off more slowly with increasing mass such that for $M > 2\ GeV/c^2$, 80% of the triggers came from this source. Fortunately, this high mass background is readily distinguishable from the prompt signal in the off-line analysis.

The net sum of all sources of di-muons yielded about one prompt pair with $M \geq M_{J/\psi}$ per one hundred triggers. It was realized in the design stage of the experiment that such a rate would not be adequate for the structure function studies and so the idea of using a more elaborate triggering scheme was pursued. The method that was finally devised relied on the information from the C and D hodoscope banks to compute a quantity that could be used to roughly distinguish the mass of the pairs. Although this system was still being constructed at the time of the test run, it proved very useful in the latter runs where it helped to enhance the fraction of events with $M > 4\ GeV/c^2$ by a factor of five.

2.3 Elements of the Experiment

In the following sub-sections, the various parts of the experiment are described in more detail. To simplify the discussion, the following coordinate system is used where the origin is defined as the mean production point in the target.

$\hat{z}$: beam axis with $+z$ pointing downstream.
$\hat{y}$: vertical axis with $+y$ pointing up.
$\hat{x}$: horizontal axis with $+x$ pointing left as viewed looking downstream.

For all equations presented in this study, variables specifying length are in units of meters. Likewise, momentum is in GeV/c, magnetic field strengths in kG and angles in radians.

2.3.1 The Beam

The apparatus was located in the experimental hall that is part of the Proton-West secondary beam facility at Fermilab. For our experiment, particles were generated at the start of this beam line from the interactions of 400 GeV/c protons with a one absorption length beryllium target. A 240 *m.* long system of magnets and collimators as illustrated in Figure 8 then defined the phase space of the secondary particles that reached our target. The segmented wire ion chambers (SWIC's) shown in the Figure provided information on the position and transverse size of the beam which aided in its tuning. The momentum acceptance of the secondaries was defined by adjusting the field settings in the series of dipole magnets located before the 6 *m.* 'momentum slit'.

A set of 'spoiler' magnets (not shown the Figure) are positioned along the beam line to reduce the flux of muons from beam particle decays that reach the experimental area. These magnets have fields outside the beam pipe so muons which become separated from the beam are given an additional 'kick' away from it. The magnets located near the secondary target, however, had little effect in our experiment due both to the small lever arm of the bending and because the background from this region was dominated by particles produced from the interaction of the 'tails' of the beam with collimator or magnet apertures.

With the dipole magnets set to transport negative particles, the tune used during the experiment produced a beam of mostly pions which had the following characteristics at our target.

$<P_{\pi^-}> = 263\ GeV/c$
$(\Delta P_{\pi^-})_{r.m.s.} = 8\ GeV/c$
$(\Delta x)_{r.m.s.} \approx (\Delta y)_{r.m.s.} \approx 1\ cm.$
$(\Delta \theta_x)_{r.m.s.} \approx (\Delta \theta_y)_{r.m.s.} \approx .3\ mr.$

The source of this information is discussed in Chapter V.

Under normal operating conditions, the beam was delivered every 15 seconds over a one second interval. During the spill, the particles did not arrive in a continuous stream but were bunched in two nanosecond *buckets* that occurred every 18.6 nanoseconds. The transmission of the beam line was checked by comparing the number of the protons incident on the primary target as measured by a secondary emission monitor (SEM) with the number of secondaries at our target determined from an ionization chamber (IC711). Besides the direct monitors of the beam flux, a series of scintillation counters were placed a few meters off to the side of our target to provide signals that were in proportion to the interaction rate in the target. Their use together with the ionization chamber results to give information on the normalization of the di-muon data is described later.

2.3.2 The Selection Magnet

The bulk of the 400 ton magnet consisted of blocks of steel from the dismantled ZGS accelerator at Argonne National Laboratory and a 168 turn copper coil constructed at Fermilab. Figure 9 shows the side view of the 3.3 *m.* (x) by 2.2 *m.* (y) by 7.4 *m.* (z) structure with the absorber pieces in place. The pole pieces were made so the vertical opening decreased in steps over the distance from the downstream to the upstream end. This allowed for a larger field near the target where the spatial distribution of the generated particles was small.

The field measurements of the magnet were done almost entirely using the Fermilab *zip–track* system. The measuring device consisted of a set of coils that were oriented along the three spatial axes. These coils were housed in a cart assembly that could be moved along a rail within the magnet by computer control. The currents induced in the coils when moving them from a field free region to a point in the magnet were integrated to give a direct measure of the field strength along each axis. The upstream end of the magnet was too narrow for the zip-track apparatus to be used so the measurements were completed with a hand-held coil. In all, over one hundred thousand values were recorded.

The vertical field data were reduced by fitting them to a sum of harmonic polynomials. These functions, like the fields components themselves, satisfy Laplace's equation and so were a natural choice for this application. The vertical field profile along the beam axis evaluated from the fits is shown in Figure 10 and corresponds to the normal magnet operating current of 2 *kA*. . The step structure of the pole pieces are apparent from the discrete jumps that are observable in the magnetic field values. The transverse momentum 'kick' of the magnet as calculated from the integral of the field strength profile in the Figure is 2.7 *GeV/c*. The use of field parametrizations and the checks that were made for systematic errors in the measurements are discussed in Chapter V.

2.3.3 The Target and Absorber

In this sub-section, the choice and effect of the materials used in the active region of the apparatus are examined. Table 1 lists some of the properties of the substances relevant to the discussion.

TABLE 1

CHARACTERISTICS OF THE MATERIALS IN THE APPARATUS

	Material	Position[a] (*m.*)	Length (*m.*)	Density (*g./cm.*^{3})	# of Absorption Lengths
Target	W alloy[b]	-.08	.22	17.1	1.7
Upstream Absorber	BeO[c]	.46	.61	3.0	1.6
	Be[d]	1.07	3.20	1.9	5.5
	C	4.27	4.12	1.8	6.4
	BeO	8.39	.61	3.0	1.6
Downstream Absorber	Fe	20.12	1.02	7.9	4.8
	Fe	21.72	1.02	7.9	4.8

(a) z location of the upstream face of the material.

(b) 89.9% W, 6.06% Ni, and 4.04% Cu.

(c) For the first half of the run, the BeO started at $z = .61$ and its length was .46 meters.

(d) These figures also include other materials (2% by weight) used for packaging the Be.

A tungsten alloy target was used during the entire run. It had transverse dimensions of 5.6 *cm.* by 5.6 *cm.* and thus contained practically all of the beam.

Since it was also long in terms of the number of pion absorption lengths, most di-muons were produced in the target as opposed to the absorber. The selection of a heavy element target optimized the yield of high mass di-muons per pion absorption length since the nuclear cross section for $M \geq M_{J/\psi}$ pair production increases faster with atomic weight than that of pion absorption. In addition, its large density decreased the distance over which production occurred which helped to make the non-prompt pairs more distinguishable in the data when the vertex analysis was done. The trade off in using the high atomic number (Z) target was an increase in the amount of muon multiple scattering which worsened the resolution of the reconstructed kinematic variables (per absorption length of material, the angular dispersion width resulting from multiple scattering is roughly proportional to $Z^{.6}$). Also, the contribution of di-muons produced from secondary pions was a concern given the number of absorption lengths of the target. More quantitative statements on these subjects are given in later chapters.

In the design of the experiment, only Be and carbon blocks were to be used in filling the volume of the selection magnet. The estimate of total number of absorption lengths needed to reduce the hadronic background to an acceptable level was based in part on the measurements by E444 of the hadron attenuation in an iron shield. The particular choice of materials came as a compromise between minimizing the muon multiple scattering and the price and availability of the substances involved. During the early stages of the run, BeO was added to both ends of the magnet until the drop in the singles rate in the C hodoscope bank began to level off. The idea was to reduce the rate of hadronic punch-through to at least a level below that from the non-prompt muons. Also, about halfway through the run, another 15 *cm.* of BeO was added upstream yielding a total of nearly 17 absorption lengths of material in target and upstream absorber. Although the last addition reduced the minimum separation between the target and absorber to 32 *cm.*, the reconstructed z vertex position of di-muons with $M > 4\ GeV/c^2$ was small enough that over 90% of the events that originated in the absorber could be separated from the target data. For the J/ψ however, these cuts were only 50% effective which left about an 8% contamination of absorber events in the final data sample.

Theoretically, the coulomb scattering of a muon by the nuclei in our target and absorber materials produces nearly Gaussian distributed differences in its position and angle from their most probable values at any z position in the apparatus. The standard deviations of the dispersions in position ($\sigma_s \equiv \sigma_x = \sigma_y$) and angle ($\sigma_\theta \equiv \sigma_{\theta_x} = \sigma_{\theta_y}$) are inversely related to the muon's momentum, P, when the fractional energy loss is small. For muons that were generated in the target and reached the downstream end of the absorber ($z_f \equiv 9.0\ m.$) in its final configuration, one expects

$$\sigma_s(z_f) = \frac{.88}{P}\ (m.\cdot GeV/c) \qquad \sigma_\theta(z_f) = \frac{.12}{P}\ (rad.\cdot GeV/c) \qquad \rho(z_f) = .90$$

where ρ is the correlation of the deviations in position and angle. The stochastic nature of the muon's energy loss in conjunction with its bending in the magnetic field contributed to the dispersion width in the x dimension as $1/P^2$, and except for $P < 10\ GeV/c$, it was less than that from multiple scattering. Likewise, the spectrometer measurement error in the position and angle of the muons at z_f was generally much smaller than this smearing. Thus, in projecting the muons back to the mean production point in the target, $z_0 \equiv 0$, the dominant source of dispersion is from the multiple scattering that had occurred before their measurement. At this position, one finds to a good approximation,

$$\sigma_s(z_0) = \frac{.50}{P}\ (m.\cdot GeV/c) \qquad \sigma_\theta(z_0) = \frac{.12}{P}\ (rad.\cdot GeV/c) \qquad \rho(z_0) = -.64\ .$$

For a pair of low momentum muons ($P < 50\ GeV/c$), the above expression for $\sigma_s(z_0)$ shows that the errors in their reconstructed positions at the target are larger than the beam width ($\approx 1\ cm.$). Hence, including the beam center as a measurement improves the estimate of the most probable vertex position in this case. Later it will be seen how ρ affects the resolution achieved for the initial muon angles when a vertex fit is done.

2.3.4 The Spectrometer

In designing the spectrometer, the goal was to achieve a momentum resolution such that the measurement error on X_F values near unity would be only a few percent. At this level, the error in X_F due to the momentum uncertainty is comparable to that from the beam momentum dispersion ($X_F \approx (P_{\mu^+} + P_{\mu^-})/P_{\pi^-}$ in this region). For the structure function studies, it was important to keep the error in X_F small since these distributions fall rapidly at high x. With this criterion, the smearing in the other five kinematic variables introduced earlier to describe di-muon production was dominated by the dispersion originating from multiple scattering.

The momentum resolution depends on both the distance over which the position measurements are made as well as the errors in the measurements. In our apparatus, multiple wire proportional chambers (MWPC's) were used upstream of a dipole magnet and drift chambers downstream of it in an arrangement that gave a 3 to 4 meter lever arm on each side (see Figure 11). Although the drift chambers provide better spatial resolution, they were not placed upstream of the analyzing magnet because they are more easily deadened by the higher flux of particles there.

The MWPC's consisted of planes of gold plated tungsten *sense wires* (20 μ. dia.) at DC ground that were positioned between sheets of an aluminum foil - mylar laminate. The foils were separated by 1.3 *cm* and maintained at negative 3700 volts during normal operating conditions. The volume between the planes was continually flushed with a gas mixture of 80% Argon, 16% CO_2, and .4% freon.

The use the aluminum/mylar laminate instead of a more conventional wire plane cathode allowed us to electrically isolate regions of the chambers by chemically etching patterns on the foils and attaching separate power supplies to the individual areas. The intent was to deaden the small parts of chambers exposed to the high flux of beam muons so the sense wires outside these regions would remain efficient. Although this idea was implemented, the intensities during the run were not large enough to make its use necessary. However, all voltages on the chambers were lowered between spills to suppress the growth of leakage currents.

The process by which a charged particle was detected with these chambers began with the liberation of electrons from its interaction with the atoms in the gas. The electrons drifted toward the nearest sense wire where some of them gained enough momentum in the increasing electric field to induce further ionization. The avalanche of electrons formed in this multiplication process then collected on the wire as the positive ions drifted toward the foils. The resulting signal traveled through an amplification circuit attached to the chamber and along a delay line (450 *ns.*) to allow the trigger electronics time to process the event.

After this, it was discriminated and then latched (60 *ns.* gate) if the event with which it was associated satisfied the trigger requirements. In this case, the position of the wire from which it originated was encoded and stored in a special memory module. The data were then transferred to the data acquisition computer by a single direct memory access (DMA) read instruction to a dedicated CAMAC module.

With only the wire number information, a particle's position at a given plane is uncertain to plus or minus half the wire separation. The 2.1 *mm.* spacing in the MWPC's translates to a r.m.s. position error transverse to the wire of 610 μ.

The MWPC system was made up of nine planes that were grouped into three modules each having the same three orientations of wires. Since the bending in the analyzing magnet occurred in the x-z plane, the y resolution was worsened to improve the x determination. This tradeoff was realized using one X and two tilt planes (denoted U and V) oriented at ± 16 degrees from the vertical in each module. Table 2 lists some of the other data on the MWPC's including the overall efficiency of each plane.

As in the MWPC's, the charge produced by a particle passing through the drift chambers was collected on sense wires. In this case, however, the wire spacing was much larger (1.9 *cm.*) and time information on the arrival of the signals was recorded. The drift times were made roughly proportional to the distances the electrons traveled by using cathode wires set at graded voltages to produce a fairly uniform electric field outside the regions of the sense wires. The pulses from the individual wires were also delayed so the trigger signal could be used as a time reference. The arrival times relative to this signal were quantized in 31 units each having an average span of about 8 *ns.*. Although this corresponds to an average r.m.s position uncertainty of 90 μ. for each bin, the actual resolution obtained from a given wire was about 200 μ. due to the time jitter of the signals involved. The readout system stored the encoded wire numbers and drift times in a local memory that was also accessed by the computer with a single DMA command.

The upstream set of six drift chamber planes were built especially for this apparatus while the others, which were grouped three across, came from an earlier Princeton experiment (E208). The drift chamber cells were similar for each

TABLE 2

MWPC SIZES, POSITIONS AND EFFICIENCIES

Module	Plane	Width	Height	# wires	z	θ	$<\epsilon>$
I	1	1.47	0.76	672	9.579	+15.09	.96
	2			672	9.604	-15.24	.98
	3			696	9.629	0.08	.99
II	4	1.74	0.81	792	11.060	+15.50	.95
	5			792	11.085	-15.44	.98
	6			824	11.111	0.16	.99
III	7	2.04	1.02	928	12.525	+15.31	.96
	8			928	12.550	-15.64	.96
	9			960	12.576	0.01	.98

Note that θ is the angle of the wires from vertical in degrees and $<\epsilon>$ is the mean plane efficiency. All lengths are in units of meters.

set and the details of their construction and operating characteristics can be found in reference 56. Tilt planes were included in each cluster of chambers with orientations similar to that of the MPWC's. Further information on these detectors is given in Table 3. The inefficiencies of the planes were generally larger than that of the MWPC's and largely arose from faultly channels in the time digitization electronics.

The last element of the spectrometer was the analyzing magnet. It was 1.5 *m.* long and had an aperture of 1.83 *m.* (x) by .91 *m.* (y). At its normal operating current of 2.4 *kA.*, the field strength near the center of the magnet was about 13 *kG.* The vertical field components were measured with the same technique described for the selection magnet. Data were taken over a grid of points in just an octant of the magnet using a hand-held coil. Tests showed that the values in remaining regions were obtainable from these measurements by symmetry. The field integrals evaluated from these data at a fixed x and y position are uniform

TABLE 3

DRIFT CHAMBER SIZES, POSITIONS AND EFFICIENCIES

Plane	Width	Height	# wires	z	θ	$<\epsilon>$
1	2.44	1.22	126	15.80	0.00	.87
2	2.44	1.22	126	15.98	0.00	.79
3	2.44	1.22	140	16.08	-18.00	.81
4	2.44	1.22	140	16.26	+18.00	.87
5	2.44	1.22	126	16.36	0.00	.93
6	2.44	1.22	126	16.54	0.01	.93
7 Right	1.07	1.83	56	18.48	0.00	.87
Center	1.07	1.83	56	18.60	0.00	.89
Left	1.07	1.83	56	18.49	0.00	.89
8 Right	1.07	1.83	56	18.55	0.00	.85
Center	1.07	1.83	56	18.66	0.00	.86
Left	1.07	1.83	56	18.54	0.00	.78
9 Right	1.07	1.83	56	19.02	-17.99	.93
Center	1.07	1.83	56	18.96	-17.99	.90
Left	1.07	1.83	56	19.01	-17.99	.90
10 Right	1.07	1.83	56	19.42	+18.01	.98
Center	1.07	1.83	56	19.35	+18.01	.84
Left	1.07	1.83	56	19.40	+18.01	.93
11 Right	1.07	1.83	56	19.71	0.01	.90
Center	1.07	1.83	56	19.83	0.01	.90
Left	1.07	1.83	56	19.72	0.00	.91
12 Right	1.07	1.83	56	19.78	0.00	.89
Center	1.07	1.83	56	19.89	0.00	.91
Left	1.07	1.83	56	19.77	0.01	.92

Note that θ is the angle of the wires from vertical in degrees and $<\epsilon>$ is the mean plane efficiency. All lengths are in units of meters.

to the few percent level over most of the area of the magnet gap and correspond to a .8 *GeV/c* transverse momentum kick. As with the selection magnet measurements, these data were reduced by fits to sums of harmonic polynominals. This was particularly important for providing a representation of the fields near the magnet coils since the point-by-point variation of the measurements was largest in this region.

2.3.5 Scintillator Hodoscopes and the Trigger

The function of the trigger system was to identify the presence of di-muons in the apparatus and to initiate read out of the associated data. An important requirement in its design was that the identification time be kept small since the signals from the wires chambers had to be delayed in the intervening period. Also, keeping the fraction of wrongly identified events low was essential since no further triggers could be processed during the time it took to record an event. At the root of the trigger system were sets of scintillation counters which provided fast but crude information on the positions of particles. These counters were arranged in planes (referred to as hodoscopes) to cover the transverse area of the apparatus. Of the six banks employed (denoted $A \rightarrow F$) two were placed upstream of the target to indicate the presence of particles outside the beam region while the remainder where situated downstream of the absorber to provide, in part, a count of the number of particles traversing the apparatus. To see what information went into forming the trigger signal, it is necessary to first examine the layout of the hodoscopes.

The A through D banks each contained two planes of counters that were oriented along the x and y axes. Table 4 lists the information on these counters and the ones in the E and F banks which were positioned vertically. A perspective view of how the sheets of scintillation material appeared downstream of the target is shown in Figure 12. The rectangular holes in the planes near the beam axis had dimensions that ranged from 5 to 15 *cm.* on a side which allowed a large fraction of the beam muons to pass undetected.

Attached to the outer end of each counter was a light pipe and photomultiplier tube assembly. They converted the light produced by a particle passing through the plastic scintillation material into an analog electrical pulse by means of a photo-cathode and amplification cascade. This signal traveled to a LRS 4416

TABLE 4

HODOSCOPE POSITIONS AND COUNTER SIZES

Bank	z	Nr. ctrs.	Width	Height	Counter Width	Counter Length
AX	-3.20	36	1.84	1.02	.102	.51
AY	-3.20	20	1.84	1.02	.102	.92
BX	-2.16	38	1.94	1.12	.102	.56
BY	-2.16	22	1.94	1.12	.102	.97
CX	9.13	28	1.42	0.64	.051	0.64
CY	9.14	48	1.42	0.64	.027	0.75
DX	16.88	44	2.24	1.10	.051	1.10
DY	16.89	48	2.24	1.10	.046	1.12
E	21.25	80	3.37	1.77	wide: .102 narrow: .051	0.88
F	22.85	80	3.37	1.77	wide: .102 narrow: .051	0.88

All lengths are in units of meters.

discriminator module which produced a digital pulse if the input analog level was above 20 milli-volts. The arrival times of the hodoscope signals had to be adjusted so all signals from a given interaction arrived simultaneously. Trimming the cable lengths for this purpose and also setting the operating voltages on the 448 phototubes were some of the more time consuming tasks that were involved in making the experiment operational.

The A and B hodoscope banks, which were each shielded by blocks of iron and concrete, covered an area outside the three inch diameter beam pipe large enough to shadow the active region of the rest of the apparatus. Two counters were used to span the widths and heights of the X and Y planes respectively in order to decrease the time variation of the signals from any one counter. In the trigger logic, however, the right-left or up-down pairs were treated as one unit.

The counters near the beam pipe were equipped with special bases that could handle high rates and were mounted on aluminum plates that could be easily moved away from the beam pipe if the intensities were such that it became necessary to increase the size of the holes in the hodoscope planes. This option, however, did not need to be used and so the counters remained positioned against the beam pipe.

Of the downstream planes, all but the CX and DX required two counters per row or column to avoid inefficiency problems and to achieve a time resolution on the order of the 18.6 *ns.* bucket spacing of the beam. As in the A and B planes, the 'OR' of the upper and lower E and F counters were used in the trigger logic. The right and left CY and DY were also combined but not until they were 'ANDed' with a signal that came from the 'OR' of all the X counters on their particular side of the plane. In effect, a hit in any of the counters on the right half of the CX bank, for example, enabled the whole right half of the CY bank. This was the only use of the CX and DX planes in the test run although they were an important part of the mass processor system in the later runs.

The inner 14 top and bottom counters of both the E and F banks were made half as wide as the outer ones since the muons from in-bending high mass events were concentrated in this region and the trigger logic required a pair to be separated by at least one counter. The non-adjacency condition was imposed so particles produced from the interaction of a muon with the materials near the counters would not be counted as two hits.

The hodoscope counter signals from the discriminator units were processed by three types of logic modules which will be referred to as *veto*, *multiplicity* and *Y match*. The time coincidence of signals from these modules together with a timing pulse formed the trigger signal. The electronics that performed these functions are described in detail in reference 57.

The veto logic used information from the A and B banks to produce a signal if a muon appeared outside the beam pipe at a position upstream of the target. By vetoing such occurrences, the number of accidental pairs was reduced. Particles were identified by the coincidence of counters between these banks using two logic modules to match the X and Y counters separately. To allow for the angular divergence of the particles, each counter in the A bank was associated with two symmetrically positioned counters in the B bank. The signals from the two logic units, which were the 'OR' of all the possible matches, were 'ORed' to form the *VETO* signal. Although using the 'AND' of the final X and Y signals would have insured at least two counters had 'fired' in each view, it would have made the system more susceptible to failure from counter inefficiencies. Since the veto rate contributed little to the dead time under our normal running conditions, the more conservative approach was used.

A multiplicity logic module was used with each of the CY, DY, E and F planes to provide information on the number of counters that were struck. The modules had various output channels each conditioned on the number and position of the counter hits. The particular channel from each module that was used to form the trigger produced a signal if two non-adjacent hits or greater than two hits were present (these signals are denoted by the 'trig' subscript: e.g., CY_{trig}).

To help suppress triggers on events not originating in the target, at least two matches were required between hits in the CY and DY counters that projected back to the target. The widths of the Y counters were made in proportion to their distance from the target to facilitate this match. The counters were logically grouped in pairs giving 12 *wide* rows in each bank. The relative y offset between the planes was such that one CY wide row was symmetrically associated with two in the DY plane and vice versa. Using a one-to-two instead of a one-to-one pairing was necessary because of the smearing of the muons' position and slope from their multiple scattering in the absorber. A logic module was used with both the CY and DY planes to determine the number of matches with the other plane. Signals indicating two or more matches (denoted CY_M and DY_M) were used to form the trigger. Including both outputs was more restrictive since it required that there be at least two wide rows hit in each plane.

The final input to the trigger was an RF timing signal (≈ 5 *ns.* width) synchronized with the bucket structure of the beam. Its use made the trigger signal more helpful for setting the zero time for the drift chambers and latching the hodoscope signals.

Summarizing all of the pieces of the trigger, one can write,

$$TRIGGER = RF \cdot CY_{trig} \cdot DY_{trig} \cdot E_{trig} \cdot F_{trig} \cdot CY_M \cdot DY_M \cdot \overline{VETO}.$$

The performance of the trigger logic was checked during the run using a feature of the hodoscope discriminator units which permitted each channel to be set and fired by computer control. Fake events could thus be generated to see if the logic modules responded correctly. Also, the time difference distribution between the *RF* pulse and any of the other trigger inputs was monitored to make sure that the timing remained intact. During the three week period when most of the data were taken, no major problems were revealed by any of these tests.

From the visual displays of hodoscopes and wire chamber information generated by the computer during the run, one could see that over 90% of the events contained at least two tracks. Beyond the basic fourfold 'trig' requirement, the *Y* match logic decreased the dead time corrected trigger rate by 15% while the veto logic was more effective, producing a factor of three reduction.

A Monte Carlo simulation of the experiment shows that the trigger requirements rejected about 20% of the J/ψ decays in which both muons were within the geometric acceptance of the apparatus. The loss due to counter inefficiencies is not included in this number but will be examined in Chapter V. The most prominent type of event loss occurred when the muons landed in the same or adjacent rows of counters in the *CY* or *DY* bank.

Besides their role in forming the trigger, the hodoscope signals provided information that was important in the off-line analysis. To record which counters had fired, the discriminator outputs were sent to latch modules (LRS 4448). These units encoded the hodoscope data into a series of bits with each bit corresponding to a given counter. A bit was set if the signal from the counter arrived at the module within a 20 *ns.* time window synchronized with the trigger. A single DMA read command transferred the entire set of 16 bit latch words (3 words per module) to the data acquisition computer. Also included in the transfer were latch words made from the various outputs of the trigger logic modules so a check could be made off-line to see if they were consistent with the set of counters that were latched.

2.4 Data Acquisition

A PDP 11/45 computer run with Fermilabs's MULTI software package controlled the data acquisition. The time required to retrieve data from the detector read-out systems was kept small by using a high speed bi-polar memory in the computer and by the partitioning of information so that only three CAMAC DMA commands had to be issued. In all, about 1.5 milliseconds were spent recording a typical event of approximately 200 words. These data were stored in the semi-conductor memory of the on-line computer until the completion of the spill and then written to magnetic tape.

To help monitor experimental conditions and detector performance, scalars (LRS 4432) were used to record the counting rates in each of the hodoscope counters and logic unit outputs. The computer recorded these data as well as the scalar sums from the beam monitoring devices at the end of each spill. Between spills, a small sample of events was analyzed to check for any problems with the detectors or the trigger logic units.

The outputs of the target monitors and some of the logic modules were scaled twice where one signal was gated during the periods in which events were being processed and hence the trigger system was inhibited. The ratios of the resulting gated to non-gated sums provided measures of the live time of the experiment.

2.5 Running Conditions

In a typical spill during the run, about 2×10^{12} protons were incident on the primary target which yielded $\approx 10^8$ pions at the end of the secondary beam line. At this intensity, around 350 events were recorded at a live time of about 50%. Integrated over the entire run, nearly twelve million events were written to tape. It should be recalled that these conditions were for the preliminary technical run reported here in which no trigger processor was used to select high mass events.

The veto rate was about 1% of the pion intensity but contributed only a few percent to the loss of live time. With the spoiler magnets turned off, this rate rose by a factor of two. The short runs taken using either a trigger without the $\overline{VETO}$ input or that required the $VETO$ signal to be present indicate that around 30% of the $VETO$ signals were accompanied by a muon in the spectrometer. In two-thirds of these events, the muon momentum was in the range expected for beam particle decays. The muon intensity inside the beam pipe was measured indirectly from a scintillation counter that had been placed over the beam hole in the E bank. Its rate showed that muons constituted about 1% of all beam particles.

The singles rates in each of the *CY*, *DY*, *E* and *F* planes measured from the '$\geq$1' outputs of the multiplicity logic modules were also around 1% of the pion intensity. Comparing these numbers to the scalars sums recorded for each bank indicates a mean multiplicity of about 7 in the *C*, 3 in the *D* and 1 in the *E* and *F* hodoscope banks. Since the *C* bank singles rate was comparable (within 30%) to the others, a small fraction of the events had produced the high multiplicity of hits in this plane. This is not unreasonable in view of the additions made to the length of the absorber and the shower like nature of the hadronic backgrounds.

For events which satisfied the trigger, the multiplicity per hodoscope plane was in the 2.1 to 2.6 range. Also in this case, there was an average of about four hits per plane in both the MWPC's and drift chambers even though the latter are effectively sensitive to twice as many out of time particles.

If the trigger rate on accidental pairs is estimated from the singles rates in the farthest downstream hodoscope planes, a value much larger than that observed in the data is found. A direct measure of the single particle flux using the '$\geq$1' multiplicity outputs for the *CY*, *DY*, *E* and *F* planes to form a trigger showed that it was about .1% of the pion intensity which is consistent with the level of accidental pairs in the data. A Monte Carlo study indicated that about a third of this factor of ten difference occurred since only 5% of the beam muons hit counters in all four banks although an average of 30% of them missed the beam hole in each bank. Another third of the reduction came from particles associated with a veto while the remainder was probably due to losses from counter inefficiencies or the trigger requirement.

CHAPTER III

EVENT RECONSTRUCTION AND SELECTION

Since the data tapes contained only uncorrelated information on the particle positions at various planes in the spectrometer, *tracks* had to be found within the pattern of hits. The problem was compounded by extra accidental hits and the small inefficiencies of the planes. The situation is illustrated in the event display in Figure 13 where the hits in the chambers are shown projected onto the x–z plane at $y = 0$. To begin this chapter, a review is given of the methods employed to find the tracks and to estimate the five parameters needed to uniquely describe the particle trajectories. This is followed by a consideration of how the track information from a pair of muons was combined in a vertex fit to better the determination of the variables describing pair production. Finally, the cuts used to define the J/ψ sample and to eliminate non-prompt backgrounds are examined.

3.1 Track Finding

Much of initial effort in the development of the pattern recognition programs went toward determining the geometrical alignments of the 33 chambers and the functions which converted the drift times to distances for the 24 drift chamber planes. The latter were derived using the time distributions of hits from drift cells uniformly illuminated by muons. The number of hits per time bin in this case is proportional to the fraction of the total drift distance to which the bin corresponds. The time verses distance relations constructed from this information show little variation from plane to plane.

Five of the six alignment constants used to specify the planes were obtained by surveying the wires relative to the chamber support structures during their construction and then later measuring the z positions and orientations of these structures relative to the coordinate system of the spectrometer. The remaining quantity, the transverse offset of a reference wire relative to the z axis of the spectrometer, had to be determined to an accuracy much smaller than the individual chamber resolutions if systematic errors were to be avoided. To this end, data were taken with the analysis magnet off to obtain hits patterns that were known to be connected by straight line trajectories. With these events, fits were done for all the offsets except the four needed to define a coordinate system. A few inconsistencies arose in the determination of these 29 values due to systematic errors in some of the other 165 alignment constants. After some additional surveying, these were resolved to a degree that the remaining effects were small. This will be made more quantitative when the track fits are discussed in the next section.

At the level of their initial accuracy, however, the alignments were good enough so the development of the track finding programs could proceed. Versions were written both at Chicago and Princeton which provided a means to cross check their accuracy. A number of comparisons were done until they agreed well with each other and with a visual inspection of event displays like the one shown in Figure 13. Since it would have been too time consuming to process the full set of data more than once, the task was divided between the programs. The Chicago version was used first to create *secondary* tapes containing most of the raw event information plus the track segments found in each half of the spectrometer. A set of *tertiary* tapes was then written using the Princeton program to do a more elaborate search within a subset of the events containing mostly high mass pairs.

The key feature of the reconstruction programs was their ability to quickly isolate the hits associated with a track. The brute force approach of trying every hit combination would have been prohibitive in terms of computer time. This was especially true for the $\approx 10\%$ of the sample that had a much larger multiplicity or smaller track separation than the more typical event in Figure 13. The search process was aided by the redundancy of measurements on each side of the spectrometer beyond the minimum needed to specify the essentially straight line trajectories in these regions (5 for the MWPC's and 8 for the drift chambers). However, the clustering of the downstream planes into two groups to optimize the slope determination also made the redundancy of the measurements less useful in terms of track finding since the hits were concentrated near the end points of the track segments. Other complications arose from the small angles of the tilt planes which highly coupled the x and y information and from the ambiguity as to which side of the drift chamber sense wires to add the drift distances.

The starting point of the program which did the first pass through the data used the struck hodoscope counters in the *DX*, *E*, and *F* banks as guides for finding hit patterns that formed straight line segments in the drift chambers. The search began on this side of the spectrometer since the density of hits was smaller on average and the chamber resolution better. A trial and error method was used within a region defined by the scintillator counters to find the largest number of hits (at least five) from the *X* chambers that passed some loose χ^2 cut when fit to a straight line in the x–z plane. The y information was ignored since there were too few *U* and *V* chambers to be useful in constraining the track in this dimension (the second program which processed the data included these hits with the aid of the upstream track information).

If a drift chamber track segment was found, it was projected to the center of the magnet and used as a pivot point for searching for a matching row of hits in the MWPC's*. Struck counters in the *CX* hodoscope plane helped to locate these rows as did the general slope-position correlation that existed for the tracks as a result of acceptance properties of the spectrometer. The *U* and *V* hits were included and their selection aided by the struck *CY* and *DY* counters and the condition that track in the y–z view project back to the target to within the uncertainty from multiple scattering. Any set of more than five hits that formed a track that projected to the pivot point within 4 *cm.* and to the target within a meter in the y dimension was recorded. Once no further MWPC segments could be found or one of the segments met a much tighter set of criteria, the search was terminated and the whole process repeated, starting again in the drift chamber region. When this cycle was exhausted, all the track segment information and most of the raw data for the event were written to a secondary tape.

Although the hodoscopes were used to speed the initial search process, an effort was made not to force any one plane of counters to have a hit in order for a track to be found. Obtaining an unbiased event sample was important so that the hodoscopes efficiencies could be calculated. The events used for the cross section analysis, however, were selected only if all of the hodoscope counters

---

* Tracks segments from the same particle projected to the center of the magnet from each side of the spectrometer generally cross within a few hundred microns.

associated with the tracks had registered hits.

To reduce the computer processing time, events with large numbers of hits (> 200) were ignored and those taking more than some fixed time limit were terminated. Other efforts included writing the most often used computer code in an assembly language. Even with these measures, it took approximately five hours of CPU time on the Cyber/175 computers at Fermilab to analyze a tape of 300 thousand events.

In the second pass through the data, each event was examined to determine if any two tracks, when reconstructed at the target from the segment information, had an invariant mass greater than 2 GeV/c^2. For the $\approx$ 10% of the data which satisfied this condition, a track finding procedure was applied to the hits associated with the segments and any others that fell within a 5 *cm.* (x) by 10 *cm.* (y) region about them. A more thorough selection was done than in the first pass, and in general, the program was able to find more hits per segment ($\approx$ .2) than were indicated on the secondary tapes.

Besides finding the track segments, hits from the entire set of planes were chosen which fit a trajectory that included the bending in the magnetic field. This linking of the two spectrometer regions helped in the selection process since it put tighter constraints on the possible values of the hit positions. Also, the *global fits* yield a factor of two better estimate of a track's momentum than is obtained from just the bend angle between its two segments.

The global and segment fit information were written to the tertiary tapes along with all the data that were present for each event on the secondary tapes. This pass through the data, which took about a fourth as long as the previous one, completed the track finding stage of the analysis.

3.2 Global Track Fits

Before the events on the tertiary tapes were further analyzed, the global fits were redone using a more accurate description of the transport properties of the analyzing magnet. The variation of the magnetic field in the transverse dimensions was taken into account as well the effect of fields that extended into the chamber regions. These corrections changed mainly the value of the momentum and had little effect on the expected trajectories of the muons in the chambers. Thus, the choice of the hits did not have to be reassessed.

To improve the determination of the track parameters, the data recorded on the tertiary tapes were used to compute more precisely the coefficients that entered into the track fitting equations. Specifically, the position of a particle at chamber i was expressed as*

$$x_i = x_o + tx_o \cdot z_{xi} + \alpha_i / P_{xz}$$

$$y_i = y_o + ty_o \cdot z_{yi}$$

where

x_o and y_o are the particle's coordinates evaluated at the mean production point in the target, z_o, by a straight line projection of its trajectory in the spectrometer.

tx_o and ty_o are its slopes at z_o defined by, $tx_o = dx/dz$ and $ty_o = dy/ds$ with $ds = (dx^2 + dz^2)^{1/2}$.

P_{xz} is the value of its momentum in the spectrometer projected on the x–z plane.

The coefficients, z_{xi} , z_{yi} and α_i were treated as constant when fitting for the above five parameters since they are weakly dependent on these quantities. The extent of this dependence can be seen from their formulation below where it has been assumed that all fields other than the vertical component in the analyzing magnet, B_y, can be ignored.

$$z_{yi} = \int_{z_o}^{z_i} (1+tx^2)^{1/2} dz$$

$$z_{xi} = z_{yi}/(1 + tx_o^2)^{1/2}$$

$$\alpha_i = .03 \int_{z_o}^{z_i} (1+tx^2)^{1/2} \left(\int_{z_o}^{z} B_y \, dz' \right) dz$$

Since the slopes of the particles in the spectrometer were seldom greater than .2, both z_{xi} and z_{yi} are fairly insensitive to the level of uncertainties in tx_o and ty_o

---

* The energy loss and multiple scattering of the particles in the chamber and hodoscope materials was small and ignored when fitting for the track parameters.

that exist from the original segment fits. Also, the magnetic field profile was such that α varies little if changes are made to any of the track parameters on the order of their resolution.

The coefficients were calculated using the initial track parameter estimates to project the track through the magnetic field region so the arguments in the integrands could be evaluated. The projection was done in a series of steps in z where the interval was made small enough so the $(1+tx^2)^{1/2}$ term could be approximated by the average of its end point values. The B_y double integral was computed analytically using the harmonic polynomial fits to the fields evaluated at the mean x and y position of the track in each region. The increase in α over an interval determined the increment in x of the track while its change in slope was obtained from the expression,

$$\Delta\left(tx/(1+tx^2)^{1/2}\right) = \frac{.03}{P_{xz}} \int_{z}^{z+\delta z} B_y \, dz \, .$$

Downstream of the magnetic field region, $d\alpha/dz$ was constant and approximately equal to the momentum kick of the magnet, .8 GeV/c. For the MWPC's, α was only non-zero for the three planes closest to the analyzing magnet where the fringe field strengths were a few hundred Gauss.

After computing the coefficients, the hits for a given track were fit to obtain new values for x_o ,tx_o ,y_o ,ty_o andP_{xz} by minimizing the expression,

$$\chi_g^{\,2} = \sum_i \left(\frac{x_i\cdot\cos(\theta_i) - y_i\cdot\sin(\theta_i) - d_i}{\sigma_i} \right)^2$$

where

θ_i = angle of the wires in plane i relative to the vertical (to simplify these equations no corrections have been made for the fact that the planes are not exactly transverse to the z axis).

σ_i = resolution of plane i.

d_i = transverse distance of the struck wire (plus drift distance for the downstream chambers) from the origin (x = y = 0).

The chamber resolutions assumed in these calculations had been estimated separately for the drift chambers and MWPC's by choosing their values so that the χ^2 distribution for the segment fits in these regions matched the theoretical expectations. The comparisons were made simpler by the fact that the theoretical probability for χ^2 to be greater than the value obtained in the fit has a flat distribution if the σ's selected equal the actual errors. Adjusting these quantities until this condition was achieved yielded 230 μ. for the drift chambers and 640 μ. for the MWPC's. The latter result is close to the value of 610 μ. expected from the wire spacing in these chambers. The resolution of 200 μ. quoted earlier for the drift chambers is smaller than the above result since it was derived by optimizing the alignments and time offsets for data taken from a small region of the chambers. Thus, systematic errors in the alignments etc., slightly worsened the overall resolutions obtained.

To identify tracks that appeared in the spectrometer one or more RF bunches out of time relative to the one producing the trigger signal, a separate fit was done for an overall time offset to the hits in the drift chambers. As long as the hits were not predominantly on the same side of the sense wires, the offsets had an accuracy of about 5 *ns.* and so could be used to eliminate these tracks.

The global fits of the tracks in the final J/ψ event sample gives the distribution of chi-squared probabilities (confidence levels), $P(\chi_g{}^2)$, shown in Figure 14a. The depletion of events in the low probability region results from the bias of the track finding programs in that they select hits on the basis of their small χ^2 contribution to the track fit. The fall off in the distribution at high probability is probably from the systematic errors in the chamber alignments. Also displayed in Figure 14 are the distributions of the number of hits per track from the MWPC's and drift chambers.

A more direct check of the quality of the global fits is obtained from examining for each chamber plane the distribution of the difference between the position of the hits and the fitted tracks. Figure 15 shows these residual plots for the X planes at the ends of each segment of the spectrometer. Although the widths of these distributions depend on the position and resolution of the plane, the means should all be zero. In general, they are offset from this value by less than 20% of the chamber resolution and the amounts show no systematic shift from plane to plane. This is true also for the residuals of tracks from smaller regions of the chambers. Thus, the track parameters derived in the fits were not significantly biased by the effects causing these differences.

The global fitting procedure also gives information on the errors of the track parameters for each set of chamber hits. Averaging over the hit configurations in the data yields the values below.

TABLE 5

SPECTROMETER RESOLUTION

Quantity	Resolution
x_o	$1.1\ mm.$
tx_o	$8.7 \cdot 10^{-5}$
y_o	$2.5\ mm.$
ty_o	$1.5 \cdot 10^{-4}$
$1/P_{xz}$	$1.6 \cdot 10^{-4}\,(GeV/c)^{-1}$

3.3 Vertex Fit

For each pair of reconstructed tracks in an event, individual fits were performed using the x and y track information separately to test the hypothesis that the pair originated from a common point in the region of the target through which the beam passes. This procedure was useful for eliminating accidental pairs and provided better estimates of the initial slopes of the muons from prompt pairs than would have been obtained by projecting the tracks back to target individually.

Since the average z vertex resolution obtained for the J/ψ events even when the x and y information were combined was still about 50% larger than the length of the target, estimating the z of the vertex by such a fit was mainly useful for isolating events produced in the absorber. In processing the data then, the z vertex position was fixed at the mean production point in the target. The muon energy loss in the absorber was another variable which produced insignificant changes in the resolutions of the vertex variables when constrained to its mean. This was because the dispersion in position and slope it caused was small compared to that from multiple scattering. Therefore, the energy loss was not allowed to vary in the fits and the initial momentum of a muon, P_v, was estimated from the value determined in the spectrometer, $P_o = P_{xz} \cdot (1+ty_o^2)^{1/2}$, by adding a correction for the mean energy lost.

The average difference between the initial momentum of a muon and that measured in the spectrometer, $f_P \equiv <P_v - P_o>$, is one of five transport equations used to account for the bending and energy loss that occurred within the selection magnet and target. These equations give the most probable initial parameters of a muon as a function of its values measured in the spectrometer. For example, $f_x \equiv <x_v - x_o>$ is the mean horizontal displacement between the projected position, x_o, and the actual x value of the vertex, x_v. Since the vertical bending in the selection magnet was small relative to the dispersion from multiple scattering, f_y and f_{ty} were equated to zero*. The other quantities were approximated by functions of P_o only and in Chapter V their derivation using the Monte Carlo program is discussed.

To illustrate the procedure that was used for determining the vertex parameters, the fit in just the x view will be considered. The spectrometer measurements of the two tracks (referenced by $i = 1$ or 2) yield two estimates of the vertex position and one for each of the slopes:

$$x_{vi} = x_{oi} + f_x(P_{oi})$$

$$tx_{vi} = tx_{oi} + f_{tx}(P_{oi}).$$

A third measure of the position was taken as the beam center, x_b, with an uncertainity given by the r.m.s. horizontal beam width, σ_{xb}. Combining the three measurements yields the best estimate of the horizontal position, $\overline{x}_v$:

$$\overline{x}_v = \sigma_s^2 \left(\frac{x_{v1}}{\sigma_{x1}^2} + \frac{x_{v2}}{\sigma_{x2}^2} + \frac{x_b}{\sigma_{xb}^2} \right)$$

$$\text{where} \quad \frac{1}{\sigma_s^2} = \frac{1}{\sigma_{x1}^2} + \frac{1}{\sigma_{x2}^2} + \frac{1}{\sigma_{xb}^2}.$$

The values of σ's in position and slope were calculated for the tracks by combining the errors obtained from the individual global track fits with those

---

* Small path length corrections that arise from the bending in the x–z plane are also disregarded in setting f_y to zero.

from the dispersion in the absorber and target materials. As discussed previously, the latter are mainly from multiple scattering and thus their values are roughly those given at the end of Section 2.3.3. The actual expressions used for these quantities included both a $1/P_o$ and a $1/P_o^2$ term where the coefficients were obtained from a Monte Carlo calculation so as to include all contributions to the errors. Given the sources of the smearing, the total dispersion in position and slope should be well represented by a binormal distribution which will be specified here by σ_{xi}, σ_{txi} and ρ_i. Since the errors in position and slope were correlated ($\rho \approx -.6$), the combination of the vertex position measurements, $\bar{x}_v$, were used to obtain better slope estimates, $\overline{tx}_{vi}$, as follows.

$$\overline{tx}_{vi} = tx_{vi} + \rho_i \frac{\sigma_{txi}}{\sigma_{xi}} (\bar{x}_v - x_{vi})$$

This typically reduced the error in the slopes by 15% to 25% where the amount depended on the momentum of the muon as well as the momentum ratio with the other muon in the pair.

The same procedure was applied to the y variables using a slightly different set of errors. The x and y information was treated separately since the errors in the parameters are nearly uncorrelated between the two views. Only the uncertainties from the spectrometer measurements are coupled but this is greatly diminished when they are combined with the errors arising from multiple scattering. With the initial slope and the momentum estimates of the muons, all the kinematics variables describing the production of the pair were calculated assuming an incident pion energy equal to the mean value of the beam.

The errors on the slopes, which are reflected in the resolutions of most of the kinematic variables, depend to a fair degree on the magnitude and concentration of the multiple scattering that occurred in the target. If the target material could have been distributed uniformly over the length of the absorber, the width of the dispersion from multiple scattering in angle, σ_θ, would have remained the same but the correction term in the above slope equation would have produced an additional 30% decrease in their uncertainities. Replacing the target, which contributed 30% to σ_θ, by one of beryllium of the same number of absorption lengths would have produced about a 50% reduction in the slope error although it would have led to a factor of two smaller data sample for the same integrated beam intensity. Since the mass resolution scales roughly in proportion to the error in the slopes, the J/ψ mass spectrum obtained from events originating in the absorber has nearly half the width as that from the target events. Such a distinction proved helpful in distinguishing these two classes of events as will be discussed in Chapter VI.

The χ^2 for the combination of the independent measurements of x_v is given by

$$\chi_x^2 = \left(\frac{\bar{x}_v - x_{v1}}{\sigma_{x1}} \right)^2 + \left(\frac{\bar{x}_v - x_{v2}}{\sigma_{x2}} \right)^2 + \left(\frac{\bar{x}_v - x_b}{\sigma_{xb}} \right)^2 .$$

The expression for χ_y^2 has an identical form and both values can be converted to probabilities (confidence levels) using the fact that there are two degrees of freedom in each view (3 measurements - 1 unknown). These statistical distributions can be used to reduce the background. The probability distributions for prompt di-muons that originated in the target should be flat, but about 75% of raw pairs in the data with a invariant mass in the J/ψ region have values less than .02 . Most of these events show the characteristics expected for accidental pairs containing a muon from a beam decay. Their appearance with small probabilities is not surprising since the width of the spatial distribution of the beam muons at the target was roughly four times larger than σ_{bx} or σ_{by} while the errors in their projected position to this region are small ($<$ 4 *mm.*) as a result of their large momentum. By rejecting di-muons with values of $P(\chi_x^2)$ or $P(\chi_x^2)$ less than .02, most of this background was eliminated with the sacrifice of only 4% of the prompt events. The remaining distribution is fairly flat and is examined in Chapter V in comparison with the Monte Carlo simulation of this spectrum.

3.4 Event Selection

In addition to the cuts to the data discussed so far, there were a number of other requirements imposed which helped to eliminate background events and simplify the calculations of the acceptance. It was useful to divide all requirements into two categories: those that were applied to the data but not to the Monte Carlo simulated events and those that were imposed on both. The former criteria are listed below.

- Events contain only two reconstructed tracks of opposite charge.
- Drift chamber tracks are 'in-time'.

- Hodoscope hits recorded with the event indicate that a veto should not have occurred.

A study of the events cut by these restrictions shows that they include 7 ± 1 % of total prompt signal where the largest contribution arises from the veto requirement. The veto condition was imposed off-line to eliminate possible background events that somehow did not prevent a trigger. In retrospect, however, it could have been omitted since the small enhancement in the fraction of background pairs in these events relative to the remainder of the data would have been eliminated by the vertex probability cuts.

The criteria that were also applied to the simulated events are given below.

- The twelve possible hodoscope counters associated with the two tracks registered hits and met the trigger requirements.
- The χ^2 probability for the vertex fit in each view was greater than 2%.
- The tracks did not hit the coils or pole pieces when projected into the analyzing magnet. This requirement effectively defined the geometric acceptance of the spectrometer since it was inclusive of any other restrictions from the detector sizes or upstream magnet apertures.
- The pair passed the cuts designed to eliminate the non-prompt pairs that remain in the data after the vertex fit requirements are imposed. These are specified in the next section.
- The reconstructed X_F of the pair was less than one.

Using all but the non-prompt background cuts, the mass spectrum of opposite sign pairs shown in Figure 16 was obtained. These data represents about four hours of running time and show clearly the domination of the triggers by low mass pairs. The J/ψ events, which appear as a distinct peak in this spectrum, were defined for the cross section analysis as pairs in the 2.7 to 3.5 GeV/c^2 mass range. This interval is expected to include over 90% of the J/ψ's in the data in nearly all kinematic regions. Figure 17 shows the J/ψ event distributions in the six kinematic variables[*] chosen to describe di-muon production. The same cuts used to obtain the full mass spectrum were applied to the total J/ψ sample in this case. The enhancement seen in the cos(θ) distribution near -1 can be

---

[*] With the coordinate system defined earlier, $\Phi_{lab} \equiv \tan^{-1}(P_{T,y}/P_{T,x})$.

identified as the largest component of accidental pairs in the J/ψ data before the addition background cuts were applied. They constitute about 3% of the sample and are similar in number and distribution to the $\mu^-\mu^-$ events that exist in this mass range. For reasons that are made more apparent in the next section, the equivalent set of positive pairs in the data is much smaller in number ($\approx$ .2%).

3.5 Non-Prompt Background Cuts

Although the overall fraction of accidental pairs in the J/ψ sample after the vertex cuts is small, they are concentrated in a fairly narrow kinematic region. Ideally, one would like to construct a cut based on some combinations of the track parameters to eliminate these events but leave the J/ψ component intact. To study this possibility, a set of background events was simulated by pairing tracks from data that were taken in a special run with a single particle trigger. The muons from this sample are overwhelmingly from the decay of hadrons; either those of the beam or those produced in the target. Before looking at the properties of these pairs, the characteristics of the single muon events are discussed.

To examine those tracks most likely to contribute to accidental pairs in the final data sample, the single particle events were processed in the same way as the di-muons except only those selection criteria relevant to individual tracks were applied. Also, a single track version of the vertex fits was performed where just the beam center provided the additional measurement at the target. A χ^2 probability greater than 2% in each view was likewise required in the selection of these events. The momentum distributions of each sign muon in the resulting sample is shown in Figure 18. One notes a clear distinction in the negative muon spectrum between the high momentum muons from beam decays from those at lower values from the decays of secondary particles. The shape of the large momentum negative spectrum is determined both from the kinematics of pion decay, which leads to the lower boundary at about 60% of $<P_{\pi^-}>$, and the effect of the beam holes in the hodoscope banks. The low energy (P $<$ 70 GeV/c) spectrum for both positive and negative particles are well reproduced by a Monte Carlo simulation of the production and decay of pions in the apparatus.[58] One can also account for the most of the 70 to 130 GeV/c negative muons by considering the decays of kaons in the beam.

The accidental pairs were generated by forming random +/- track combinations from the single particle trigger events and applying the same cuts used on the actual di-muon data. It was helpful to normalize the number of pairs which survived the selection criteria to the background in the di-muon trigger data so the effectiveness of any further cuts could be judged in terms of the absolute fractions of the background remaining. The high X_F, $\cos(\theta) \approx -1$ di-muon data were chosen for this purpose. They are heavily dominated by accidental pairs as demonstrated in Figure 19 by the large asymmetry in the di-muon $\cos(\theta)$ distributions at high X_F and by the consistency of the shape of this background with that predicted by the simulated accidental pairs. The normalization point in these plots is the left most bin of the $X_F > .9$ data where the background to signal ratio appears to be around 80 based on the few events in the right most bin (i.e. noting that $d\sigma/d\cos(\theta)$ for the signal is symmetric about $\cos(\theta) = 0$ and the acceptance near $\cos(\theta) = -1$ was roughly a factor of two smaller than at the other extreme).

With this normalization, the simulated background is compared in Figure 20 to the data as functions of the kinematic variables describing di-muon production. Similar plots were done for the $\mu^-\mu^-$ pairs in the data and the backgrounds generated from combining negative single tracks. A good agreement was achieved in the shapes of the distributions from these two sources which thus provided a check on the methodology.

Having established a means to simulate the non-prompt background, a search was done for ways to distinguish it from J/ψ decays. One useful fact was that most accidental pairs at this mass were formed with a muon from a beam decay in combination with one of very low momentum. Thus, the ratio of negative to positive muon momentum for these background pairs were much larger on average than that for the signal. Also, the beam muons had a small angular divergence since they had to have remained close to the beam axis for the pair to have passed the vertex fit requirements. In fact, the feature of these pairs that results in their appearing near $\cos(\theta) = -1$ is the small transverse momentum of the negative track in combination with its large energy. From these observations, it was found that a simple cut could be devised to isolate the non-prompt signal using both the square of the negative muon's transverse momentum, P^2_{T-}, and the momentum ratio P_{μ^-}/P_{μ^+}. The effectiveness of these quantities in separating the background from the data is illustrated in Figure 21. Here one compares the scatter plots in these variables of the data, the simulated non-prompt pairs, and the Monte Carlo generated J/ψ events. The cluster of points in the lower part of the background plot corresponds to the enhancement seen in the data when contrasted with the Monte Carlo simulation. The area below the dotted line in the Figures indicates the cut imposed to eliminate these events and is defined by

$$P_{T-}^2 < .32 \cdot P_- / P_+ - .4 \quad (GeV^2/c^2) \, .$$

The events that fill the upper left edge of the background plot have a similar topology as the beam muon events except with the sign of the tracks reversed. Although the positive momentum spectrum does not extend as high as the negative, such pairs still appear near the other extreme of the $\cos(\theta)$ range. To help reject these and other background events not eliminated by the above cut, it was required that the reconstructed momentum of each muon at the target be greater than 10 GeV/c. This resulted in a negligible loss of the J/ψ events while reducing much of the non-prompt background near $X_F = 0$.

Applying all of these cuts to the J/ψ data eliminated about 90% of the accidental events and yielded the distributions shown in Figures 22 and 23. The loss of prompt pairs seen from the $\cos(\theta)$ distributions reveals the price paid for rejecting a large fraction of this type of background. A closer examination shows that essentially all events in the data with $P_T < 1.2$ GeV/c and $\cos(\theta) < -.8$ have been eliminated. This was unavoidable, however, given the similar topology of two types of events in this kinematic region. Thus, the improvement introduced by these cuts came from the reduction of the backgrounds in the adjacent kinematic areas.

The small fraction of non-prompt pairs that remain in the data after the cuts were ignored when calculating cross sections integrated over the angular variables. For the $\cos(\theta)$ and ϕ distributions, however, the background determined by the method described here was subtracted from the data. As can be seen in Figure 22, the corrections over most of the range of $\cos(\theta)$ are less than 1%. The largest amounts occur at the extremes of this variable at small X_F where they are as high as 15% (the $X_F > .9$ region was not considered since it was omitted from angular distribution analysis). Similar values apply to the $\cos(\theta)$ spectrum when it is divided into regions of ϕ.

CHAPTER IV

CONTINUUM SUBTRACTION

From the mass distribution in Figure 16, one can see that a small fraction of the events in the J/ψ region can be associated with the production mechanisms which lead to the continuum spectrum of di-muon masses. This prompt background therefore has to be subtracted from the data before the cross sections can be calculated. In this chapter, a description is given of how the continuum fractions in the J/ψ mass region were derived in the various kinematic regimes.

The basic procedure in the continuum determination involved fitting the mass spectra in the 2.2 to 4.4 GeV/c^2 range to a linear combination of functions representing the sources of the di-muons. The data selected for this purpose were required to pass all the criteria listed in section 3.4 . To begin, the functional forms chosen for these fits are described.

4.1 Parametrizations of the Mass Distributions

The shape of the di-muon mass spectra expected from J/ψ decays alone was studied from Monte Carlo simulations of its production and measurement. These distributions depend only on the mass resolution of the detector since the decay width of the J/ψ is very small in comparison. The spectra were examined separately for events originating from the target and the absorber because of the difference in the width and mean of these distributions. For the former events, denoted J/ψ_{tgt}, the following empirical form was found to provide a good fit to the spectra independent of the kinematic region selected.

$$\frac{dN}{dM}(J/\psi_{tgt}) = \frac{N_{tgt}}{\left(1 + \left(\frac{M - M_o}{\Lambda_M}\right)^2 + \left(\frac{M - M_o}{.4}\right)^4\right)^2}$$

Here, N_{tgt} is a normalization factor, Λ_M is a measure of the width of the distribution, and M_o is the mass corresponding to the peak of the spectrum. The last quantity generally falls within a few tens of MeV/c^2 of the 'actual' J/ψ mass of 3.097 GeV/c^2. The values derived for Λ_M are fairly independent of X_F, P_T and ϕ but increase by about 50% in going from low to high $|\cos(\theta)|$.

One might expect that a Gaussian shape would have worked just as well in this application since the most of the smearing in the mass measurement comes from the error induced by multiple scattering. Although this function matches the main body of the spectrum ($\sigma_{tgt} = 180$ MeV/c^2 when averaged over all kinematic regions), the 'tails' in the simulated data are broader as a result of the skewness of the distribution representing the energy loss of the muons in the absorber.

Since the J/ψ events that originated in the absorber are reconstructed as if they were produced in the target, the opening angles of the muons are underestimated and thus their mass spectra appears shifted toward lower values. These events constitute only about 8% of the sample, and so for simplicity, their contribution was represented by

$$\frac{dN}{dM}(J/\psi_{abs})=N_{abs}\cdot\exp\left\{-\left(\frac{M-M_o+\Delta M}{\sqrt{2}\cdot\sigma_{abs}}\right)^2\right\}$$

where N_{abs}/N_{tgt}, ΔM and σ_{abs} were fixed to their values obtained in a Monte Carlo simulation of all events. The mass shift, ΔM, that results from the separation of the target and absorber materials is 250 MeV/c^2 and the value of $\sigma_{abs}/\sigma_{tgt}$ is about .5 as a consequence of the different amount of muon multiple scattering for these two classes of events.

The ψ' decay mass spectrum was represented by

$$\frac{dN}{dM}(\psi')=f_{\psi'}\cdot\left(\frac{dN}{dM}(J/\psi_{tgt},M+M_{J/\psi}-M_{\psi'})+\frac{dN}{dM}(J/\psi_{abs},M+M_{J/\psi}-M_{\psi'})\right)$$

so that $f_{\psi'}$ measured the ψ' contribution relative to the J/ψ decays. Finally, the continuum component (denoted *cnt*) was parametrized by

$$\frac{dN}{dM}(cnt)=N_{cnt}\cdot EXP\left(S_1\cdot M+S_2\cdot M^2\right)\ .$$

An illustration of the degree to which the sum of these functions conformed to the shape of the mass spectra is given in Figure 24 where the fit is shown to the $X_F > .1$ data. Besides the resulting match, the parametrizations of the continuum and the continuum plus ψ' components are also shown. Thus, with the seven parameters (N_{tgt}, M_o, Λ_M, $f_{\psi'}$, N_{cnt}, S_1 and S_2) allowed to vary in the fit, a reasonable interpolation of the continuum spectrum into the J/ψ mass region is obtained. Another check of this fit comes from the consistency of the result for the ψ' component, $f_{\psi'} = .012 \pm .001$, with that from other experiments (see section 7.3 for details).

From the parametrizations of the mass spectrum for each source of dimuons, the continuum fraction, R_{cnt}, was calculated with the following expression.

$$R_{cnt} = \frac{\int_{2.7}^{3.5}\left(\frac{dN}{dM}(cnt) + \frac{dN}{dM}(\psi')\right)\cdot dM}{\int_{2.7}^{3.5}\left(\frac{dN}{dM}(J/\psi_{tgt}) + \frac{dN}{dM}(J/\psi_{abs}) + \frac{dN}{dM}(cnt) + \frac{dN}{dM}(\psi')\right)\cdot dM}$$

The definition of continuum here includes the relatively small ψ' component and thus allows the factor, 1 - R_{cnt}, to correct for all non - J/ψ events in the mass range (2.7 to 3.5 GeV/c^2) used for the cross sections calculations. From the $X_F > .1$ results, $R_{cnt} = .098 \pm .002$ where the error is from statistics only.

To determine R_{cnt} as a function of the kinematic variables, the methods described above were repeated for the data divided into various bins of these variables. Due to the limited number of events in some of the regions, however, large bin to bin fluctuations arose if all seven parameters were allowed to float in the mass fits. For this reason, various constraints were imposed on these variables, especially in the low statistics regions. In particular, $f_{\psi'}$ was fixed in all subsequent fits to the value obtained from the $X_F > .1$ data. This was motivated both by the similar shapes of differential cross sections expected for the J/ψ and ψ' from the production mechanisms discussed earlier and by the observation that in regions where $f_{\psi'}$ can be determined to within 50% of its magnitude, no large systematic variations are seen. In any event, the uncertainty in the size of the ψ' component contributes little to the error in R_{cnt} in regions where the continuum fraction is large.

4.2 Results for X_F and P_T

The variation of R_{cnt} with X_F was determined from the fits to the mass spectra in 18 equal X_F regions from .1 to 1. The values for X_F less than .1 were not derived since the mass spectra in this regime decrease rapidly below the J/ψ peak and thus the shape of the continuum is uncertain. For $X_F > .8$, M_o and Λ_M were fixed at the values derived for these variables in the X_F bin below this cutoff. This is a good approximation since the Monte Carlo study indicated that these quantities change little at large X_F. Figure 25 shows the mass fits in three of the X_F regions and Figure 26 is a plot of the values of R_{cnt} obtained. Thus, the continuum component dominates the signal at high X_F.

The data in Figure 26 were parametrized using the following functional form.

$$R_{cnt}(X_F) = \frac{1}{1 + A\cdot(1 + B\cdot X_F{}^2\,)\cdot(1 - X_F)^C} \quad .$$

This choice was motivated by the fact that the X_F cross sections of both the J/ψ and the high mass continuum are well fit by the form $(1 - X_F)^C$. The empirical factor, $(1+B\cdot X_F{}^2\,)$, was included to improve the quality of the match to the data. Fitting the above function to the R_{cnt} measurements yields the curve shown in Figure 26 and the parameters

$$A = 22.4 \pm 1.4 \qquad B = 3.8 \pm 1.0 \qquad C = 2.1 \pm .11 \ .$$

In computing R_{cnt} as a function of both X_F and P_T^2, the data were divided into 8 equal X_F bins between .1 and .9 and each of these areas divided in 4 P_T^2 regions. The data above X_F of .9 were not used in cross section calculations differential in P_T^2 since there were not enough events to accurately extract the small J/ψ signal from the continuum. The resulting values of $R_{cnt}(X_F,P_T^2)$ are plotted in Figure 27. Here one notes that the continuum component decreases as P_T^2 becomes larger.

To parametrize this data, the same function applied to the $R_{cnt}(X_F)$ results was used except A was replaced by $A'\cdot(1 + P_T^2/D)^E$. This particular P_T^2 dependence was chosen since it works well in fitting the di-muons cross sections in general. The assumption in using this functional form is that the R_{cnt} dependence on P_T^2 does not change with X_F. This is warranted at the level of statistical accuracy of the data by the quality of the fit shown in the Figure. Here, B and C were fixed to their values from the P_T^2 integrated results. The remaining three parameters are

$$A' = 14.2 \pm 1.1 \qquad D = .78 \pm .45 \qquad E = .65 \pm .16 \ .$$

4.3 Results for $\cos(\theta)$ and ϕ

The angular distributions were calculated in 16 regions of X_F and P_T^2 in the analysis, and so the variation of R_{cnt} with $\cos(\theta)$ and ϕ in each area had to be determined. Due to the lack of data, this could only be done for the 8 lowest P_T^2 regions. The assumptions used for the others are discussed later.

Special consideration had to be made when correcting for the continuum contribution in these cases since each mass spectrum includes a small continuum component of non-prompt events and the data are separately corrected for this background (see section 3.5). To avoid double subtracting, the estimated non-prompt component in each region of $\cos(\theta)$ and ϕ was subtracted from the values of R_{cnt} derived from the mass fits. The size of this correction, however, is only large ($\approx$ 30%) in the high $|\cos(\theta)|$ bins ($|\cos(\theta)| > .7$) at low X_F. The results shown here incorporate these corrections.

When determining the dependence of R_{cnt} on $\cos(\theta)$ and ϕ individually, it was found that the results were symmetric about $\cos(\theta) = 0$ and $\phi = 0$. This is expected since the angular distributions of the J/ψ and continuum should also be symmetric about these points. Therefore, to improve the statistics in the mass fits, the data were binned in regions of $|\cos(\theta)|$ and $|\phi|$. The values obtained for R_{cnt} as a function of $|\phi|$ in each of the X_F and P_T^2 regions are shown in Figure 28. Here, no $|\phi|$ dependence is discernible. This is also true for the $|\phi|$ dependence when the data are further divided into regions of $|\cos(\theta)|$ although a variation with $|\cos(\theta)|$ is observed. It was thus assumed that R_{cnt} can be expressed as a function of $\cos(\theta)$ only. The R_{cnt} dependence on $|\cos(\theta)|$ is shown in Figure 29.

The variations of R_{cnt} with $|\cos(\theta)|$ are due to the changes in the continuum cross sections since the J/ψ decay angular distributions derived from our data are essentially flat. Since these cross sections are expected to be of the form, $1 + \alpha \cdot \cos^2(\theta)$, the following parametrization was used to fit the R_{cnt} data.

$$R_{cnt}(\cos(\theta)) = \frac{1}{1 + \frac{F}{1 + \alpha\cdot\cos^2(\theta)}}$$

The curves in Figure 29 are the result of these fits and Table 6 lists the values derived for α. Although the errors are large, most values of α are consistent with the expectation of $\alpha = 1$ for the Drell-Yan process (i.e., $q\overline{q} \rightarrow \mu^+\mu^-$). Also, the relative flatness of the distributions in the highest X_F bins is consistent with the change in α with X_F observed in both E444[12] and this experiment[55] for high mass ($M > 4\ GeV/c^2$) di-muon production.

For the data in the P_T^2 bins above 4.5 GeV^2/c^2, no continuum corrections were made (note that in the analysis, the angular distributions were arbitrarily normalized). If instead one assumed that the shape observed for $R_{cnt}(\cos(\theta))$ in each X_F region is the same at large P_T^2 but that its magnitude decreases with P_T^2 as in Figure 27, then the values computed for the angular distributions would only differ from the $R_{cnt} = 0$ results by less than half of their statistical errors.

TABLE 6

RESULTS FOR α IN THE FITS TO $R_{cnt}(\cos(\theta))$

	$P_T^2 < 1.5$	$1.5 < P_T^2 < 4.5$
$.1 < X_F < .3$	1.2 ± .7	3.2 ± 1.9
$.3 < X_F < .5$	1.4 ± .5	1.5 ± .8
$.5 < X_F < .7$	.9 ± .4	2.0 ± .7
$.7 < X_F < .9$	-.4 ± .3	.1 ± .7

CHAPTER V

DETERMINATION OF THE BEAM CHARACTERISTICS AND DETECTOR ACCEPTANCES

A knowledge of the acceptance characteristics of the apparatus is required to convert the observed event distributions into cross sections in the relevant kinematic variables. The acceptance was calculated using the Monte Carlo approach whereby the production, transport and detection of a large number of events are simulated by computer to determine the fraction that would have appeared in the data. In this chapter, the development and testing of the Monte Carlo computer program are discussed together with its application in deriving quantities needed for event reconstruction.

5.1 Beam Characteristics and Event Generation

To simulate di-muons for our experiment, the properties of the incident beam had to be determined. The size of the beam spot (σ_{xb} and σ_{yb}) and mean momentum were also required for the vertex fits and the calculation of the kinematics variables. Because of the brevity of the test run, special detectors were not installed to measure the beam directly. Instead, its characteristics were derived from a combination of indirect measurements and Monte Carlo simulations of particle transport in the secondary beam line.

The particle composition of the beam was obtained from an experiment which determined the particle yields in a secondary beam line similar to ours.[59] In extrapolating their measurements to our momentum setting, one predicts that besides the pions, the beam contained 1.8 ± .4 % kaons and .5 ± .2 % anti-protons. For reasons described in the next chapter, these small contributions can be treated as if they are pions from the point of view of simulating J/ψ production.

The properties of the secondary beam line were studied with the commonly used Monte Carlo program called HALO.[60] It simulates the transport of both hadrons and the muons from their decays. The layout of beam elements shown in Figure 8 were used as input to this program together with the magnetic field and collimator settings recorded during the run. The predicted transverse size of the beam agrees within 20% of that measured from the SWIC profiles. Also, the predicted fraction of muons in the beam is consistent with observations to this accuracy. It is difficult, however, to use this program to determine the absolute beam momentum to the level of a few percent due to the lack of precise information on the alignments, bend angles and calibration curves of the magnets in the beam line. However, the momentum spread, $\Delta P_{\pi^-}/P_{\pi^-}$, is more accurately predicted since it is mainly dependent on the setting of the momentum slit.

The observed momentum spectrum of beam associated muons was used, together with the HALO program, to determine the mean pion energy. The central beam momentum of the HALO program was adjusted so that the resultant muon momentum spectrum agreed with the distribution derived from the single particle trigger data. The tracks selected from the data for this study were required to meet all the criteria that applied to individual tracks in the regular di-muon sample plus a requirement which helped to eliminate those that originated outside of the beam region at the target. In addition, only those muons which appeared to the left of the C bank beam hole were used. This made the comparison insensitive to the uncertainities in the vertical positions of the holes relative to the beam. The momentum distribution of resulting events is displayed in Figure 30a. As noted earlier, the cut-off in the muon spectrum around 150 GeV/c is a result of the kinematics of the two body decays of the pions in the beam ($P_{\mu^-,min.} \approx (m_\mu/m_\pi)^2 \cdot P_{\pi^-} = .57 \cdot P_{\pi^-}$). Although the decay spectrum at the target was roughly flat from this edge up to about 200 GeV/c, the measured distribution falls off rapidly at higher momentum since the muons were closer to the centers of the beam holes and thus had a smaller probability of hitting the triggering counters.

In simulating the secondary beam for this study, the 2% component of kaons was also considered since their shorter lifetime and broader muon momentum distribution ($P_{\mu^-,min.} = .08 \cdot P_{\pi^-}$) makes their contribution to the muons in the data much more likely than that of the pions for P_{μ^-} below $.57 \cdot P_{\pi^-}$. The muons generated by the HALO program were used as input to the detector Monte Carlo program and subjected to the same requirements as the tracks in the single particle trigger data. In this process, only .6% of the beam muons present at the target reached the final sample and 20% of these were from kaon decays.

The best match between the predicted muon spectrum and the high momentum part of the data is shown in Figure 30b and was obtained using 268 GeV/c as the central momentum in the HALO program. The error in measuring the beam tune in this manner is estimated to be about 2%. The simulated spectrum in this Figure was normalized to the data in the momentum bin with the largest number of events. One area of disagreement is the region below the peak which is expected to be populated mostly by muons from kaon decays. Although part of this difference is due to not accounting for the tail of the muon momentum spectrum of secondary pion decays, most of it is probably from systematic errors in the many factors which determine the relative kaon contribution. Correcting for this difference in either case, however, has little effect on the match in the peak region which is dominated by the primary pion decays.

Using the 268 GeV/c beam tune, the HALO program was run to simulate the pion momentum spectrum incident at our target. Figure 31a shows this distribution which has a mean of 263 GeV/c and r.m.s. fractional width of 3%. The mean is shifted from the central value for which the beam was tuned since the momentum distribution of the pions produced at the primary target falls rapidly over the range of momentum acceptance of beam line. One advantage of using the beam energy derived in this way is that the calculation of X_F in the region near $X_F = 1$, where it is approximately $(P_{\mu^+} + P_{\mu^-})/P_{\pi^-}$, is insensitive to a systematic error in the field strength of the analyzing magnet since all the momenta are based on the spectrometer measurements.

In our Monte Carlo program, the beam momentum is generated from a simple parametrization of the spectrum discussed above. The momentum of the nucleons in the target elements were drawn from a Fermi gas distribution (270 MeV/c cutoff) modified with a high momentum 'tail' as prescribed in reference 61. The resulting beam-nucleon center of mass energy spectrum is given in Figure 31b. The 9% r.m.s. width of this distribution is almost entirely due to the smearing from Fermi motion. However, the contribution of this dispersion to the errors in the kinematic variables is only large relative to the other sources of smearing for the values of X_F near zero.

Another piece of information obtained from the beam simulation is the angular divergence of the pions at the target. This beam characteristic is incorporated in our Monte Carlo program by representing the distribution of slopes of the incident particles in either the x–z or y–z plane by a Gaussian shape with $\sigma = .3\ mr$. The smearing induced in the reconstructed kinematic variables from this dispersion, however, is generally small relative to that from multiple scattering. The azimuth angle of the beam particle and the nucleon are generated from an isotropic distribution. These values thus complete the information needed to specify the transformation from the lab frame to the beam-nucleon center of mass system.

The spatial characteristics of the beam at the target were inferred from the spectrum of the reconstructed di-muon vertex positions. In this application, the vertex fits were done without including the beam center as a measurement so the calculated positions and their errors did not depend on any assumptions about the beam. Events having an expected vertex resolution in x (y) less than 5 *mm.* and that pass the standard set of cuts are shown in Figure 32a (32b). After accounting for the measurement error, the underlying r.m.s. widths of the distributions are 10.5 *mm.* in the horizontal view and 9.7 *mm.* in the vertical view. They agree to within 20% of the HALO predictions and that crudely derived from the SWIC displays. These values are used for σ_{xb} and σ_{yb} in the vertex fitting routine that was applied in selecting the J/ψ events. Using the data to determine these quantities has the advantage that any degradation of the vertex resolution arising from such effects as a small movement of the beam center during the run, or misalignments of the wire chambers, are partially accounted for in the definition of the beam size.

The means of the vertex distributions are zero since they defined the x and y origin of the beam coordinate system. Thus, for the position of the beam relative to the target, one had to assume that the SWIC used to center the beam had been properly aligned with respect to the target. However, the symmetry of the vertex spectra and the size of their widths in comparison with the target dimensions ($5.7 \times 5.7 cm.$) indicate that the beam could not have been far off center.

As an approximation in the Monte Carlo simulation, a Gaussian beam shape is used with the measured r.m.s. vertex distribution widths taken as the standard deviations. Also the target is assumed to have an unlimited width. The z position of the interaction is generated from the distribution expected given the atomic weight dependence of production cross section and the absorption lengths of the target and absorber materials. The specifics on what quantities are used are discussed in the next chapter.

With the interaction point specified, the Monte Carlo program then generates particles according to the cross sections being studied. The remainder of the chapter deals with just the simulation of di-muons events relevant to the acceptance calculations. The differential cross sections used in this case are examined later.

5.2 Muon Transport

The trajectory of each muon in the apparatus is simulated by treating its interactions with the materials and the magnetic field in a series of steps. For the entire target and upstream absorber length, 32 intervals were chosen so that approximations could be used to simplify the transport equations in each region (e.g., treating the energy loss as continuous when calculating the muon's bending in the magnetic field). Only the vertical component of the magnetic field is applied and it is assumed to be independent of x and y. This is justified for the active region of the selection magnet since using the actual field profile as parametrized from the field measurement data produces changes in the muon's position in the spectrometer that are small relative to the dispersion from multiple scattering. As an approximation then, the field integrals computed from these functions evaluated along the beam axis are used to calculate the bending in each region.

Multiple scattering is included by incrementing the position and slopes of the muons by an amount that is generated from the binormal scattering distribution appropriate to the material in that region. The energy loss is drawn from four source distributions: ionization, bremsstrahlung, pair production and nuclear interactions. For the amount of material in the absorber, the Landau distribution is applicable for representing the losses from ionization and accounts for most of the average energy loss. The others contribute mainly to the 'tails' of the energy loss distribution.

The tracking of the muon is terminated if either all of its energy is lost or it hits a magnet coil or one of the pole pieces. Thus, muons bent outside the absorber area are treated as if they do not return to the active region of the apparatus. The Monte Carlo simulation itself gives support for this assumption in that muons passing the downstream geometric cuts rarely come close to these limits in the selection magnet. Also, this type of event is likely to be eliminated in the data by the vertex fit requirements since the tracks will not project back to the target correctly with the bending correction assumed in the fit. Those muons reaching the end of the selection magnet are projected into the center of the analyzing magnet, just as the tracks in the data, to eliminate the ones that land outside the aperture. The last step of the transport program simulates the energy loss and scattering in the non-magnetic iron walls at the downstream end of the apparatus.

5.3 Trigger and Hodoscope Efficiencies

If both muons successfully traverse the spectrometer, their positions are evaluated at hodoscope planes to determine the struck counters. If this set satisfies the trigger, the event is assigned a weight based on the efficiencies of the counters involved. For the actual data, all 12 possible counters associated with the two tracks were required to be on which is slightly more restrictive than the number always necessary to have produced a trigger (The exceptions were the rare cases when both muons were on the same side of the CX or DX bank and thus only one counter had to have fired to enable the Y counters). Ignoring the effect of small overlap that occurred in the E and F counters, the event weight is thus the product of the 12 counter efficiencies.

The counter efficiencies were determined using the di-muon data sample itself. Care was taken to avoid the bias that some subset of the counters in each event had to have registered for it to have been recorded. This problem was resolved by considering only those hits which if removed would not have prevented the trigger. The efficiency calculations involved dividing each counter into at least seven regions and determining the individual efficiencies by the fraction of the times the counter had registered when a track was present which projected into the given area. Since the average multiplicity of each hodoscope plane was about 2.4, there were enough cases where an extraneous hit occurred for the efficiencies to be calculated to a few percent accuracy in most regions of the planes. The results were found in good agreement with those obtained from a limited set of data taken with individual counter banks removed from the trigger. In this latter case, the errors were larger but the method was more straightforward since it did not rely on events with extra hits.

In most regions of the planes, the efficiencies were above 95%. However, there were a number of bad areas in the D bank that stemmed mainly from problems with 12 of the counters. The efficiency in these cases changed from a high value near the phototube end to a level below 50% at the other extreme. This type of degradation also occurred to a lesser extent in a number of the Y counters on the right side of the D bank. These effects are illustrated in Figure 33 which shows the inefficiency 'density' in the D bank.

One possible cause of the efficiency loss in these cases is that the gains of the phototubes were not large enough to convert the more attenuated light signal from the far end of the scintillation material to a signal that was cleanly above the discriminator thresholds. However, the efficiency verses high voltage curves produced for each counter near the beginning of the run to set their operating voltages showed no indiction that these counters were systematically different from any of the others. Another problem that could have led to this characteristic inefficiency was that the signals from the counters were mis-timed in a way that they arrived late relative to the trigger. This explanation is supported by the fact that the efficiency loss is not obvious in the hodoscope illumination displays of the raw data which include out-of-time hits. In either case, the simulated efficiencies should correctly account for the loss of acceptance.

A study using the Monte Carlo program shows that in addition to the 20% reduction in the overall J/ψ acceptance from the trigger logic requirements, a 30% loss occurred from the counter inefficiencies. The last factor translates into a geometric mean efficiency of 97% for each plane when one considers that twelve counters had to be on for the event to pass the cuts on the data. Since J/ψ events with a given value of X_F and P_T were not mapped into specific areas of the counter planes, the reduction in the acceptance due to inefficiencies is nearly uniform as a function of these variables. Even when further subdividing the acceptance loss into bins of cos(θ) or ϕ as shown in Figure 34, the variation is not large.

5.4 Event Reconstruction

The most accurate means of simulating the track reconstruction is to generate fake hit patterns and apply the track finding programs used on the data. However, this would contribute substantially to the amount of computer time needed to do the acceptance calculations and so a study of this process was done to see what simplifications could be made. For this purpose, the Monte Carlo program provided the track parameters required to generate a set of hits for each muon. The simulation of the extraneous hits, which appeared either randomly or correlated with the tracks (from delta rays, for example), were included by adding patterns found in actual events after stripping off the hits used in the global fits. The detection efficiencies of the chambers were taken into account when generating the hits using the values measured from the data for groups of 8 wires in the MPWC's and individual wires in the drift chambers. The simulation also reproduced the small deadened regions of the chambers that had been caused by the materials which bonded the sense wires to their support structures.

For those tracks reconstructed, the study showed that the global fits gave an unbiased estimate of the track parameters and the errors on the measurements were not noticeably worsened from the occasional inclusion of misidentified hits. Also, the resolution of the parameters was found to be fairly independent of the track's position which is not surprising given the redundancy of the measurements. However, it was estimated that 7 ± 1 % of the pairs were lost in the track finding process. The tracks were usually lost as the result of either particular patterns of missing hits or extra hit combinations produced by the correlated backgrounds. More important, however, was the conclusion that the losses showed no significant dependence on the kinematic variables describing the events.[62]

Based on the findings of this study and the fact the MWPC and drift chamber plane were large enough to intercept all muons passing the other geometric cuts, any pair passing the trigger requirements in the Monte Carlo program was assumed to be reconstructed. The actual losses that had occurred in the data were then corrected for separately when calculating the absolute cross sections (see section 6.3).

With this simplification, the simulation of the track reconstruction reduced to recreating the measurement errors on the track parameters. One method was to generate the errors from the covariance matrices obtained from the global fits of a randomly selected set of tracks in the data. This approach insured that the variation in the resolution that resulted from the different missing hit combinations would be properly reproduced given the observation that the errors are fairly independent of the track's trajectory. For most applications of the Monte Carlo, however, it was adequate just to simulate the momentum smearing since the errors on the other variables generally had little effect on the resolutions of the vertex parameters. In this case, the mean momentum resolution, $\sigma_P = 1.6\times 10^{-4} \cdot P^2$, was used.

With the addition of the track reconstruction algorithm, the Monte Carlo program provided all the information needed to derive the transport equations used in the vertex fits. As discussed in section 3.3, these equations relate the set of track parameters of a muon at the vertex to those measured in the spectrometer. Using the previously introduced notation, the three non-zero functions are

$$f_x \equiv <x_v - x_o> \qquad f_{tx} \equiv <tx_v - tx_o> \qquad f_P \equiv <P_v - P_o>.$$

The approach used to obtain expressions for these quantities involved simulating a large sample of single muons that covered the range of angles and momenta encountered in the data and fitting the distributions of difference terms listed above to functions of the reconstructed track parameters. The simulated muons were required to pass a loose cut based on their projection to the target to reproduce the rejection of events that occurred from the vertex fit requirements if either of the muons had suffered a large energy loss. In general, all three quantities are well represented by parametrizations involving just the spectrometer momentum. This is true in particular for f_x since the track position was evaluated at the mean production point in the target.

Since the general expression for the mean energy loss from ionization can be written as a constant plus a term logarithmic in energy, this form was used in the fit for f_P yielding

$$f_P = 2.54 + .51 \cdot \ln(P_o)\ .$$

For the parametrizations of f_x and f_{tx}, a $1/P_o$ term was included to represent the bending in the magnetic field and a $1/P_o^2$ term was added to account for the energy loss. This produced

$$f_x = 10.30/P_o - 17.4/P_o^2$$

$$f_{tx} = 2.627/P_o - 5.2/P_o^2 \,.$$

The $1/P_o$ coefficient in the f_{tx} expression is roughly the transverse momentum kick of the selection magnet while the same factor in f_x is related to the second integral of the magnetic field.

Although the application of the transport equations to the simulated di-muons yields in principle unbiased estimates of the vertex parameters, this is not guaranteed for the data because of possible errors in the field measurements. Errors in the fields of the selection magnet affect the coefficients derived for the f_x and f_{tx} parametrizations and the field errors of the analyzing magnet alter the momentum that is used to evaluate these equations. However, there are two properties of the data which allow a test of our determination of the transport characteristics of the magnets. The first is that the di-muons originated from a common point and thus the distribution of the quantity

$$\Delta X \equiv \frac{(x_o + f_x)|_{\mu^+}}{\sigma_{\Delta X}} - \frac{(x_o + f_x)|_{\mu^-}}{\sigma_{\Delta X}}$$

should have a mean of zero. Since there are small biases even in the Monte Carlo simulation of this spectrum because of the simple parametrization used for the transport equations, the actual test of this condition was done by comparing the Monte Carlo distribution with the data. Normalizing ΔX by $\sigma_{\Delta X}$ was useful since it provided a scale on which to judge any disagreements. The other feature of data which is sensitive to the field strengths assumed for the magnets is the central mass value of the J/ψ spectrum. Again, this is best evaluated by comparing the full J/ψ mass distribution to the corresponding results of a Monte Carlo simulation. To do either of these studies, both the resonant decays and the continuum were generated using empirical fits to the initial estimates of the J/ψ cross sections and the continuum ratios (R_{cnt}). However, the peak positions of the ΔX distribution or the mass spectrum are nearly independent of the cross sections assumed.

When these comparisons were first done, shifts between the distributions were observed that depended on variables that characterized the momentum of the pairs chosen (e.g. X_F or $1/P_{\mu^+} + 1/P_{\mu^-}$). The differences were noticeable relative to the resolutions in mass and ΔX, but were consistent with the $\approx 1\%$ uncertainty in the calibration of the magnetic field measurements. To correct for these disagreements by a small rescaling of the fields, the problem arose of decoupling the effect of each magnet. Fortunately, the mass offset can be determined independently of errors in the selection magnet field values by calculating the mass using the initial slope estimates based on f_{tx} only and selecting events with $X_F > .5$. In this case, the roughly equal number of in-bending and out-bending pairs cancel on average any bias in the opening angles determined with this transport function. With this approach, it required a 1% increase in the momentum of the tracks in the data to align its mass spectra with the Monte Carlo predictions. Such an increase is equivalent to rescaling the fields in the analyzing magnet by the same fraction.

After correcting the momentum measurements, the selection magnet field values used in the Monte Carlo program still had to be slightly modified so the resulting transport equations produced ΔX distributions for the data that matched the results from the simulation. In this case, a 0.5% decrease was required which again was consistent with the calibration accuracy of the field measuring devices. The transport equations listed earlier are the ones that resulted from this study and were used to obtain Figures 35 and 36. These plots show respectively the mass and ΔX comparisons in four regions of X_F. In each plot, the predicted distribution is scaled to match the number of events from the data. In general, the agreement is good although the width of the mass peak of the data is slightly wider than expected in two of the X_F bins.

Figure 37 shows the vertex χ^2 probability distributions obtained from the J/ψ data in comparison to the Monte Carlo results (note that the $P(\chi^2) < .02$ cut has been applied). Thus, the two spectra are in reasonable agreement. Both the data and the Monte Carlo distributions are not exactly flat as expected theoretically due to the lower values of $P(\chi^2)$ from the 8% contamination of absorber events. The target events better satisfy the assumptions implicit in the vertex fit and a Monte Carlo simulation of these pairs alone shows almost no increase at small probabilities.

5.5 Detector Resolution

After the fine tuning described above, the Monte Carlo program can be used to determine the resolution in the kinematic variables of interest. This is done by comparing the reconstructed variables with those generated. In Figure 38, these relations are illustrated in the form of scatter plots of the generated verses reconstructed values of X_F, P_T, $\cos(\theta)$, and ϕ for data in the J/ψ mass region.

The r.m.s. error in X_F ranges from .017 to .035 and is largest at both high X_F where the beam momentum smearing dominates and at low X_F where the effects from Fermi motion produce the most dispersion. The errors in the other variables result mainly from those in the reconstructed slopes of the muons. Since the slope uncertainities are roughly proportional to the inverse momentum of the muons, the product of the momentum and angle that appears in the P_T calculation makes its error fairly independent of the X_F or P_T of the event. This is also true of the mass for nearly symmetric events. In fact, the average mass resolution of 180 Mev/c^2 at the J/ψ is nearly equal to that for P_T with the appropriate change of units. The smearing in ϕ increases as P_T goes to zero since the axis defining ϕ vanishes in this limit. For P_T much larger than its resolution, the error in ϕ is typically .2 *rad.* and is nearly independent of X_F. The uncertainty in $\cos(\theta)$ also shows little variation with X_F or P_T but changes from about .05 near $\cos(\theta)=0$ to much smaller values at the extremes of this variable.

5.6 Data Comparisons

For the last cross check of the di-muon simulation process, the selection criteria that are listed in section 3.4 were applied to the data and Monte Carlo events. The two sets of distributions should then agree provided that the correct differential cross sections were used to generate the pairs and the simulation was done properly. To test the simulation while avoiding some of the bias resulting from the use of cross sections derived from the Monte Carlo calculated acceptances, comparisons were done of the characteristics of the individual muons of the pairs. The cross sections used to generate the J/ψ events in this study were from the final iterated results that are given in Chapter VII. The continuum contribution was included using the R_{cnt} functions given earlier.

Figure 39 shows the illuminations of the counters in the six hodoscope planes for the J/ψ data with $X_F > .1$ and the corresponding Monte Carlo predictions.

The simulated events are normalized to the data by matching the total number of muons. The statistical error on the number of simulated muons in each bin is always less than half of that of the data. In general, the match is fairly good even in the upper DY plane which contained a number of the bad counters. The worst area of agreement is in the upper CY plane where the apparent inefficiencies of some of the counters are the result of the 'shadowing' of D bank losses onto this plane.

Other muon characteristics that were compared were the distributions of the momenta and the vertex angles relative to the beam axis. Figure 40 shows that a good match is achieved for both the positive and negative muons of the pair.

CHAPTER VI

CROSS SECTION CALCULATION

This chapter deals with the determination of the absolute cross sections for the J/ψ data.

6.1 General Formulation and Simplifications

The relation between the number of J/ψ's produced, $N_{J/\psi}(V)$, in the kinematic region V, and the corresponding cross sections is given by

$$N_{J/\psi}(V) = \sum_{i,j,k} N_k \cdot \sigma_{i,k}(V) \cdot f_{i,j} \cdot \rho_j \cdot A_i^{-1} \cdot N_{AV} \cdot \lambda_j \cdot (1-e^{-l_j/\lambda_j}) \cdot e^{-NA_j} \qquad [6.1]$$

where

k denotes the particle types in the beam (π^-, K^-, $\overline{p}$).

j denotes the materials along the beam axis (target, hadron absorber).

i denotes the atomic elements in a given material.

N_k = number of incident particles of type k.

$\sigma_{i,k}(V)$ = cross section per nucleus of element i for the production of J/ψ's within kinematic region, V, by incident particle type k.

$f_{i,j}$ = fractional weight of element i in material j.

ρ_j = density of material j.

A_i = atomic weight of element i.

N_{AV} = Avogadro's number.

λ_j = absorption length of material j.

l_j = length of material j.

NA_j = total number of pion absorption lengths from the upstream end of the target to the beginning of material j.

The contribution to the J/ψ signal from the interaction of secondary particles produced in the target is ignored in this expression but will be considered later in the chapter.

To simplify equation 6.1, the importance of the 1.8% kaons and .5% anti-protons in the beam had to be assessed. The ratio of K^- to π^- induced J/ψ production has been measured by the NA3 group[13] at a beam momentum of 150 GeV/c and found to be consistent with a value of one, independent of X_F in the range, $0 < X_F < .7$. At larger X_F, the ratio decreases and is about .5 at $X_F \approx 1$. Their measurement of $\bar{p}$ to π^- initiated production at the same momentum shows its value decreases from 1.4 at $X_F = 0$ to about .1 at high X_F. Thus, the kaon and anti-proton contributions were roughly in proportion to their number. Since the final systematic error on the results are at the 10% level, the kaon and anti-proton components of the beam were assumed to behave like pions. Specifically, $\sigma_{i,k}$ was written as $\sigma_i \equiv \sigma_{i,\pi}$ and N_π defined by $\sum\limits_k N_k$.

The target and absorber were composed of a number of different elements so the atomic weight dependence of the production cross section was needed to further reduce equation 6.1. The most statistically accurate results on the J/ψ A-dependence have been obtained by the NA3 experiment which took data with both a hydrogen and platinum target.[13] With the parametrization,

$$\sigma(\pi^- P_t \rightarrow J/\psi X) = A^b_{P_t} \cdot \big(r_p \cdot \sigma(\pi^- p \rightarrow J/\psi X) + r_n \cdot \sigma(\pi^+ p \rightarrow J/\psi X) \big)$$

where r_n and r_p are the proton and neutron fractions of P_t respectively, they found b=.97 ± .02 for the $X_F > 0$ cross section measured at a beam momentum of 200 GeV/c. Experiment E444 derived the result, $b\ (X_F > 0) = .97 \pm .07$, by fitting A_i^b to the J/ψ cross sections obtained from 225 GeV/c pions incident on carbon, copper and tungsten targets.[12] For $P_{\pi^-} = 40$ GeV/c, other groups at CERN[9] and Serpukhov[7] have also measured values of $b\ (X_F > 0)$ that are consistent with these results.

For the variation of b with X_F or P_T, the results from these groups are less clear and so to avoid any ambiguity in this regard, our cross sections were quoted per tungsten (W) nucleus. The other elements in the target and absorber, which account for about 15% of the J/ψ signal, were normalized to tungsten assuming $b = 1$. Choosing any of the other measured values for $b\ (X_F > 0)$ change the cross sections by amounts less than 1%. These differences are more than a factor of ten smaller than the total systematic error from other sources. With $\sigma_i \sim A_i$, equation 6.1 can be inverted to yield

$$\sigma(V) = \frac{N_{J/\psi}(V) \cdot A_W}{N_\pi \cdot \sum_j \rho_j \cdot N_{AV} \cdot \lambda_j \cdot (1 - e^{-l_j/\lambda_j}) \cdot e^{-NA_j}} \qquad [6.2]$$

for the tungsten nucleus cross sections.

The remaining quantities required to evaluate this expression are the pion absorption cross sections, σ_{abs}. They were taken from the results of a Fermilab experiment[63] which measured the transmission of 280 GeV/c negative pions in various targets ranging in atomic weight from Li to Pb. With the parametrization, $\sigma_{abs} = \hat{\sigma}_{abs} \cdot A^{b_{abs}}$, they obtained the values, $\hat{\sigma}_{abs} = 26.57 \pm 1.03$ mb. and $b_{abs} = .755 \pm .01$. Their measurements at lower pion energies gave similar results and agree well with those reported at Serpukhov.[64]

With these quantities, the absorption lengths were calculated with the following expression.

$$\lambda_j = \frac{1}{\hat{\sigma}_{abs} \cdot \rho_j \cdot N_{AV} \sum_i f_{i,j} \cdot A_i^{b_{abs}-1}} \qquad [6.3]$$

The values of l/λ listed in Table 1 (section 2.3.3) for the materials in the apparatus were obtained in this way. Besides entering the cross section calculations, the absorption length values are used in the Monte Carlo program together with the assumption on the A-dependence of J/ψ production to generate the z positions of the interactions. Using equation 6.2 and the information from Table 1, one predicts that 10.6% of all J/ψ's produced in our experiment originated in the absorber.

6.2 Z Vertex Distributions

To check the consistency of the quantities obtained from other experiments with our data and to the examine the question of secondary production, comparisons were done between the data and the Monte Carlo predictions for the distribution of the reconstructed z position of the vertex, z_v. The procedure used to estimate the initial z values is more complicated than that presented earlier for the transverse positions since z_v appears multiplied by the slope variables in the fitting equations. However, the slopes could be expanded about the values obtained from the $z_v = 0$ fits to linearize the equations since the slopes are fairly insensitive to changes in the vertex position assumed in their calculation.

Another approximation used to simplify the equations in the fit was to ignore the differences in the amount of bending of the muons in the selection magnet associated with the changes in the vertex positions. The average z_v resolution obtained for the J/ψ data when combining both the x and y information in these fits is 32 *cm.* .

The events used for the comparison were required to pass the standard set of cuts for di-muon data except that the χ^2 probability was based on the unconstrained z_v results. The probability distribution in this case is flatter than that from the constrained z_v fits since there is no bias against events originating from the absorber. The kinematic variables were ***not*** recalculated using the new vertex information so the lower mass limit of the data was extended to 2.55 GeV/c^2 to account for the shift in mass of the J/ψ absorber events.

With these changes, the comparison of the z_v distributions for events with $X_F > 0$ is shown in Figure 41a where the Monte Carlo results have been normalized to agree with the data near $z_v = 0$. Although the shape of the distributions in the target region agree, the simulated spectrum falls about a factor of two below the data in the absorber area. If this enhancement in the data is due to the production of J/ψ's by particles generated by beam interactions, then the smaller momentum of the secondaries should lead to an X_F spectrum for the absorber events that is weighted toward lower X_F values relative to the target data. To test this possibility, an effort was made to obtain a sample of events largely from the absorber and a second sample primarily from the target. The selection criteria were

$$\text{absorber:} \quad .7 < z_v < 2. \quad \text{and} \quad 2.55 < \text{M} < 3.0 \text{ GeV}/\text{c}^2$$

$$\text{target:} \quad z_v < .5 \quad \text{and} \quad 2.80 < \text{M} < 3.4 \text{ GeV}/\text{c}^2 .$$

To search for an enhancement of the absorber events at low X_F, the ratio of the event yields in the two samples was plotted as a function of X_F. The result is shown in Figure 41b together with the Monte Carlo predictions for these ratios. In comparing the two distributions, one sees that the enhancement occurs almost uniformly in X_F although there is a rise in data ratios at low X_F relative to the Monte Carlo results. However, the excess of absorber events in the low X_F region only account for about 10% of the total enhancement. Thus, secondary production is unlikely to be the main cause of this effect.

Other more obvious explanations as to the origin of this difference were explored although none proved fruitful. A study of the mass spectra of the absorber events, for example, showed that they were clearly distinct from the those of the target events in that they have a smaller width (about a factor of two) and lower average mass ($\Delta M = 250\ Mev/c^2$). Also, the x and y vertex position distributions of the absorber events do not indicate that a significant fraction of them were produced from a portion of the beam having missed the target.

Since our experiment was not optimized to explore the physics questions relating to this difference, the disagreement was left as unresolved. In the Monte Carlo program, however, the absorption lengths were rescaled by a factor of 1.4 in order reproduce the observed fraction of absorber events in the data. With this correction, the calculated acceptances better reflect the mixture of absorber and target events in the data. However, the expected fraction of absorber events in the final J/ψ sample only increases from 5% to 7.5% with this change. The modification of the Monte Carlo program also had the effect of reducing the acceptances almost uniformly by about 6% relative to the unscaled results. Even if one views this value as a contributing error to the overall normalization of the data, it is still smaller than the other systematic uncertainties.

6.3 Normalization

The final input needed to evaluate equation 6.2 is the number of J/ψ's produced per incident pion. This was expressed as

$$\frac{N_{J/\psi}(V)}{N_\pi} = \frac{N_{\mu^+\mu^-}(V)\cdot(1 - R_{cnt}(V))}{B_{\mu^+\mu^-}\cdot E_R\cdot Acc(V)\cdot NL_\pi} \qquad [6.4]$$

where

$N_{\mu^+\mu^-}(V)$ = the number of reconstructed muons pairs in kinematic region V which pass the cuts specified in section 3.4.

$R_{cnt}(V)$ = the fraction of continuum events in the J/ψ mass region.

$B_{\mu^+\mu^-}$ = the branching fraction of J/ψ decays to muons pairs. The measured value[65] of this quantity is .074 ± .012 although it is not numerically substituted in most of the results that are presented.

E_R = the reconstruction efficiency. This factor corrects for J/ψ events missed by the track finding programs or where cut by those requirements that were specifically applicable to the data. As discussed earlier, each of these losses is about 7% independent of the kinematic region considered. This yields $E_R = .86 \pm .015$.

$Acc(V)$ = the Monte Carlo calculated acceptance in kinematic region V.

NL_π = the total number of hadrons incident on the target when the trigger system was not inhibited.

The last two factors are described below.

The acceptance calculated with the Monte Carlo program, *Acc* ,accounts for all loses of J/ψ events not included in E_R. It is defined as the ratio of the number of reconstructed pairs in kinematic region V to the number generated in this volume of phase space. Since some of the events observed in V are the result of smearing from the nearby kinematic regions, care had to be taken to make the simulated cross sections consistent with the data. The empirical functions used for this purpose are given in the next chapter and were the result of an iterative process.

To compute NL_π, the number of hadrons that were incident on the target for each spill was needed as well as the live time of the experiment during these periods. As described in section 2.4, the live time was measured by comparing the scaler rates of signals that were summed both continuously and only when the trigger was not inhibited. Of the two target monitors employed to provide such signals, only one worked consistently throughout the run and so was used for this calculation. The values derived generally fall in the 45% to 55% range for most of the experiment with the exception of the short series of runs where the pion intensity was increased by a factor of 2.5 as part of a study of rate dependent effects in the hardware.

To provide a check of these results, the '$\geq$1' multiplicity outputs corresponding to the downstream hodoscope banks were summed in this manner but the veto signal was not used in gating these scalers since it was correlated with the hodoscope signals. The ratio of the target monitor determination of the live time to that from any of the hodoscope banks does not vary by more than 5% over the roughly one hundred runs in which the data was taken. This consistency is thus a good indication of the reliability of target monitor data.

The number of particles in the beam was measured using an ionization chamber located 60 *cm.* upstream of our target. The charge liberated when the beam passed through the gas in this device was integrated in five concentric sections and then converted to digital signals at the end of the spill. The calibration of the inner four rings, which roughly matched the transverse area of the target, was done by exposing a thin copper plate to the beam for a few hours. The amount of ^{24}Na produced in the region of copper that coincided with the four inner rings was then measured by detecting the gamma rays from its decay. Using this number, the cross section for producing ^{24}Na by high energy pions and the sum of the chamber signals during the exposure yields a calibration of $1.74 \pm .2 \times 10^4$ hadrons per chamber count. This value agrees within 5% of that obtained from a cross calibration with another ionization chamber positioned 24 *m.* upstream of our target. The second chamber had been calibrated earlier with this and other techniques by the group using the beam before us. The stability of the ionization chamber results were verified by observing that the ratios of the chamber count to the total number of hits in the downstream hodoscope banks show no apparent drift when examined for the set of runs used in the analysis.

From the live time and beam flux obtained for the individual spills, NL_π was computed for each run first. The data was also divided by run number and the ratios, $N_{\mu^+\mu^-}/NL_\pi$, formed to check for systematic errors that would appear as a change in these quantities over the course of the experiment. Although the ratios are roughly consistent in the latter two-thirds of the runs, they vary in the others and have a mean value that is about 15% smaller. This difference was traced to a problem that had occurred intermittently in recording the hodoscope latch words to tape for these runs. In such cases, the events were always eliminated off-line since the latch information indicated they did not satisfy the trigger logic. To compute NL_π for the whole data sample then, its value was summed for the last two thirds of the runs and divided by the fraction of the total number of J/ψ events they contained. This yielded $NL_\pi = 1.49 \pm .19 \times 10^{12}$ where the error reflects both the live time and ionization chamber calibration uncertainties.

Combining equation 6.2 and 6.4 and substituting the values of all known quantities gives the normalization expression below.

$$B_{\mu^+\mu^-}\cdot\sigma(V) = \frac{(1.20 \pm .15 \times 10^{-3})\cdot N_{\mu^+\mu^-}(V)\cdot(1 - R_{cnt}(V))}{Acc(V)} \quad (nb./W\ nucleus) \quad [6.5]$$

The error in this result is dominated by the uncertainty in NL_π.

CHAPTER VII

RESULTS

In this chapter, the total and differential J/ψ cross sections are presented and compared to production models described earlier. To begin, the general features of the data are examined.

7.1 Empirical Fits to the Cross Sections in X_F and P_T^2

The distribution of J/ψ events in X_F, after the continuum corrections are applied, is shown in Figure 42 together with the Monte Carlo calculated acceptance. The errors on the data points reflect both counting statistics and the uncertainty in the determination of the continuum fractions. The number of simulated events used in the determination of the acceptance values were large enough such that their statistical error always contributed less than 10% than that of the data to the errors on the cross sections.

The steep fall off in the acceptance seen near $X_F = 0$ is also accompanied by a restriction of the pairs to small P_T values. Thus, the acceptance determination in this regime is fairly dependent on the differential cross section assumed in the Monte Carlo program. Because of this condition and the uncertainty from the possible secondary production contributions at low X_F, the differential cross sections in this variable are reported only for $X_F > .1$. The plateau in the acceptance above $X_F = .5$ arises from the fact that most of the symmetric ($|\cos(\theta)| < .5$) out-bending pairs are detected. Their number approaches that of the more easily contained in-bending pairs at high X_F. Above $X_F = .95$, the acceptance increases rapidly due to the smearing of the lower X_F events into these bins. Although this effect also makes the acceptance very dependent on the Monte Carlo source spectrum, an even greater systematic uncertainty arises from the extrapolation of continuum background function $R_{cnt}(X_F)$ into this region. Given these possible problems, the X_F cross sections above values of .95 are not quoted.

From the data and acceptance of Figure 42, and the normalization derived in the last chapter, the values of $B_{\mu^+\mu^-}\cdot d\sigma/dX_F$ were calculated. They are plotted in Figure 43a. Also shown are the results in three P_T^2 regions and the matches achieved from fitting the cross sections to the form

$$B_{\mu^+\mu^-}\cdot d\sigma/dX_F = A\cdot(1 - X_F)^C.$$

Except for the small systematic deviations at high X_F, this function provides a good fit to the shape of the spectrum. These plots and the values obtained for C that are listed in the figure caption show that the fall off in the large X_F cross section increases at larger P_T^2. This trend is illustrated in more detail in Figure 44 where the values of C derived in smaller bins of P_T^2 are plotted against this variable. Since the change in C appears at low P_T^2, it is unlikely to be due to a phase space restriction of the longitudinal momentum of the J/ψ. Also, the definition of X_F accounts for the change in the maximum longitudinal momentum with P_T^2 and so would naively incorporate the effect of such a constraint on the shape of the spectrum (note that $P_{L,max}$ changes by only 4% between P_T^2 values of 0 and 10 GeV^2/c^2).

Another view of the behavior noted above comes from examining the change in the P_T^2 spectra with X_F. For the study of the P_T^2 distributions presented in this work, the data were divided into eight equal X_F bins from .1 to .9 . The region above $X_F = .9$ was excluded since the continuum fraction could not be determined as a function of P_T^2 in this bin while that below $X_F = .1$ was omitted for reasons similar to those given for the $B_{\mu^+\mu^-}\cdot d\sigma/dX_F$ cross sections. The variation of the acceptance with P_T^2 is fairly small in most of the areas as can be seen in Figure 45. Nearly all of the values shown here were evaluated from the results of polynomial fits in powers of P_T^2 to the acceptances determined in each X_F region. These functions smoothed out the bin-to-bin statistical fluctuations ($<$ 5% of the acceptance) that arose from dividing the limited number of simulated events into a large number of regions. The points at low P_T^2, where there is a more rapid change in the acceptance, were obtained individually. In these regions, the cross sections are decreasing while the geometric acceptance is nearly flat, so the effect of the smearing in P_T^2 leads to the apparent losses in acceptance that are observed. Although the resolution in P_T^2 worsens as P_T increases

($\sigma_{P_T^2} \approx .4 \cdot P_T$), the change in the acceptance due to the smearing remains small ($< 10\%$) over the kinematic range considered.

The differential cross sections obtained from these results are plotted in Figure 46 and show that the low P_T^2 slopes of the spectra become steeper at higher X_F. The shapes at larger P_T^2, however, are fairly independent of X_F as is expected from the plateau observed in the C verses P_T^2 plot.

The curves drawn in the plots are the cross sections used in the Monte Carlo program to obtain the acceptances for the data points shown. In the simulation, the angular distribution of di-muons in their rest frame was assumed isotropic which will be shown later to be consistent with the data. The match with the measured cross sections was achieved by iteratively fitting them to the ad hoc form

$$B_{\mu^+\mu^-} \cdot \frac{d\sigma}{dX_F dP_T^2} = \frac{A \cdot (1 - X_F)^C}{(1 + (P_T^2)^B / S)^T}$$

where

$$S = D + E \cdot (1 - X_F)^2$$

$$T = F + G \cdot (1 - X_F)^2$$

and using the results in the Monte Carlo program to generate a new set of acceptances. With just two cycles, the values* below were obtained and produced a χ^2/d.o.f. of 1.2 when compared to the data shown in Figure 46.

$A = 4.1 \pm .1 \times 10^3$ (*nb./* W nucleus)

$B = .82 \pm .02$	$C = 2.36 \pm .03$
$D = 2.8 \pm .5$	$E = 37. \pm 8.$
$F = 5.8 \pm .6$	$G = 27. \pm 7.$

At small X_F, both S and T are large so the shape of the P_T^2 spectrum is roughly exponential over the range of data in the plots. The decrease in S and T as the $(1 - X_F)^2$ term goes to zero produces a power law behavior at low P_T^2 while yielding a similar large P_T^2 spectrum for all X_F.

---

* The error in the value of A does not include the uncertainty in the normalization of the data.

To characterize the changes in the P_T^2 spectra that are observed, the values of $<P_T>$ and $<P_T^2>$ computed from the data are plotted in Figure 47 as a function of X_F. The errors on the data points are statistical only. In section 7.5, some ideas on the origin of this behavior are discussed.

7.2 Nuclear Effects in J/ψ Production

Since a parton model interpretation of J/ψ production predicts that the cross section in any kinematic region should be linearly proportional to the number of nucleons in the target elements, it is important to consider how well measurements conform to this expectation before applying these ideas. Although there is a consistency among experimental determinations of the A-dependence of the total cross section, disagreement exits as to its variation with X_F. The NA3 experiment,[13] which ran with a hydrogen and platinum target simultaneously, found that the ratio, $d\sigma(H_2)/d\sigma(P_t)$, is roughly flat below $X_F = .4$ and then increases until it is about a factor of three larger near $X_F = 1$. The Omega experiment at CERN also observed a similar trend using tungsten and hydrogen targets.[9] These changes are unlikely to be due to the different proton to neutron ratios in the two targets since the same set of measurements with a positive pion beam gave similar results. In experiment E444,[12] J/ψ production was measured on a series of nearly isoscalar targets (A $>$ 12) and the cross sections fit to the form, $d\sigma \sim A^b$. Their results show that b is independent of X_F at a statistical level that is clearly distinguishable from that derived from the NA3 findings.

For the A-dependence variation in P_T, all three experiments mentioned above find that b increases as P_T becomes larger. This behavior is also observed in our data from comparing the P_T cross sections of events from the target and absorber. Our results are in fact in good agreement with the E444 measurements despite our inability to account for the absolute number of absorber events. To illustrate the size of this A-dependence effect, the P_T^2 variation of the nucleon ($\equiv$ (proton + neutron)/2) to tungsten cross section ratio derived in these two cases will be examined.

For our data, the $X_F > .1$ absorber to target cross section ratio is plotted in Figure 48a as a function of P_T^2 (similar results are obtained if the data are divided into smaller X_F regions). To use these values to obtain the nucleon to tungsten cross section ratios, the A-dependence was parametrized by,

$b(P_T^2) = C + D \cdot P_T^2$, and the data were fit using the approximation

$$d\sigma(\text{absorber})/d\sigma(\text{target}) \approx (A_O/A_W)^b \ .$$

This formulation allows the value of D to be extracted without knowing the absolute cross section ratios. The curve shown in Figure 48a is the result of the fit which yielded $D = .025 \pm .004$. Given this result and assuming any of the values for C derived from the measurements of the other experiments, the above approximation is good to within 5%.

The predictions for the absolute ratios of the nucleon to tungsten cross sections derived from the E444 A-dependence measurements are plotted in Figure 48b and compared to the variation expected from the parametrization obtained from our data (the normalization was done by eye). If the extrapolation above $P_T^2 \approx 8\ GeV^2/c^2$ is valid, then this ratio falls by about a factor of ten from $P_T^2 = 0$ to $16\ GeV^2/c^2$. This variation is about twice as large as measured by the NA3 group although their values also fall off slower at lower P_T^2 where a direct comparison can be made.

Theoretically, there is no well established reason why this change occurs although a simple explanation is that the J/ψ scatters in the nucleus to produce an enhanced yield at high P_T. The average value measured for b $(X_F > 0)$ is in fact consistent with predictions based on the J/ψ - nucleon absorption cross section obtained indirectly from photoproduction experiments.[13] For the study of the P_T^2 spectra presented in section 7.5, this point of view is taken to evaluate the A-dependence corrections to the parton cross section predictions.

7.3 J/ψ and ψ' Total Cross Sections

Computing the $X_F > .1$ J/ψ cross section from equation 6.5 with the values, $Acc = .072$, $N_{\mu^+\mu^-} = 7.23 \times 10^4$ and $R_{cnt} = .10$, yields

$$B_{\mu^+\mu^-} \cdot \sigma_{J/\psi}(X_F > .1) = 1080 \pm 140 \quad (nb./W\,\text{nucleus}).$$

The error quoted does not include a contribution from the systematic uncertainty in Acc.

Although some potential problems were noted in the last section for the $X_F < .1$ data, it is useful to have an estimate of the $X_F > 0$ cross section to make comparisons with other experimental results that are usually quoted in this form.

Besides recalculating the quantities above to obtain this value, it was also derived by multiplying the $X_F > .1$ result by the fractional increase expected from the fusion fits to $d\sigma/dX_F$ given in section 7.4 . The calculations all agree within two percent and give

$$B_{\mu^+\mu^-} \cdot \sigma_{J/\psi}(X_F > 0) = 1510 \pm 200 \ \ (nb./W\,\text{nucleus}).$$

The above value and other experimental results[66] are plotted in Figure 49 as a function of the pion beam momentum. The targets used to obtain these results were either tungsten or platinum with the exception of the lowest momentum value which was measured on copper. All values were made comparable to the tungsten data assuming $\sigma \sim A$. Including only the heavy target data in this comparison makes the results fairly independent of the A-dependence parametrization chosen. Using $\sigma \sim A^{.8}$, for example, changes the copper target value by less than its error.

The curves shown in Figure 49 were obtained from the approximate form of the fusion model prediction:

$$\sigma_{J/\psi} \sim F_{gg}(\tau_{J/\psi}) + K_{q\bar{q}}/K_{gg} \cdot F_{q\bar{q}}(\tau_{J/\psi}).$$

The overall normalization to the data was done by eye. The cross sections were calculated with the same inputs used to estimate the cross section ratios in Section 1.10 (i.e. the CDHS gluon distribution for the nucleon, $n_\pi = 2.2$ in equation 1.24 for the pion, the quark structure functions given in equations 1.3 and 1.13, and $K_{q\bar{q}}/K_{gg} = 1.4$). Thus, our result compares well with the other measurements and the variation of the values with beam energy is in good agreement with the shape of the weighted sum of the gg and $q\bar{q}$ excitation functions.

The ratio of the ψ' to J/ψ cross section was calculated using the value obtained for their $X_F > .1$ event ratios, $f_{\psi'}$, by the method described in section 4.1, and the ratio of their acceptances in this same X_F region. Since the differential cross section of the ψ' is not well measured, it was assumed to have the same form as the J/ψ in the Monte Carlo calculation of its acceptance. The ψ' acceptance is then 20% smaller than the J/ψ. From these results, one obtains

$$B(\psi' \rightarrow \mu^+\mu^-) \cdot \sigma_{\psi'} / B(J/\psi \rightarrow \mu^+\mu^-) \cdot \sigma_{J/\psi} = .015 \pm .003 \ .$$

The error includes an estimate of the systematic uncertainty in $f_{\psi'}$. This value agrees well with other measurements:

.018 ± .005 for $P_{\pi^-} = 150\ GeV/c$ (all X_F)[8]
.021 ± .006 for $P_{\pi^-} = 225\ GeV/c$ ($X_F > 0$)[12]
.017 ± .009 for $P_{\pi^+} = 225\ GeV/c$ ($X_F > 0$).[12]

Using our result and the known branching ratio (.53 ± .02)[65] for the ψ' to J/ψ decay transition, one predicts that the fraction of J/ψ's produced from ψ' decays in our experiment was .069 ± .013 .

The cross section ratios given above are also consistent with measurements done with other incident particles when one first subtracts the known indirect production contribution in each case (e.g., measurements show that about 40% of the J/ψ's are produced in $\pi^- N$ interactions from the decays of other charmonium states - see section 1.7). For photoproduction of the J/ψ and ψ' , a Fermilab group[17] reports a value for $\sigma_{\psi'}/\sigma_{J/\psi}$ of .20 ± .05 from measurements using a deuterium target ($<E_\gamma> = 150\ GeV/c$). The events chosen for this determination were ones where there were no additional charged tracks or photons in the forward spectrometer of their apparatus and so the result is a good measure of the direct production ratio. This sample actually represents a large fraction of all events as expected since their hydrogen target data show that roughly 70% of the J/ψ's are produced elastically (i.e., $\gamma p \rightarrow J/\psi p$). To compare this result to our data, 60% (100%) percent of the J/ψ's (ψ' 's) were assumed to be produced directly in pion interactions and the value of $B_{\mu^+\mu^-}$ was computed for the J/ψ and ψ' by averaging the measured muon and electron values. This gives $\sigma_{\psi',direct}/\sigma_{J/\psi,direct} = .21 \pm .06$. A similar calculation using cross sections obtained from proton induced production[12] ($P_p = 225\ GeV/c$) yields a value of .28 ± .16 where a 50% direct component was assumed for the J/ψ according to the measurements[40] of the χ decay contributions at higher energies. Thus, all ratios are in agreement although the errors are large for the proton result. One point to note is that at the beam energies of these measurements, the J/ψ cross section is not changing rapidly with energy so the effect on the ratios from the difference in M^2/S_0 of the two states at a given energy should not be large from the point of view of the fusion model. As mentioned earlier, the consistency of these ratios may be an indication that the indirect production fractions of the J/ψ and ψ' in hadronic interactions are not much larger than the values observed thus far.

The ψ' to J/ψ production ratio for our data was predicted using the scaling expression in equation 1.38. The function $h(\tau)$ was approximated by the gluon excitation function used to obtain the $\sigma^{J/\psi}$ verses P_{π^-} predictions. One sees from Figure 49 that this excitation function provides a good representation of the variation of the cross sections at high beam momenta. Thus one predicts

$$\frac{\sigma_{\psi',\mathrm{direct}}}{\sigma_{J/\psi,\mathrm{direct}}} = \frac{M^3_{J/\psi}\cdot\Gamma(\psi' \rightarrow l^+l^-)\cdot F_{gg}(\tau_{\psi'})}{M^3_{\psi'}\cdot\Gamma(J/\psi \rightarrow l^+l^-)\cdot F_{gg}(\tau_{J/\psi})} .$$

The excitation function ratio, $F_{gg}(\tau_{\psi'})/F_{gg}(\tau_{J/\psi})$, computed at our beam energy is .7 . Using this in the above expression yields .16 ± .03 for the cross section ratio where the error is from the measurement of the leptonic decay widths. This value is in agreement with our result which would be true even if $h(\tau)$ were assumed to be the same for the two states.

7.4 Fusion Analysis - The X_F Dependence of the Production

In Section 1.8, the formalism was developed for treating the total $(X_F > 0)$ cross section as a sum of $q\bar{q}$ and gg subprocesses. The dynamics were represented by the unknown parton cross sections K^j_{gg} and $K^j_{q\bar{q}}$ for forming charmonium state j, and the assumption that the fusion constraints are applicable. To extract the gluon structure functions and the magnitudes of the parton cross sections from our measurements of $d\sigma/dX_F$, a form of equation 1.19 in which the excitation functions appear differential in X_F was used to fit the data. The terms entering this equation are discussed below.

The $q\bar{q}$ production spectra of charmonium state j was represented by

$$\frac{dF_{q\bar{q}}}{dX_{F,j}} = \frac{1}{x_\pi + x_n} \sum_{i=u,d,s} \left(f_{q_i/\pi}(x_\pi)\cdot f_{\bar{q}_i/n}(x_n) + f_{\bar{q}_i/\pi}(x_\pi)\cdot f_{q_i/n}(x_n)\right)$$

where x_π and x_n are defined from the fusion relations in equations 1.10 and 1.11 with $\tau = M_j^2/S_o$. The quark structure functions were evaluated using the measurements listed in Chapter 1. The shape of gluon excitation functions were allowed to vary in the fit by introducing the variables n_n and n_π which entered as powers of (1 - x) in the standard parametrization of the gluon structure functions for the pion and nucleon respectively (see equation 1.24). With these substitutions, the gluon fusion spectrum is

$$\frac{dF_{gg}}{dX_{F,j}} = \frac{(n_\pi + 1)\cdot(n_n + 1)}{4}\cdot\frac{(1 - x_\pi)^{n_\pi}\cdot(1 - x_n)^{n_n}}{x_\pi + x_n}\ .$$

To convert these distributions to ones that represent the contribution to the J/ψ spectrum, the effect of the decay transitions were simulated by the convolution

$$\frac{dF^{S_j}}{dX_F} = \int_{X_{F,j}^{\min}}^{X_{F,j}^{\max}} \frac{dF}{dX_{F,j}}\cdot S_j(X_{F,j} \rightarrow X_F)\ dX_{F,j}$$

where $S_j(X_{F,j} \rightarrow X_F)$ is the probability density that charmonium state j, with longitudinal momentum fraction $X_{F,j}$, decays to a J/ψ characterized by X_F. These functions are defined below.

J/ψ: $\delta(X_{F,J/\psi} - X_F)$

χ_1: $B(\chi_1 \rightarrow J/\psi)\cdot\left(\ (1 - M^2_{J/\psi}/M^2_{\chi_1})\cdot(X^2_{F,\chi_1} + 4\tau_{\chi_1})^{1/2}\right)^{-1}$

χ_2: $B(\chi_2 \rightarrow J/\psi)\cdot\left(\ (1 - M^2_{J/\psi}/M^2_{\chi_2})\cdot(X^2_{F,\chi_2} + 4\tau_{\chi_2})^{1/2}\right)^{-1}$

ψ' : $B(\psi' \rightarrow J/\psi)\cdot\delta(X_F - X_{F,\psi'}\cdot M_{J/\psi}/M_{\psi'})$

The χ_1 and χ_2 expressions follow from the two body kinematics of the radiative transitions, $\chi \rightarrow \gamma + J/\psi$ where the transverse momentum of the particles are ignored and for lack of better information, the decay distributions are assumed to be isotropic ($X_{F,max}$ and $X_{F,min}$ can then be simply derived from kinematic limit considerations). The change in the smeared X_F cross sections that occurs when accounting for the particles' transverse momentum in these processes was found to be negligible by comparing the spectra obtained from an exact Monte Carlo simulation with that derived using these analytical forms.

Since the dominant decay mode of the ψ' to a J/ψ is through the emission of two pions, the dynamics of the transition is more of a factor in determining the smearing of the X_F spectra in this case. The measurements of the $\pi\pi$ invariant mass spectrum[67] shows that it is peaked near $4\cdot M_\pi$ so the J/ψ generally has a small momentum in the ψ' rest frame ($M_{\psi'} - M_{J/\psi} - 4\cdot M_\pi = .03\ GeV/c^2$). As a simple representation of the decays from this source, which only contribute to the cross section at the 10% level, the J/ψ was assumed to be produced at rest in this frame. This translates into the relation $X_{F,J/\psi} = X_{F,\psi'}\cdot M_{J/\psi}/M_{\psi'}$.

The parametrization used to fit the differential cross section in X_F is

$$\frac{d\sigma}{dX_F} = K^{J/\psi}_{gg} \cdot \sum_j A_j \left(\frac{dF^{S_j}_{gg}}{dX_F} + R_K \cdot \frac{dF^{S_j}_{q\bar{q}}}{dX_F} \right)$$

where

$$A_j \equiv K^{j}_{gg}/K^{J/\psi}_{gg} \equiv K^{j}_{q\bar{q}}/K^{J/\psi}_{q\bar{q}} \quad ; \quad R_K \equiv K^{J/\psi}_{q\bar{q}}/K^{J/\psi}_{gg} .$$

This form is less general than that given for $\sigma_{J/\psi}(X_F > 0)$ in Section 1.8 in that the gg to $q\bar{q}$ cross section ratios are assumed to be independent of the charmonium state being produced. Although this is in line with the duality model, it was introduced here to simplify the discussion. It will be seen below, however, that this assumption does not affect the conclusions.

The experimental distribution $d\sigma/dX_F$ was fit to this form with the four parameters, $K^{J/\psi}_{gg}$, R_K, n_π and n_n allowed to vary. The quantities A_j ($j \neq J/\psi$) were constrained so that the $X_F > 0$ contribution from each source j always matched that observed experimentally (i.e., 62% J/ψ, 18% χ_1, 13% χ_2 and 7% ψ' - see section 1.7). The ratios of the values of A_j that resulted were always near that of the total cross sections of these charmonium states since the X_F integrated excitation functions of these states are roughly equal. To obtain the parton cross sections for J/ψ production, a linear A-dependence was assumed and the value of $B_{\mu^+\mu^-}$ was set to 7.4 %. Fitting the data in the $.1 < X_F < .95$ range in this manner yields

$$K^{J/\psi}_{gg} = 28 \pm 5 \quad nb. \text{ / nucleon}$$

$$n_\pi = 2.2 \pm .1$$

$$n_n = 6.3 \pm .4$$

$$R_K = 0.0 \pm .005 \quad .$$

The error quoted for the cross section reflects both the uncertainty in the normalization of the data and the measurements of the branching ratio while those listed for n_n and R_K are statistical only. For n_π , the error includes an estimate of the effect of the uncertainty in the mean beam energy (this dominates the statistical value).

Figure 50 shows the fit to the data together with the individual contributions of each of the charmonium states. Note that only the gluon terms enter into these results since R_K is zero. The χ^2 per degree of freedom obtained for the fit is 76/30, and although it is large in part because of the mismatch at high X_F, it is not an unreasonable value given the small errors on the data points and simplicity of the parametrizations chosen for the gluon structure functions.

The first point to be considered in examining these results is the sensitivity of the fits to the shapes of each of the gluon structure functions. From the plot in Figure 51 of the relation between x_π, x_n and X_F for $\tau = M^2_{J/\psi}/S_o$, one can see that x_n is 'probed' over a small region (.02 to .1) for $X_F > .1$ and that its variation with X_F is largest at low X_F values. Thus, the high x portion of the gluon structure function of the pion that is obtained in the fit is nearly proportional to the cross section at high X_F since x_n is nearly constant in this region. In fact, if values for n_n in the range of 5 to 8 are assumed, the results for n_π vary on the order of .1, the size of the error on n_π. At the extremes of this interval however, the agreement of the fit with the data at low X_F is noticeably worse.

Using the gluon structure function of the nucleon derived by the CDHS group in the fit causes negligible differences in both the match to the data and the parameters derived. Since the normalization of $f_{g/n}$ in its standard parametrization is based only on its shape in a small region of x_n, this result further establishes the value obtained for the parton cross section.

The expectation for gluon distribution in the pion discussed in section 1.8 was that its high X_F behavior should be one power in (1 - x_π) larger than that of the quark distribution. Given the NA3[30] and E444[12] measurements for $f_{q/\pi}$, this is consistent with our result.

To see why the fit 'prefers' a zero quark contribution and how significant this is relative to the R_K value of 1.4 expected from the ratios of the J/ψ production cross sections and the duality model, the fit was redone constraining R_K to this value and n_n to 6.3 . Figure 52 shows the match to the data and the individual $q\overline{q}$ and gg contributions each summed over all charmonium production. Thus, the suppression of the quark contribution in the fit arises since its X_F spectrum is less steep than the data and the gluon parametrization alone overestimates the large X_F cross section as in Figure 50. This result is true even if R_K for the χ components is allowed to vary relative to that of the J/ψ and ψ' .

The fractional contribution of $q\bar{q}$ fusion to the $X_F > .1$ cross section is about 15% in this fit and is consistent with the predictions given in section 1.8 that were derived from the π^+ to π^- cross section ratios in a manner that did not depend on assumptions about the gluon distributions. With this normalization, the quark contribution alone at high X_F is larger than the measured cross section. Thus, the significance of the $R_K = 0$ depends to a large extent on how well the high x behavior of the quark structure function of the pion is known. Although the NA3 results for $f_{q/\pi}$ were chosen here since they seemed representative of measurements that have been made, other groups have reported powers of the $(1 - x_\pi)$ factor in the quark structure function parametrization that fall anywhere in the range of 1. to 1.6 . This is to be compared with the NA3 value of 1.2 where one notes that the errors claimed in all of these measurements are less than .2 (these differences, however, have little effect on the integrated excitation functions).

Another consideration in judging the differences in the two estimates of the quark contribution is the error in the determination of R_K from the π^+ to π^- production ratios. The value obtained from the three measurements discussed in section 1.10 was $R_K = 1.35 \pm .4$. This result also required assumptions about the gluon structure functions. However, these distributions are sufficiently determined by the fits to the data for R_K at this level that their uncertainty contributes much less to R_K than the errors on the measurement of the cross section ratios.

In viewing these uncertainties as a whole, it would require $R_K = .9$ and the steepest of the measured pion quark structure functions to match the data to the degree seen in Figure 50. Thus, it is hard to reconcile the differences in the quark contribution found in the two approaches within the framework of the fusion model.

Our conclusions from the general fit to the X_F spectrum are not unique. The Goliath collaboration has done a similar analysis on their J/ψ data and also find a zero contribution from quark fusion.[46] In addition, they measure $n_\pi = 1.9 \pm .3$ using the CDHS gluon structure function measurement for the nucleon. The NA3 group likewise has examined their data in this manner although one cannot make direct comparisons to their results since they first subtract from the X_F cross sections what they regard as a diffractive contribution based on their A-dependence studies.[13] However, others[45] who have analyzed their uncorrected data within the duality framework find the predictions overestimate the high X_F cross section in a manner similar to that seen in Figure 52. Other measurements of $d\sigma/dX_F$ for J/ψ production generally have large statistical errors at high X_F or have not had the continuum component subtracted and so their consistency with the duality model at lower X_F ($<$ .7) has been the main claim for the success of this approach by theorists.

7.5 Gluon Radiation Model - The P_T Dependence of the Production

In section 1.10, the prediction for the cross section variation in X_F and P_T^2 was given assuming the underlying production process is $gg \rightarrow gJ/\psi$. The gluon structure functions are the input to this calculation and so they were represented in the standard form and n_π and n_n derived from fits to the data. The equation used to relate the measured differential cross section with that predicted in equation 1.35 is

$$\left(B_{\mu^+\mu^-} \cdot \frac{d\sigma}{dX_F dP_T^2}(W) \right)_{\text{meaured}} = \frac{C_N \cdot B_{\mu^+\mu^-}}{.6} \cdot A_W^{b(P_T^2)} \cdot \left(\frac{d\sigma}{dX_F dP_T^2}(\text{nucleon}) \right)_{\text{predicted}} .$$

Here it is assumed that the A-dependence effects observed in the data are from final state scattering of the J/ψ so an empirical correction to the nucleon cross sections should be approximately valid. To illustrate the extent to which the choice of $b(P_T^2)$ has on the results, the fits were done using both $b = 1$ and $b = .92 + .025 \cdot P_T^2$. The intercept in the latter parametrization was derived from the E444 measurements while the slope came from our data as discussed in section 7.2 . Note that b is written in a form independent of X_F which appears to be the case at least in the low P_T^2 region where the statistics of our data are adequate to study it. The factor of 1/.6 in the above equation accounts for the fraction of directly produced J/ψ's with the assumption that the other components have similar differential cross sections. Finally, a normalization factor, C_N, is included as a variable in the fit and should be unity if the magnitude of the predictions are correct. The biggest uncertainty in this regard is the value taken for α_s which enters cubically in the expression for $d\sigma/dt$. From the results discussed in section 1.3, a value of .3 was chosen although numbers anywhere from .2 to .4 have been used in J/ψ production calculations.

The one problem that had to be considered in doing the fits is the logarithmic divergence of the predicted cross section as P_T^2 approaches zero. Comparisons with the data thus have to be restricted to the interval above some minimum value of P_T^2. To minimize the sensitivity of the results to this cutoff and to emphasize the match to the power law behavior of the cross sections at large P_T^2, the fits were done by minimizing the square of the difference between the logarithm of the measurements and the predictions without any weighting from errors on the data values. Taking the minimum value of P_T^2 to be 1.5 GeV^2/c^2 produces the results below. The corresponding comparisons with the data are shown in Figures 53 and 54.

	$b = 1$	$b = .92 + .025 \cdot P_T^2$
C_N	14 ± 3	11 ± 2
n_π	$1.44 \pm .1$	$1.46 \pm .1$
n_n	$2.0 \pm .2$	$8.7 \pm .7$

Since the deviation between the predicted curves and data enter into the 'χ^2' of the fit as the square of the linear distance in these logarithmic plots, one can see that choosing a cutoff different from the first three bins will have little effect on the match at large P_T^2. In both fits, the resulting curves conform to the data fairly well above $P_T^2 = 3$ GeV^2/c^2 although the match for the $b \neq 1$ fit is not as good at low X_F. The errors quoted for C_N arise from the uncertainity in the normalization of the data and measured value of $B_{\mu^+\mu^-}$. Because the usual least-squares minimization procedure was not used, the errors on the gluon structure function parameters were estimated as the changes that cause the predictions at large P_T^2 to be on average outside the error bars on the data.

The most obvious feature of these results is that the predictions are over a factor of ten smaller than the measurements. Although one might think of increasing α_s to improve the comparison, it would seem more likely that at least one of the assumptions in this model is wrong. The only other predictions of this type have been done for the P_T spectrum of J/ψ production at $X_F = 0$ for proton - proton interactions. One study obtains a good agreement using $\alpha_s = .4$ while another analysis would find a factor of 7 times smaller cross section with

$\alpha_s = .4$ (both assume $n_n = 5$ based on the counting rule arguments). It is not clear what assumptions differed in these cases to cause such a disagreement. The model predictions for inelastic photo- and muo-production of the J/ψ, based on a similar gluon radiation subprocess as considered here, are closer in matching the normalization of the measurements[16] and agree reasonably well with the shapes of both the observed[14] P_T^2 spectrum and the distribution of the quantity $E_{J/\psi,lab}/E_{\gamma,lab}$.

Although the normalization of the predictions in our case fall short of the data, there are some features of these results relating to their dependence on the structure functions that are worth noting. This dependence arises since the mean values of the momentum fractions of the incident gluons, $<x_\pi>$ and $<x_n>$, that enter the cross section expressions for a given X_F increase as P_T^2 becomes larger. Also, they are larger at a given X_F than the fusion results which assume $P_T = 0$. These changes are the consequence of the fact that it requires larger initial gluon energies to produce the J/ψ and the final state gluon at larger P_T. Some of the effects relating to these changes are discussed below.

- The values of n_π determined in the fits are mainly influenced by the X_F variation of the differential cross sections. Although one naively expects these values to equal that obtained in the fusion case, they are in fact smaller by about .8. These differences are largely the result of two trends. The first is that for a given value of n_π, the predicted X_F distribution falls off faster at high X_F in the gluon radiation model since x_π is on average larger for a particular X_F. Also, the fall off in $d\sigma/dX_F$ for the data at high X_F is more rapid at large P_T^2 than in the P_T^2 integrated results (see Figure 43). However, the predicted change in the X_F spectrum with P_T^2 is larger than that observed in the data if n_π from the fusion results is used in the calculations. Thus, smaller values of n_π resulted when this quantity was allowed to vary in the fits. Whether such distributions are reasonable given that the scale of the interaction is different than in the fusion case is not known.
- A larger value of n_n produces a more rapid fall off in the predicted P_T^2 spectrum due to the increase of $<x_n>$ with P_T^2. Since n_n is not well constrained by the shape of the X_F distribution in the fits, it increased to account for the P_T^2 variation of the A-dependence correction in the second fit. The value

that results with this correction, $n_n = 8.7 \pm .7$, is closer to that expected from the fusion fits (6.3 ± .4).

- The increase in $<x_\pi>$ with P_T^2 has the greatest affect on the predicted P_T^2 cross sections at high X_F since $f_{g/\pi}(x_\pi)$ changes rapidly with x_π in this region. This is in fact the main reason why the predicted P_T^2 distributions are steeper in this X_F region. From the fits shown in the Figures, one sees that the predictions roughly match the changes in the low P_T^2 (2 to 6 GeV^2/c^2) spectra of the data at high X_F. However, the data in the highest X_F bin are not adequate to determine if this behavior occurs at larger values of P_T^2. Similar predictions[68] have been made for the X_F variation of the P_T^2 cross sections for high mass di-muon production. Here, a decrease in the values of $<P_T^2>$ at high X_F have also been observed.[55,57]

In summary, reasonable fits to the data are achieved with this model even with a large difference in the A-dependence assumption. However, given the small magnitude of the predicted cross section and the lack of independent constraints on the gluon structure functions, one cannot make definite conclusions from our results.

7.6 Angular Distributions

As noted in section 1.12, the general form of the J/ψ decay angular distributions is

$$\frac{d\sigma}{d\phi\, d\cos(\theta)} \sim 1 + \alpha\cdot\cos^2(\theta) + \beta\cdot\sin(2\theta)\cos(\phi) + \gamma\cdot\sin^2(\theta)\cos(2\phi)$$

where α, β and γ are functions of X_F and P_T. For our study, $\cos(\theta)$ and ϕ are defined relative to Collin-Soper reference system in the muon pair rest frame (see section 1.4). In this section, the values derived for these coefficients are presented and comparisons are made to the predictions based on the $gg \to gJ/\psi$ production mechanism.

The distributions of events in $\cos(\theta)$ and ϕ, uncorrected for acceptance, are shown in Figure 55 in various X_F and P_T^2 regions. Since the cross sections in the angular variables will be shown to be essentially flat, the density of points in the plots are in proportion to the acceptance. The scarcity of events with $\cos(\theta) < -.8$ at low P_T^2 is the result of the non-prompt background cut. One can also see that at higher P_T^2, the area in which the acceptance is finite becomes smaller.

The fits to the angular cross sections were done in 16 regions: 4 in X_F (.1 → .3 → .5 → .7 → .9) by 4 in P_T^2 (0 → 1.5 → 4.5 → 7.5 → ∞). For $P_T^2 < 4.5\ GeV^2/c^2$, the data were divided into 8 cos(θ) by 8 ϕ equal area bins while at larger P_T^2, a 5 by 5 grid was used. Since large fluctuations occur in the cross sections in areas where the acceptances are very small, bins were eliminated from the fits if the acceptance was less than .001 or if it was smaller than .005 and the number of events was below 10. In most regions, however, the acceptance is over 10%.

In each region, the form of the cross section given above was fit to the data with the normalization allowed to vary. The resulting coefficients are plotted in Figure 56 together with predictions based on the $gg \rightarrow gJ/\psi$ production mechanism. The latter values were calculated using equations 1.40 to 1.44 and the gluon distributions obtained in the last section from the fits using the P_T^2 varying A-dependence. Using the other set of parameters for the gluon structure functions or the fusion fit results, however, do not change the predictions significantly. The χ^2/d.o.f. values obtained from the fits are listed in Table 7 under the Spin 1 heading. Also shown are the results from fits assuming flat distributions (i.e., $\alpha = \beta = \gamma = 0$) and that expected theoretically. In the latter two cases, only the normalization is allowed to vary in the fits. Thus one sees little evidence from this information for any structure in the angular cross sections.

As an illustration of some of the actual distributions, the cross sections interated over ϕ are shown in Figures 57 and 58 for each of the 16 regions (here 10 bins in cos(θ) are used). The solid lines in the plots are the results of fits to these data assuming $\alpha = 0$. Letting α float in these cases or determining γ from the cos(θ) integrated cross sections produces values in agreement with those from the simultaneous fits and thus indicates there is no large systematic error that is correlated in cos(θ) and ϕ.

The values of α, β and γ obtained are all within 2.3 standard deviations of zero and 60% are within 1 σ (the correlation of their errors are generally less than 50%). Nearly all of the χ^2's obtained for the fits in the $P_T^2 < 7.5\ GeV^2/c^2$ regions convert to confidence levels that are less than .25 . The systematic effect causing these low values is observable in the $d\sigma/d\phi$ distributions as a signal that

TABLE 7

χ^2/d.o.f. FOR THE ANGULAR DISTRIBUTION FITS

P_T^2	X_F	Spin 1	Flat	$gg \rightarrow gJ/\psi$
$0 \rightarrow 1.5$	$.1 \rightarrow .3$	$58/43 = 1.3$	$64/46 = 1.4$	$145/46 = 3.2$
	$.3 \rightarrow .5$	$75/48 = 1.6$	$83/51 = 1.6$	$217/51 = 4.3$
	$.5 \rightarrow .7$	$65/48 = 1.4$	$72/51 = 1.4$	$163/51 = 3.2$
	$.7 \rightarrow .9$	$58/50 = 1.2$	$60/53 = 1.1$	$97/53 = 1.8$
$1.5 \rightarrow 4.5$	$.1 \rightarrow .3$	$46/41 = 1.1$	$47/44 = 1.1$	$102/44 = 2.3$
	$.3 \rightarrow .5$	$65/46 = 1.4$	$73/49 = 1.5$	$140/49 = 2.8$
	$.5 \rightarrow .7$	$82/50 = 1.6$	$89/53 = 1.7$	$156/53 = 2.9$
	$.7 \rightarrow .9$	$59/48 = 1.2$	$60/51 = 1.2$	$72/51 = 1.4$
$4.5 \rightarrow 7.5$	$.1 \rightarrow .3$	$11/15 = 0.7$	$14/18 = 0.8$	$37/18 = 2.1$
	$.3 \rightarrow .5$	$22/17 = 1.3$	$26/20 = 1.3$	$63/20 = 3.1$
	$.5 \rightarrow .7$	$28/19 = 1.5$	$36/22 = 1.6$	$38/22 = 1.7$
	$.7 \rightarrow .9$	$28/18 = 1.5$	$37/21 = 1.8$	$39/21 = 1.9$
$7.5 \rightarrow \infty$	$.1 \rightarrow .3$	$2/8 = 0.3$	$6/11 = 0.5$	$8/11 = 0.7$
	$.3 \rightarrow .5$	$12/19 = 0.6$	$16/22 = 0.7$	$16/22 = 0.7$
	$.5 \rightarrow .7$	$12/19 = 0.6$	$14/22 = 0.6$	$26/22 = 1.2$
	$.7 \rightarrow .9$	$9/13 = 0.7$	$10/16 = 0.6$	$13/16 = 0.8$

is roughly proportional to $cos(\phi)$. However, the amplitudes of these components are generally less than 5% of the average values of the cross sections and thus are only significant when compared to the small statistical errors in these data. For the $P_T^2 > 7.5$ results, the χ^2's are on average lower than the values expected theoretically. This may be due to subtleties in estimating the errors on the cross sections when there is a small number of events per bin.

Because of the conditions noted above, it is best to compare the χ^2/d.o.f. values when assessing the other fits to the data instead of the absolute confidence levels. Given the similarity of the values obtained in assuming $\alpha = \beta = \gamma = 0$ with those from the fits using the general form of the cross section, one cannot reject the hypothesis that the J/ψ's are produced unpolarized in the regions of X_F and P_T^2 explored here. Chosing a different reference system to define $\cos(\theta)$ and ϕ yields the same conclusion since the coefficients transform linearly under a coordinate rotation at a given X_F and P_T^2.

The χ^2's/d.o.f. obtained from the fits using the predictions for the $gg \rightarrow gJ/\psi$ process are all greater than those from the flat distribution assumption and thus give no indication that this model provides a better representation of the data. Much of the difference in the quality of the fits results since the predicted values of γ are always larger than .14 which is usually significantly greater than that measured in the data. It is perhaps not surprising that this model fails to conform with the data given its prediction for the magnitude of the cross section is a factor of ten smaller than that observed. Also, the angular distributions of the data include contributions from the decays of other charmonium states and may also be affected by the mechanism producing the strong A-dependence of the P_T^2 cross sections.

7.7 Conclusions

This thesis has presented the results on J/ψ production from an experiment which measured di-muons generated in pion - nucleus interactions. The total J/ψ and ψ' cross sections reported agree well with other measurements. The characteristics of the distributions in X_F, P_T^2 and the angular variables were examined. One notes that the P_T^2 spectrum becomes steeper at high X_F. Also, the angular distributions are consistent with the hypothesis that the J/ψ's are produced unpolarized over the X_F and P_T^2 range of the data.

The differential cross section in X_F was interpreted in terms of the general form of the fusion model to extract the gluon structure function of the pion and nucleon. These results compare well with expectations and other measurements. However, no evidence is seen for a quark fusion component in the X_F distribution which is expected to contribute to the total cross section at the 15% level. This prediction is based on both the duality model and the ratios of the J/ψ production cross sections measured with π^+ and π^- beams.

The large P_T^2 behavior of the cross section was compared to the gluon radiation model where the fundamental production mechanism is assumed to be $gg \rightarrow gJ/\psi$. Although the predicted shapes of the X_F and P_T^2 cross sections match the data when the gluon structure functions are varied in a fit, the cross sections of this model are about an order of magnitude smaller than the data and do not provide a better representation of the angular distributions than is obtained by assuming that the J/ψ decays are isotropic. One sees from this model, however, how the cross section dependence on the structure functions could lead to a steeper P_T^2 spectrum at high X_F.

Experimentally, the most important question that remains to be resolved in J/ψ production is the size of the contribution from the decays of other charmonium states. It is doubtful, however, that such knowledge will provide a much greater insight into the charmonium production mechanism given the limited success of the current models.

REFERENCES

1. M. Gell-Mann, Phys. Lett. **8**, 214 (1964);

   G. Zweig, CERN report 8419/TH 412.

2. B. J. Bjorken and S. L. Glashow, Phys. Lett. **11**, 255 (1964).

3. J. Aubert *et al.*, Phys. Rev. Lett. **33**, 1404 (1974).

4. J. Augustin *et al.*, Phys. Rev. Lett. **33**, 1406 (1974).

5. G. Goldhaber *et al.*, Phys. Rev. Lett. **37**, 255 (1976).

6. W. Buchmuller, CERN-TH.3938/84, 1984.

7. Yu. M. Antipov *et al.*, Phys. Lett. **60B**, 309 (1976);

   Yu. B. Bushnin *et al.*, Phys. Lett. **72B**, 269 (1978).

8. M. Abolins *et al.*, Phys. Lett. **82B**, 145 (1979).

9. M. Corden *et al.*, Phys. Lett. **96B**, 411 (1980);

   M. Corden *et al.*, Phys. Lett. **98B**, 220 (1981);

   M. Corden *et al.*, Phys. Lett. **110B**, 415 (1982).

10. E. Anassontzis *et al.*, Fermilab-Conf-82/49-Exp, 1982.

11. J. Branson *et al.*, Phys. Rev. Lett. **38**, 1331 (1977);

    J. Branson, *Measurement of Inclusive Muon Pair Production by 225 GeV/c* π^+, π^-, *and Proton Beams with a Large Acceptance Spectrometer*, thesis, unpublished, Princeton University (1977).

12. K. J. Anderson *et al.*, Phys. Rev. Lett. **42**, 944 (1979);

    G. Hogan, *Production of High Mass Muon Pairs by 225 GeV/c Hadron Beams and a Determination of the Pion Structure Function*, thesis, unpublished, Princeton University (1979);

    C. Newman, *Measurement of High Mass Muon Pairs Produced in Hadronic Collisions and a Deterimination of the Pion Structure Function*, thesis, unpublished, University of Chicago (1979).

13. J. Badier *et al.*, CERN-EP/83-86, 1983;

    Ph. Charpentier, *Etude de la Production Hadronique des Resonances J/ψ et Υ de 150 a 280 GeV/c*, thesis, unpublished, L'Universite de Paris Sud (1984).

14. T. Markiewicz, *Muoproduction of the J/ψ* (3100), thesis, unpublished, University of California at Berkeley (1982).

15. J. Aubert *et al.*, Nucl. Phys. **B213**, 1 (1983).

16. T. Nash, Fermilab-Conf-83/75-Exp, 1983.

17. M. Binkley *et al.*, Phys. Rev. Lett. **48**, 73 (1982);

    M. Binkley *et al.*, Phys. Rev. Lett. **50**, 302 (1983).

18. B. Denby *et al.*, Phys. Rev. Lett. **52**, 795 (1984).

19. F. E. Close, *An Introduction to Quarks and Partons*, Academic Press, New York (1979).

20. J. D. Bjorken and E. A. Paschos, Phys. Rev. **185**, 1975 (1969);

    R. P. Feynman, Phys. Rev. Lett. **23**, 1415 (1969).

21. K. Rith, THEP 83/5 (Freiburg University), 1983.

22. For a general review of the applications of QCD, see E. Reya, Phys. Rep. **69**, 197 (1981).

23. G. Lepage, in Proc. of the Int. Lepton/Photon Symp., Cornell (1983).

24. J. G. H. de Groot *et al.*, Zeit. Phys. **C1**, 143 (1979);

    J. G. H. de Groot *et al.*, Phys. Lett. **82B**, 456 (1979);

    H. Abramowicz *et al.*, Zeit. Phys. **C17**, 283 (1983).

25. H. Abramowicz *et al.*, Zeit. Phys. **C12**, 289 (1982).

26. J. Collins, D. Soper and G. Sterman, Phys. Lett. **134B**, 263 (1984).

27. J. Kubar, M. Le Ballac, J. Meunier and G. Plaut, Nucl. Phys. **B175**, 251 (1980).

28. I. Kenyon, Rep. Prog. Phys. **45**. 1261 (1982).

29. J. Collins and D. Soper, Phys. Rev. **D16** 2219 (1977).

30. J. Badier *et al.*, CERN-EP/83-48, 1983.

31. J. Owens, Phys. Rev. **D30** 943 (1984).

32. M. Green, M. Jacob and P. Landshoff, Il Nuovo Cimento **29**, 123 (1975).

33. D. Sivers, Phys. Rev. **D11**, 3253 (1975).

34. T. Sjostrand, LU TP 82-3 (Lund), 1982.

35. K. J. Anderson *et al.*, Phys. Rev. **D21**, 3075 (1980).

36. C. Carlson and R. Suaya, Phys. Rev. **D18**, 3075 (1980).

37. Y. Lemoigne *et al.*, Phys. Lett. **113B**, 509 (1982).

38. F. Binon *et al.*, CERN-EP/84-13, 1984.

39. S. Hahn *et al.*, Phys. Rev. **D30**, 671 (1984).

40. C. Kourkoumelis *et al.*, Phys. Lett. **81B**, 405 (1979).

41. The measurements at 39.5 GeV/c are from ref. 9 and those at 150 and 200 GeV/c are from ref. 13.

42. J. Gunion, Phys. Rev. **D10**, 242 (1974).

43. F. Close, in Proc. of the 19th Int. Conf. on HEP, Tokyo (1978).

44. S. Brodsky and J. Gunion, Phys. Rev. **D19**, 1005 (1979).

45. V. Barger, W. Keung and R. Phillips, Zeit. Phys. **C6**, 169 (1980).

46. J. McEwen, CERN-EP/82-151, 1982.

47. V. Barger, W. Keung and R. Phillips, Phys. Lett. **91B**, 253 (1980).

48. V. Novikov *et al.*, Phys. Rep. **41**, 1 (1978).

49. J. Sakurai, Phys. Lett. **46B**, 207 (1973).

50. H. Fritzsch, Phys. Lett. **67B**, 217 (1977).

51. R. Baier and R. Ruckl, Zeit. Phys. **C19**, 251 (1983).

52. C. Chang, Nucl. Phys. **B172**, 425 (1980).

53. E. Berger and D. Jones, Phys. Rev. **D23**, 1521 (1981).

54. C. Lam and Wu-Ki Tung, Phys. Rev. **D18**, 2447 (1978).

55. J. Alexander, *A Study of Massive Muon Pair Production at High* X_F, thesis, unpublished, University of Chicago (1985).

56. G. Gollin *et al.*, IEEE Trans. in Nucl. Sci., **NS-26**, 59 (1979).

57. S. Palestini, *Foward Production of High Mass Muon Pairs in Pion-Nucleon Interactions*, thesis, unpublished, Princeton University (1984).

58. For this study, pion production was simulated using the cross sections measurements in, J. Whitmore *et al.*, Phys. Rev. **D16**, 3137 (1977).
59. H. Atherton *et al.*, CERN report 80-07, 1980.
60. Ch. Iselin, CERN report 74-17, 1974.
61. A. Bodek and J. Ritchie, Phys. Rev. **D23**, 1070 (1981).
62. For the details of this study, see reference 55.
63. A. Carroll *et al.*, Phys. Lett. **80B**, 319 (1979).
64. S. Denisov *et al.*, Nucl. Phys. **B61**, 62 (1973).
65. This result is from the particle properties data listed in M. Aguilar-Benitez *et al.*, Rev. Mod. Phys. **56**, 1 (1984).
66. The following is a list of the beam momentum values (in GeV/c) corresponding to the data points in Figure 49 and the references from which the cross sections were obtained: (27) ref. 7; (39.5) ref. 9; (125) ref. 10; (150,200,280) ref. 13; (225) ref 12.; (263) this experiment.
67. Tung-Mow Yan, Phys. Rev. **D22**, 1652 (1980).
68. F. Halzen and D. Scott, Phys. Rev. **D19**, 216 (1979).

Figure 1 -- Charmonium spectrum below the $D\overline{D}$ threshold.

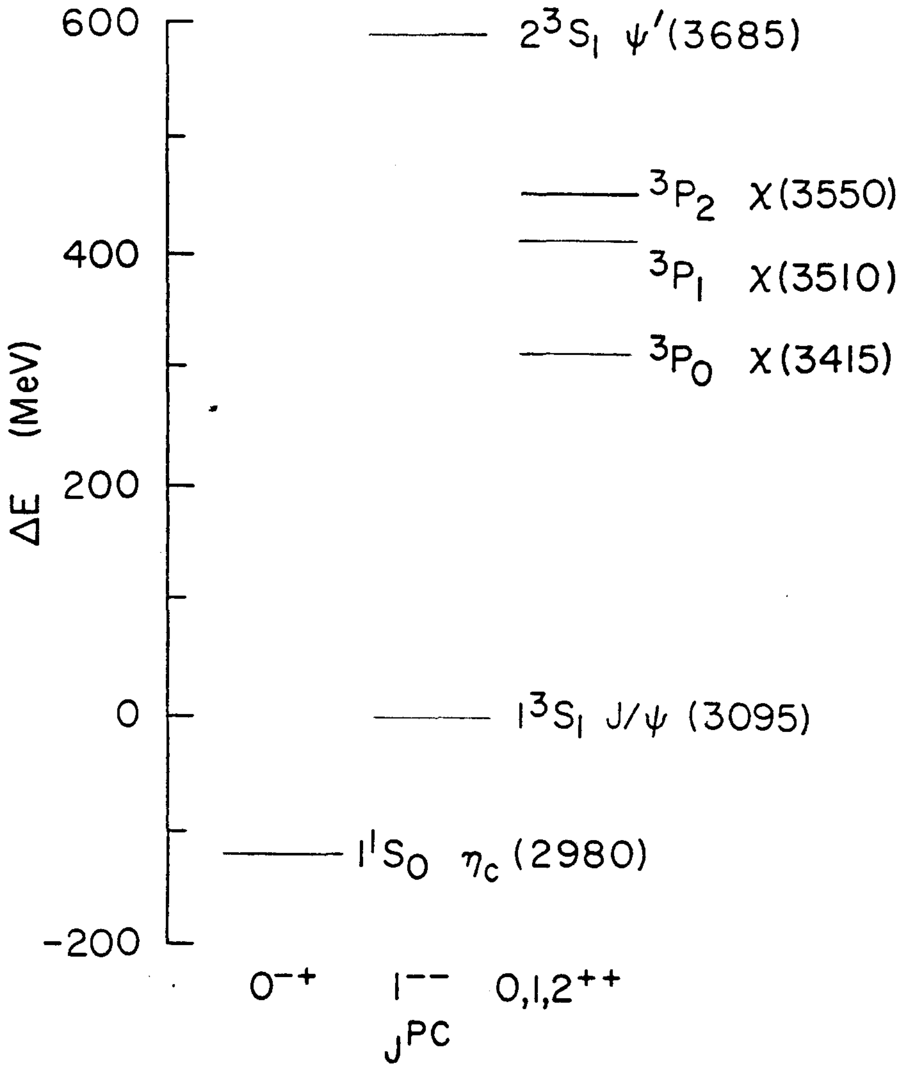
600
400
200
0
-200
ΔE (MeV)
2³S₁ ψ′(3685)
³P₂ χ(3550)
³P₁ χ(3510)
³P₀ χ(3415)
1³S₁ J/ψ (3095)
1¹S₀ η_c (2980)
0⁻⁺
1⁻⁻
0,1,2⁺⁺
J^PC

Figure 2 -- Illustration of deep inelastic scattering processes.

a) General picture of the scattering: a single photon is exchanged between a lepton of momentum l and nucleon of momentum P.

b) Parton model picture: the photon exchange occurs elastically with a single parton.

c) → e) Lowest order QCD corrections to the process in diagram b.

(a)

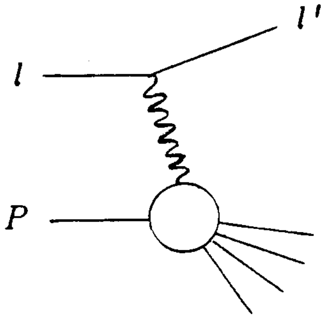

(b)

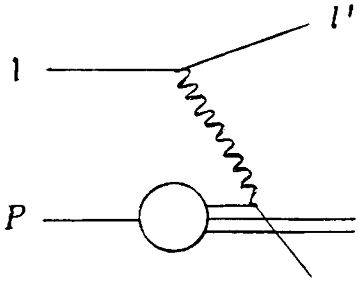

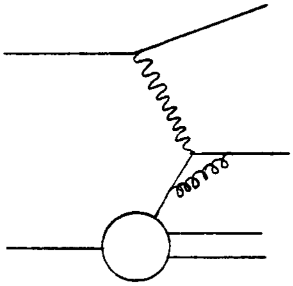

(c)

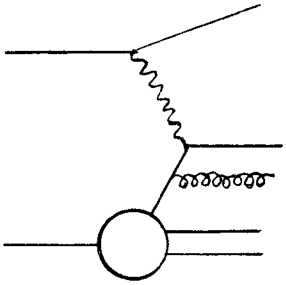

(d)

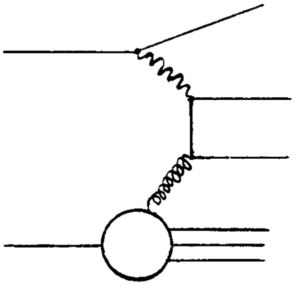

(e)

Figure 3 -- Illustration of direct fusion processes.

a) Lepton pair production from $q\overline{q}$ annihilation in the interaction of hadrons h_1 and h_2.

b) Lowest order J/ψ production mechanism through electromagnetic interactions.

c) Lowest order J/ψ production mechanism through strong interactions.

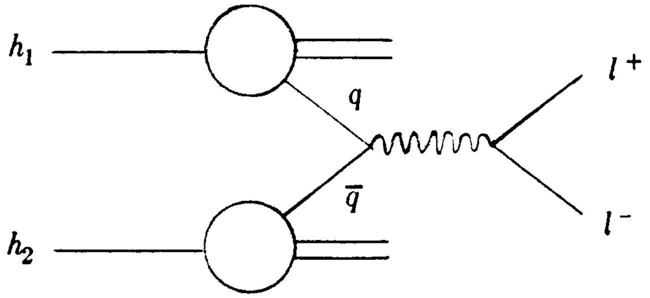
h_1
q
l^+
$\overline{q}$
l^-
h_2

(a)

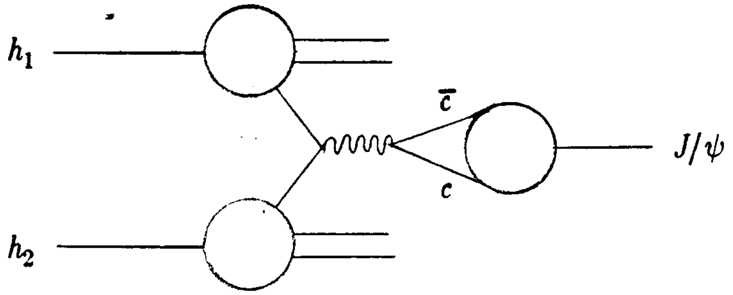
h_1
$\overline{c}$
J/ψ
c
h_2

(b)

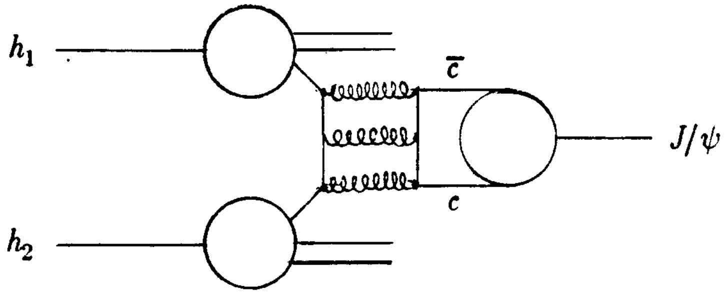
h_1
$\overline{c}$
J/ψ
c
h_2

(c)

Figure 4 -- Definition of the Collins-Soper reference system. $P^*_{\pi^-}$ and P^*_p are the pion and nucleon momentum in the di-muon center of mass system.

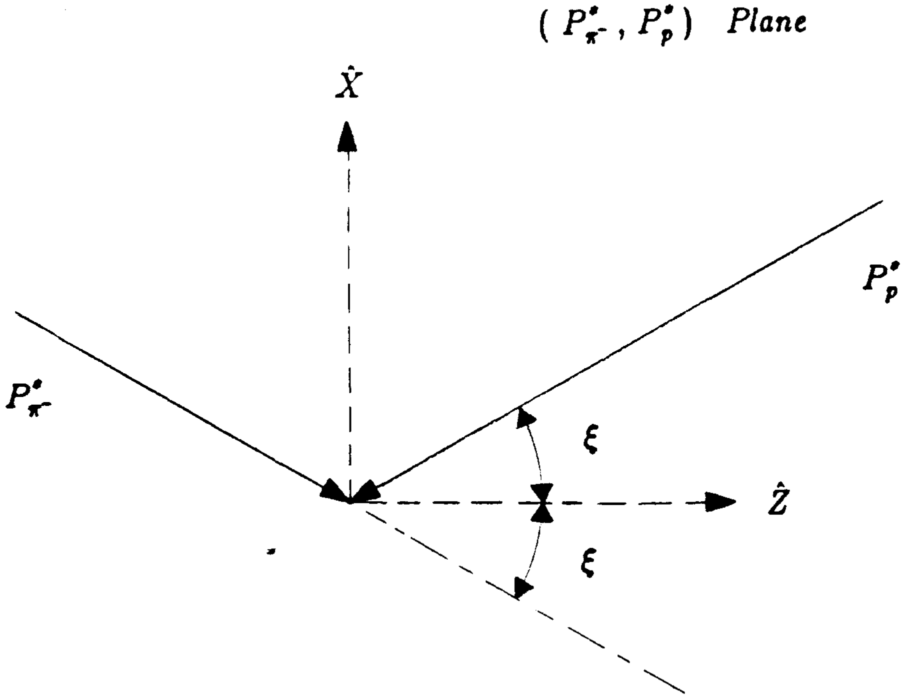

$$\xi \approx \tan^{-1}\left(\frac{P_T}{M}\right)$$

$$\hat{X} \equiv -(\hat{P}^*_{\pi^-} + \hat{P}^*_p) \,/\, |\hat{P}^*_{\pi^-} + \hat{P}^*_p|$$
$$\hat{Y} \equiv -(\hat{P}^*_{\pi^-} \times \hat{P}^*_p) \,/\, |\hat{P}^*_{\pi^-} \times \hat{P}^*_p|$$
$$\hat{Z} \equiv +(\hat{P}^*_{\pi^-} - \hat{P}^*_p) \,/\, |\hat{P}^*_{\pi^-} - \hat{P}^*_p|$$

Figure 5 -- J/ψ production diagrams involving final state gluon emission in the interaction of hadrons h_1 and h_2.

a) Lowest order quark - anti-quark production.

b) Lowest order gluon - gluon production.

c) Illustration of the parton sub-process of diagram b for which the predictions for the large P_T production of the J/ψ are based.

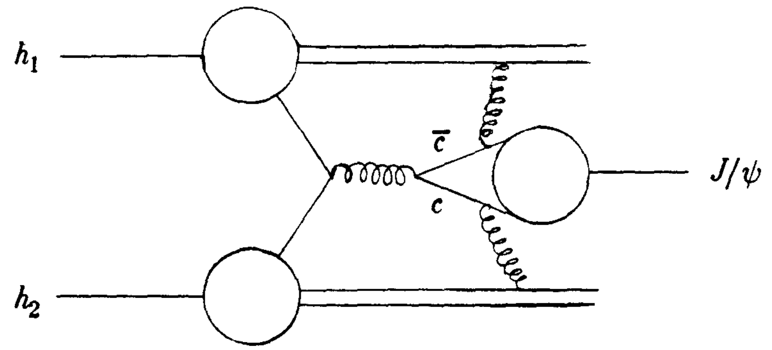

(a)

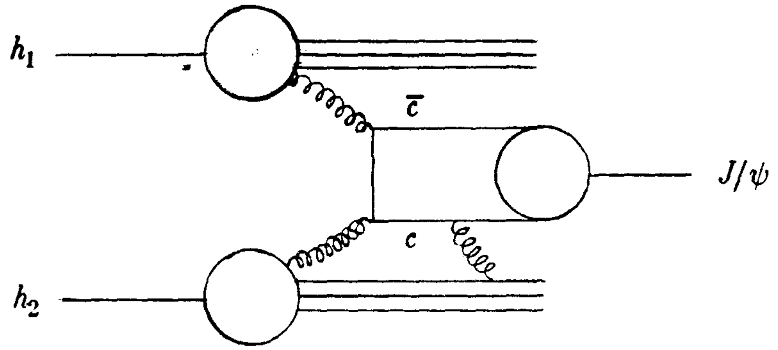

(b)

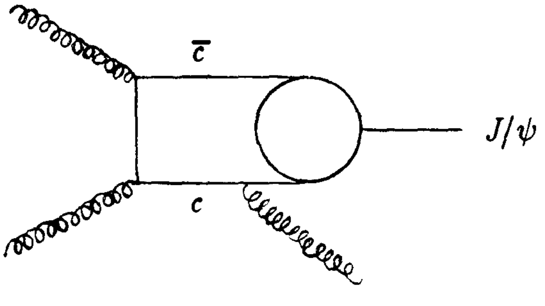

(c)

Figure 6 -- Plan view of the E615 apparatus.

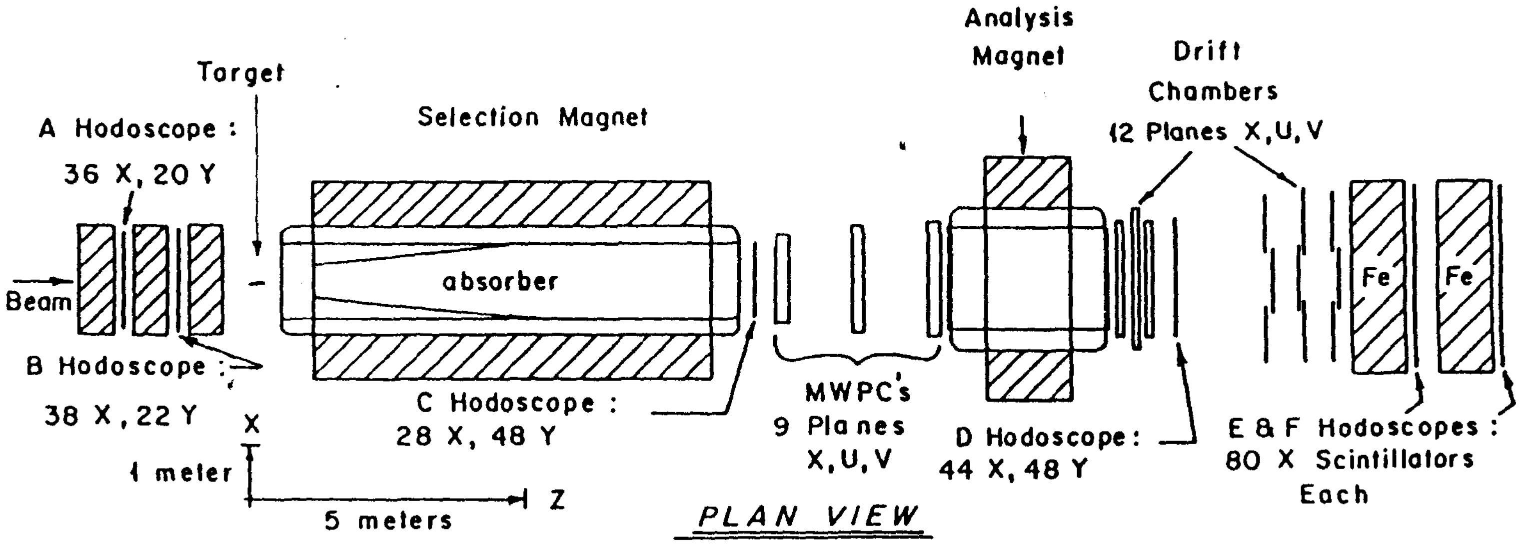
Target
A Hodoscope :
36 X, 20 Y
Beam
B Hodoscope :
38 X, 22 Y
X
1 meter
5 meters
Z
Selection Magnet
absorber
C Hodoscope :
28 X, 48 Y
MWPC's
9 Planes
X, U, V
PLAN VIEW
Analysis
Magnet
D Hodoscope :
44 X, 48 Y
Drift
Chambers
12 Planes X, U, V
Fe
Fe
E & F Hodoscopes :
80 X Scintillators
Each

Figure 7 -- Di-muon mass spectrum measured by experiment E444.

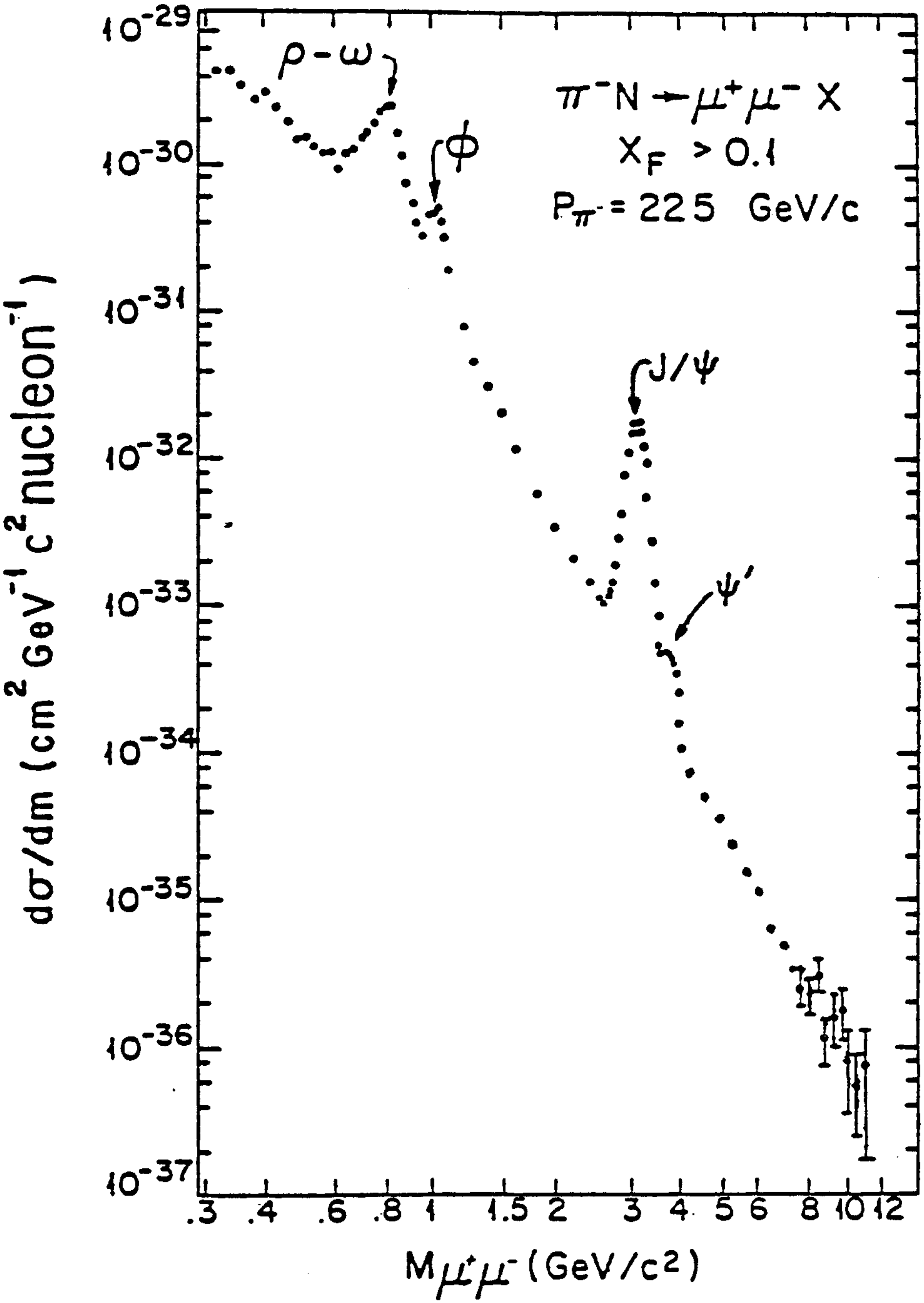
$\pi^- N \to \mu^+ \mu^- X$
$X_F > 0.1$
$P_{\pi^-} = 225$ GeV/c
$\rho - \omega$
ϕ
J/ψ
ψ'
$d\sigma/dm$ (cm^2 GeV^{-1} c^2 nucleon^{-1})
10^{-29}
10^{-30}
10^{-31}
10^{-32}
10^{-33}
10^{-34}
10^{-35}
10^{-36}
10^{-37}
.3 .4 .6 .8 1 1.5 2 3 4 5 6 8 10 12
$M_{\mu^+\mu^-}$ (GeV/c^2)

Figure 8 -- Plan view of the Proton-West secondary beam line.

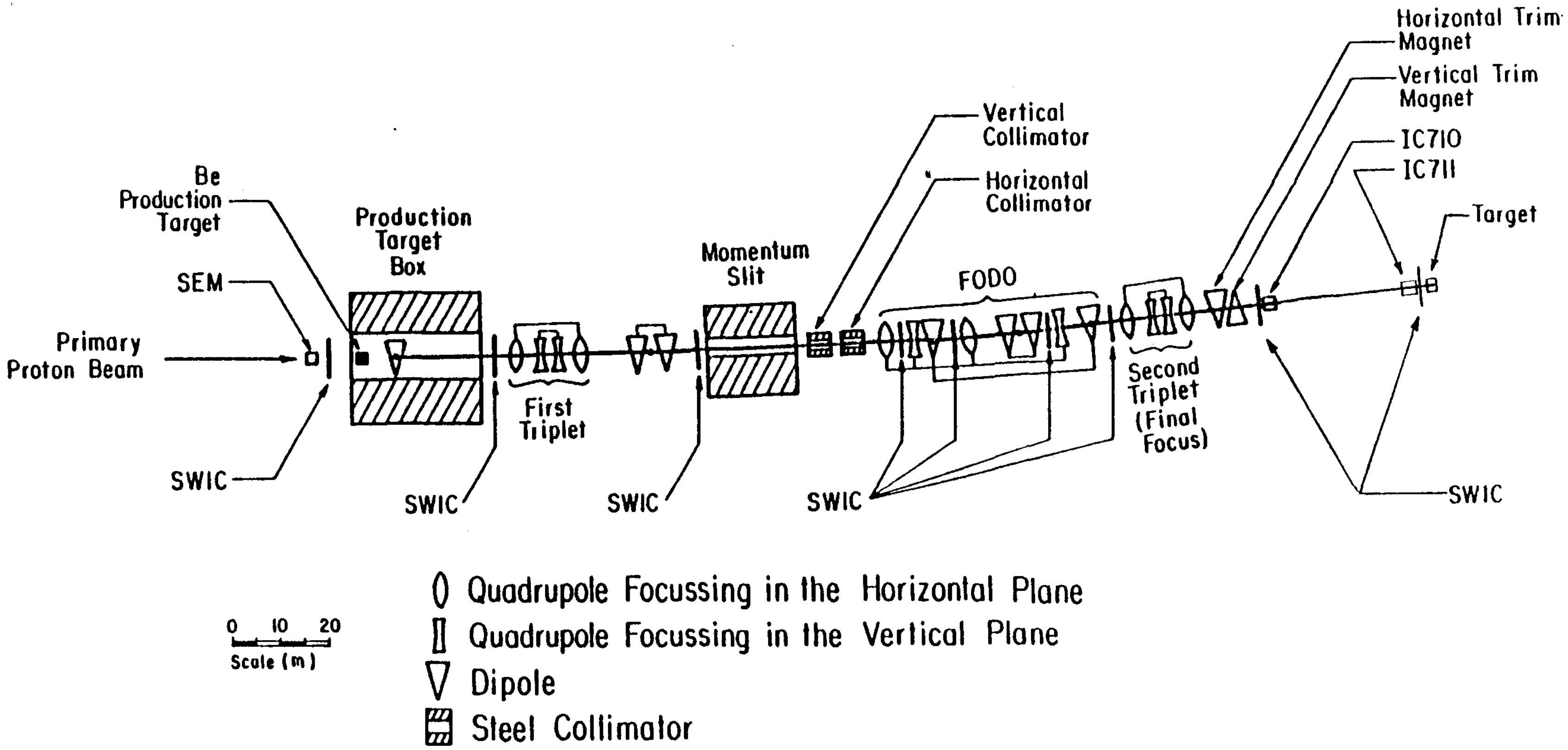
Horizontal Trim Magnet
Vertical Trim Magnet
IC710
IC711
Target
Vertical Collimator
Horizontal Collimator
Be Production Target
Production Target Box
Momentum Slit
FODO
SEM
Primary Proton Beam
First Triplet
Second Triplet (Final Focus)
SWIC
SWIC
SWIC
SWIC
SWIC
0 10 20
Scale (m)
Quadrupole Focussing in the Horizontal Plane
Quadrupole Focussing in the Vertical Plane
Dipole
Steel Collimator

Figure 9 -- Elevation view of the selection magnet with the absorber installed.

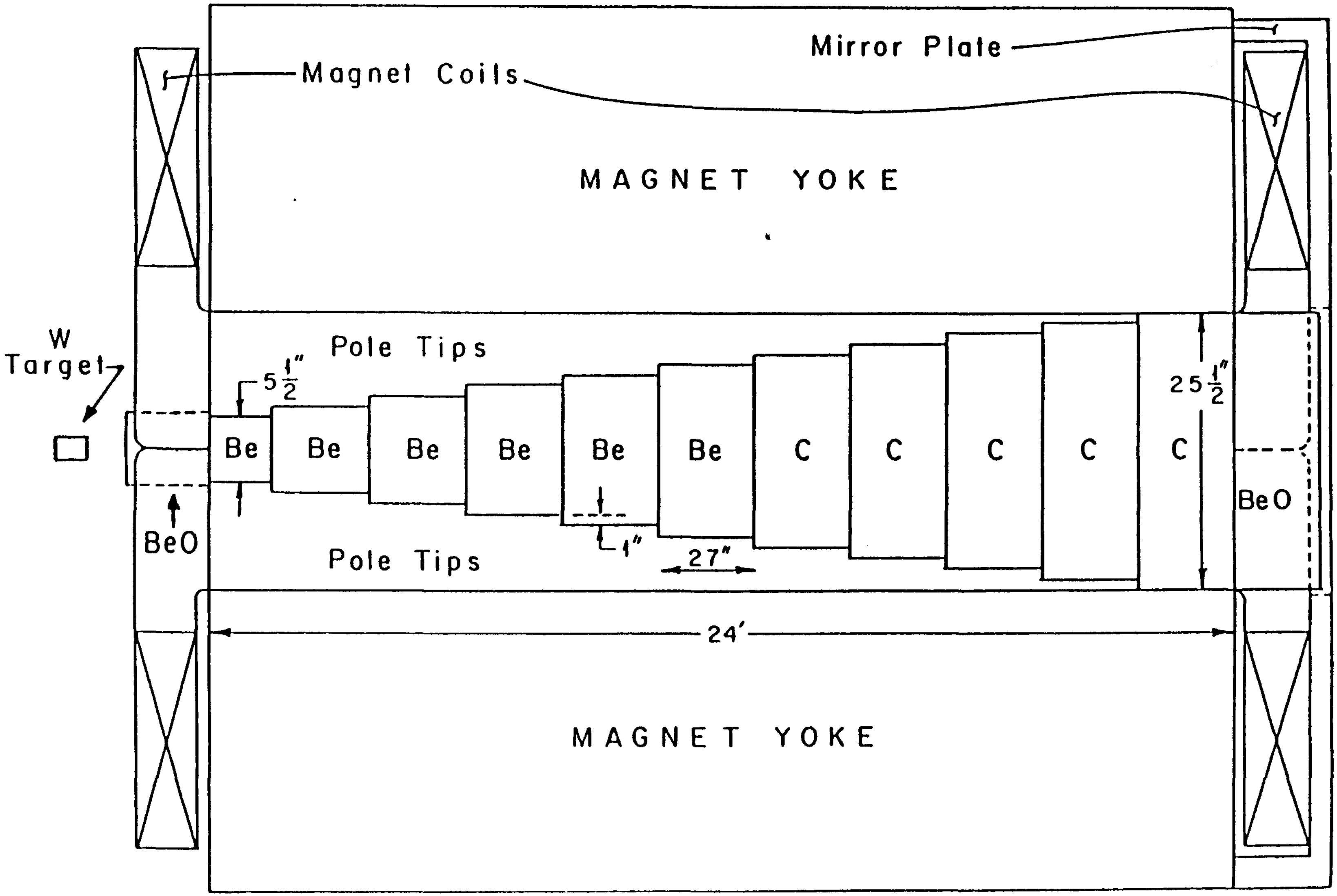
Mirror Plate
Magnet Coils
MAGNET YOKE
W
Target
Pole Tips
$5\frac{1}{2}''$
Be
Be
Be
Be
Be
Be
C
C
C
C
C
$25\frac{1}{2}''$
BeO
BeO
1"
27"
Pole Tips
24'
MAGNET YOKE

Figure 10 -- Vertical field strength (B_y) profile of the selection magnet measured along the beam axis.

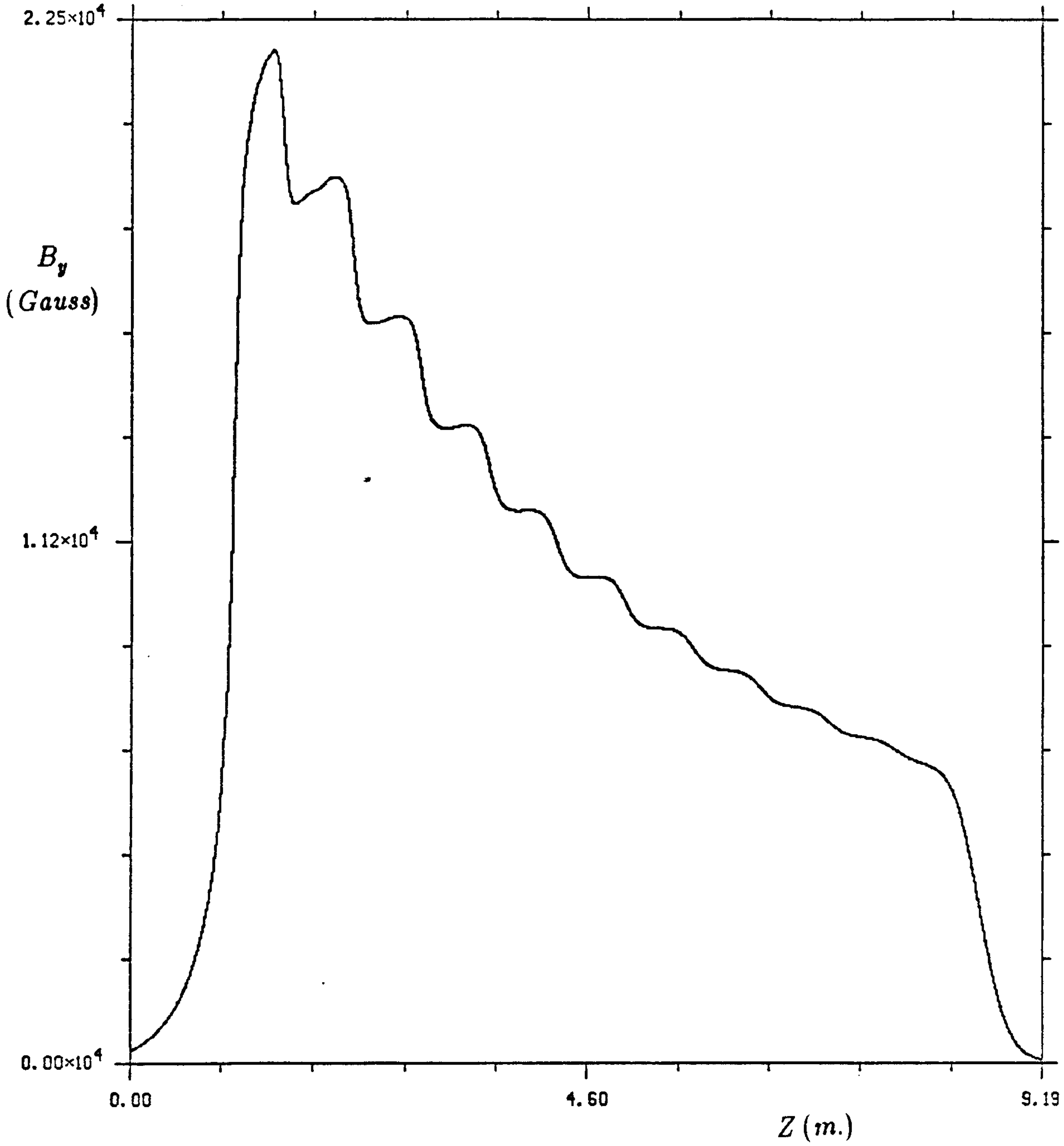
2.25×10^4
1.12×10^4
0.00×10^4
B_y
(Gauss)
0.00
4.60
9.19
Z (m.)

Figure 11 -- Layout of the spectrometer.

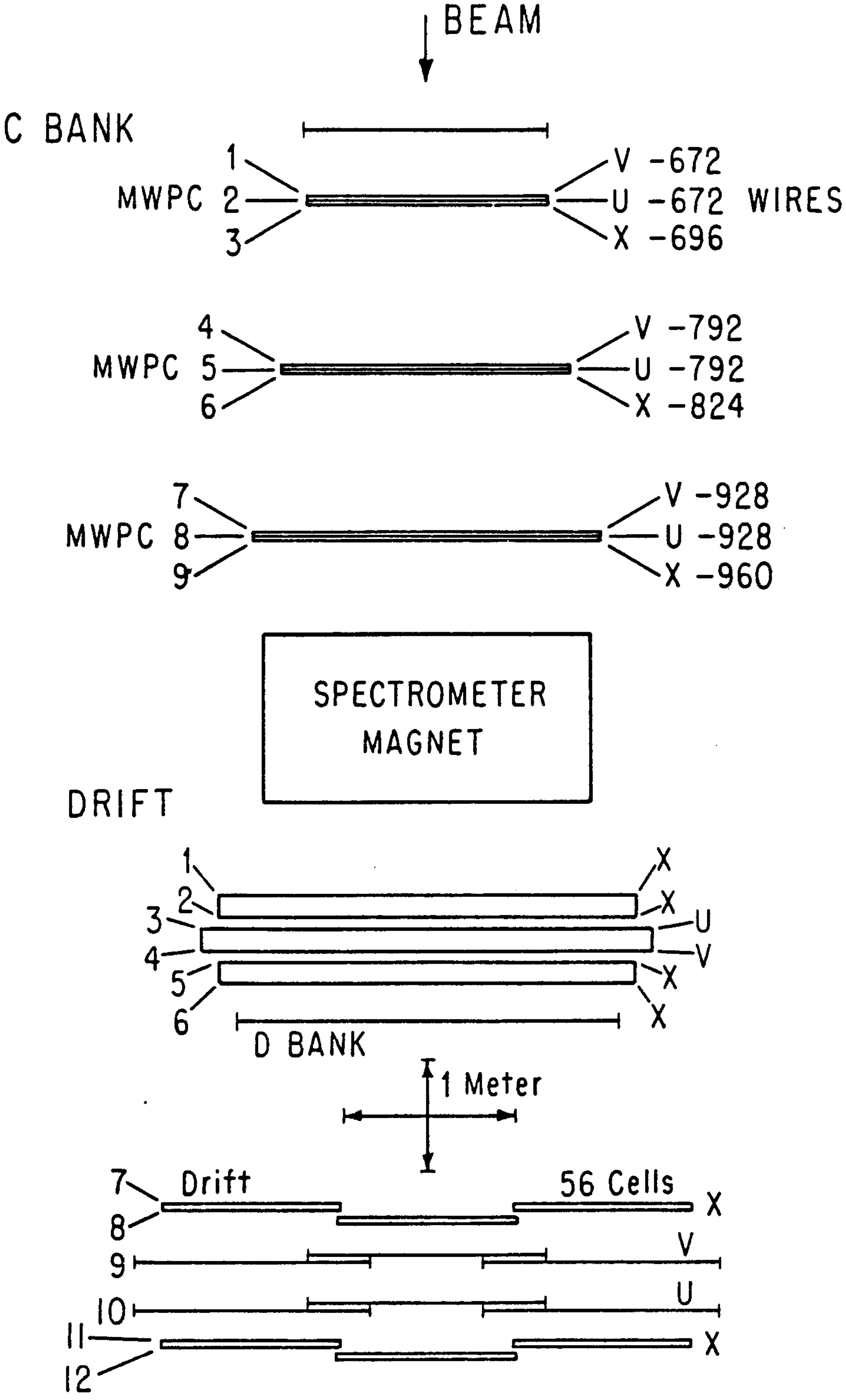
BEAM
C BANK
MWPC
1
2
3
V -672
U -672
X -696
WIRES
MWPC
4
5
6
V -792
U -792
X -824
MWPC
7
8
9
V -928
U -928
X -960
SPECTROMETER
MAGNET
DRIFT
1
2
3
4
5
6
X
X
U
V
X
X
D BANK
1 Meter
7
8
Drift
56 Cells
X
9
V
10
U
11
12
X

Figure 12 -- Perspective view of the hodoscope trigger planes with a di-muon event superimposed (not to scale; see Table 4 for details on the sizes and numbers of counters in the planes).

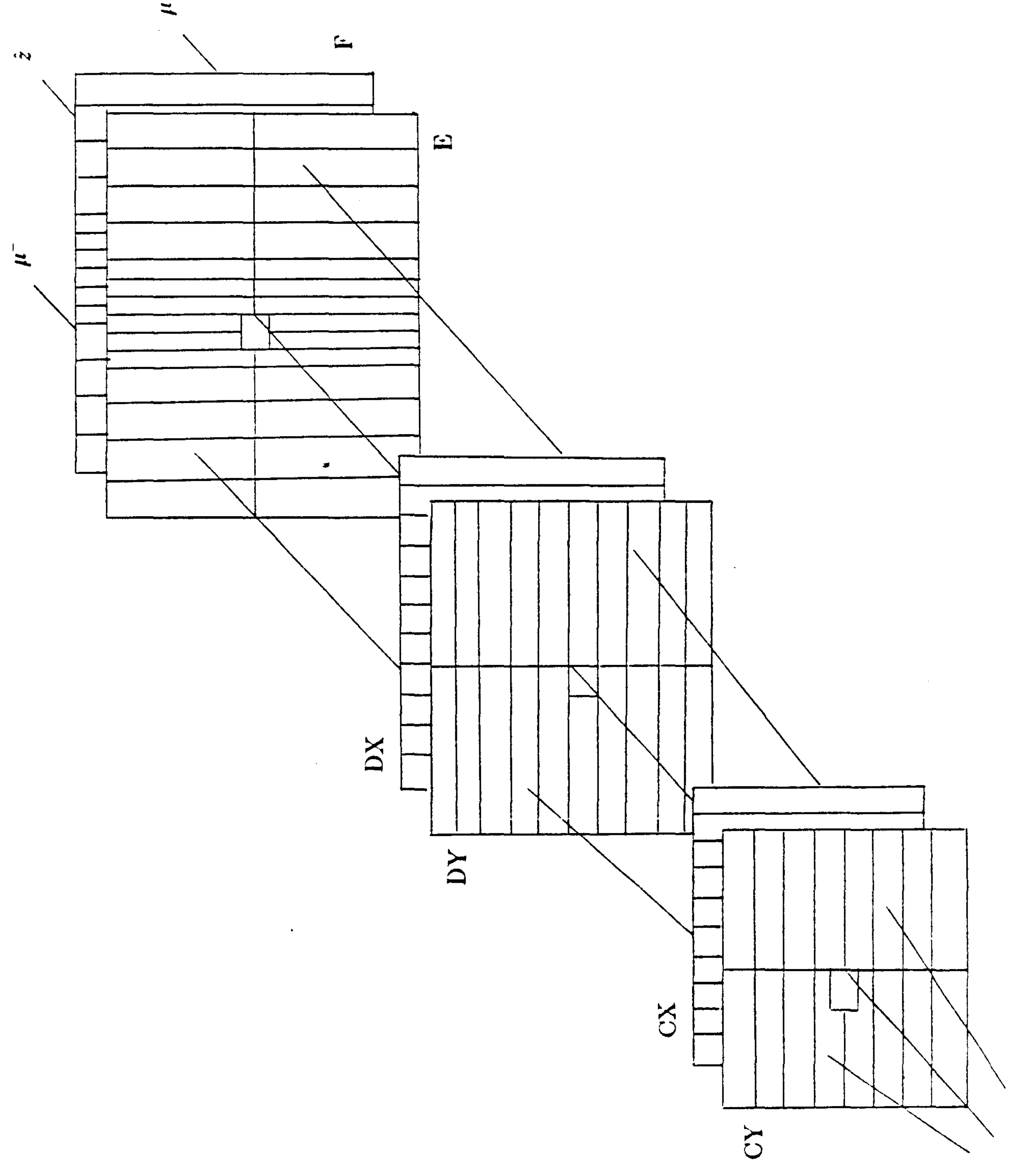
$\hat{z}$
μ^+
F
E
μ^-
DX
DY
CX
CY

Figure 13 -- Display of the pattern of hits in the wire chambers and hodoscopes for a typical event. The positions of the hits are shown in the x–z plane at $y = 0$. The solid lines illustrate the tracks that were reconstructed for this event.

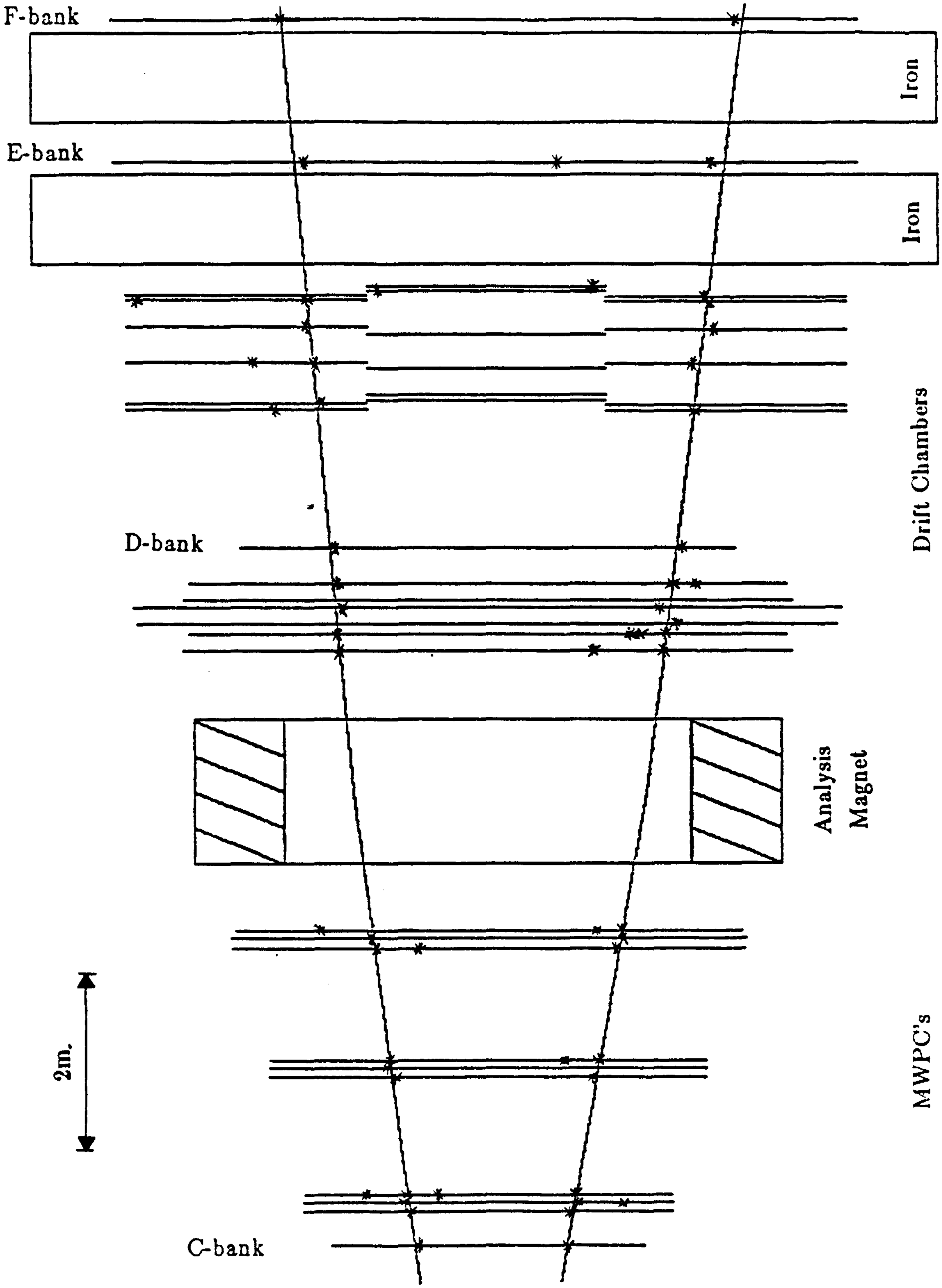
F-bank
Iron
E-bank
Iron
Drift Chambers
D-bank
Analysis Magnet
2m.
MWPC's
C-bank

Figure 14 -- (a) Chi-squared probability ($P(\chi_g^2)$) distribution from the global tracks fits and the distributions of the number of (b) MWPC and (c) drift chamber hits per track.

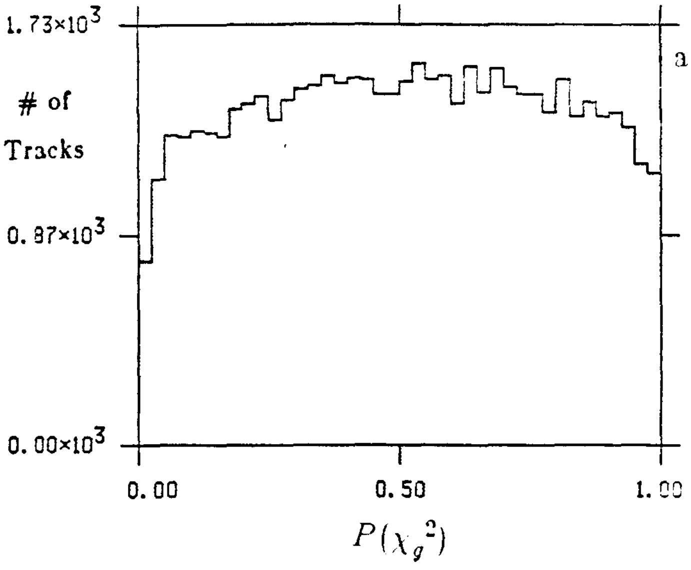
1.73×10³
of
Tracks
0.87×10³
0.00×10³
0.00
0.50
1.00
$P(\chi_g^2)$
a

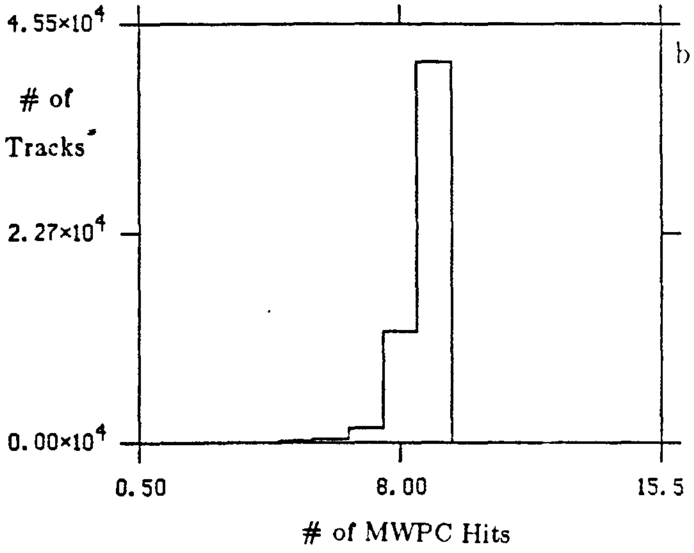
4.55×10⁴
of
Tracks
2.27×10⁴
0.00×10⁴
0.50
8.00
15.5
# of MWPC Hits
b

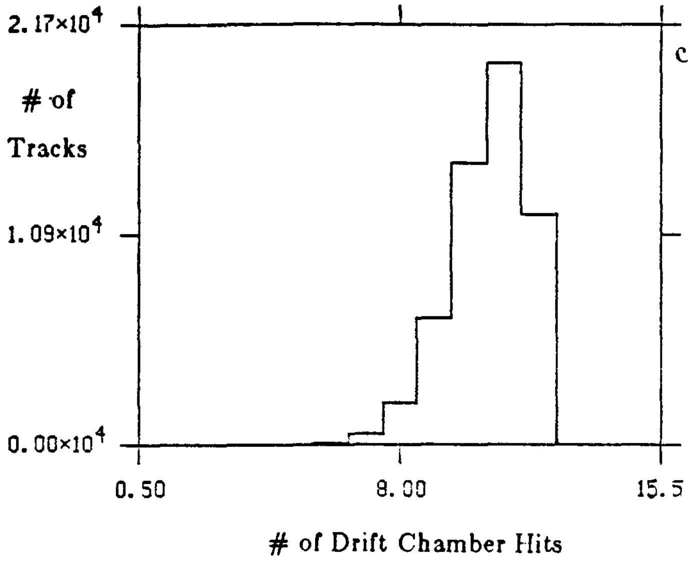
2.17×10⁴
of
Tracks
1.09×10⁴
0.00×10⁴
0.50
8.00
15.5
# of Drift Chamber Hits
c

Figure 15 -- Distributions of the global track fit residuals (Δd) for the X planes at the ends of each segment of the spectrometer.

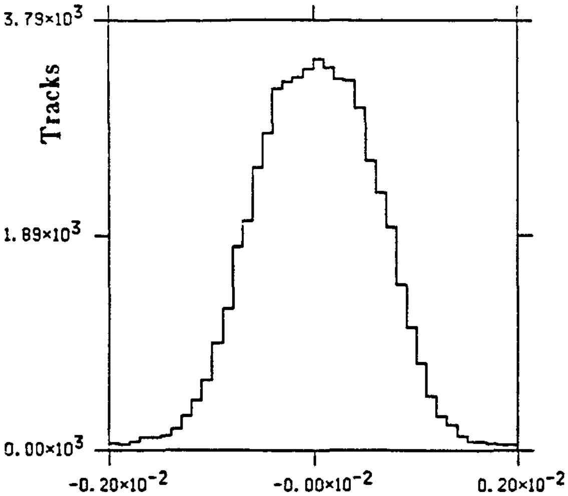

Δd $(m.)$: MWPC Plane #3

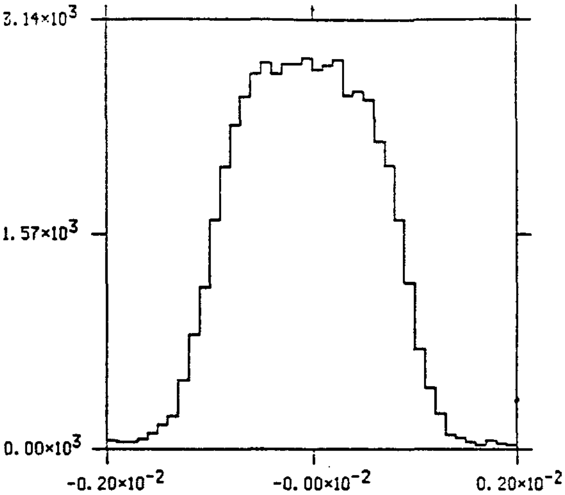

Δd $(m.)$: MWPC Plane #9

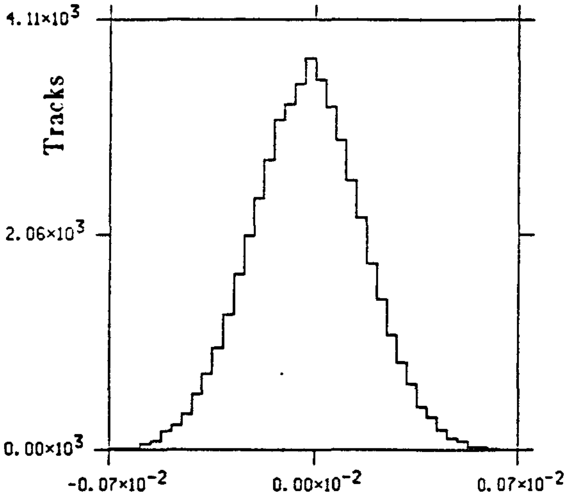

Δd $(m.)$: Drift Plane #1

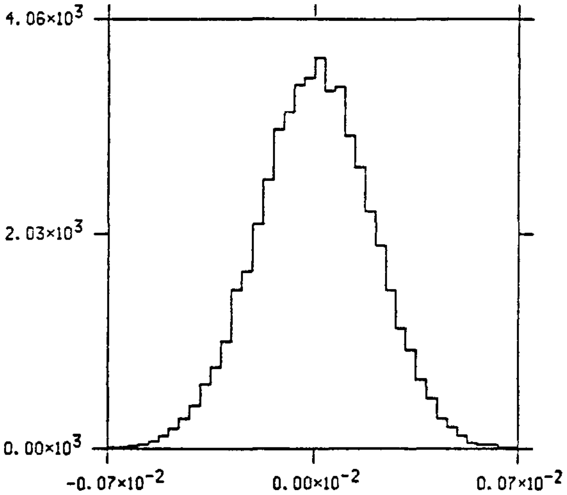

Δd $(m.)$: Drift Plane #12

Figure 16 -- Mass distribution of the events recorded during a four hour run.

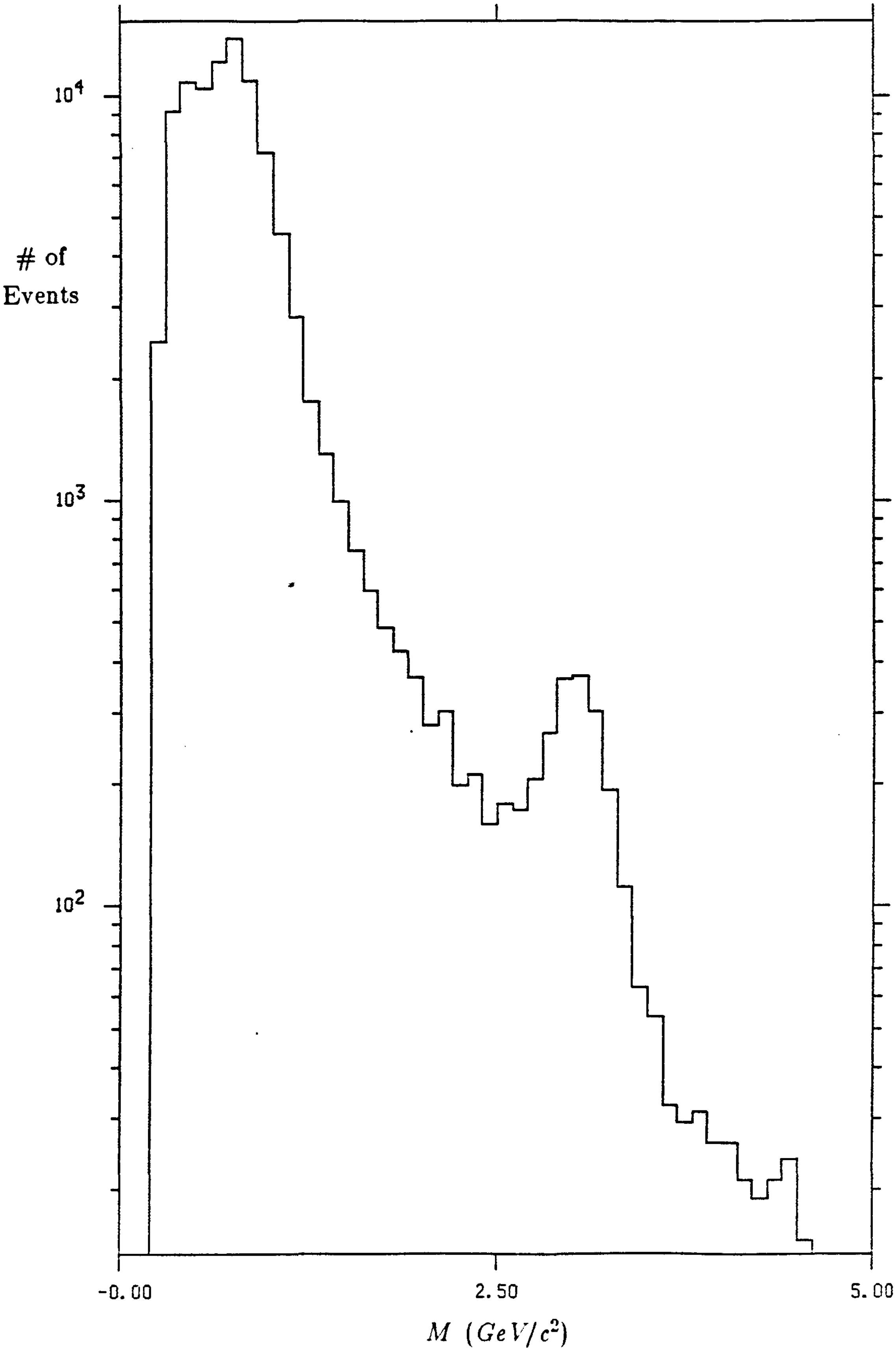

10^4
10^3
10^2
# of Events
-0.00
2.50
5.00
$M \ (GeV/c^2)$

Figure 17 -- Distributions of J/ψ events ($2.7 < M < 3.5$ GeV/c^2) in the six kinematic variables describing di-muon production.

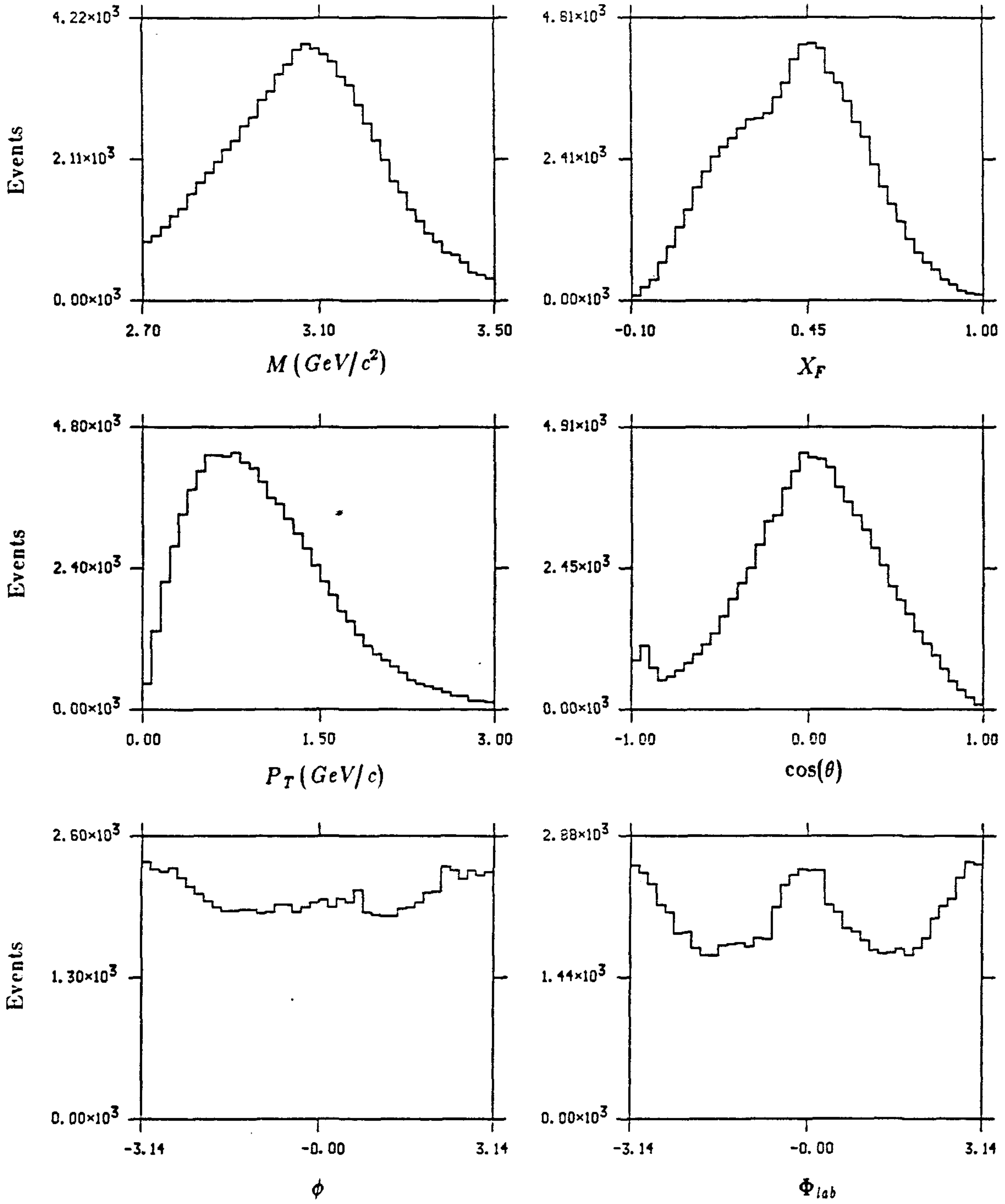
4.22×10^3
2.11×10^3
0.00×10^3
Events
2.70
3.10
3.50
$M\,(GeV/c^2)$
4.81×10^3
2.41×10^3
0.00×10^3
-0.10
0.45
1.00
X_F
4.80×10^3
2.40×10^3
0.00×10^3
Events
0.00
1.50
3.00
$P_T\,(GeV/c)$
4.91×10^3
2.45×10^3
0.00×10^3
-1.00
0.00
1.00
cos(θ)
2.60×10^3
1.30×10^3
0.00×10^3
Events
-3.14
-0.00
3.14
ϕ
2.88×10^3
1.44×10^3
0.00×10^3
-3.14
-0.00
3.14
Φ_{lab}

Figure 18 -- Momentum spectra of negative and positive sign muons from data recorded with a single particle trigger.

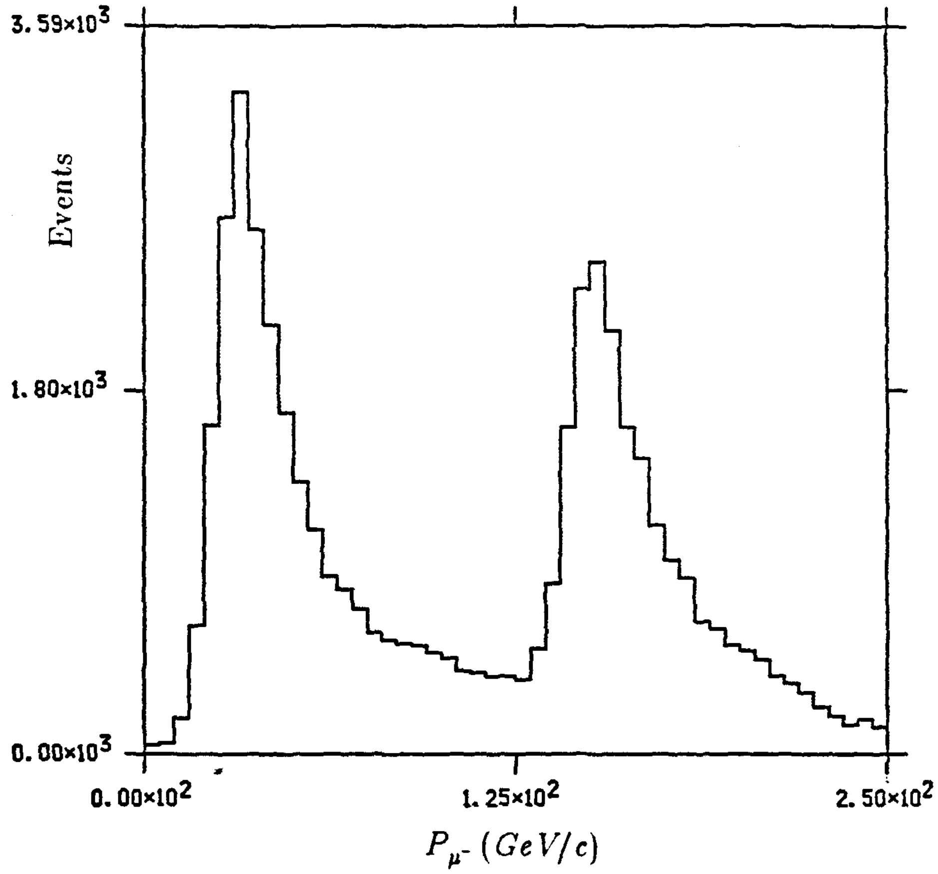
3.59×10³
1.80×10³
0.00×10³
Events
0.00×10²
1.25×10²
2.50×10²
P_{μ^-} (GeV/c)

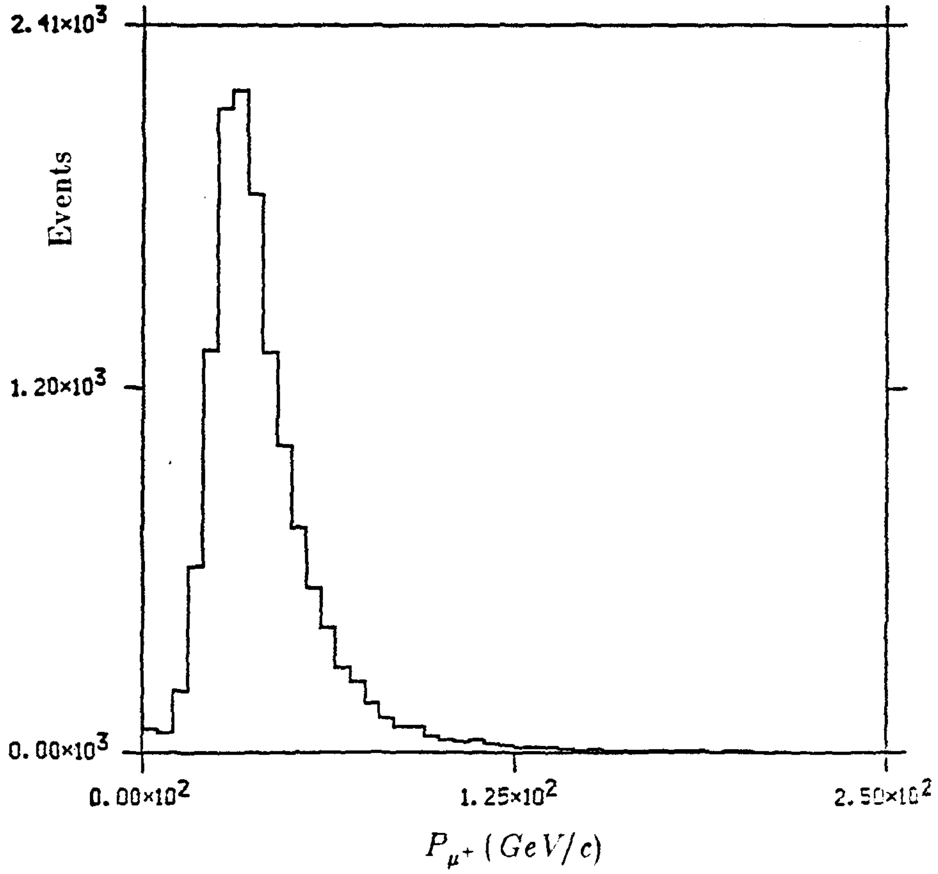
2.41×10³
1.20×10³
0.00×10³
Events
0.00×10²
1.25×10²
2.50×10²
P_{μ^+} (GeV/c)

Figure 19 -- Comparisons of the $\cos(\theta)$ distributions of the J/ψ data (solid lines) and the simulated accidental pairs (crosses) in four X_F regions before the non-prompt background cuts are applied.

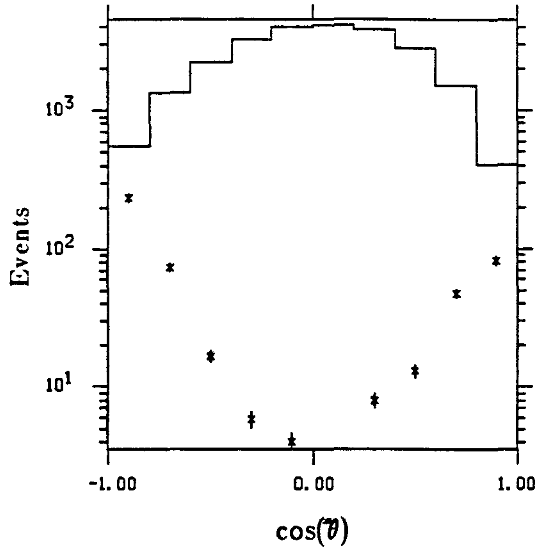

($0. < X_F < .3$)

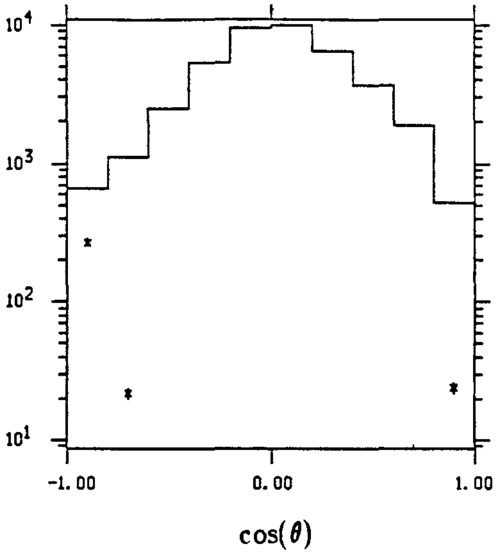

($.3 < X_F < .6$)

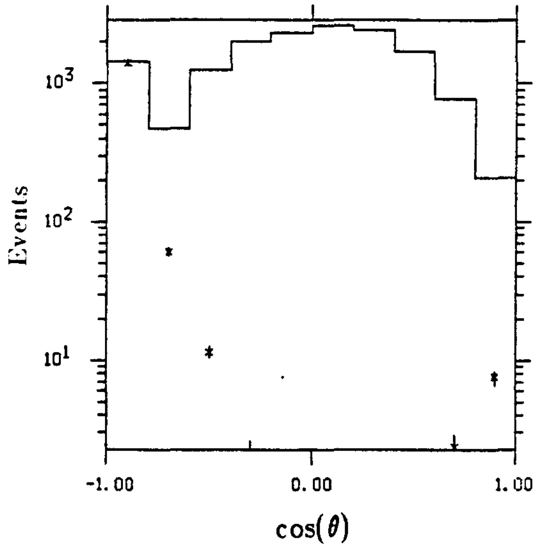

($.6 < X_F < .9$)

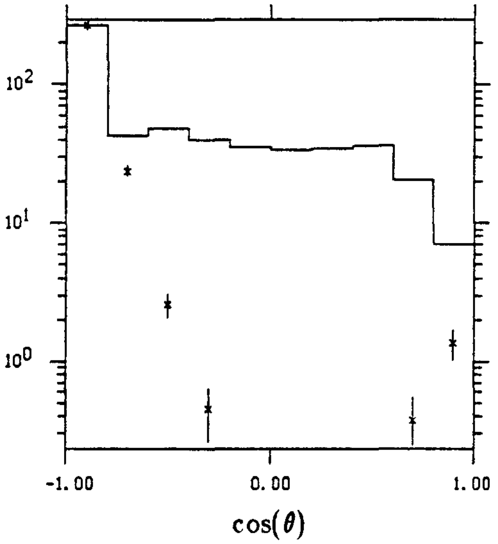

($.9 < X_F < 1.$)

Figure 20 -- Comparisons of the J/ψ data (solid lines) and the simulated accidental pairs (crosses) in the six kinematic variables before the non-prompt background cuts are applied.

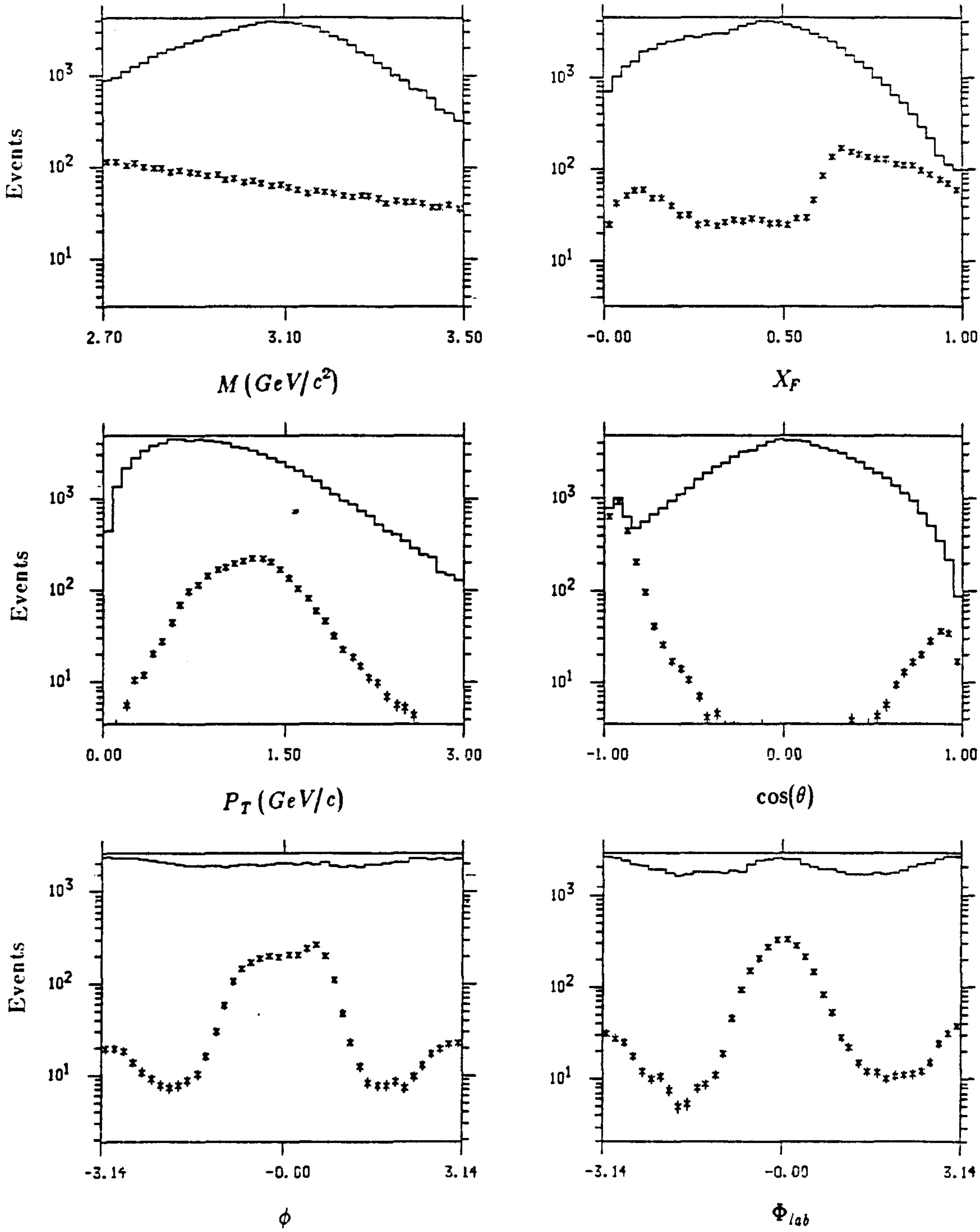
Events
10^3
10^2
10^1
2.70
3.10
3.50
$M\,(GeV/c^2)$
-0.00
0.50
1.00
X_F
0.00
1.50
3.00
$P_T\,(GeV/c)$
-1.00
0.00
1.00
$\cos(\theta)$
-3.14
-0.00
3.14
ϕ
Φ_{lab}

Figure 21 -- Scatter plots of the (a) simulated accidental pairs, (b) data and (c) simulated J/ψ events in the variables chosen to distinguish the non-prompt background. The events that appear below the dotted line are excluded from the final data sample.

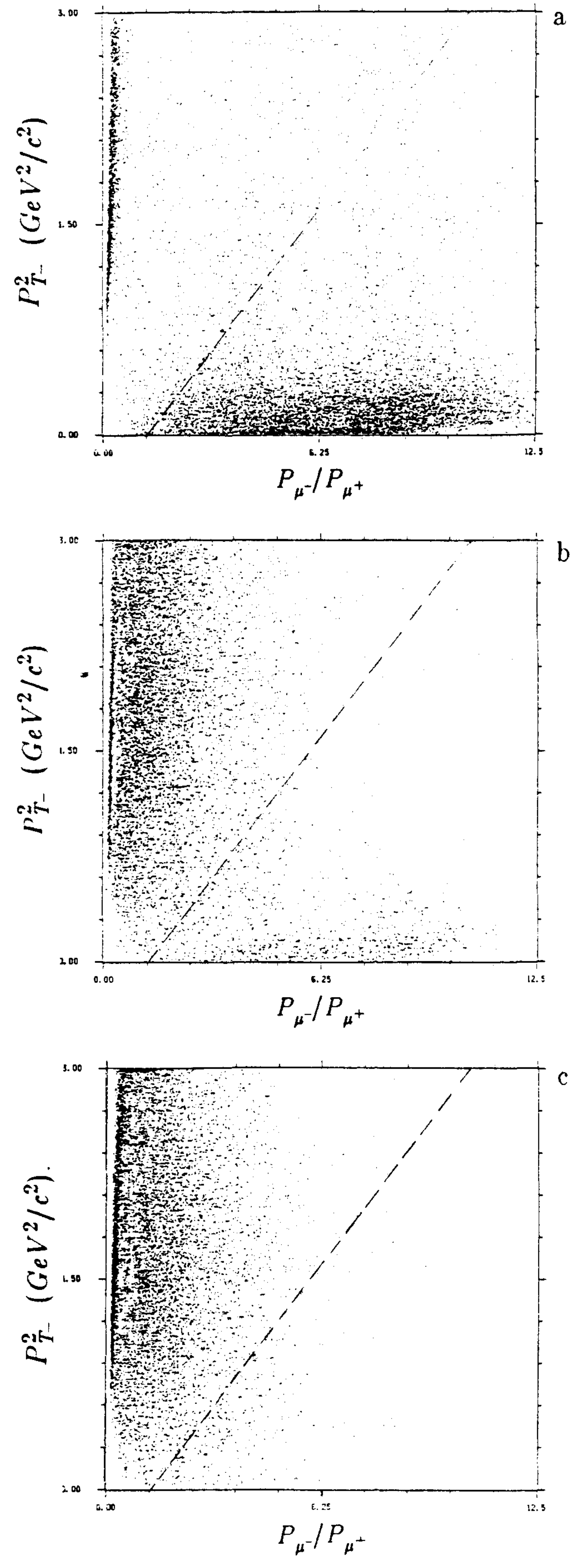
a
3.00
1.50
0.00
$P^2_{T^-}$ (GeV^2/c^2)
0.00
6.25
12.5
P_{μ^-}/P_{μ^+}
b
3.00
1.50
0.00
$P^2_{T^-}$ (GeV^2/c^2)
0.00
6.25
12.5
P_{μ^-}/P_{μ^+}
c
3.00
1.50
0.00
$P^2_{T^-}$ (GeV^2/c^2)
0.00
6.25
12.5
P_{μ^-}/P_{μ^+}

Figure 22 -- Comparisons of the cos(θ) distributions of the J/ψ data (solid lines) and the simulated accidental pairs (crosses) in four X_F regions after the non-prompt background cuts are applied.

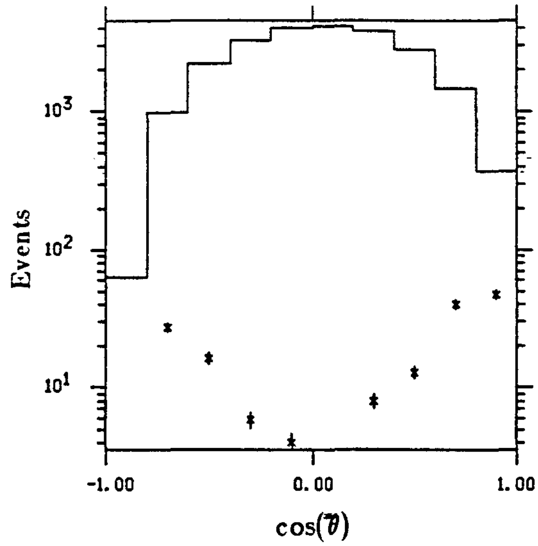

(0. < X_F < .3)

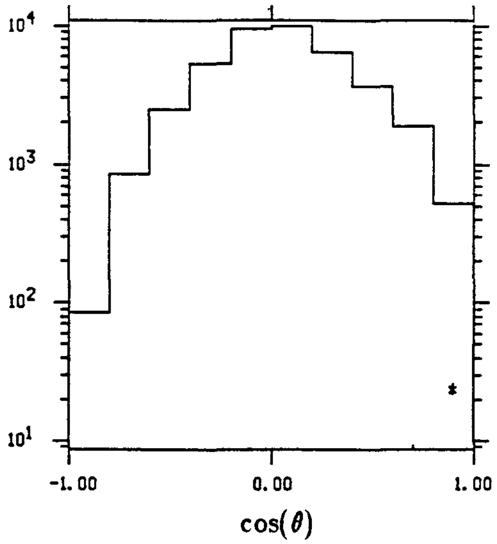

(.3 < X_F < .6)

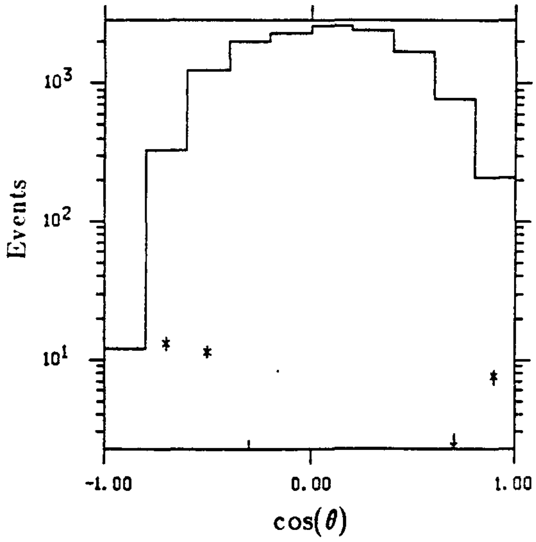

(.6 < X_F < .9)

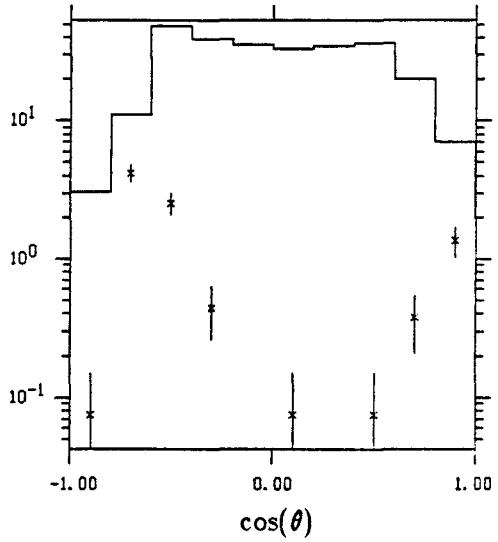

(.9 < X_F < 1.)

Figure 23 -- Comparisons of the J/ψ data (solid lines) and the simulated accidental pairs (crosses) in the six kinematic variables after the non-prompt background cuts are applied.

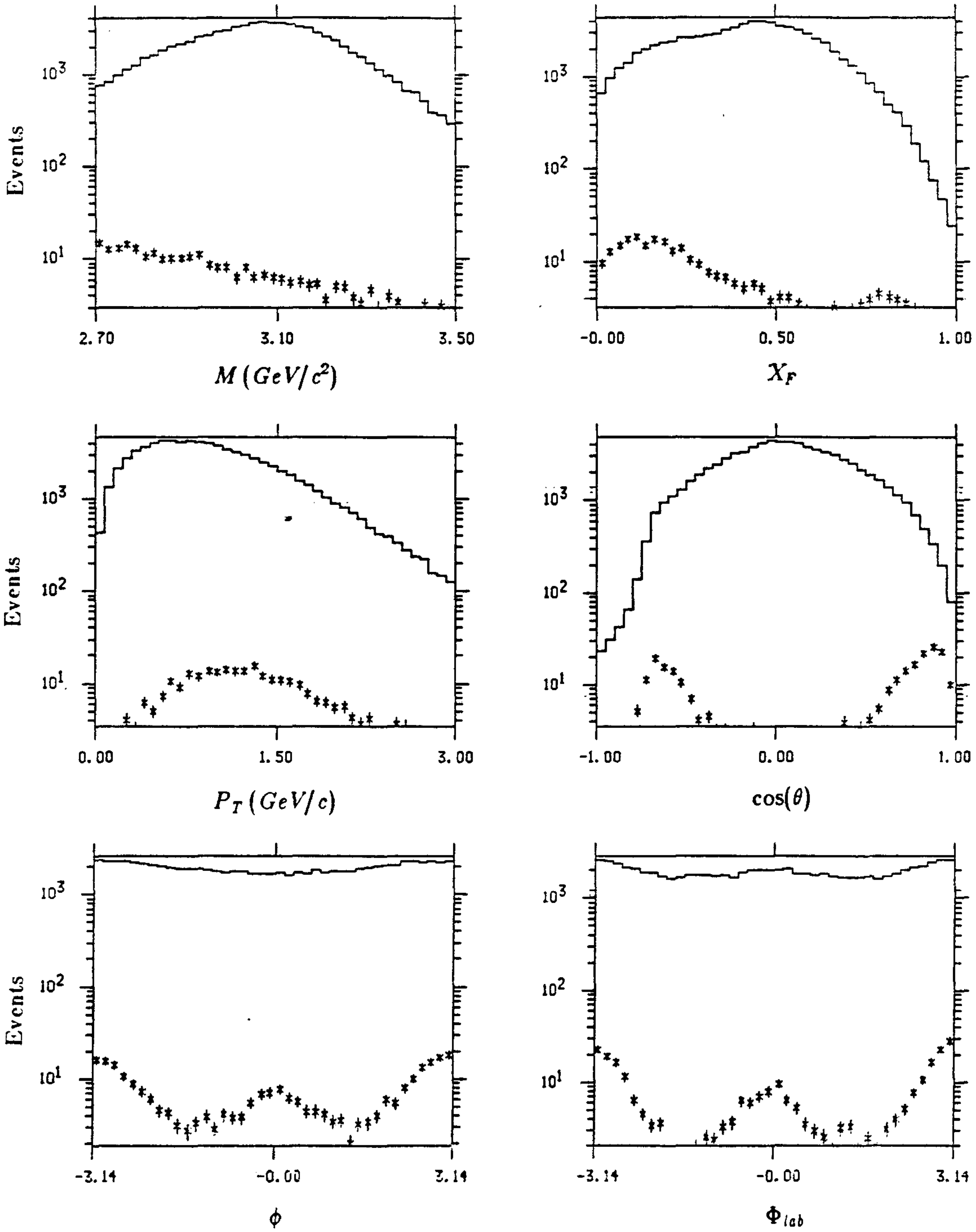
Events
10^3
10^2
10^1
2.70
3.10
3.50
$M\,(GeV/c^2)$
-0.00
0.50
1.00
X_F
0.00
1.50
3.00
$P_T\,(GeV/c)$
-1.00
0.00
1.00
$\cos(\theta)$
-3.14
-0.00
3.14
ϕ
Φ_{lab}

Figure 24 -- Mass spectrum of events with $X_F > .1$. The result of the empirical fit to the data (upper curve) is shown together with the representations of the continuum and the continuum plus ψ' contributions.

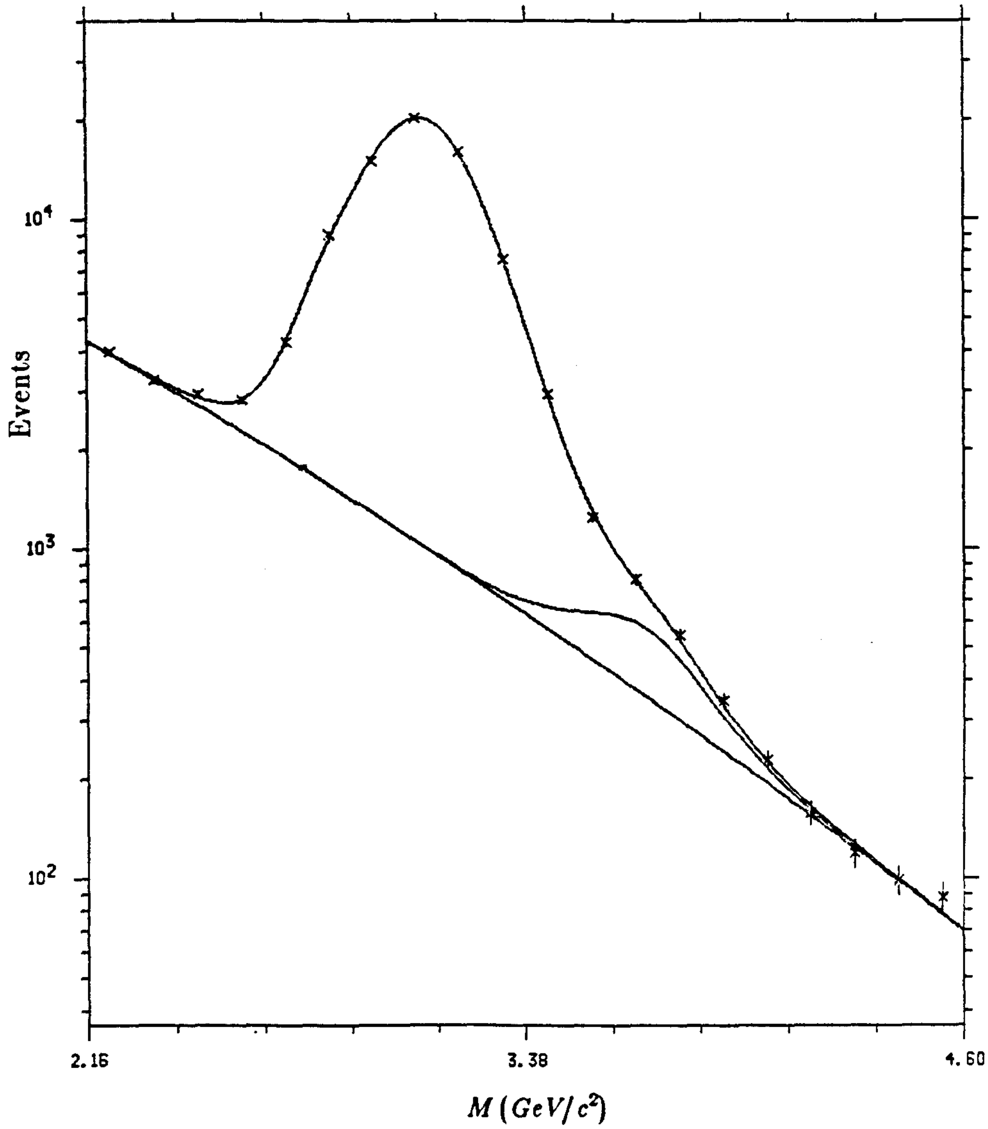
Events
10^4
10^3
10^2
2.16
3.38
4.60
$M\,(GeV/c^2)$

Figure 25 -- Mass spectrum of events in three X_F regions. The results of the empirical fits to the data (upper curves) are shown together with the representations of the continuum and the continuum plus ψ' contributions.

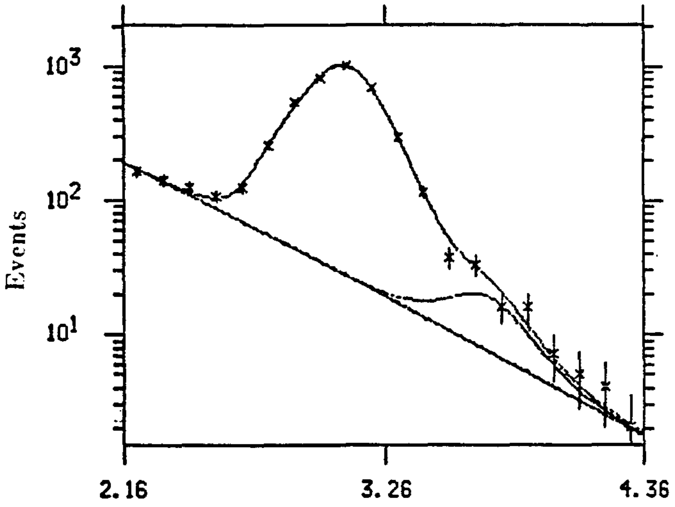

$M\ (GeV/c^2)\ :\ .10 < X_F < .15$

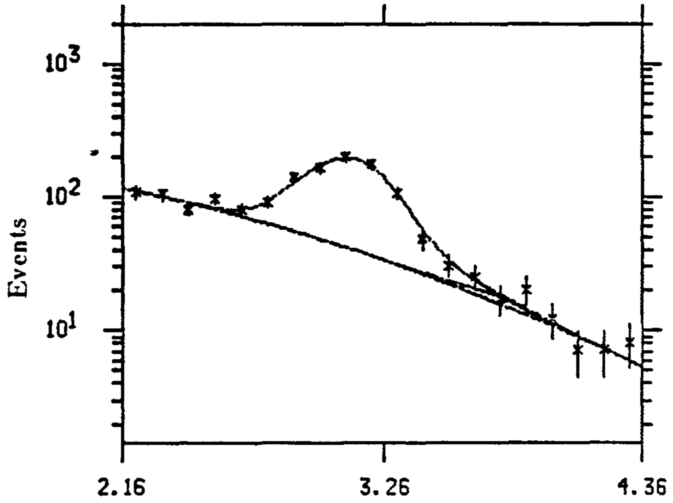

$M\ (GeV/c^2)\ :\ .80 < X_F < .85$

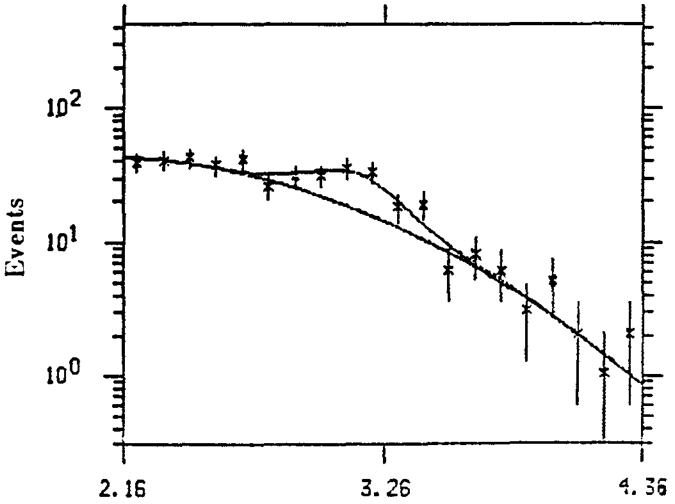

$M\ (GeV/c^2)\ :\ .90 < X_F < .95$

Figure 26 -- The continuum fraction (R_{cnt}) as a function of X_F. The parametrization of the data (solid curve) is described in the text.

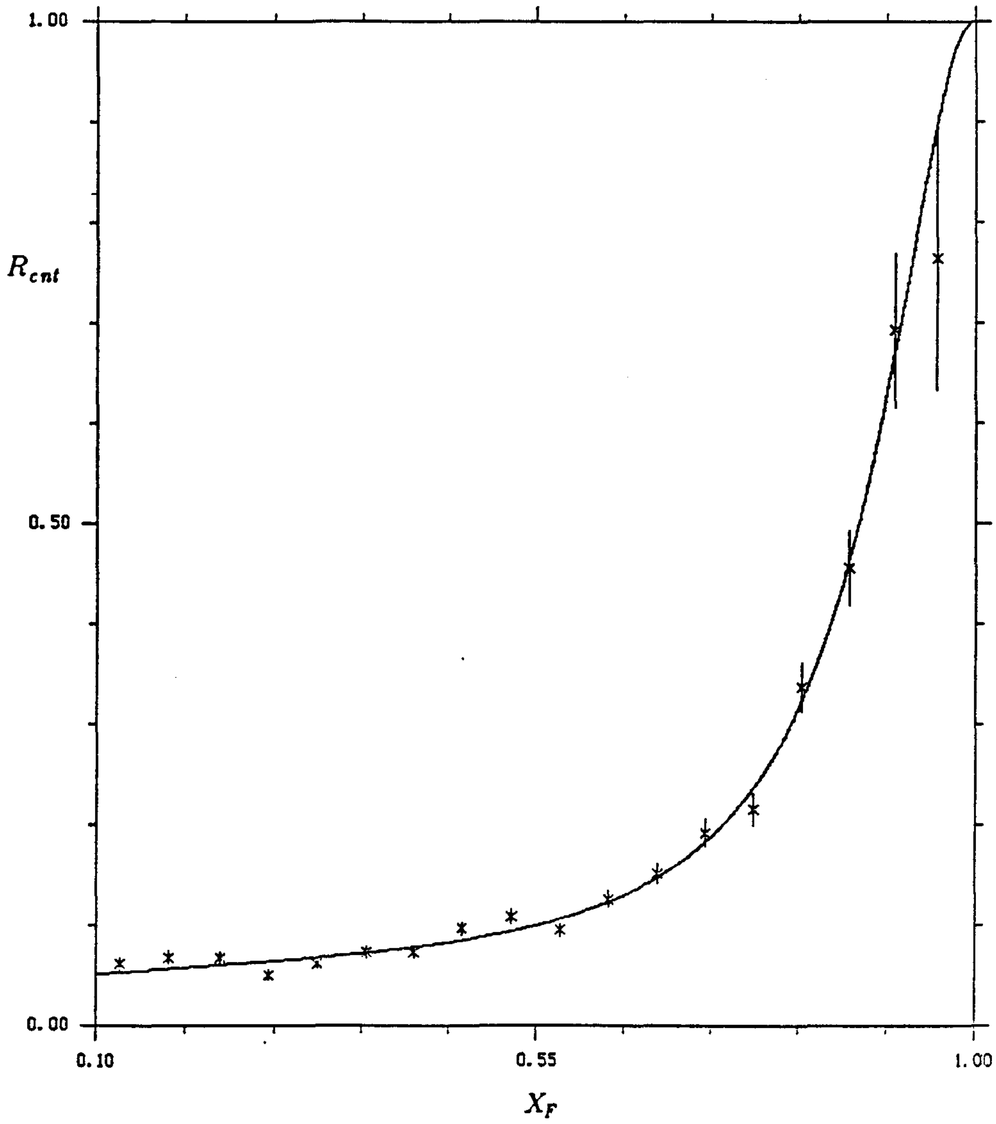
1.00
0.50
0.00
R_{cnt}
0.10
0.55
1.00
X_F

Figure 27 -- The continuum fraction (R_{cnt}) as a function of P_T^2 (in GeV^2/c^2) in 8 X_F regions. The parametrization of the data (solid curves) is described in the text.

a) $.1 < X_F < .2$ b) $.2 < X_F < .3$
c) $.3 < X_F < .4$ d) $.4 < X_F < .5$
e) $.5 < X_F < .6$ f) $.6 < X_F < .7$
g) $.7 < X_F < .8$ h) $.8 < X_F < .9$

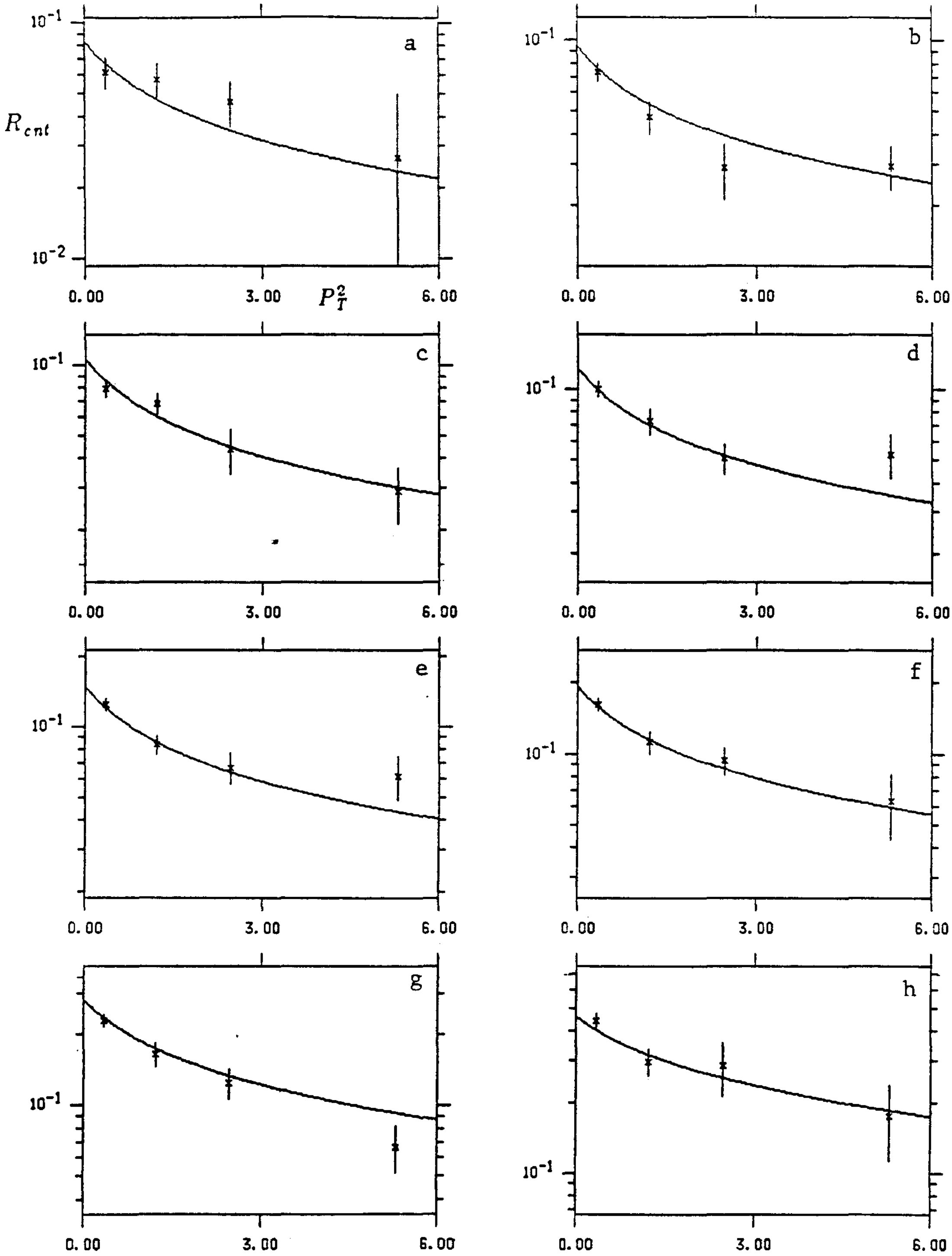
a
b
c
d
e
f
g
h
R_{cnt}
P_T^2
10^{-1}
10^{-2}
0.00
3.00
6.00

Figure 28 -- The continuum fraction (R_{cnt}) as a function of $|\phi|$ in eight regions of X_F and P_T^2. The solid curves show the results of the fits to the data assuming that R_{cnt} is constant.

Plot Assignments

	$P_T^2 < 1.5$	$1.5 < P_T^2 < 4.5$
$.1 < X_F < .3$	a	e
$.3 < X_F < .5$	b	f
$.5 < X_F < .7$	c	g
$.7 < X_F < .9$	d	h

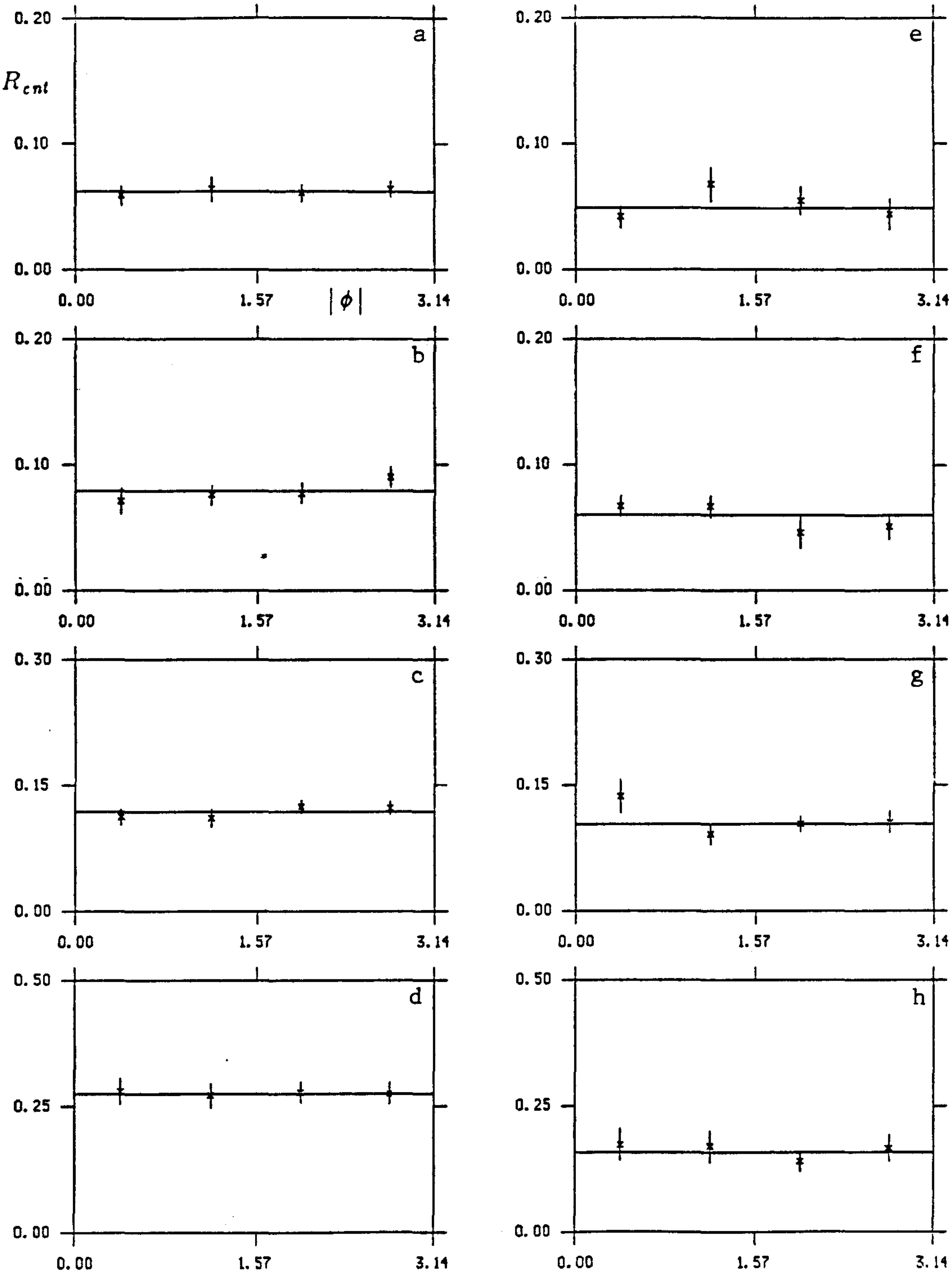
a
R_{cnl}
0.20
0.10
0.00
0.00
1.57
$|\phi|$
3.14
b
0.20
0.10
0.00
0.00
1.57
3.14
c
0.30
0.15
0.00
0.00
1.57
3.14
d
0.50
0.25
0.00
0.00
1.57
3.14
e
0.20
0.10
0.00
0.00
1.57
3.14
f
0.20
0.10
0.00
0.00
1.57
3.14
g
0.30
0.15
0.00
0.00
1.57
3.14
h
0.50
0.25
0.00
0.00
1.57
3.14

Figure 29 -- The continuum fraction (R_{cnt}) as a function of $|\cos(\theta)|$ in eight regions of X_F and P_T^2. The parametrizations of the data (solid curves) are described in the text.

Plot Assignments

	$P_T^2 < 1.5$	$1.5 < P_T^2 < 4.5$
$.1 < X_F < .3$	a	e
$.3 < X_F < .5$	b	f
$.5 < X_F < .7$	c	g
$.7 < X_F < .9$	d	h

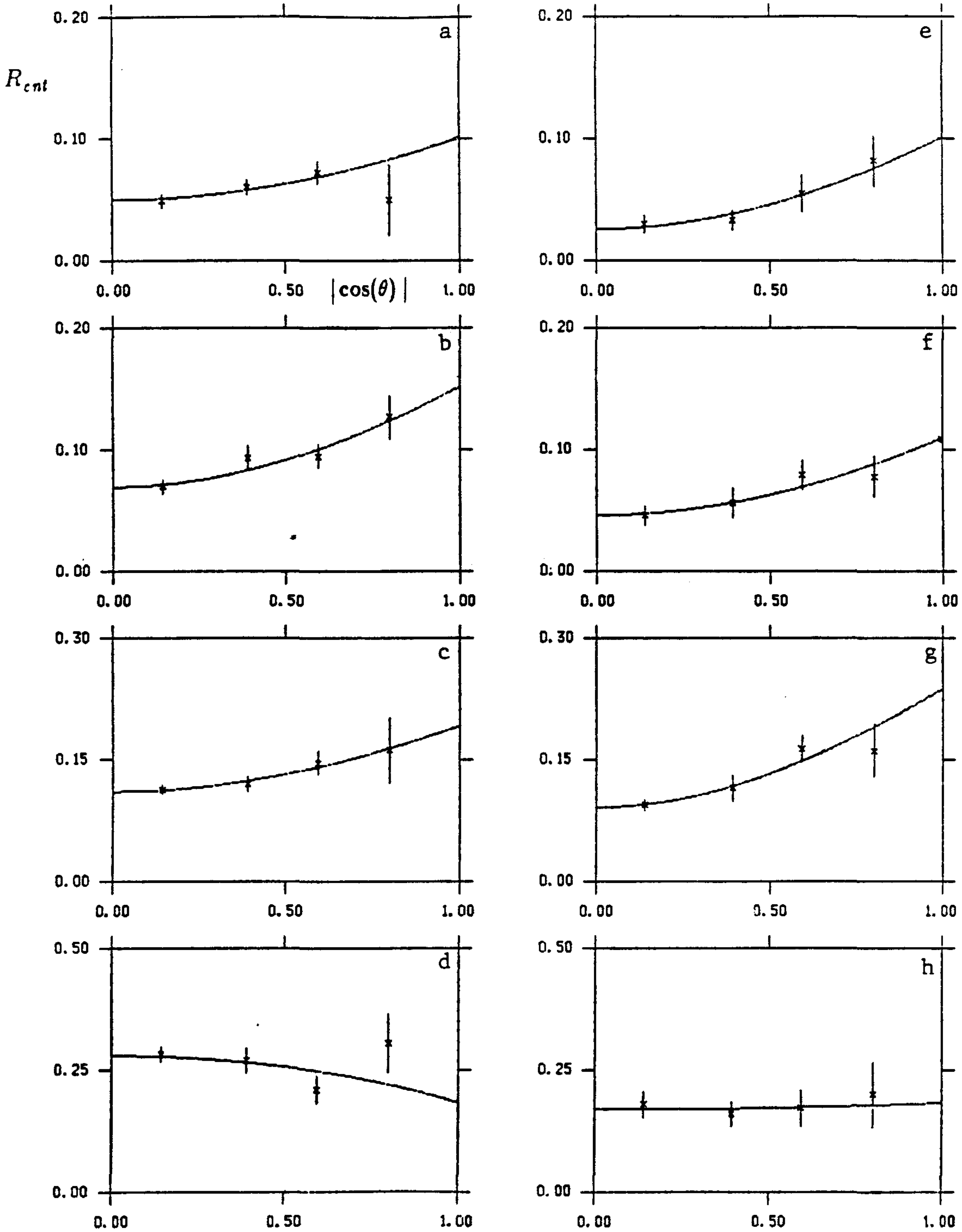
R_{cnt}
$|\cos(\theta)|$
a
b
c
d
e
f
g
h
0.00
0.10
0.15
0.20
0.25
0.30
0.50
0.00
0.50
1.00

Figure 30 -- Momentum spectrum of negative sign muons selected from single particle trigger data.

a) Full spectrum.

b) Comparison of the high momentum portion of the spectrum with the prediction (crosses) from a Monte Carlo simulation of muons from beam decays.

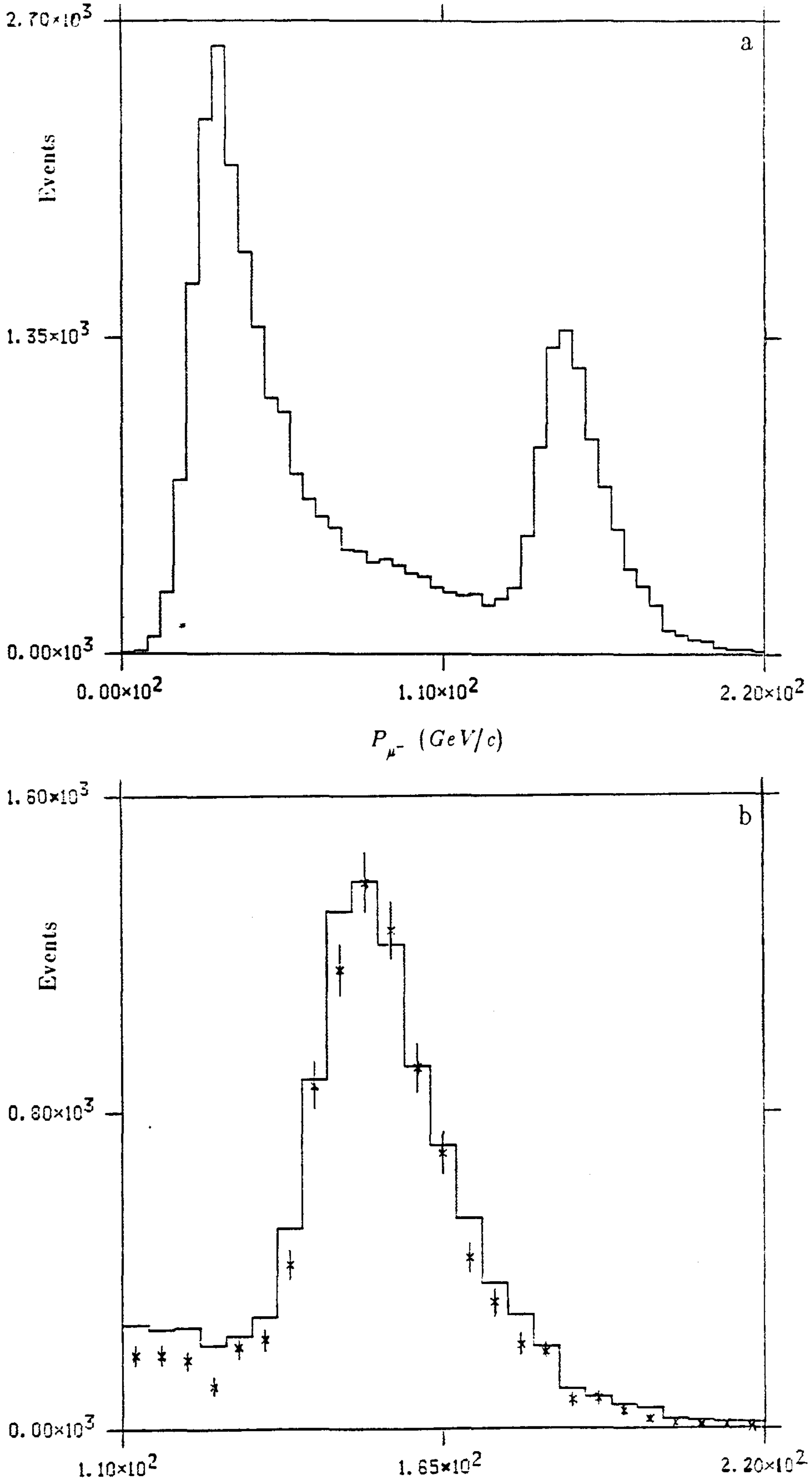
2.70×10^3
a
Events
1.35×10^3
0.00×10^3
0.00×10^2
1.10×10^2
2.20×10^2
P_{μ^-} (GeV/c)
1.60×10^3
b
Events
0.80×10^3
0.00×10^3
1.10×10^2
1.65×10^2
2.20×10^2
P_{μ^-} (GeV/c)

Figure 31 -- The simulated distributions of the (a) beam momentum and (b) pion-nucleon center of mass energy.

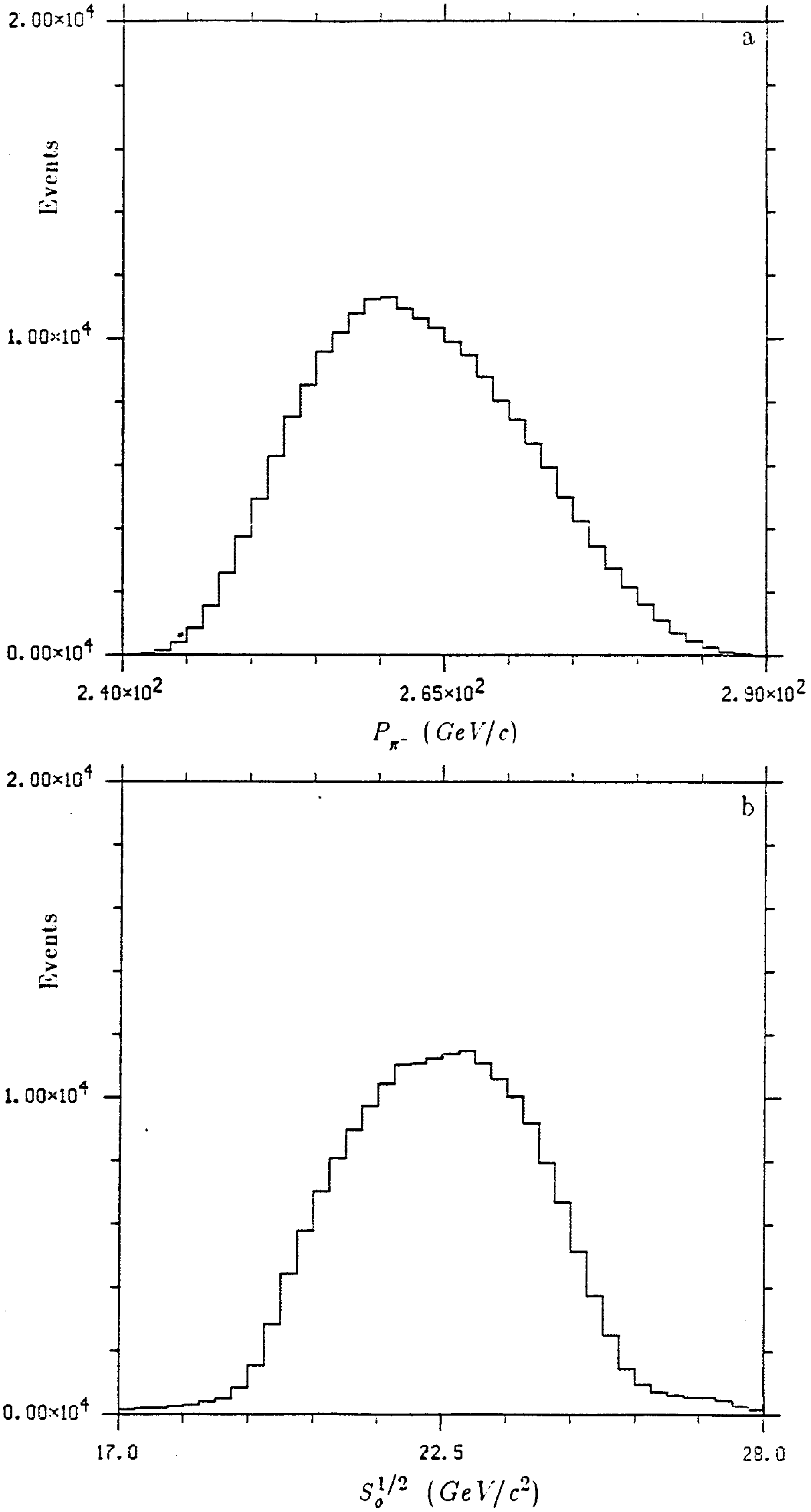
2.00×10^4
a
Events
1.00×10^4
0.00×10^4
2.40×10^2
2.65×10^2
2.90×10^2
P_{π^-} (GeV/c)
2.00×10^4
b
Events
1.00×10^4
0.00×10^4
17.0
22.5
28.0
$S_o^{1/2}$ (GeV/c^2)

Figure 32 -- Distributions of the reconstructed x and y vertex positions for events with resolutions in these quantities less the 5 *mm*. The arrows indicate the size of the target.

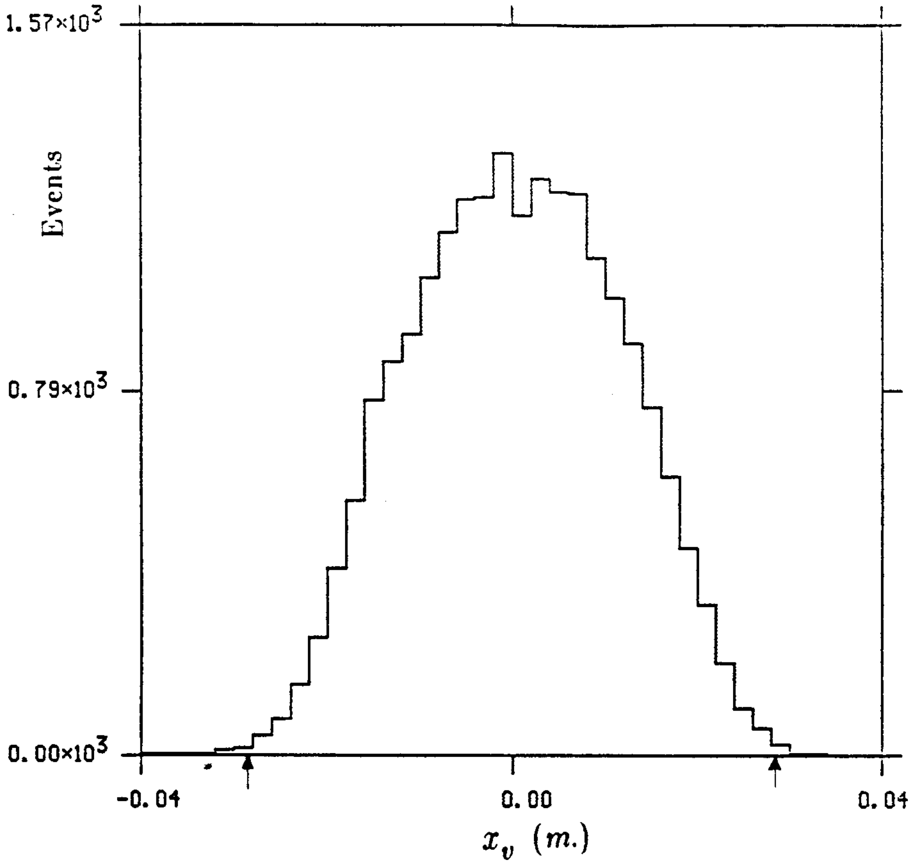
1.57×10³
0.79×10³
0.00×10³
Events
-0.04
0.00
0.04
x_v (m.)

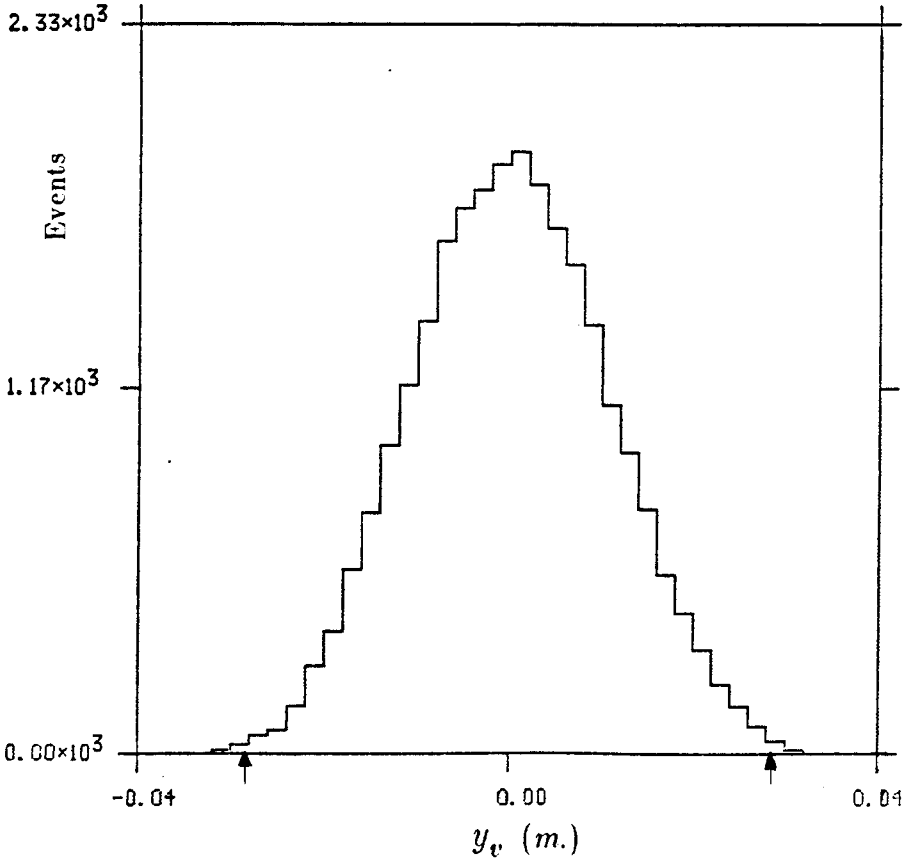
2.33×10³
1.17×10³
0.00×10³
Events
-0.04
0.00
0.04
y_v (m.)

Figure 33 -- Inefficiency density of the D bank. The boxes in the upper portion of the plot indicate the size of the overlap region of the X and Y counters. The number of points in each such area is the joint inefficiency of the counters in that region. The box in the center of the plot represents the beam hole.

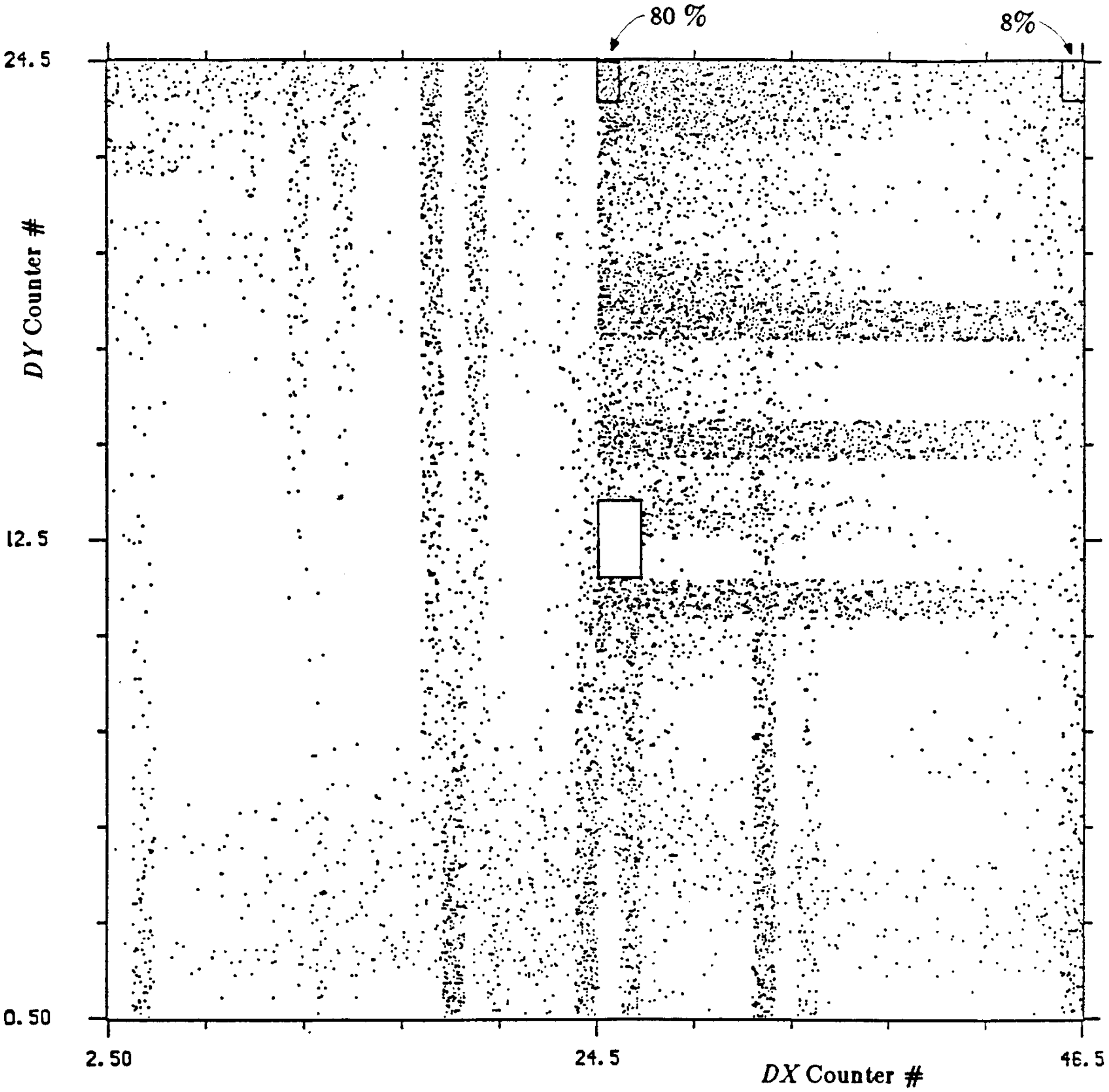
80 %
8%
24.5
12.5
0.50
DY Counter #
2.50
24.5
46.5
DX Counter #

Figure 34 -- Acceptance loss due to the hodoscope counter inefficiencies as a function of cos(θ) and ϕ in four regions of X_F and P_T^2.

a),e) $.1 < X_F < .5$ $P_T^2 < 4.5\ GeV^2/c^2$
b),f) $.5 < X_F < .9$ $P_T^2 < 4.5\ GeV^2/c^2$
c),g) $.1 < X_F < .5$ $P_T^2 > 4.5\ GeV^2/c^2$
d),h) $.5 < X_F < .9$ $P_T^2 > 4.5\ GeV^2/c^2$

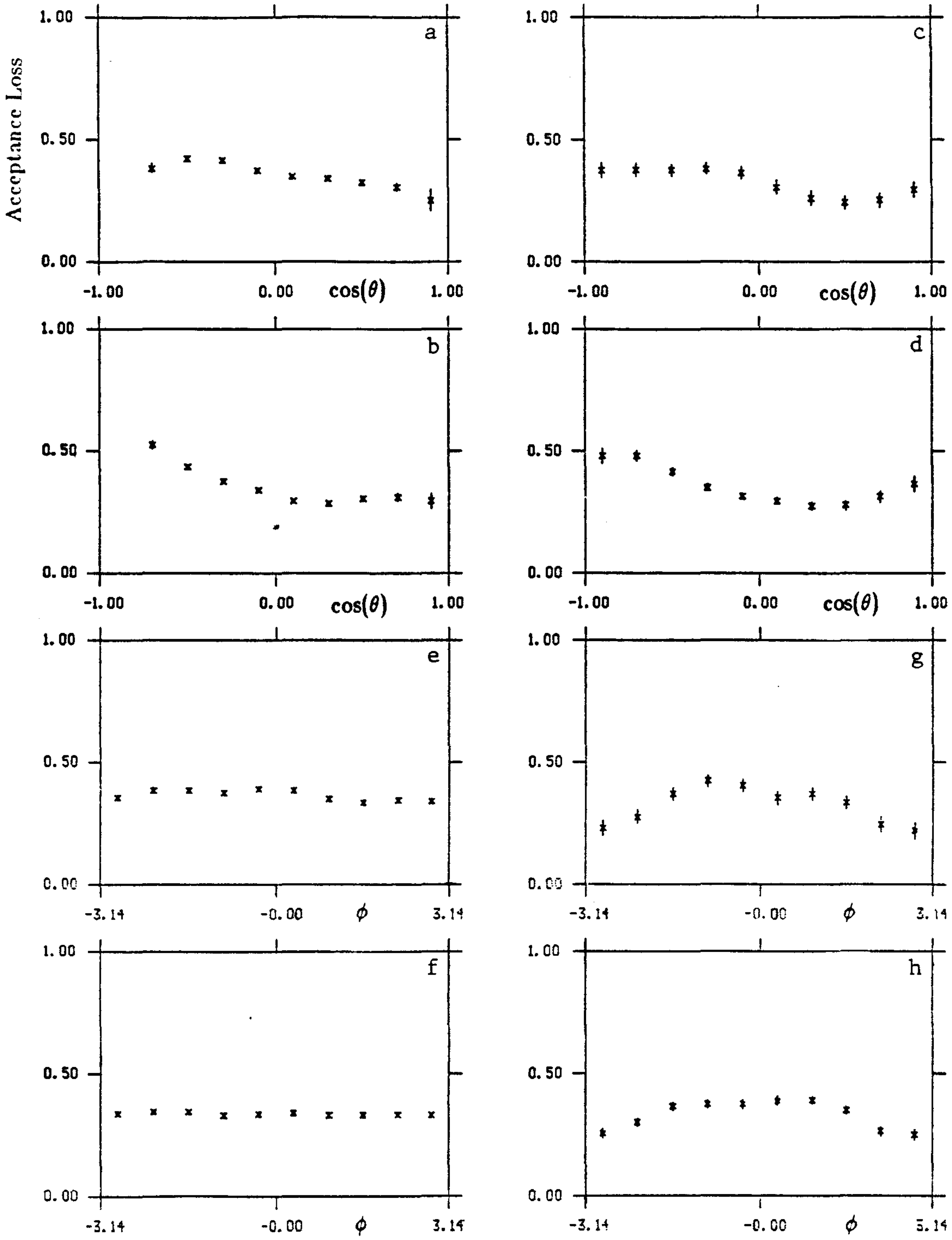
Acceptance Loss
1.00
0.50
0.00
-1.00
0.00
1.00
cos(θ)
a
b
c
d
-3.14
-0.00
3.14
φ
e
f
g
h

Figure 35 -- Comparisons of the data (solid lines) and Monte Carlo (crosses) mass spectra in four X_F regions.

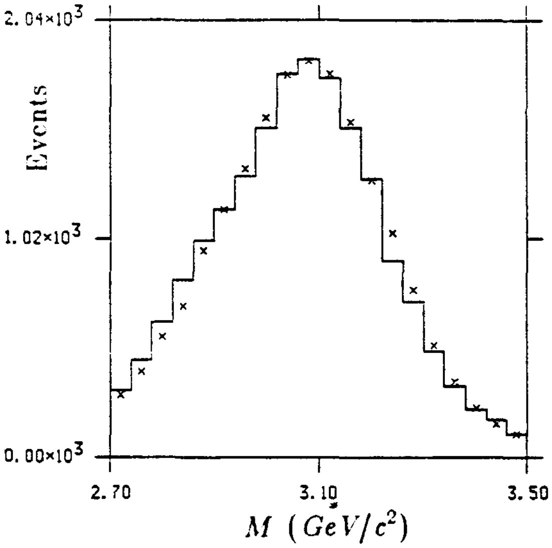

$(.1 < X_F < .3)$

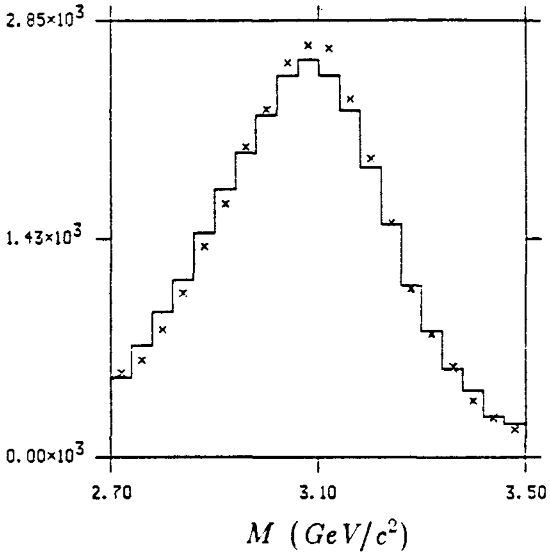

$(.3 < X_F < .5)$

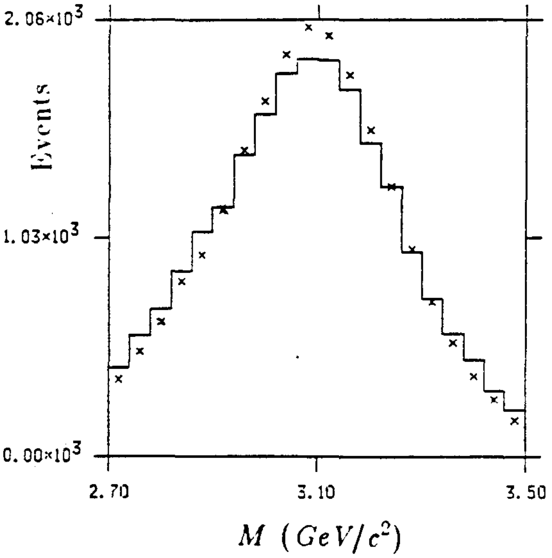

$(.5 < X_F < .7)$

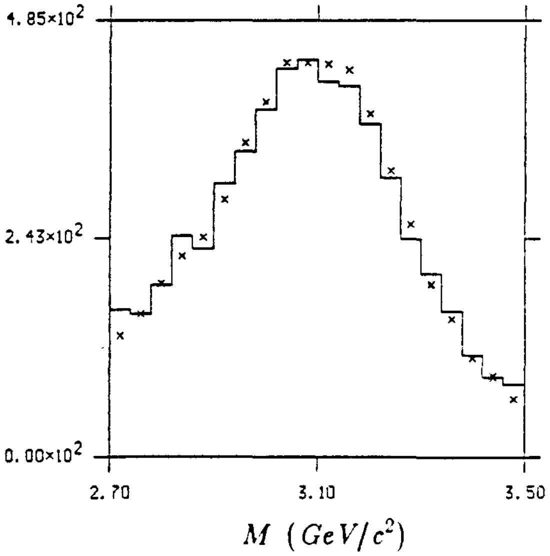

$(.7 < X_F < .9)$

Figure 36 -- Comparisons of the data (solid lines) and Monte Carlo (crosses) ΔX distributions in four X_F regions.

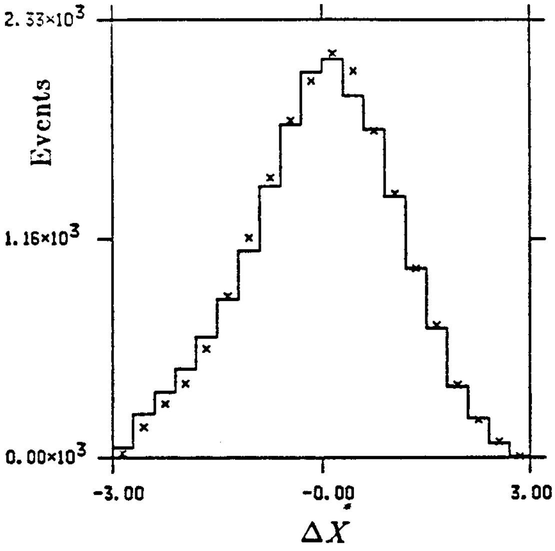

(.1 < X_F < .3)

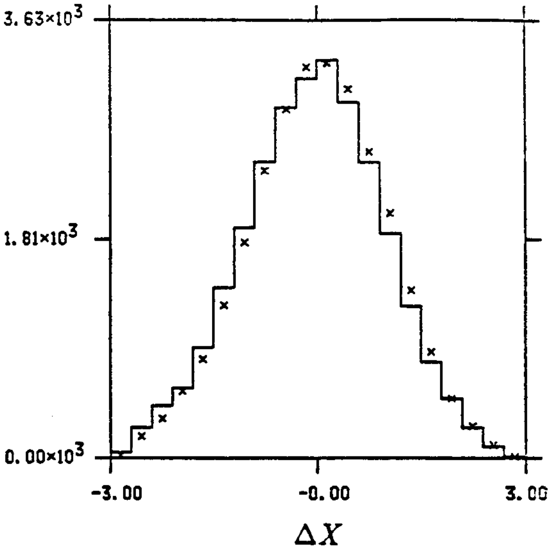

(.3 < X_F < .5)

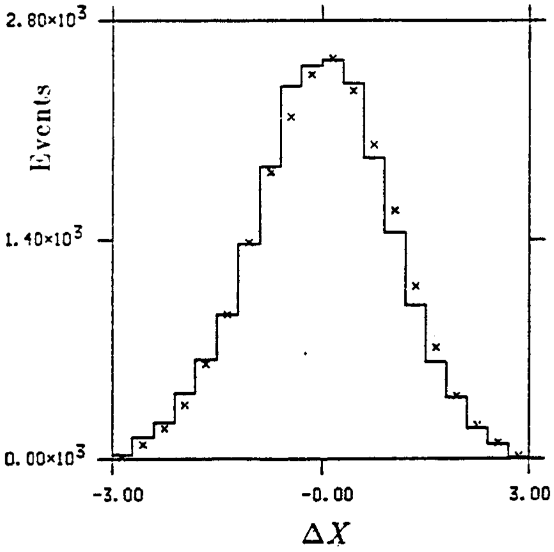

(.5 < X_F < .7)

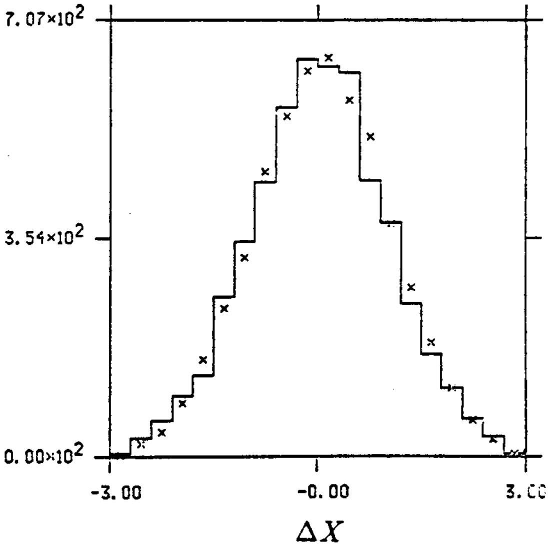

(.7 < X_F < .9)

Figure 37 -- Comparisons of the data (solid lines) and Monte Carlo (crosses) χ^2 probability distributions from the x and y vertex fits.

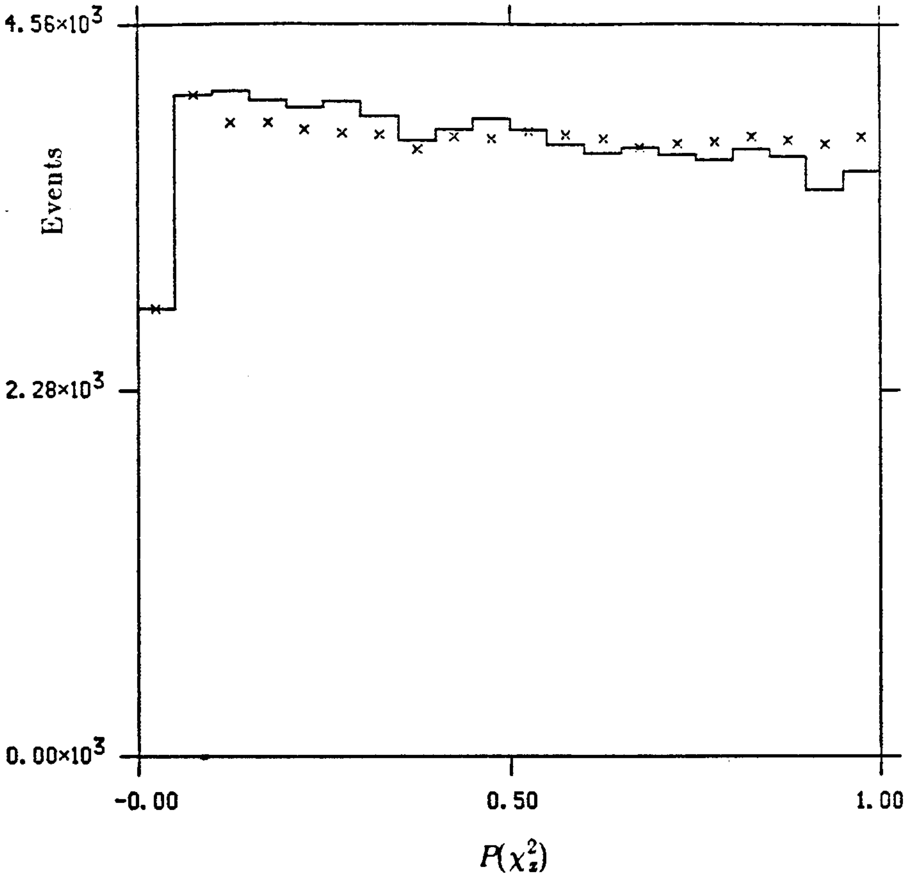
4.56×10^3
2.28×10^3
0.00×10^3
Events
-0.00
0.50
1.00
$P(\chi_z^2)$

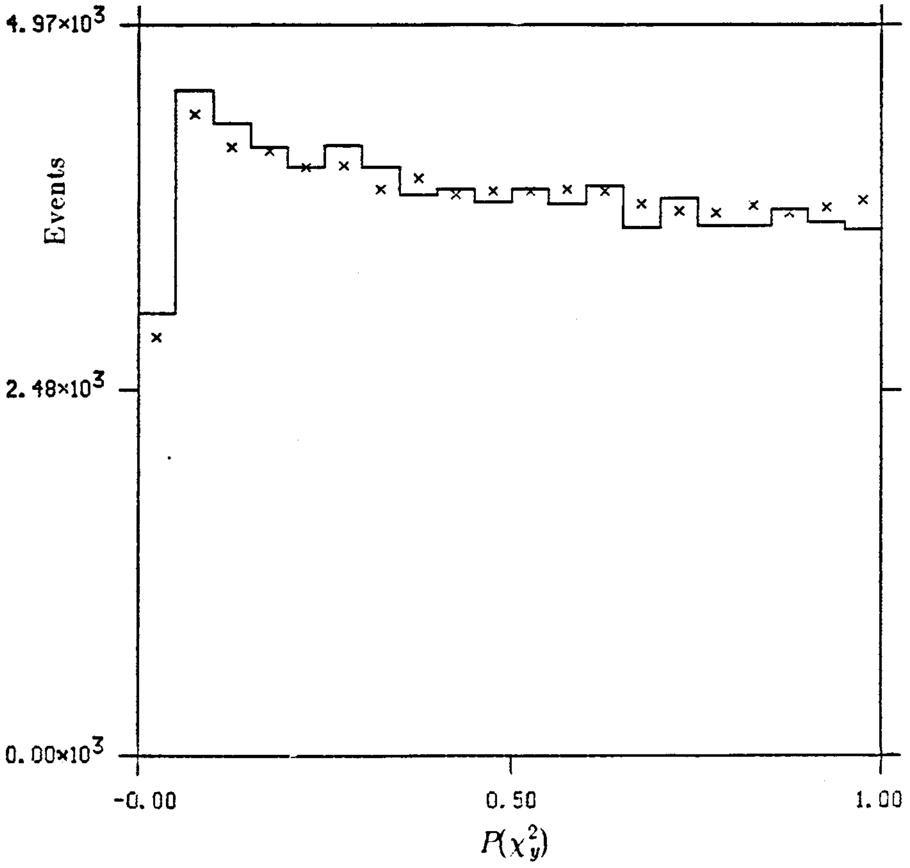
4.97×10^3
2.48×10^3
0.00×10^3
Events
-0.00
0.50
1.00
$P(\chi_y^2)$

Figure 38 -- Comparisons of the generated (gen.) and reconstructed (rec.) values of X_F, P_T, $\cos(\theta)$ and ϕ from a Monte Carlo simulation of J/ψ production and measurement.

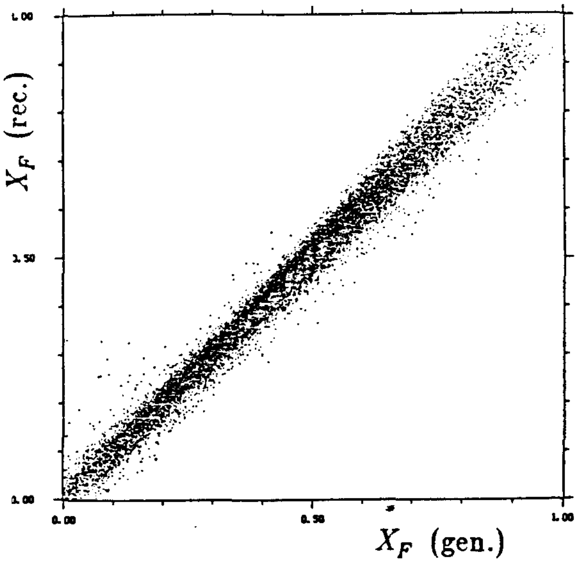
1.00
0.50
0.00
X_F (rec.)
0.00
0.50
1.00
X_F (gen.)

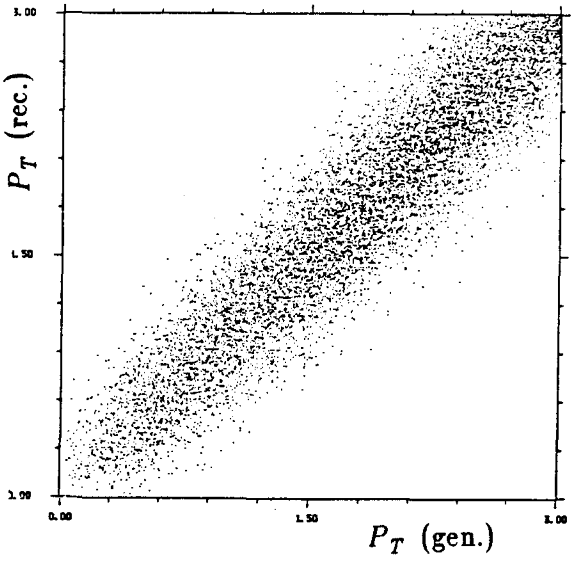
3.00
1.50
0.00
P_T (rec.)
0.00
1.50
3.00
P_T (gen.)

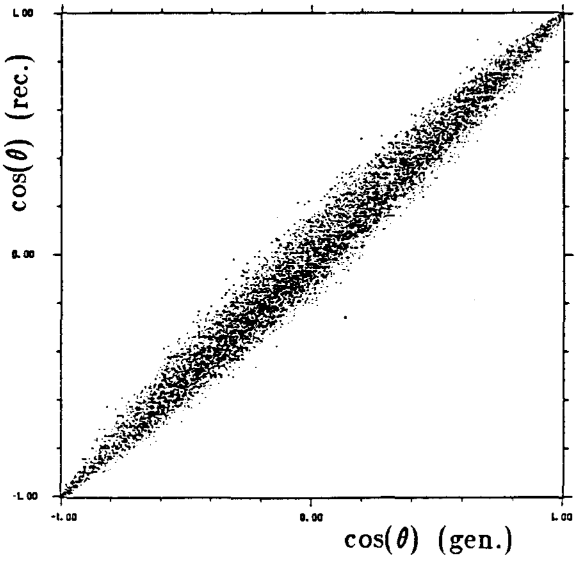
1.00
0.00
-1.00
cos(θ) (rec.)
-1.00
0.00
1.00
cos(θ) (gen.)

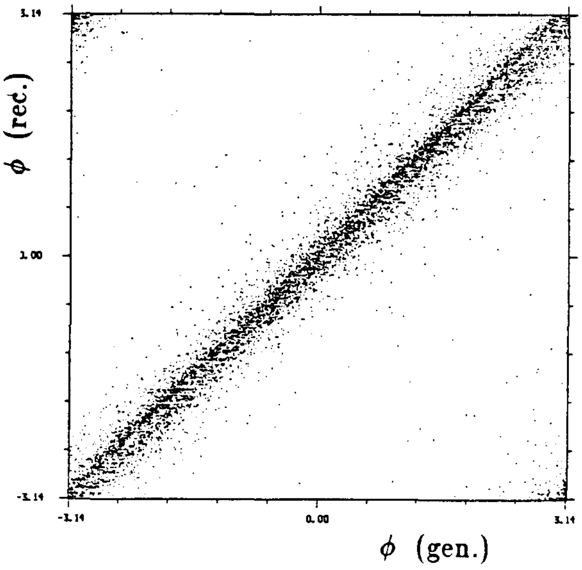
3.14
0.00
-3.14
ϕ (rec.)
-3.14
0.00
3.14
ϕ (gen.)

Figure 39 -- Comparisons of the data (solid lines) and Monte Carlo (crosses) hodoscope counter illuminations for $X_F > .1$ events. Each bin corresponds to one counter.

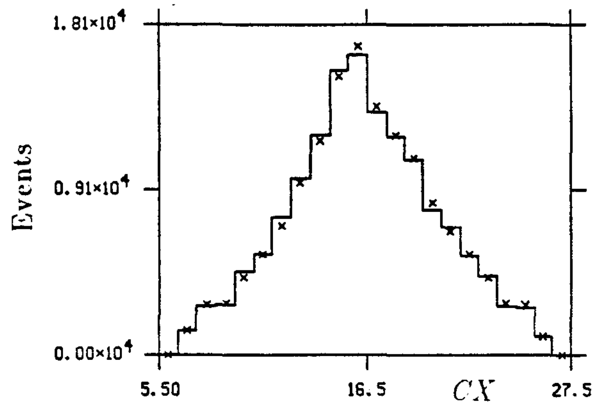
1.81×10⁴
0.91×10⁴
0.00×10⁴
Events
5.50
16.5
CX
27.5

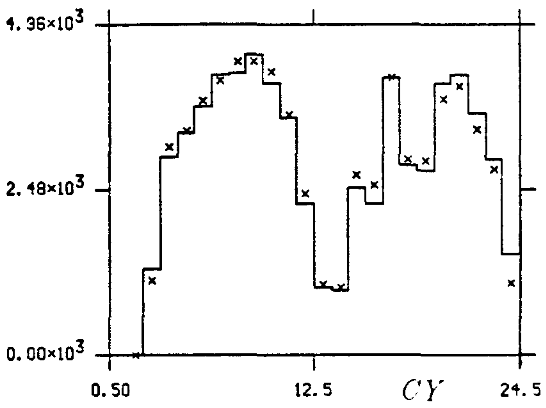
4.96×10³
2.48×10³
0.00×10³
0.50
12.5
CY
24.5

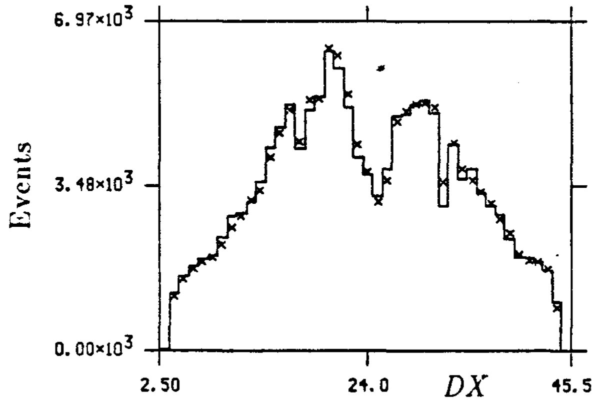
6.97×10³
3.48×10³
0.00×10³
Events
2.50
24.0
DX
45.5

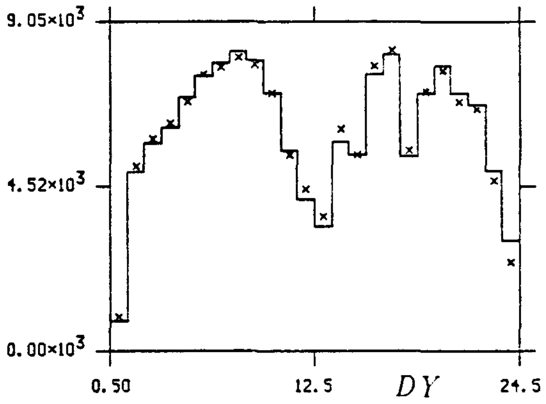
9.05×10³
4.52×10³
0.00×10³
0.50
12.5
DY
24.5

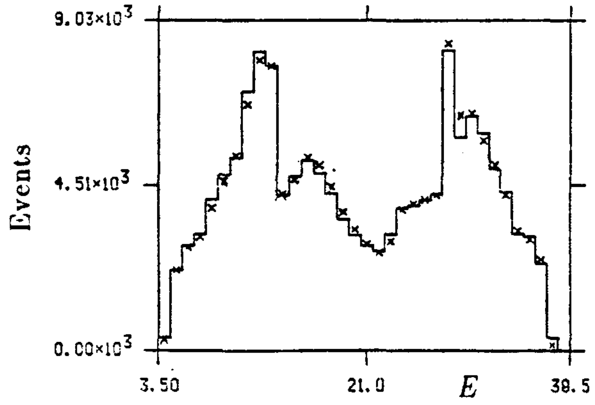
9.03×10³
4.51×10³
0.00×10³
Events
3.50
21.0
E
38.5

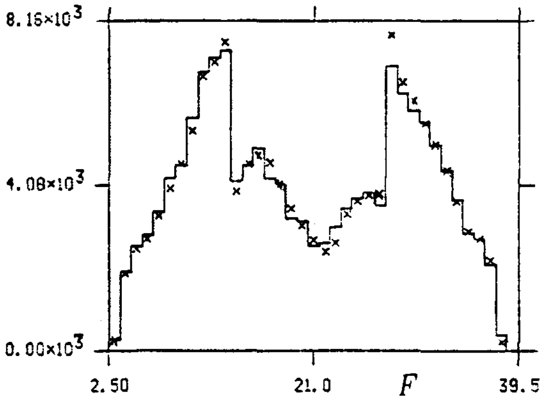
8.16×10³
4.08×10³
0.00×10³
2.50
21.0
F
39.5

Figure 40 -- Comparisons of the data (solid lines) and Monte Carlo (crosses) muon momentum and vertex angle distributions for $X_F > .1$ events.

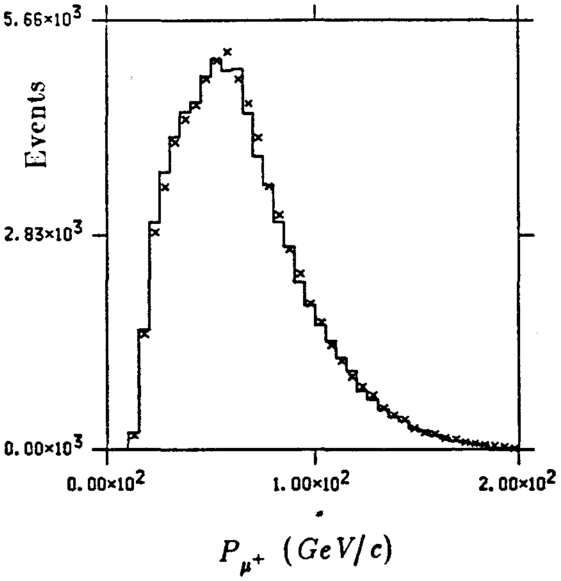
5.66×10³
2.83×10³
0.00×10³
Events
0.00×10²
1.00×10²
2.00×10²
P_{μ^+} (GeV/c)

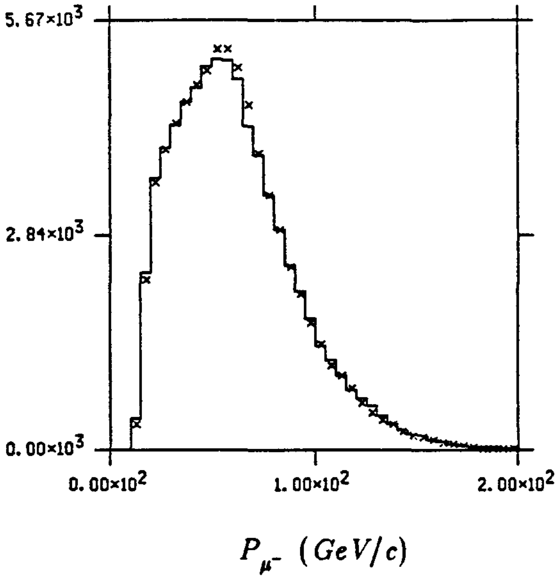
5.67×10³
2.84×10³
0.00×10³
0.00×10²
1.00×10²
2.00×10²
P_{μ^-} (GeV/c)

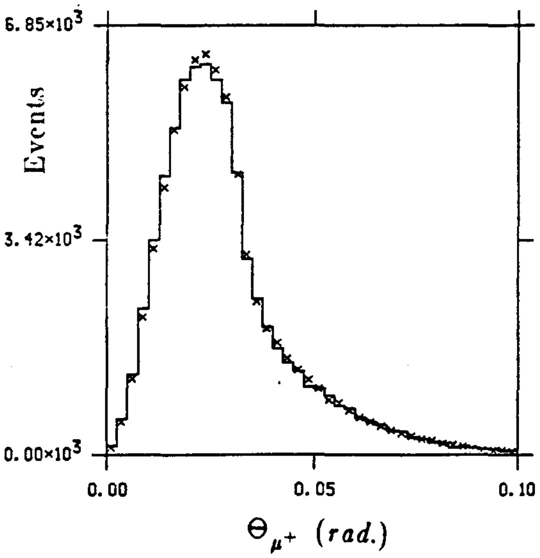
6.85×10³
3.42×10³
0.00×10³
Events
0.00
0.05
0.10
Θ_{μ^+} $(rad.)$

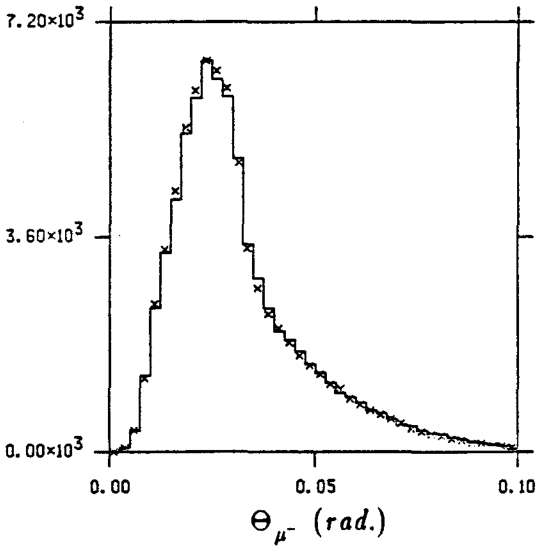
7.20×10³
3.60×10³
0.00×10³
0.00
0.05
0.10
Θ_{μ^-} $(rad.)$

Figure 41 -- Comparison of the data (solid lines) and the Monte Carlo (crosses) (a) z vertex distribution and (b) ratios of absorber to target event yields as a function of X_F. The box in the top plot indicates the target length and the arrow denotes the upstream end of the absorber in its final configuration.

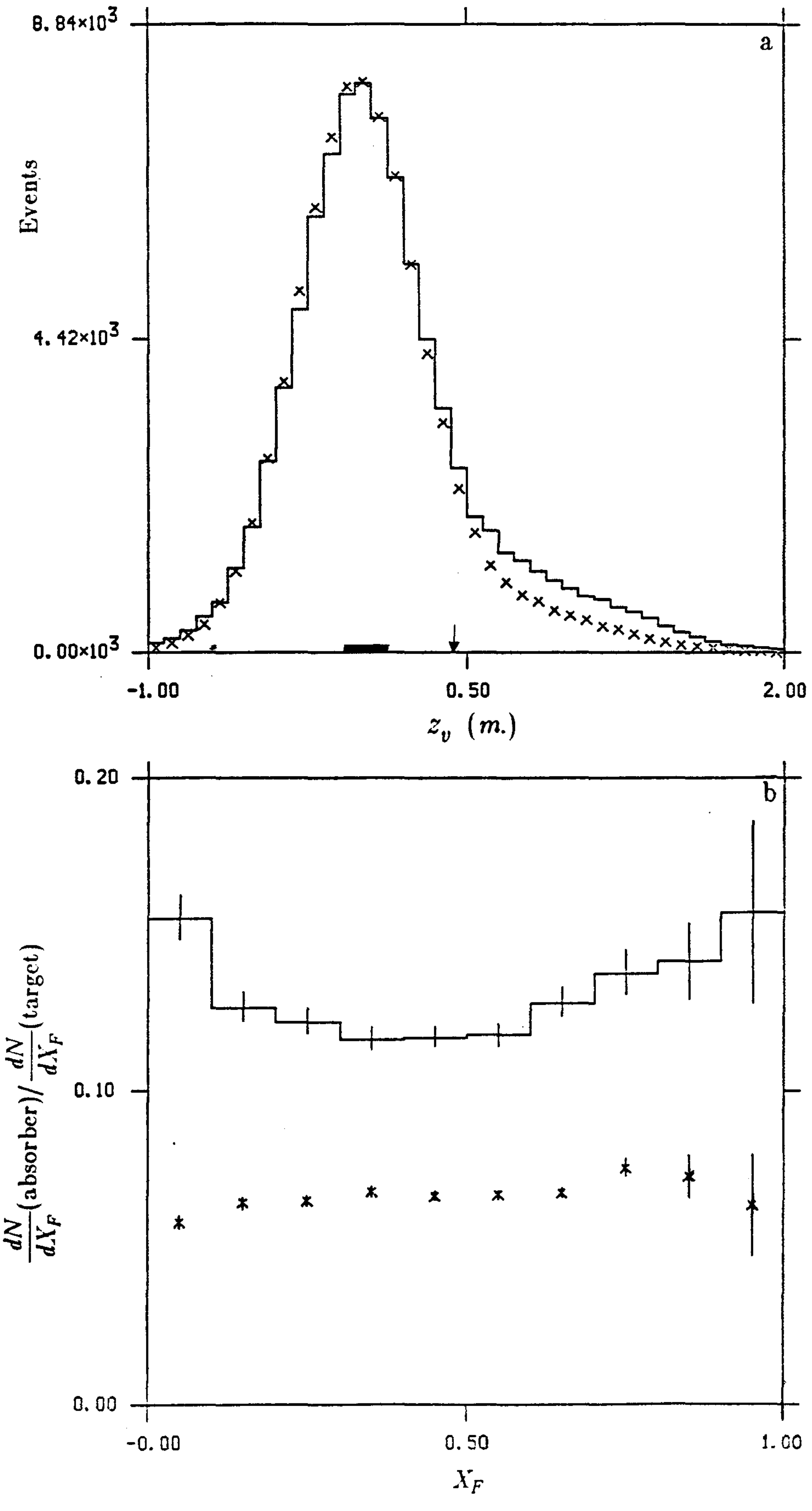
a
8.84×10^3
4.42×10^3
0.00×10^3
Events
-1.00
0.50
2.00
z_v (m.)
b
0.20
0.10
0.00
$\frac{dN}{dX_F}$(absorber)/$\frac{dN}{dX_F}$(target)
-0.00
0.50
1.00
X_F

Figure 42 -- (a) The X_F distribution of J/ψ events uncorrected for acceptance and (b) the X_F dependence of the acceptance. The regions outside the dotted lines were excluded from the differential cross section calculations.

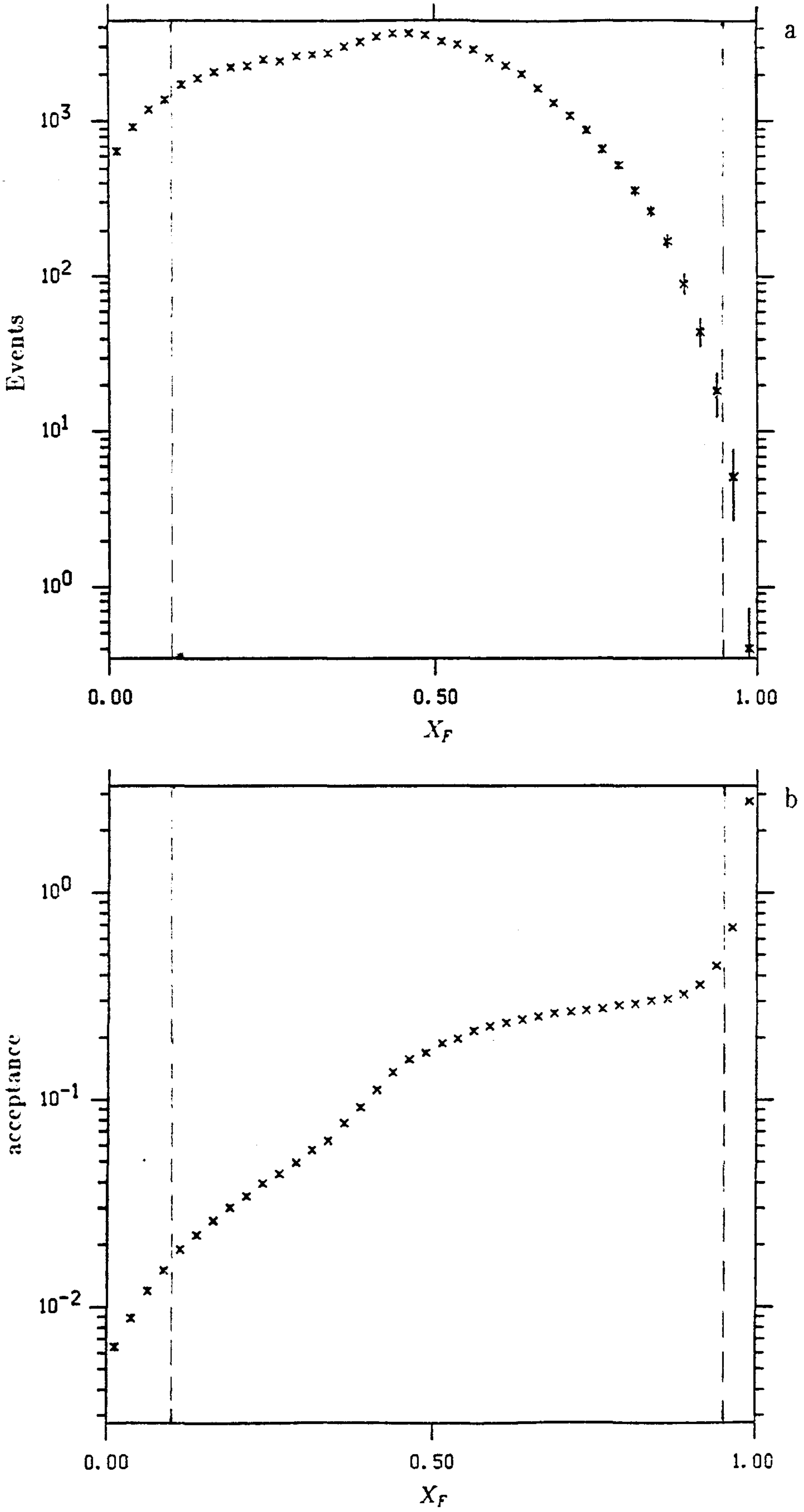
a
Events
10^3
10^2
10^1
10^0
0.00
0.50
1.00
X_F
b
acceptance
10^0
10^{-1}
10^{-2}
0.00
0.50
1.00
X_F

Figure 43 -- $B_{\mu^+\mu^-}\cdot d\sigma/dX_F$ in four regions of P_T^2. The solid curves are the results of fits to the data of the form $A\cdot(1-X_F)^C$. The values of C obtained are listed below.

	Plot	C
all P_T^2	a	$2.77 \pm .01$
$P_T^2 < .6$	b	$2.45 \pm .02$
$.6 < P_T^2 < 2.6$	c	$2.86 \pm .02$
$P_T^2 > 2.6$	d	$3.20 \pm .03$

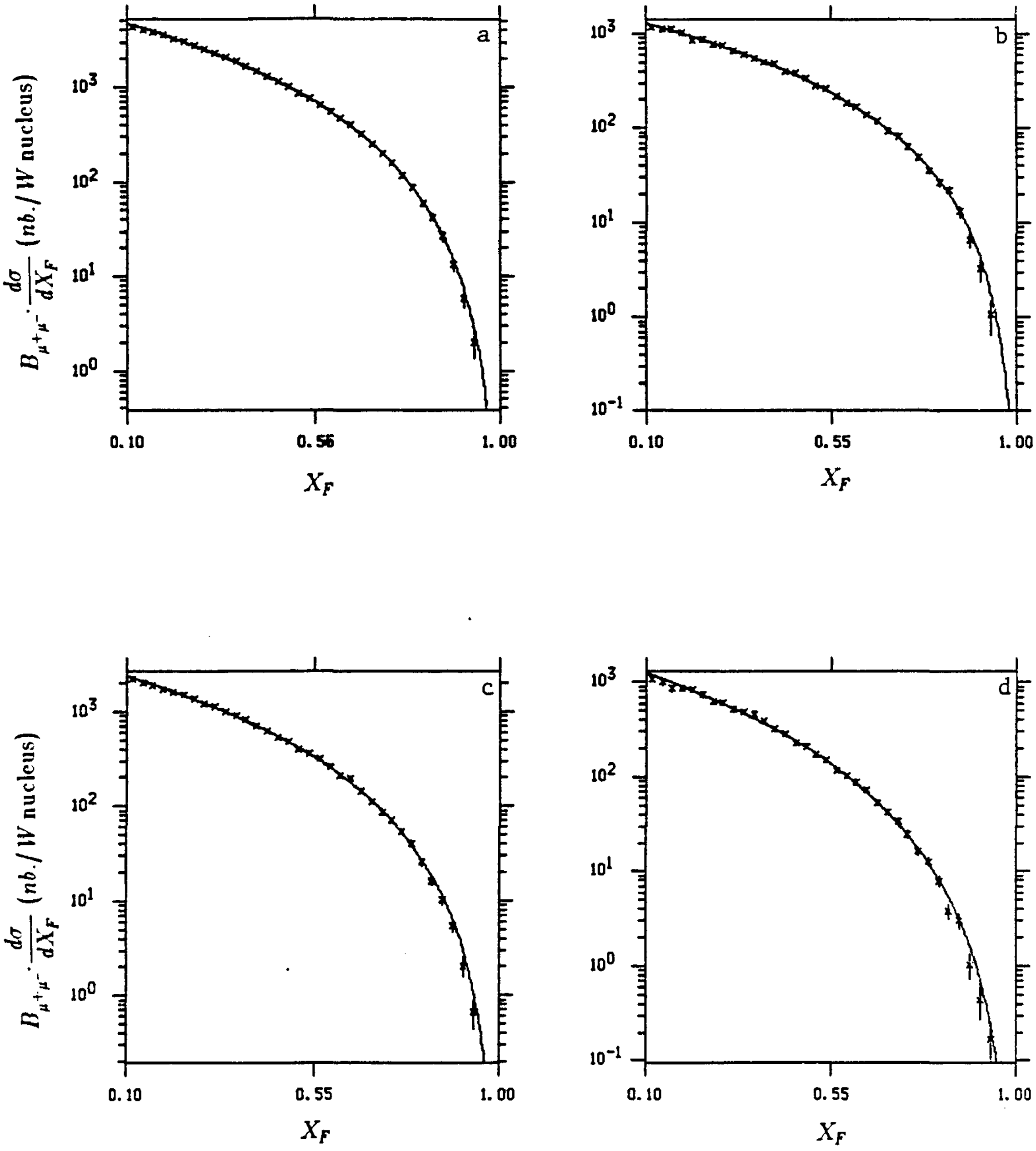
a
b
c
d
$B_{\mu^+\mu^-} \cdot \frac{d\sigma}{dX_F}$ (nb./W nucleus)
10^{-1}
10^0
10^1
10^2
10^3
0.10
0.56
0.55
1.00
X_F

Figure 44 -- The variation of C with P_T^2. The values of C were obtained from fitting the X_F cross sections in each bin of P_T^2 to the form $A\cdot(1 - X_F)^C$.

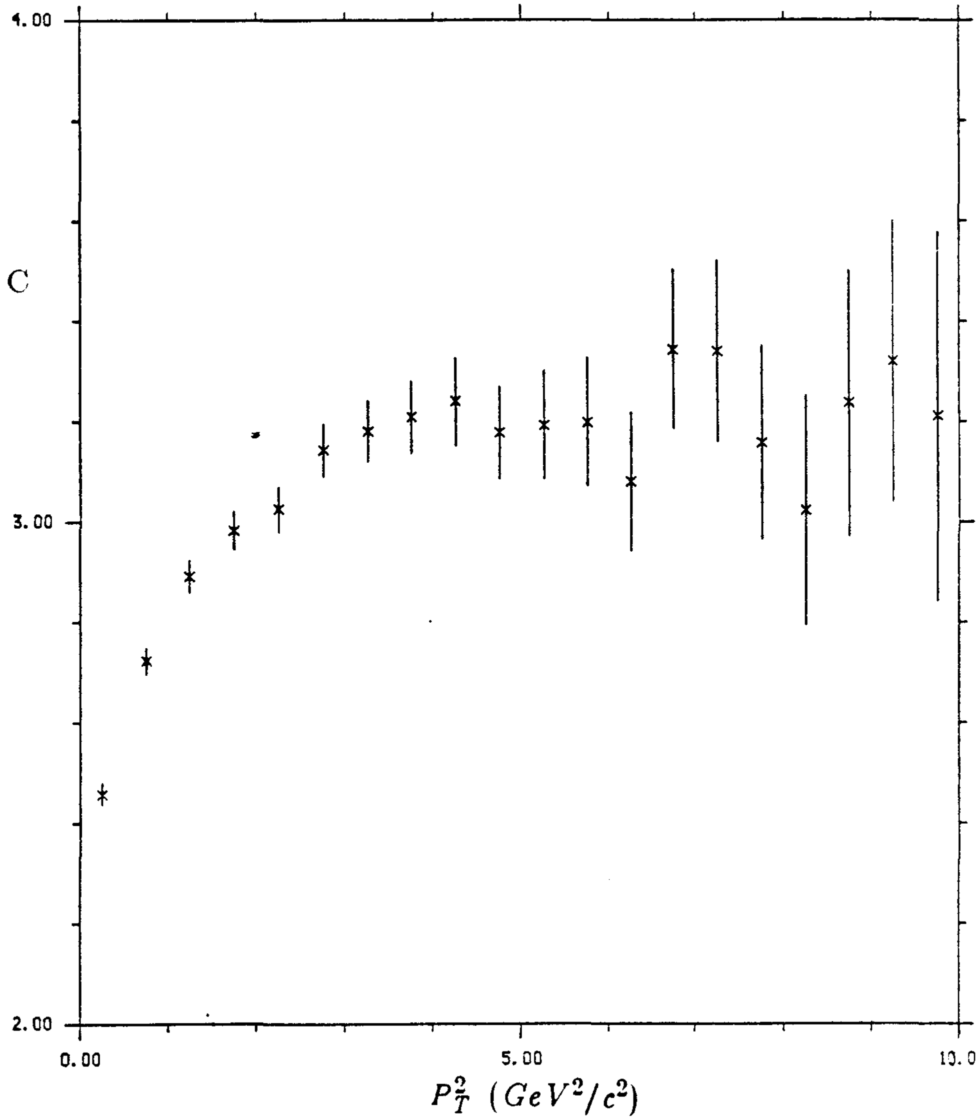
4.00
3.00
2.00
C
0.00
5.00
10.0
P_T^2 (GeV^2/c^2)

Figure 45 -- The acceptance as a function of P_T^2 in eight regions of X_F.

a) $.1 < X_F < .2$	b) $.2 < X_F < .3$
c) $.3 < X_F < .4$	d) $.4 < X_F < .5$
e) $.5 < X_F < .6$	f) $.6 < X_F < .7$
g) $.7 < X_F < .8$	h) $.8 < X_F < .9$

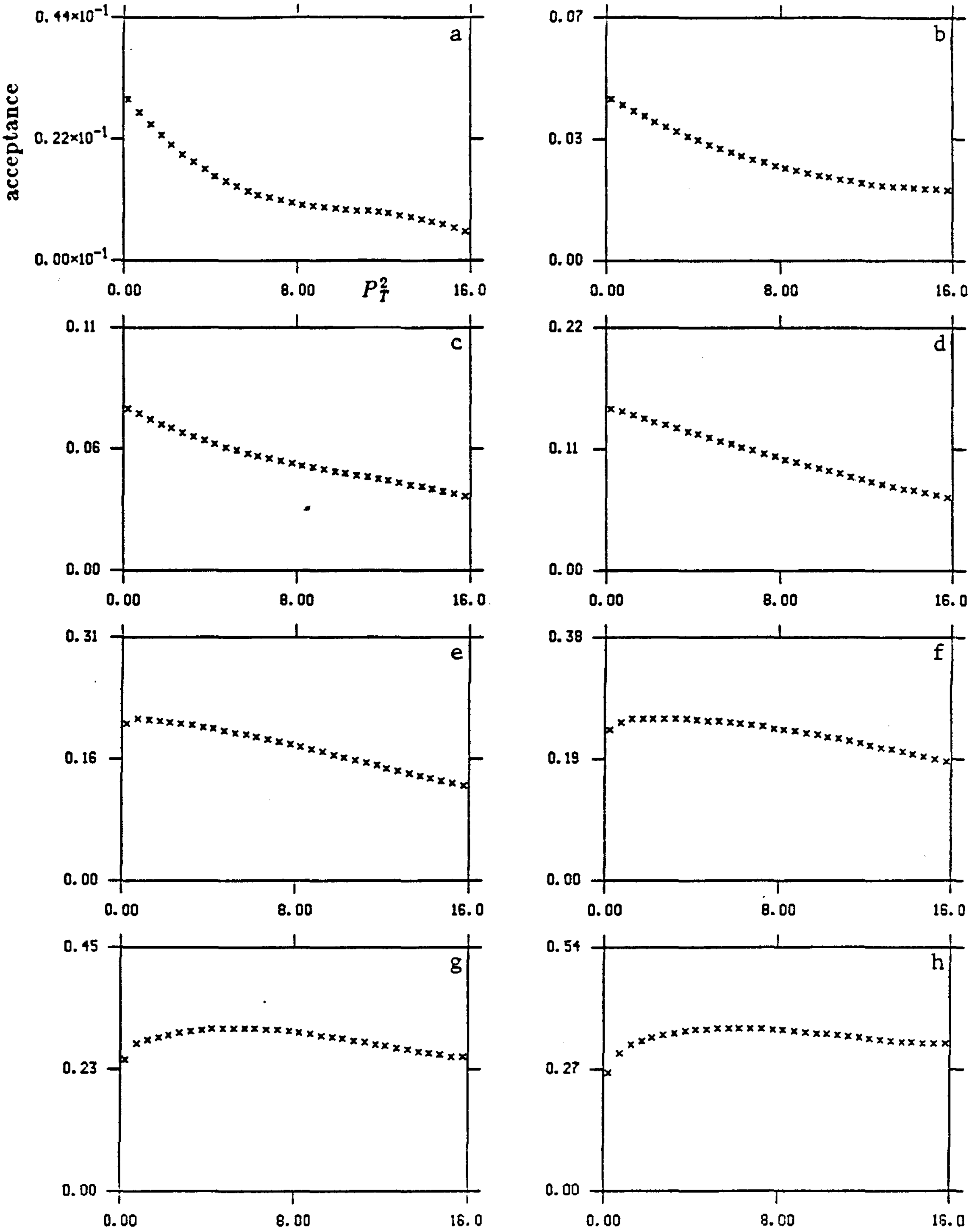
acceptance
P_T^2
a
0.44×10⁻¹
0.22×10⁻¹
0.00×10⁻¹
0.00
8.00
16.0
b
0.07
0.03
0.00
c
0.11
0.06
0.00
d
0.22
0.11
0.00
e
0.31
0.16
0.00
f
0.38
0.19
0.00
g
0.45
0.23
0.00
h
0.54
0.27
0.00

Figure 46 -- $B_{\mu^+\mu^-} \cdot d\sigma^2 / dX_F dP_T^2$ in eight regions of X_F. The solid curves are the result of an empirical fit to the data that is described in the text.

a) $.1 < X_F < .2$ b) $.2 < X_F < .3$
c) $.3 < X_F < .4$ d) $.4 < X_F < .5$
e) $.5 < X_F < .6$ f) $.6 < X_F < .7$
g) $.7 < X_F < .8$ h) $.8 < X_F < .9$

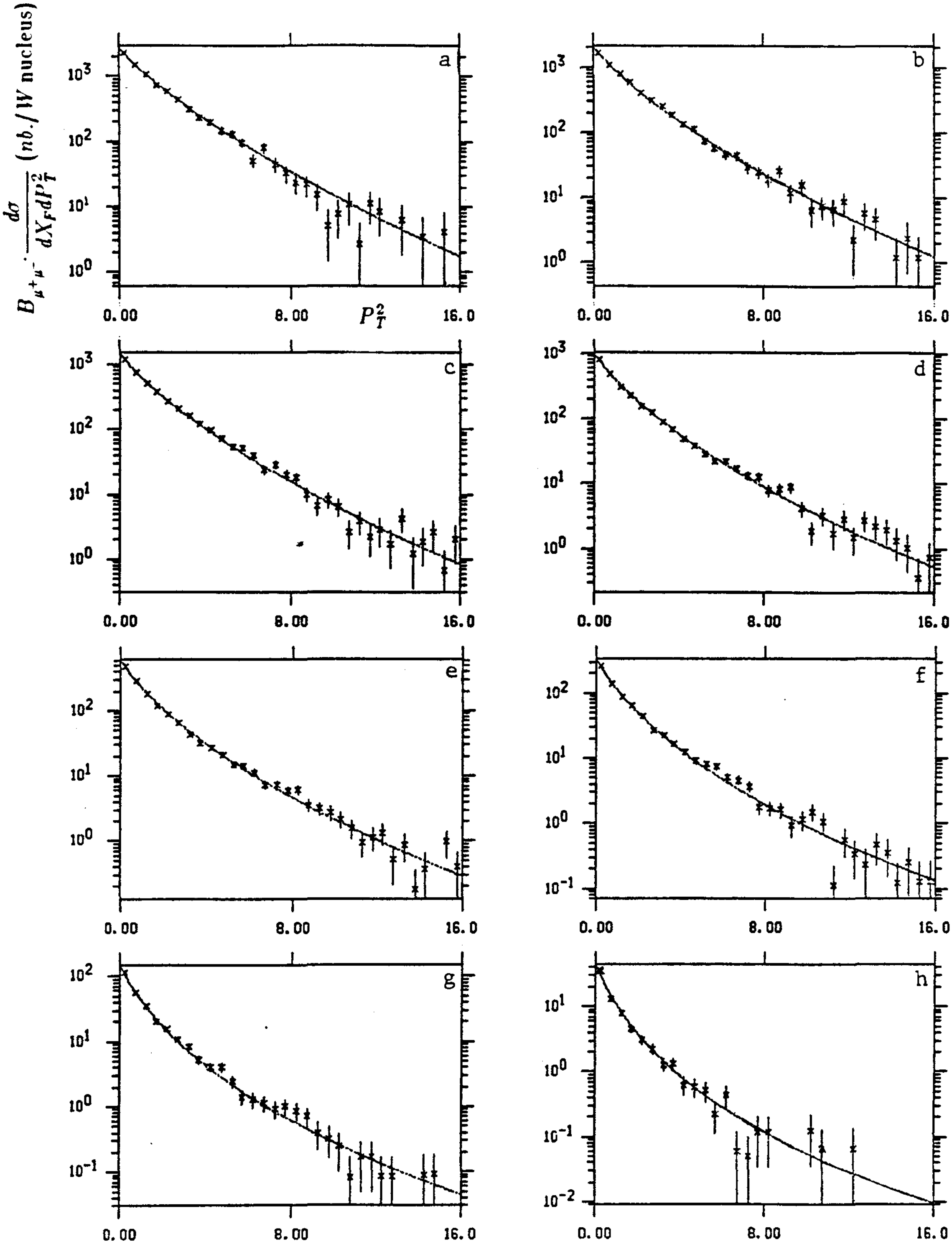
$B_{\mu^+\mu^-} \cdot \frac{d\sigma}{dX_F dP_T^2}$ (nb./W nucleus)
P_T^2
a
b
c
d
e
f
g
h
10^3
10^2
10^1
10^0
10^{-1}
10^{-2}
0.00
8.00
16.0

Figure 47 -- Plots of $<P_T>$ and $<P_T^2>$ as a function of X_F.

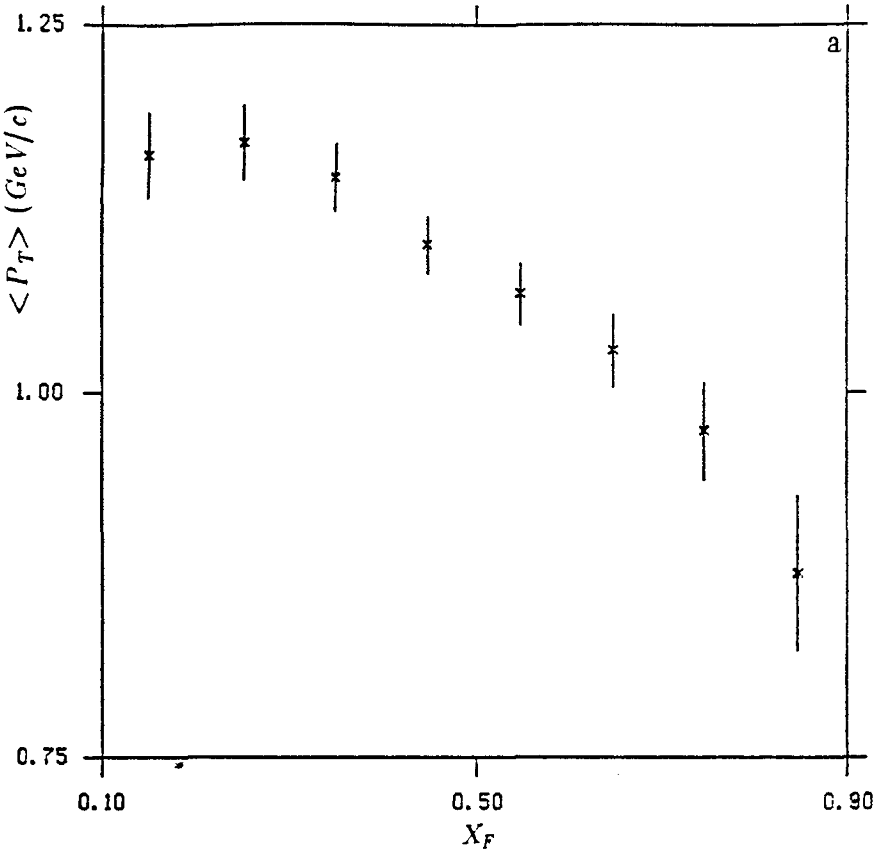
a
1.25
1.00
0.75
$<P_T>$ (GeV/c)
0.10
0.50
0.90
X_F

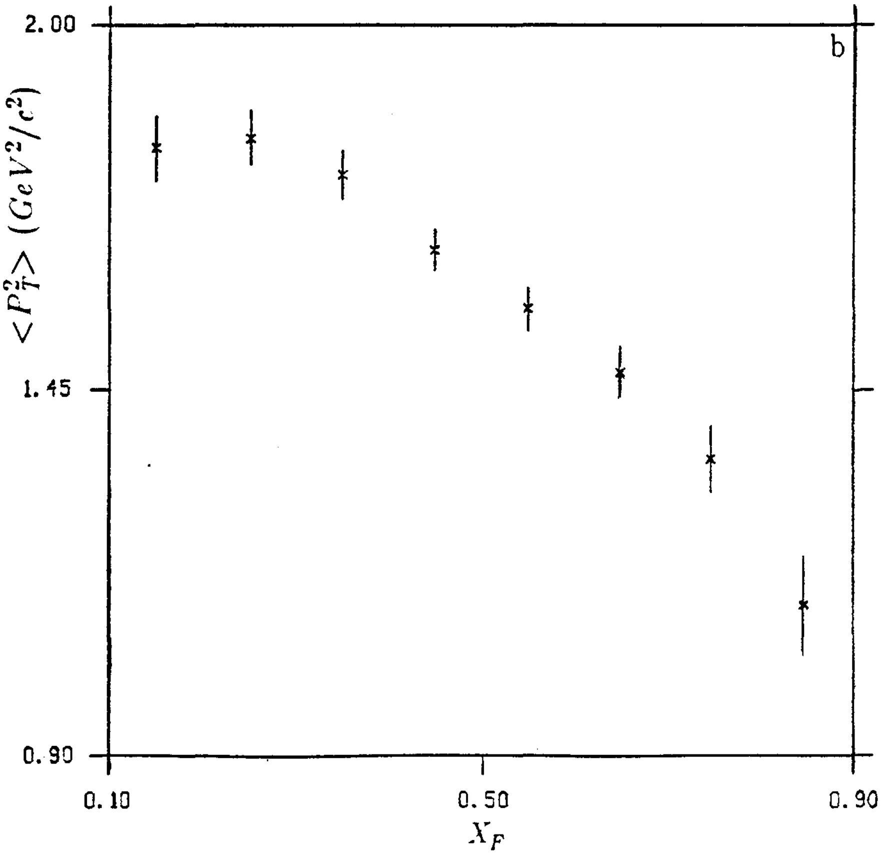
b
2.00
1.45
0.90
$<P_T^2>$ (GeV^2/c^2)
0.10
0.50
0.90
X_F

Figure 48 -- (a) The absorber to target cross section ratio as function of P_T^2. The fit to the data (solid curve) is described in the text. (b) The crosses show the P_T^2 dependence of the nucleon to tungsten cross section ratio predicted from the E444 measurements. The solid curve is the variation expected from this experiment and was normalized to the data points by eye.

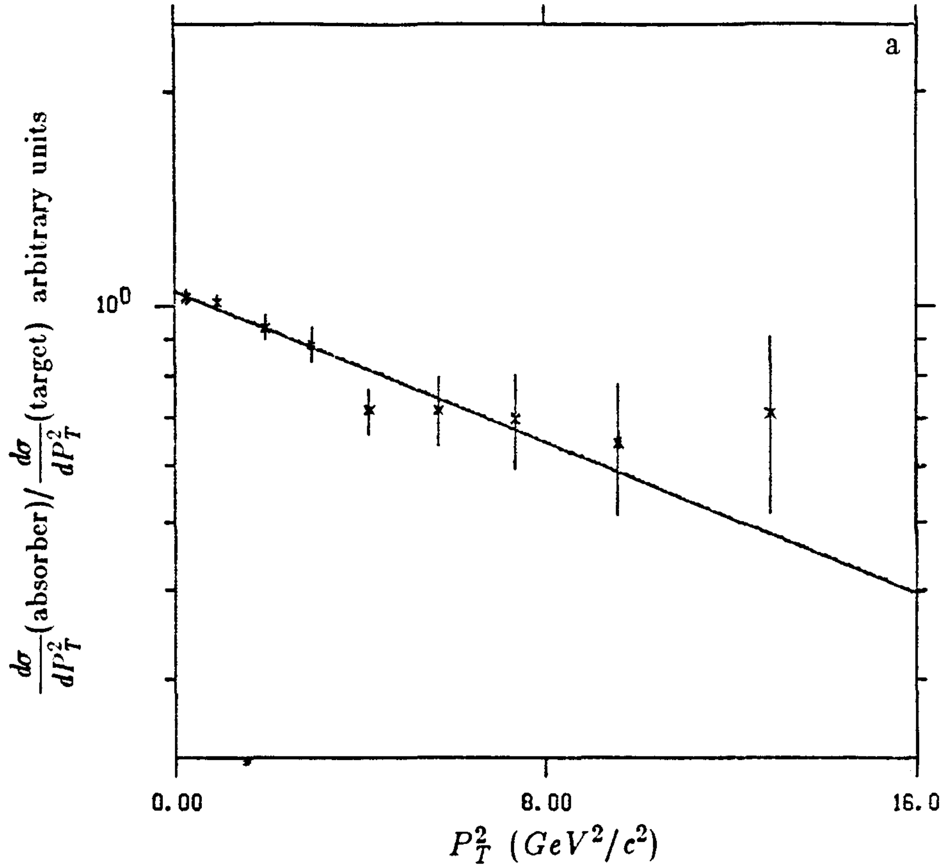
a
10^0
$\frac{d\sigma}{dP_T^2}$(absorber)/$\frac{d\sigma}{dP_T^2}$(target) arbitrary units
0.00
8.00
16.0
P_T^2 (GeV^2/c^2)

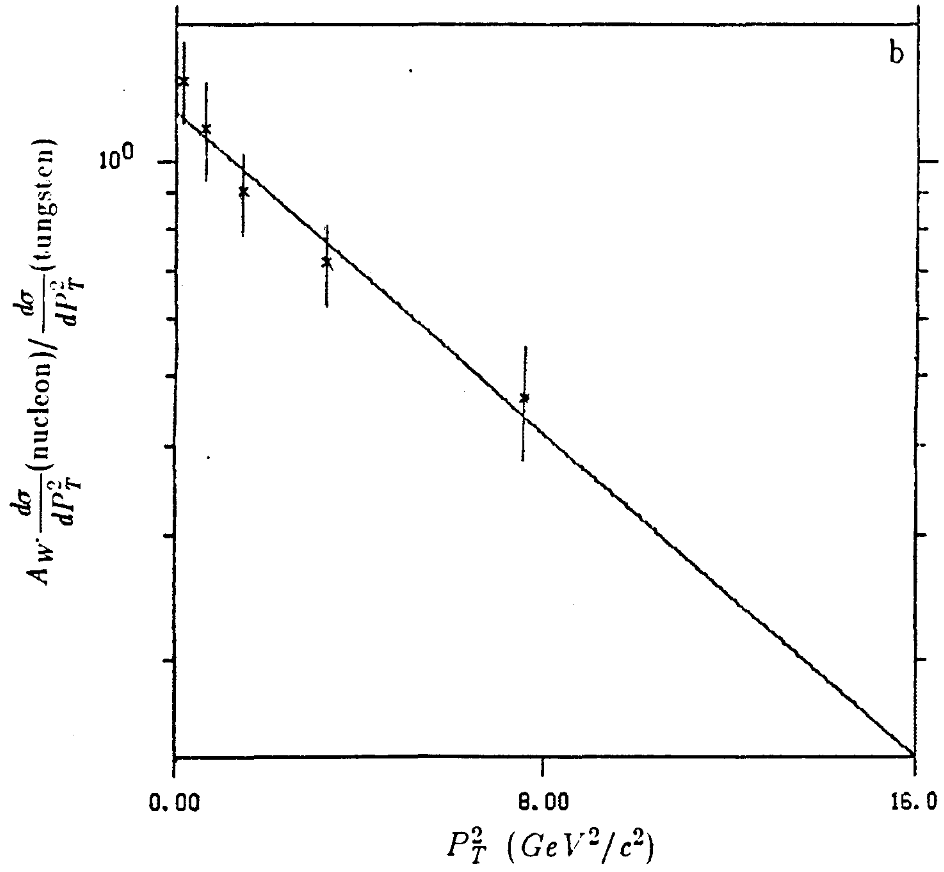
b
10^0
$A_W \cdot \frac{d\sigma}{dP_T^2}$(nucleon)/$\frac{d\sigma}{dP_T^2}$(tungsten)
0.00
8.00
16.0
P_T^2 (GeV^2/c^2)

Figure 49 -- $B_{\mu^+\mu^-} \cdot \sigma(X_F > 0)$ as a function of the pion beam momentum. The sources of the data are given in reference 66 (our result is indicated by the circle). The curves are the fusion model predictions where the sum of the gluon and quark contributions was normalized to the data by eye.

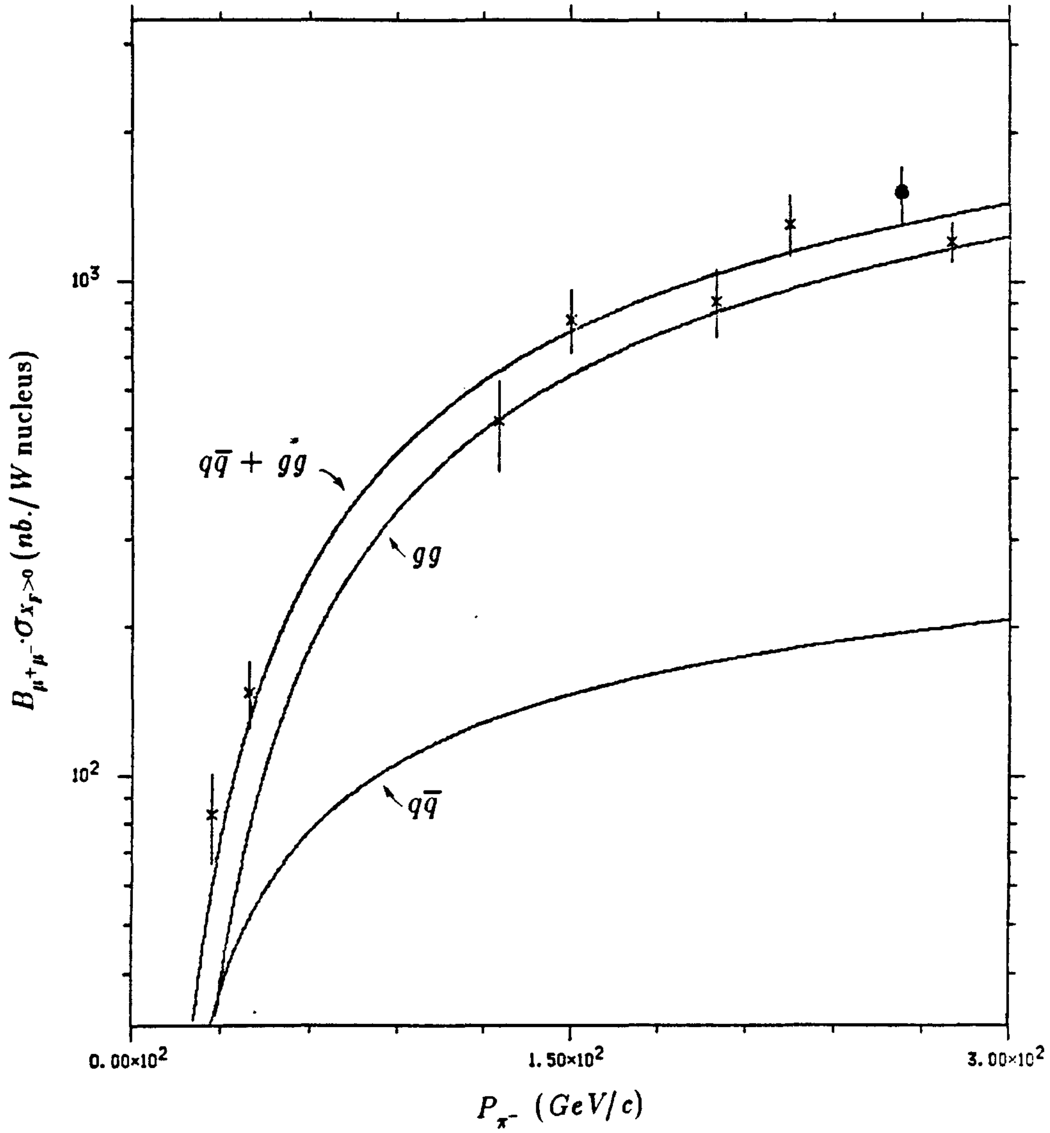
$B_{\mu^+\mu^-} \cdot \sigma_{x_F>0}$ (nb./W nucleus)
10^3
10^2
$q\bar{q} + \overset{*}{g}g$
gg
$q\bar{q}$
0.00×10²
1.50×10²
3.00×10²
P_{π^-} (GeV/c)

Figure 50 -- Fusion model fit to $B_{\mu^+\mu^-} \cdot d\sigma/dX_F$. The curves show the total and individual contributions from the charmonium states.

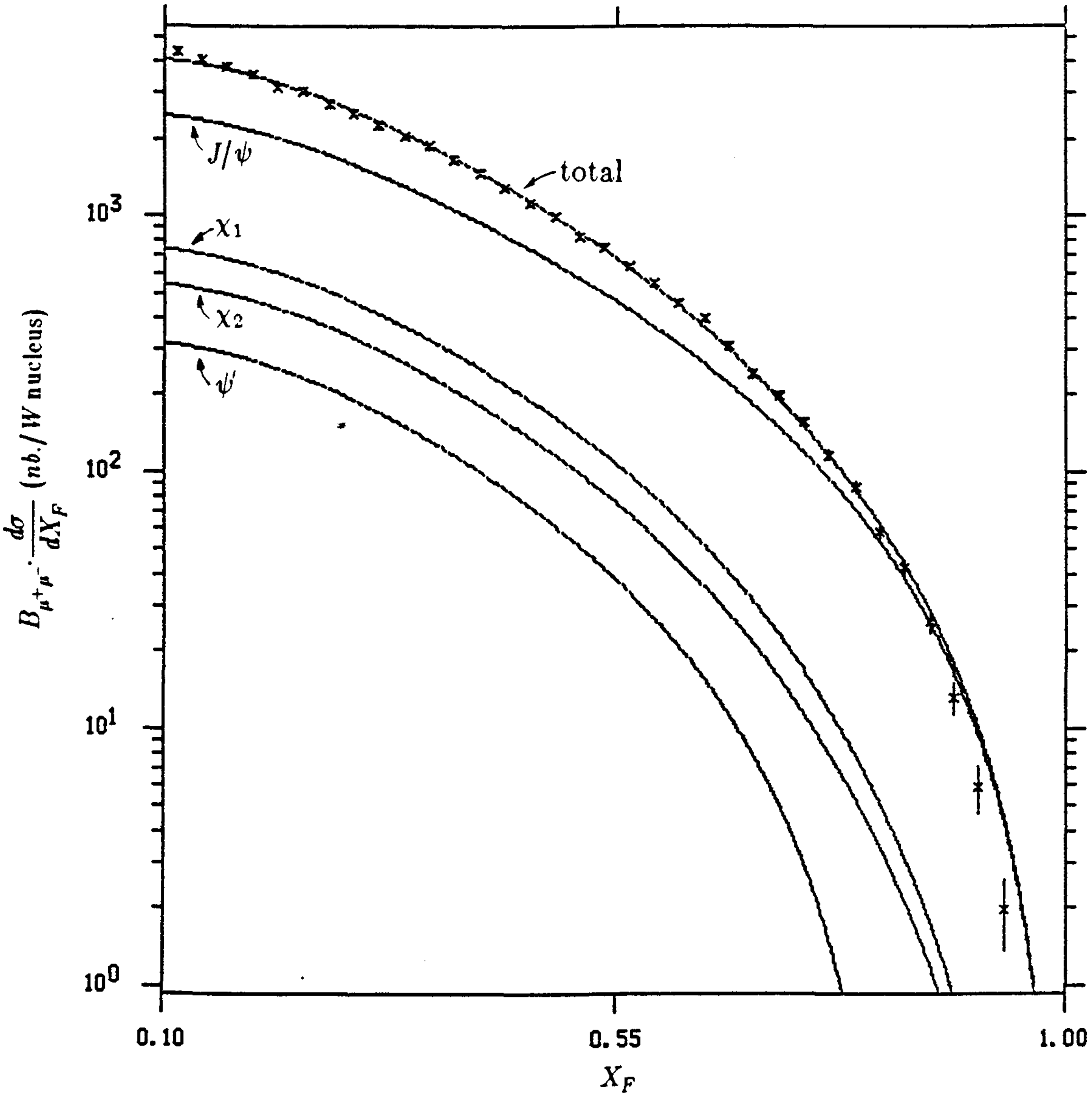
total
J/ψ
χ1
χ2
ψ'
10³
10²
10¹
10⁰
0.10
0.55
1.00
X_F
$B_{\mu^+\mu^-} \cdot \frac{d\sigma}{dX_F}$ (nb./W nucleus)

Figure 51 -- The pion (x_π) and nucleon (x_n) momentum fractions as a function of X_F. These curves were derived from the fusion constraint equations with $\tau = M^2_{J/\psi}/S_o$.

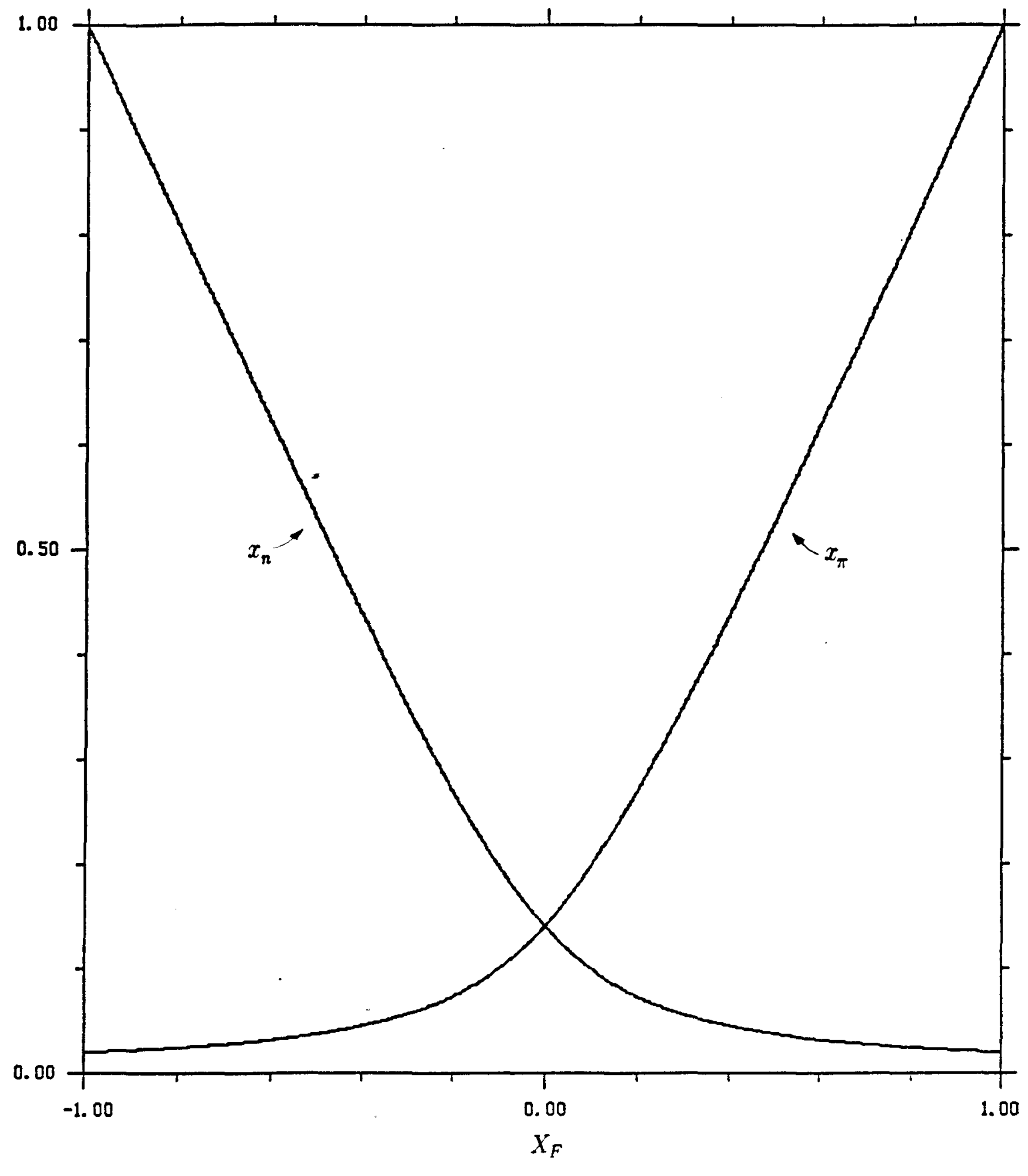
1.00
0.50
0.00
-1.00
0.00
1.00
X_F
x_n
x_π

Figure 52 -- Fusion model fit to $B_{\mu^+\mu^-} \cdot d\sigma/dX_F$ with R_K fixed to 1.4 and n_n to 6.3 . The curves show the total and individual contributions from quark and gluon fusion.

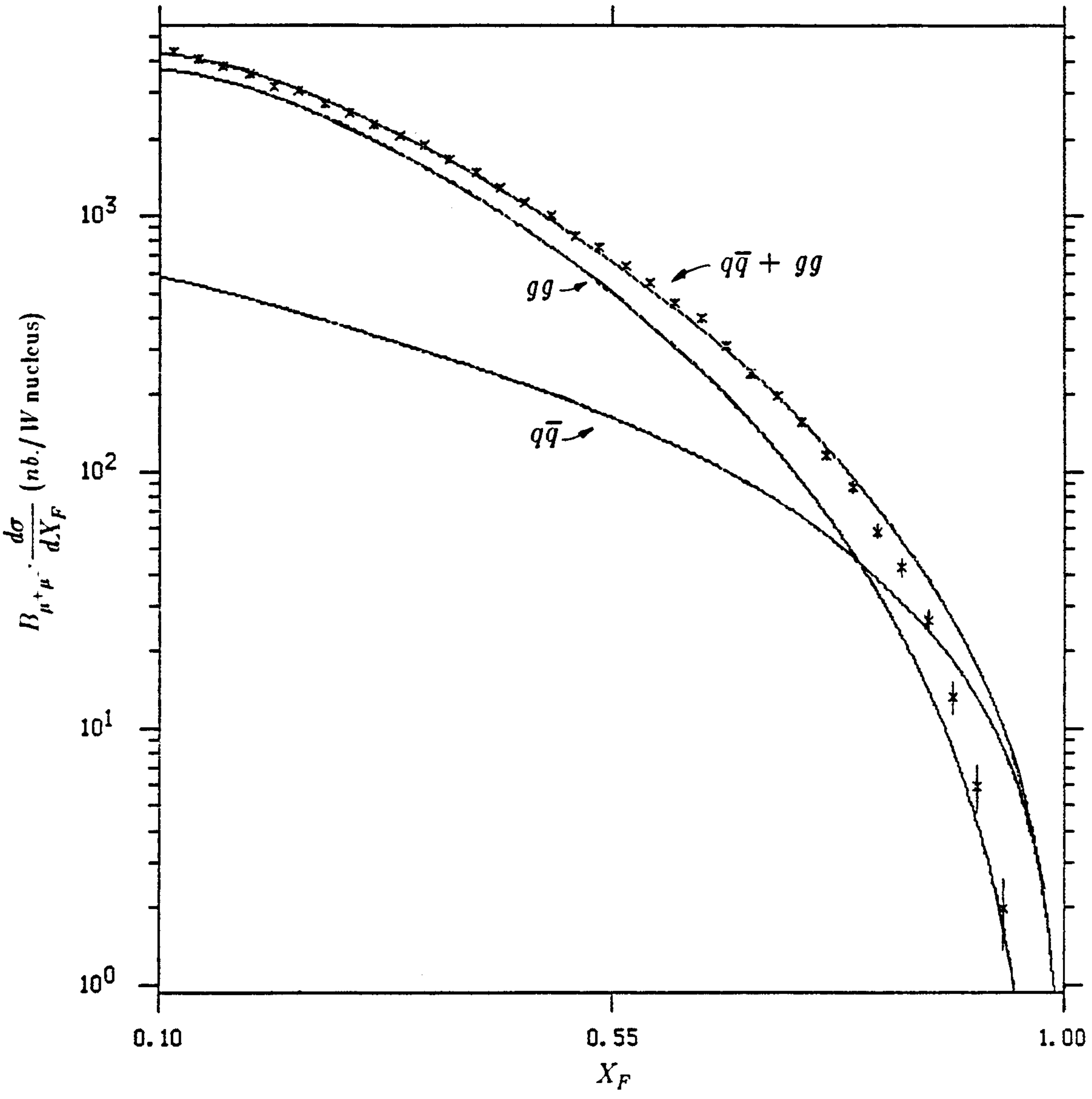
10^3
10^2
10^1
10^0
0.10
0.55
1.00
X_F
$B_{\mu^+\mu^-} \cdot \frac{d\sigma}{dX_F}$ (nb./W nucleus)
$q\bar{q} + gg$
gg
$q\bar{q}$

Figure 53 -- Gluon radiation model fit to $B_{\mu^+\mu^-} d\sigma^2/dX_F dP_T^2$ assuming $b = 1$. Only the data above $P_T^2 = 1.5\ GeV^2/c^2$ (third bin) is used in the fit because of the divergence of the prediction at low P_T^2.

a) $.1 < X_F < .2$ b) $.2 < X_F < .3$
c) $.3 < X_F < .4$ d) $.4 < X_F < .5$
e) $.5 < X_F < .6$ f) $.6 < X_F < .7$
g) $.7 < X_F < .8$ h) $.8 < X_F < .9$

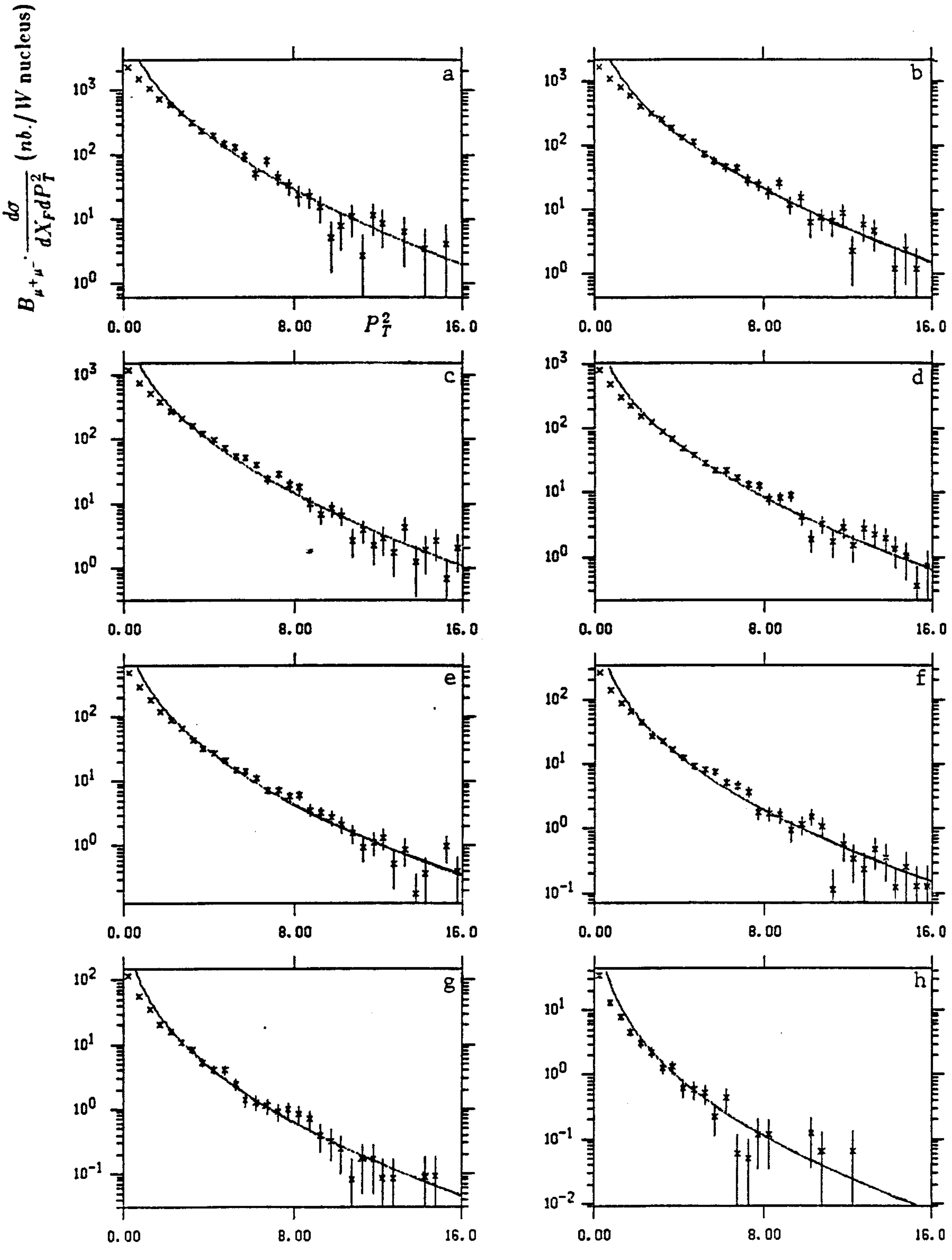
$B_{\mu^+\mu^-} \cdot \frac{d\sigma}{dX_F dP_T^2}$ (nb./W nucleus)
P_T^2
a
b
c
d
e
f
g
h
10³
10²
10¹
10⁰
10⁻¹
10⁻²
0.00
8.00
16.0

Figure 54 -- Gluon radiation model fit to $B_{\mu^+\mu^-} \cdot d\sigma^2 / dX_F dP_T^2$ assuming $b = .92 + .025 \cdot P_T^2$. Only the data above $P_T^2 = 1.5\ GeV^2/c^2$ (third bin) is used in the fit because of the divergence of the prediction at low P_T^2.

a) $.1 < X_F < .2$ b) $.2 < X_F < .3$
c) $.3 < X_F < .4$ d) $.4 < X_F < .5$
e) $.5 < X_F < .6$ f) $.6 < X_F < .7$
g) $.7 < X_F < .8$ h) $.8 < X_F < .9$

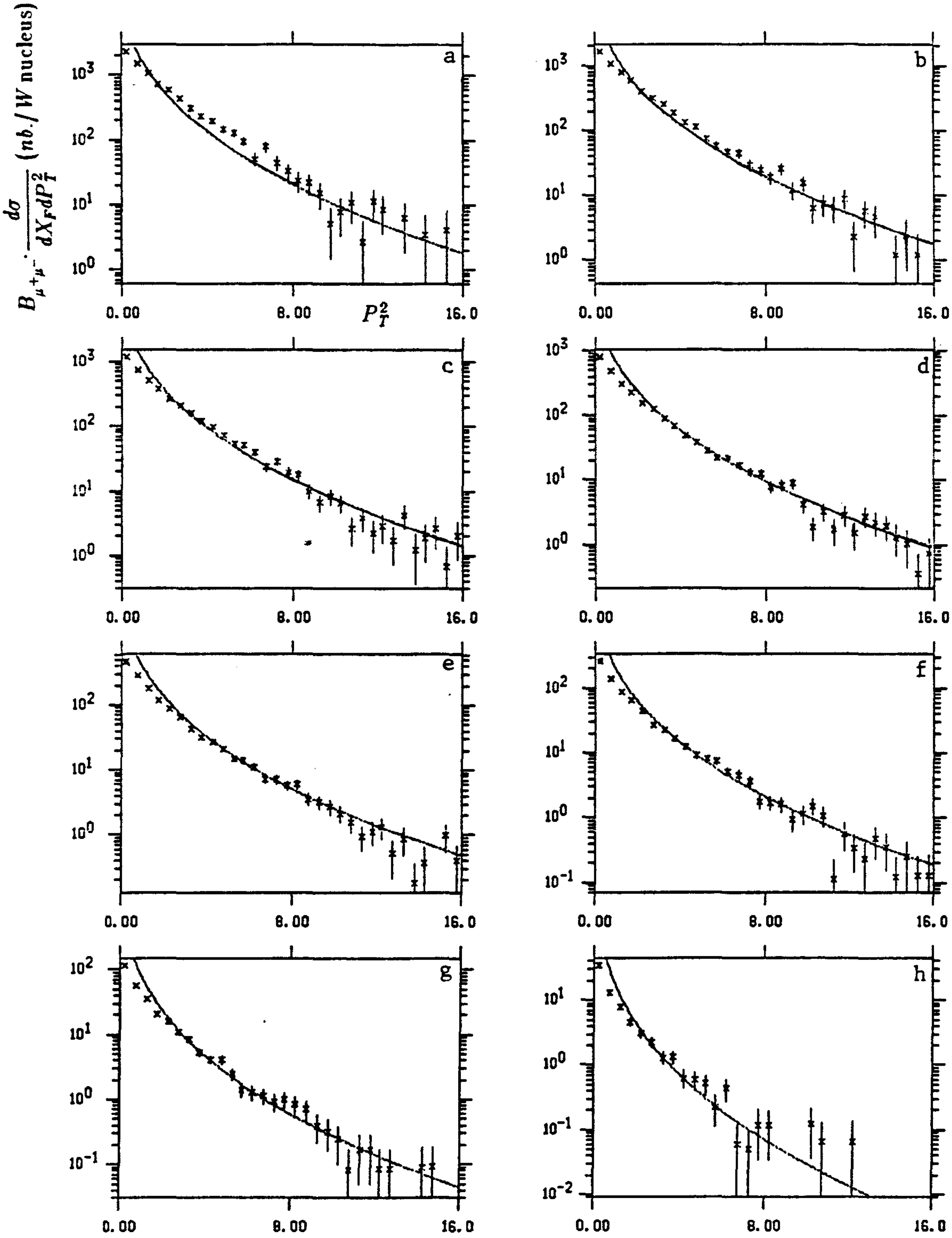
$B_{\mu^+\mu^-} \cdot \frac{d\sigma}{dX_F dP_T^2}$ (nb./W nucleus)
P_T^2
a
b
c
d
e
f
g
h
10^{3}
10^{2}
10^{1}
10^{0}
10^{-1}
10^{-2}
0.00
8.00
16.0

Figure 55 -- Event distributions in $\cos(\theta)$ and ϕ in four regions of X_F and P_T^2.

a) $.1 < X_F < .5 \quad P_T^2 < 4.5\ GeV^2/c^2$
b) $.5 < X_F < .9 \quad P_T^2 < 4.5\ GeV^2/c^2$
c) $.1 < X_F < .5 \quad P_T^2 > 4.5\ GeV^2/c^2$
d) $.5 < X_F < .9 \quad P_T^2 > 4.5\ GeV^2/c^2$

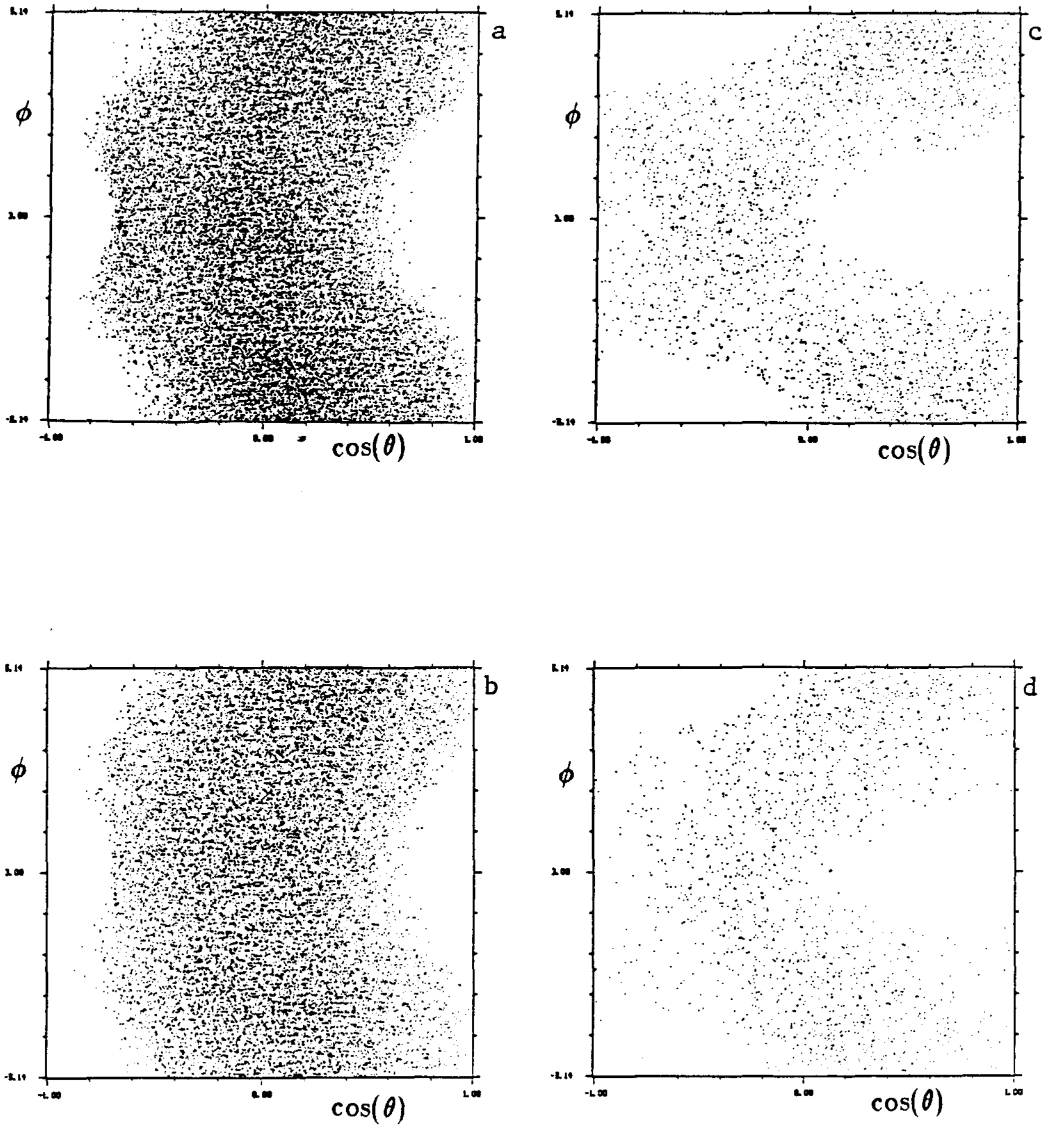
a
b
c
d
φ
cos(θ)
3.14
0.00
-3.14
-1.00
0.00
1.00

Figure 56 -- The results of fits for α, β and γ as a function of X_F in four P_T^2 regions. The curves are the gluon radiation model predictions.

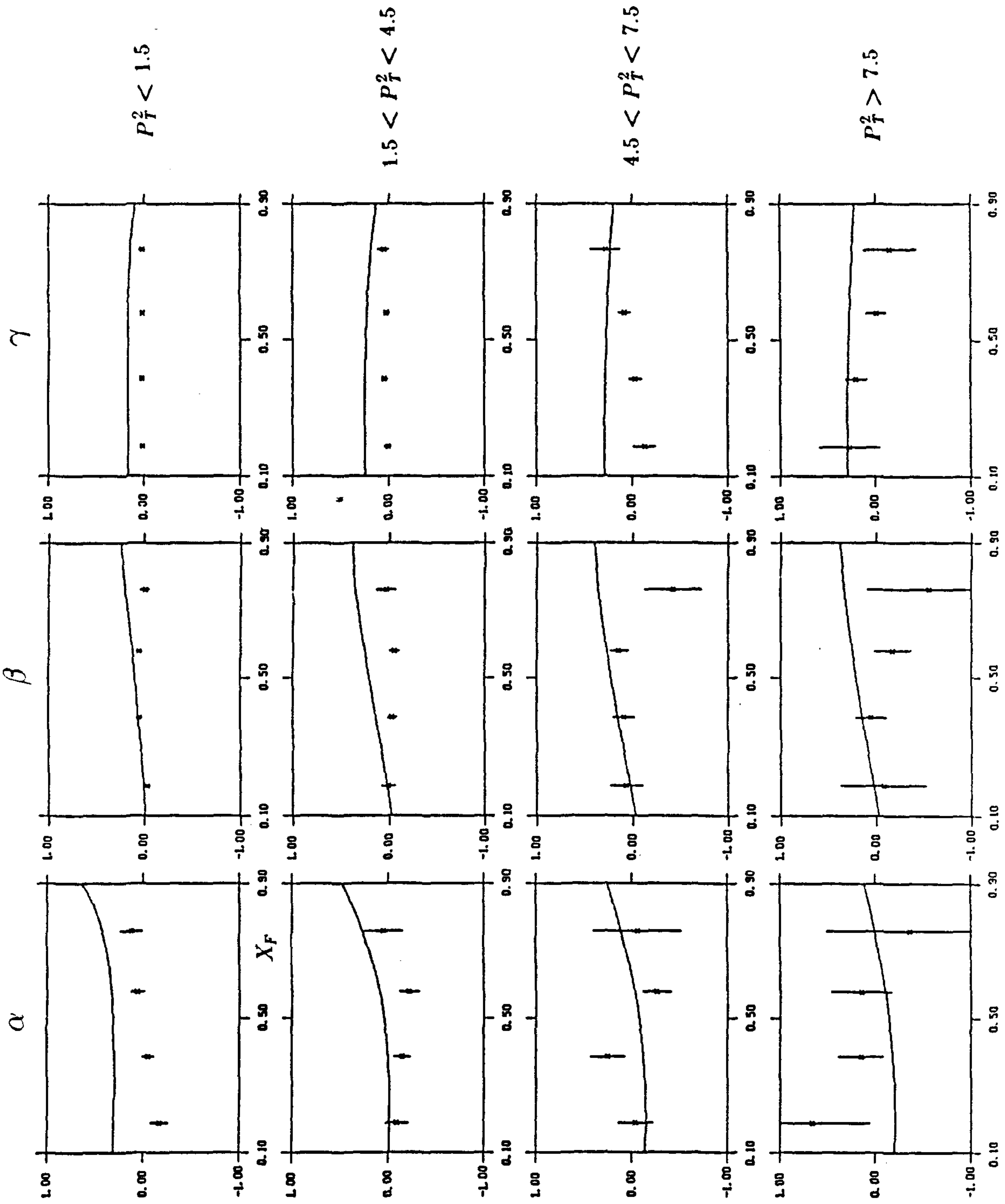
α
β
γ
X_F
$P_T^2 < 1.5$
$1.5 < P_T^2 < 4.5$
$4.5 < P_T^2 < 7.5$
$P_T^2 > 7.5$
1.00
0.00
-1.00
0.10
0.50
0.90

Figure 57 -- $d\sigma/d\cos(\theta)$ in four X_F and two P_T^2 regions ($P_T^2 < 4.5 GeV^2/c^2$). The curves are the results of the fits to the data assuming $\alpha = 0$.

Plot Assignments

	$P_T^2 < 1.5$	$1.5 < P_T^2 < 4.5$
$.1 < X_F < .3$	a	e
$.3 < X_F < .5$	b	f
$.5 < X_F < .7$	c	g
$.7 < X_F < .9$	d	h

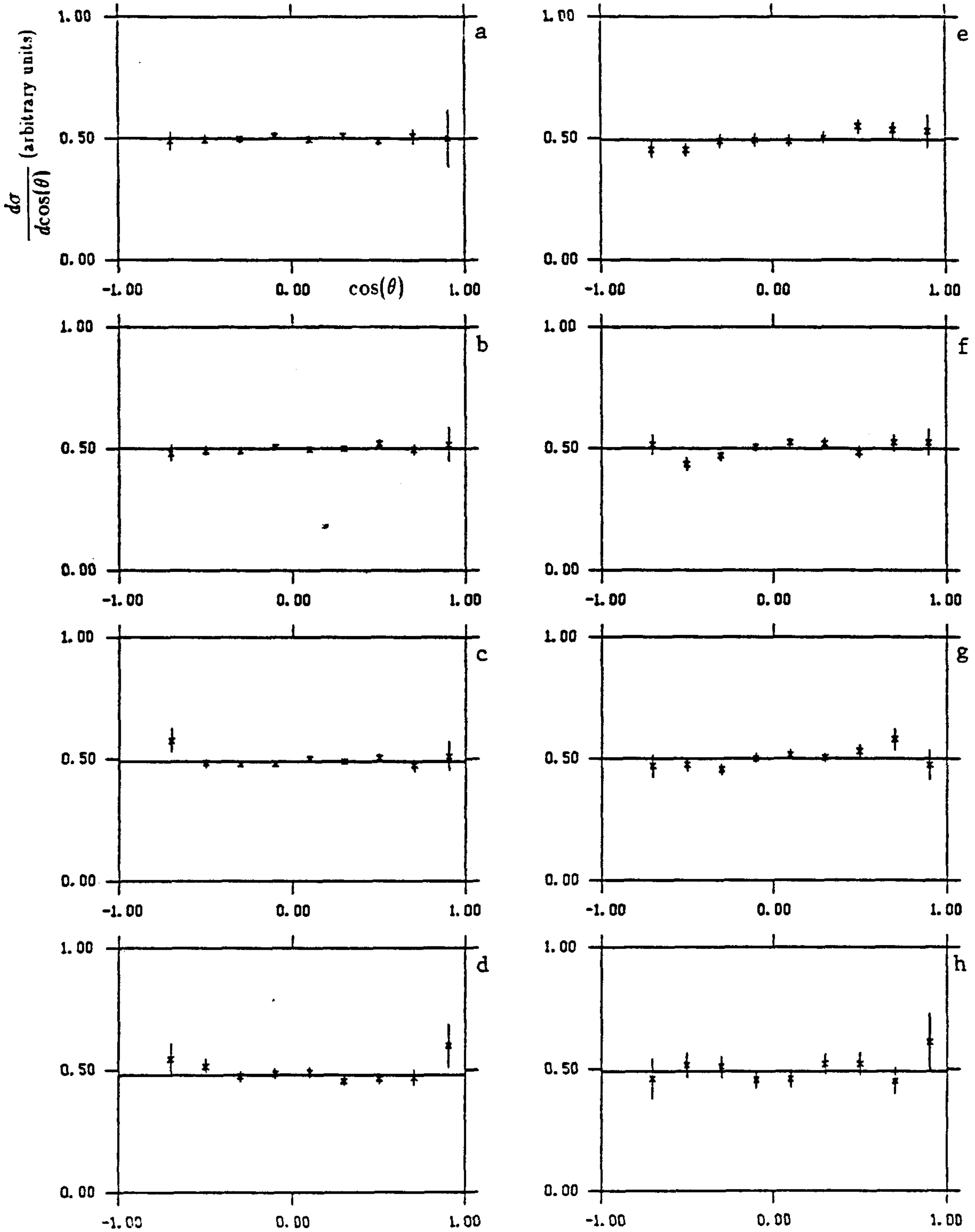
$\frac{d\sigma}{d\cos(\theta)}$ (arbitrary units)
cos(θ)
1.00
0.50
0.00
-1.00
0.00
1.00
a
b
c
d
e
f
g
h

Figure 58 -- $d\sigma/d\cos(\theta)$ in four X_F and two P_T^2 regions ($P_T^2 > 4.5 GeV^2/c^2$). The curves are the results of the fits to the data assuming $\alpha = 0$.

Plot Assignments

	$4.5 < P_T^2 < 7.5$	$P_T^2 > 7.5$
$.1 < X_F < .3$	a	e
$.3 < X_F < .5$	b	f
$.5 < X_F < .7$	c	g
$.7 < X_F < .9$	d	h

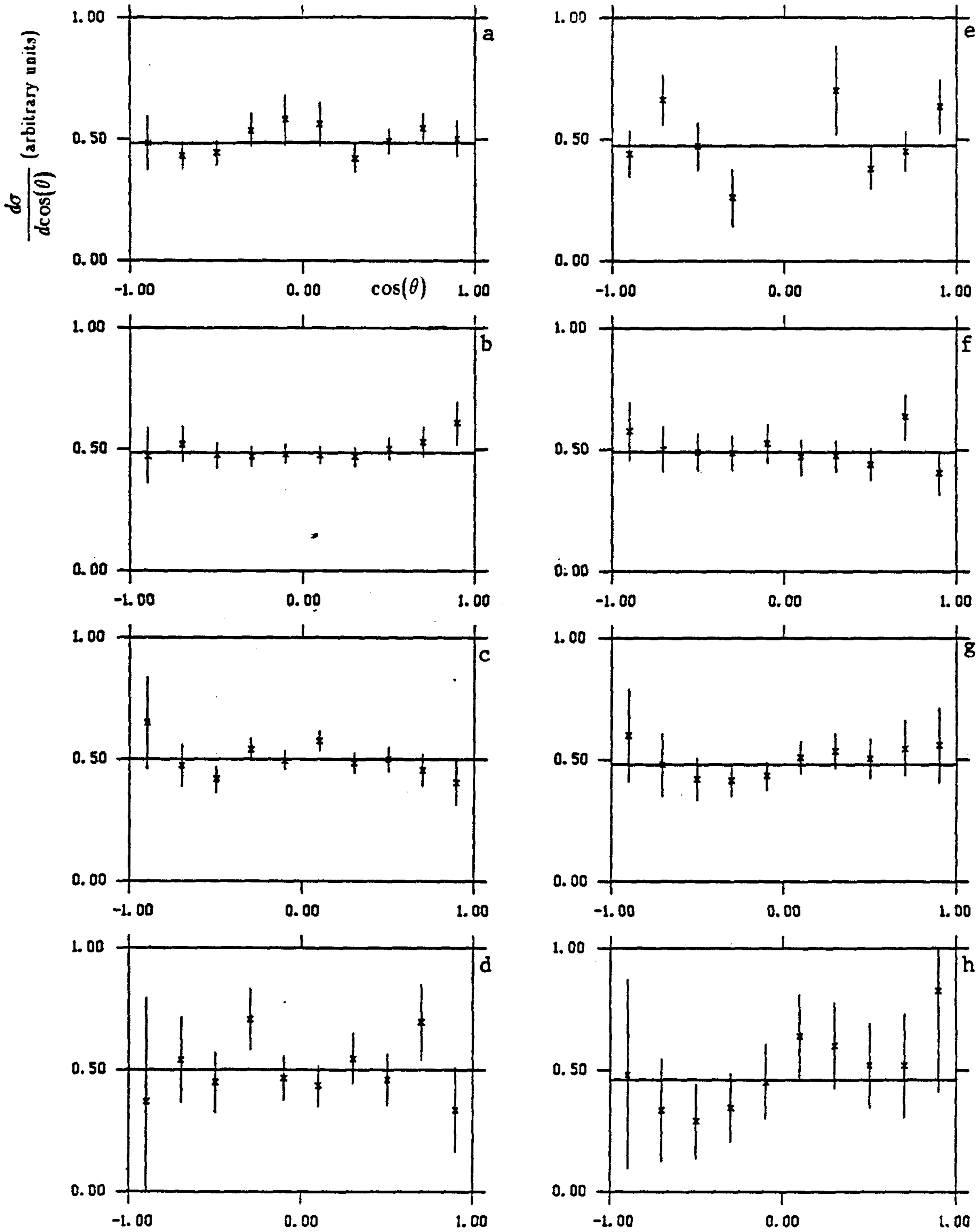
$\frac{d\sigma}{d\cos(\theta)}$ (arbitrary units)
1.00
0.50
0.00
-1.00
0.00
cos(θ)
1.00
a
b
c
d
e
f
g
h